Gyroscopes Orbiting Gargantuan Black Holes: Spinning Secondaries in Extreme Mass Ratio Inspirals

by

Lisa V. Drummond

B.Sc. (2014) and M.Sc. (2016),
The University of Melbourne

Submitted to the Department of Physics
in partial fulfillment of the requirements for the degree of

Doctor of Philosophy in Physics

at the

MASSACHUSETTS INSTITUTE OF TECHNOLOGY

May 2024

Authored by:	Lisa V. Drummond Department of Physics May 15, 2024
Certified by:	Scott A. Hughes Professor of Physics, Thesis Supervisor
Accepted by:	Lindley Winslow Associate Department Head of Physics

Gyroscropes Orbiting Gargantuan Black Holes: Spinning Secondaries in Extreme Mass Ratio Inspirals

by

Lisa V. Drummond

Submitted to the Department of Physics
on May 15, 2024 in partial fulfillment of the requirements for the degree of

DOCTOR OF PHILOSOPHY IN PHYSICS

ABSTRACT

Large mass ratio binary black hole systems are essential for studying the two-body problem in general relativity and are key sources of low-frequency gravitational waves. These sources will be detectable by the Laser Interferometer Space Antenna (LISA), which is a planned space-based gravitational-wave observatory. At lowest order, the secondary body (smaller black hole) follows a geodesic of the more massive black hole's spacetime. Post-geodesic effects are needed to model the system accurately. Failure to incorporate these effects can introduce bias in tests of general relativity and compromise precision measurement of the larger black hole's properties. One very important post-geodesic effect is the gravitational self-force, which describes the small body's interaction with its own contribution to a binary's spacetime and includes the backreaction of gravitational-wave emission driving inspiral. Another post-geodesic effect, the spin-curvature force, is due to the smaller body's spin coupling to spacetime curvature. Exploiting the large mass-ratio approximation, this thesis presents a suite of mathematical and computational tools for precisely calculating bound orbits and inspiral of spinning bodies around rotating black holes.

In Chapters 3 and 4, we employ a frequency-domain formulation to describe completely general orbits of spinning bodies in curved spacetime. The small body's spin influences orbital frequencies and accumulated phases which are direct gravitational-wave observables. In Chapter 5, we combine the leading orbit-averaged backreaction of point-particle gravitational-wave emission with the spin-curvature force to construct the trajectory and associated gravitational waveform of a spinning body inspiraling into a Kerr black hole. To achieve this, we use a near-identity transformation (NIT) to rapidly compute trajectories for generic orbit and spin configurations. This efficiency is essential for the high-dimensional, long-duration waveforms of large mass-ratio binary systems. In Chapter 6, we describe how the framework of Chapters 3 and 4 can be used to generate gravitational wave fluxes for spinning bodies on completely generic orbits and discuss a "shifted geodesic" approximation scheme which could speed up the evaluation of these fluxes. This thesis introduces methods for accurately modeling completely general orbits of spinning bodies in large mass ratio binary black hole systems, enhancing gravitational-wave models for the LISA science program, and introducing a limit that can be computed precisely as a benchmark for calculations across all mass ratios.

Thesis supervisor: Scott A. Hughes
Title: Professor of Physics

Acknowledgments

I would like to extend my deepest gratitude to my advisor, Scott Hughes. I am so incredibly fortunate to have had you as an advisor; thank you for sharing your immense scientific knowledge and for your endless understanding and kindness. I want to thank Halston Lim for being an amazing role model when I first joined the group and for encouraging me to join PhysREFS. I also want to thank Devin Becker – I am so glad that you joined Scott's group! You are one of my favorite people to discuss science with and I love attending conferences with you. I would also like to thank the other members of my thesis committee, Salvatore Vitale and Claude Canizares, for the time spent reviewing my thesis and for your thoughtful suggestions. Finally, thank you to Andrew Melatos for continuing to collaborate with and mentor me during my PhD, and for providing extremely helpful career advice. I am so glad that you were my MSc advisor and your role in my career has been absolutely invaluable.

I would like to thank all of the collaborators who worked with me during grad school. Thank you to Alex Hanselman, who was the first undergraduate I had the pleasure of working with as a grad student. It is amazing to see the work you are doing in grad school, and I am so excited to see where your career takes you! Thank you to Viktor Skoupý and Georgios Lukes-Gerakopoulos for collaborating with me and Scott, it was a privilege to work with you. Viktor, thank you for coming to MIT and sharing your research and ideas with us. Your enthusiasm is infectious and I hope to keep collaborating with you throughout my career! A big thank you to Phil Lynch, from whom I learned so much; you are a fantastic collaborator and taught me everything I know about NITs. Also, thank you to Celina and Julia Pasiecznik, working with both of you is an absolute delight. Thank you so much for hosting me at McGill and I hope we can continue exploring exciting science together!

I would like to give a special thanks to Vojtěch Witzany, for his excellent advice and for being an amazing science role model. I also want to thank Jonathan Thompson, Zach Nasipak, Gabriel Piovano, Phil Lynch, Josh Mathews, Lucy McNeill, Max Isi and Lilli Sun for their career and job search advice. Thank you also to Barry Wardell, Niels Warburton, Laura Sberna, Thomas Sotiriou, Silke Weinfurtner, and John Baker for taking time to discuss research proposal ideas with me. All of your advice was enormously helpful and I deeply appreciate it!

Thank you to the amazing graduate students at MKI. There are too many people to thank all of you here, but just know I appreciate you all so much and I am so lucky to have such an amazing community here at MIT. :) Thank you also to my wonderful Melbourne friends who have stayed in touch with me despite the enormous distance between us! Thank you to Graeme Berk, for your kindness, support, and endlessly interesting science conversations; phone calls with you always make me so happy. I hope your life in Singapore is filled with

many otter sightings! Thank you to Srivatsa Badariprasad, I have learned so much from you and our travel adventures are always a delight! Thank you to Jenny Peng and Liz Kindred for always being ready to have a call despite the time difference. Your continuing friendship means so much to me, and seeing you every time I return to Melbourne makes me very happy.

Thank you to my roommates, Kaliroë, Enid and Cammie, who have made me feel at home in Boston. I am lucky to have the best roommates I could possibly imagine. A special thank you to my roommates' cats, Kalypso and Sharma <3. Thank you to the many other cats and dogs who have provided emotional support during my PhD: Kitty (aka Boots), Luna, Lucky, Bilbo, Hopie and Bodie!

Finally, thank you to my family – Mum and Dad, your unconditional support and belief in me means so much and has been indispensable, not just during my PhD, but throughout my entire physics career. I cannot emphasize enough how grateful I am to you. Thanks to my brother-in-law Tony for your friendship and all the laughs. May you continue to count banana slugs wherever you go in California! Thank you to my twin sister Katie, I miss you everyday and I can't wait for us to live in the same state again. I love you so much.

Contents

List of Figures

List of Symbols

This list defines commonly-used symbols in this thesis for convenience; it is not exhaustive.

μ	Mass of secondary black hole
M	Mass of primary black hole
ε	Mass ratio of the EMRI system
p^μ	Four-momentum of secondary body
u^μ	Four-velocity of secondary body
$g_{\mu\nu}$	Metric of the background spacetime
a	Spin parameter of the primary black hole
(t, r, θ, ϕ)	Boyer-Lindquist coordinates
E	Energy per unit mass
L_z	Axial angular momentum per unit mass
K, Q	Forms of the Carter constant
z	Cosine of θ
p	Semilatus rectum of orbit
e	Eccentricity of orbit
I	Inclination angle of orbit
x_I	Cosine of I
χ_r	Radial relativistic true anomaly angle
χ_θ	Polar relativistic true anomaly angle
$R^\alpha_{\nu\lambda\sigma}$	Riemann curvature tensor of background spacetime
$S^{\alpha\beta}$	Spin tensor of secondary body
S^α	Spin vector of secondary body
S	Magnitude of spin vector of secondary body
s	Dimensionless secondary spin parameter viz., $s = \frac{S}{\mu^2}$
σ	Dimensionless secondary spin parameter viz., $\sigma = \frac{S}{M\mu}$
ψ_p	Secondary spin precession phase
$\Upsilon_{r/\theta/\phi/s}$	Radial/polar/azimuthal/spin-precession frequency conjugate to Mino-time
$\Omega_{r/\theta/\phi/s}$	Radial/polar/azimuthal/spin-precession frequency conjugate to coordinate-time
ψ_4	Weyl Newman-Penrose curvature scalar
h	Gravitational wave strain

Chapter 1

The Small and the Supermassive: Introduction to EMRI modeling

The discovery of gravitational waves (GWs) opened a new window into the Universe, inaugurating the field of gravitational-wave astronomy [1]. GWs are ripples in spacetime caused by accelerating massive objects. The chief emitters of GWs are coalescing binary systems of compact objects, such as black holes (BHs) and neutron stars. I discuss the different types of black holes in Sec. 1.1.1, including massive and supermassive black holes which have masses ranging from 10^5 to 10^9 solar masses and reside at the center of almost every galaxy. Future space-based gravitational wave detectors will enable observations of binary coalescences involving massive black holes, allowing us to probe their environment, as well as study their origin and growth. In Sec. 1.1.2, we briefly discuss black hole binary dynamics and its significance for GW observations. When a smaller compact object ($\sim 1 - 100 M_\odot$) enters a strong-gravity orbit around a massive black hole, a system called an extreme mass-ratio inspiral (EMRI) is created. Gravitational waves produced by these systems will allow us to tightly constrain theories of gravity and properties of massive black holes. Providing a motivation for and overview of EMRI modeling is the focus of this introductory chapter.

1.1 Astrophysical black holes

1.1.1 Black hole demographics

Broadly speaking, there are two main classes of astrophysical black holes: stellar and (super)massive. Stellar black holes typically have masses from 5 to several tens of solar masses and form after the collapse of massive progenitor stars. In addition, there is considerable evidence for massive black holes (MBHs) with masses between $\sim 10^5 - 10^7 M_\odot$, and supermassive black holes (SMBHs) with masses between $\sim 10^7 - 10^9 M_\odot$. Intermediate mass black holes (IMBHs) lie in the mass range between the stellar and massive classes. Primordial black holes (PBHs), which are hypothesized to have formed in the very early Universe, are another proposed class of black holes. Because their formation predates the first stars in the Universe, their masses can potentially lie outside the range observed for stellar black holes.

Stellar black holes are the final evolutionary stage of stars with masses between $\sim$

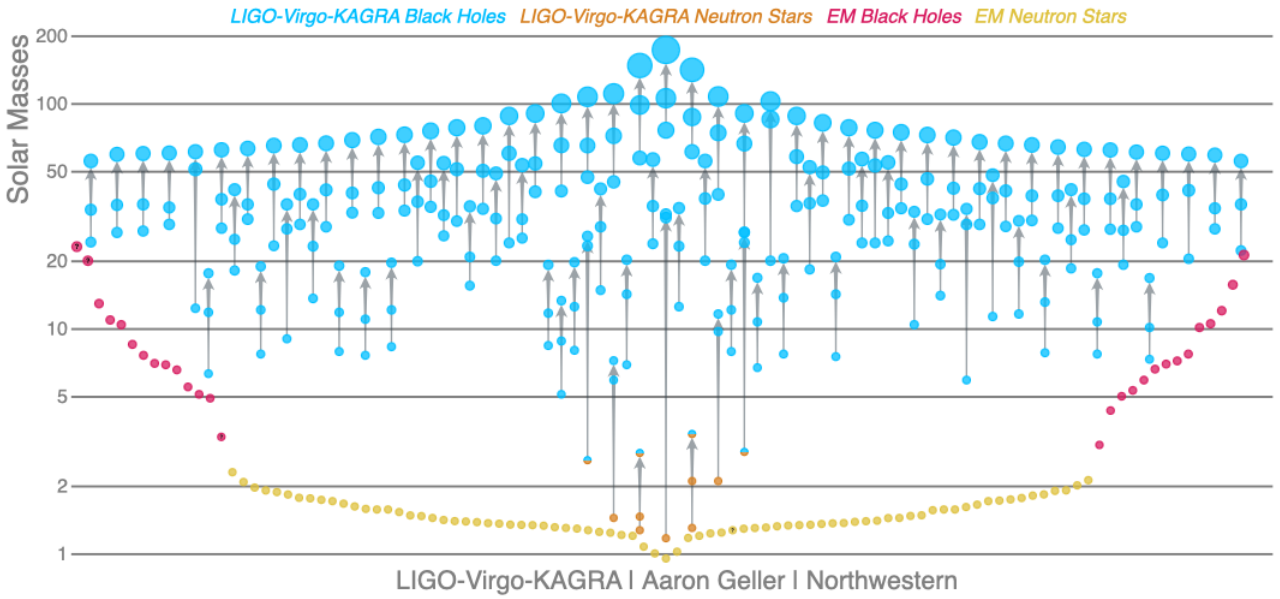

Figure 1.1: Schematic displaying the mass distribution of stellar compact objects. The blue circles correspond to LVK black holes, while the red circles correspond to stellar black holes detected electromagnetically. Image credit: Aaron Geller and the LVK collaboration, Northwestern.

$25 - 150M_\odot$. They have been observed both electromagnetically, primarily through X-rays emitted by the material surrounding the black hole, and via gravitational waves using laser interferometry. The first stellar black hole detected was in the X-ray binary Cygnus X-1, with a mass between 15 and 25 $M_\odot$, significantly exceeding the maximum mass of a neutron star [2], [3]. The first gravitational-wave detection of a coalescence of two stellar black holes was GW150914 [1], shown in Figure 1.2a. A census of stellar black hole demographics through both electromagnetic and gravitational wave observations is shown in Figure 1.1. These observations have shown evidence for an upper ($\sim 50 - 150M_\odot$) and lower ($\sim 2 - 5M_\odot$) mass gap. The mass distribution of neutron stars and black holes observed electromagnetically before the direct detection of gravitational waves displayed a clear lower gap [4]. Since then, gravitational wave detections such as GW190814 and GW230529 have provided evidence for the existence of compact objects in the lower mass-gap [5], [6]. There have also been more recent candidates for mass-gap objects discovered electromagnetically; see Refs. [7], [8]. These candidates can be seen in Figure 1.1.

There is strong evidence that the radio source Sagittarius A* at the Galactic Center is a massive black hole, with a mass of approximately $4 \times 10^6 M_\odot$. This estimate is derived from observing the orbits of S-stars near the Milky Way's center [9]. The Event Horizon Telescope (EHT), a global array of radio telescopes, has directly imaged Sagittarius A* and the supermassive black hole at the center of M87 [10], [11]. Electromagnetic observations suggest that all galaxies with central bulges likely host MBHs or SMBHs. Quasars, powered

by accretion onto SMBHs, have been observed at redshifts up to $z \approx 10$ [12]. The formation mechanisms for MBHs and SMBHs are not well understood; they likely formed through a combination of gas accretion and mergers of smaller black holes, but the initial masses and formation processes of the seed black holes remain unknown.

Observational evidence for intermediate-mass black holes with masses around $\mathcal{O}(100M_{\odot})$ has been scarce. The gravitational wave event GW190521 provided the first definitive evidence of an IMBH [13]. Additionally, gravitationally lensed gamma-ray bursts, such as GRB950830, offer further support for the existence of IMBHs [14]. While there is no conclusive evidence for primordial black holes (PBHs), their potential existence could address key astrophysical questions. For example, asteroid-sized PBHs are considered potential dark matter candidates, while heavier PBHs could serve as seeds for the formation of supermassive black holes.

1.1.2 Black hole binaries and the relativistic two-body problem

Currently operating gravitational wave detectors LIGO, Virgo, and KAGRA (LVK) are ground-based Michelson interferometers with Fabry-Perot cavities. Binary black holes are the primary sources of gravitational waves detected by LVK, enabling extensive tests of general relativity in the strong gravity regime [15], [16]. These tests probing strong-field gravity are essential for advancing our fundamental understanding of gravity. Traditional tests of general relativity have primarily examined weak-field gravity within the Solar System, such as the Gravity Probe B experiment [17], where deviations predicted by alternative theories may not be measurable. In addition to exploring fundamental aspects of gravity, gravitational waves from binary black holes provide insights into the astrophysical formation channels of compact objects [18].

We now discuss the various approximation schemes for modeling binary black holes systems in different regimes. As the binary's orbit decays due to gravitational-wave emission and coalesces, it progresses through three dynamic stages: inspiral, merger/plunge and ringdown, shown in Figure 1.2a. During inspiral, the binary is widely separated, and small corrections to Newtonian gravity accurately describes its evolution. Hence, it is well-described by Post-Newtonian theory. When the system enters the merger phase, deviations from Newtonian gravity become larger and the black holes coalesce in a strongly relativistic process. Typically, approximations cannot be used to describe this highly non-linear regime and the system is modeled using numerical relativity. After coalescence is the ringdown phase, where the remnant of the merger equilibriates to the Kerr solution for a rotating black hole [19]. During ringdown, the spacetime transitions to a perturbative regime described by the Kerr metric plus a perturbation. The three regimes are shown in Figure 1.2b.

In addition, certain types of black hole binaries are well-suited to a similar perturbative treatment. For example, consider a stellar black hole orbiting close to a massive black hole. This system is called an extreme mass ratio inspiral or EMRI, and the science we can achieve with EMRIs motivates much of the work in this thesis. The smaller black hole acts as a test body which perturbs the primary black hole's spacetime, allowing us to describe the binary using a perturbation to the Kerr metric to characterize the smaller body. This approach, known as black hole perturbation theory, will be discussed in more detail in the following sections of this chapter.

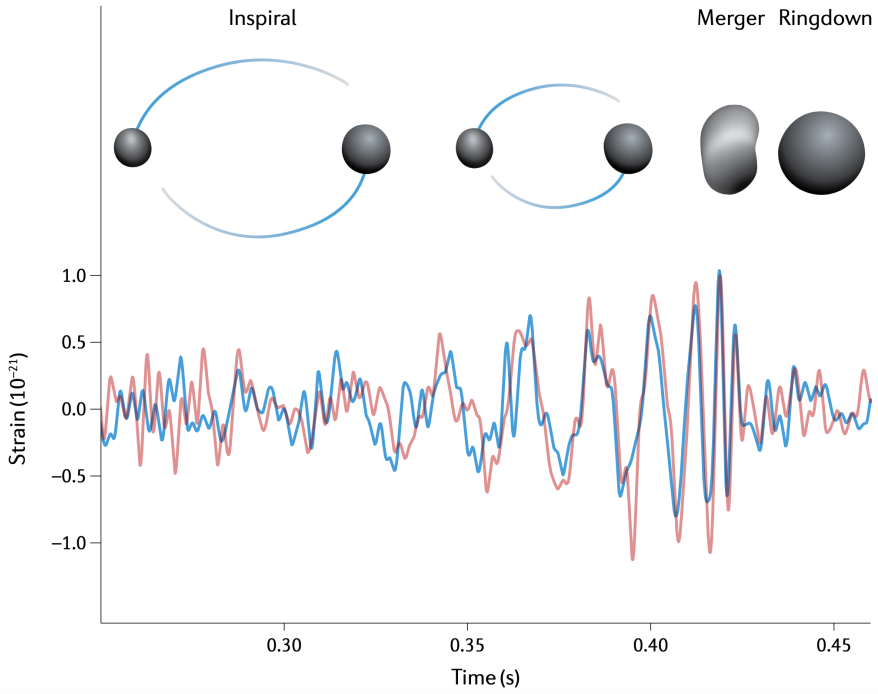

(a)

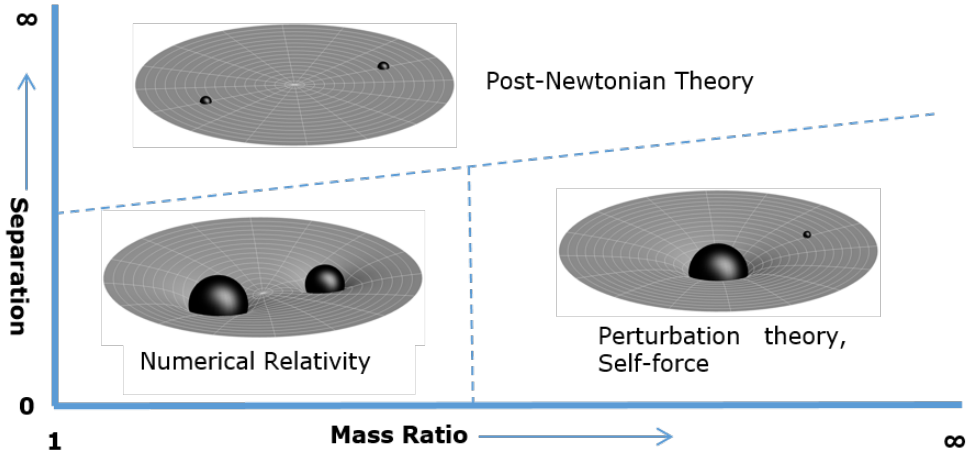

(b)

Figure 1.2: (a) The top diagram shows the three stages (inspiral, merger and ringdown) of a coalescing binary black hole system. The red and blue curves show the first gravitational wave signal (GW150914) from the Hanford and Livingston detectors respectively. Image ©LVK collaboration, adpated version of figure taken from Nature Reviews Physics volume 3, pages 344–366 (2021) [20] and reproduced under a Creative Commons Attribution 3.0 Unported license. (b) Diagram displaying different limits of the general relativistic two-body problem and the different methods used to model gravitational waves in each of these limits. Image ©Timothy Rias, image from Wikipedia and reproduced under a Creative Commons Attribution-Share Alike 3.0 Unported license.

1.2 Unlocking the potential of EMRIs

1.2.1 Motivation for EMRI science

Currently operating detectors LIGO, Virgo, and KAGRA (LVK) are ground-based and focus on GWs generated by pairs of stellar-mass compact objects in the frequency range ∼10–1000 Hz; they have detected more than one hundred signals with the commencement of Observing Run 4 (O4) in May 2023. Complementing this effort, Pulsar Timing Arrays such as NANOGrav survey ultra-low nanohertz frequencies and recently detected the first GW background signal [21]. On the horizon, in collaboration with NASA, ESA's recently adopted space-based interferometer LISA will target a rich population of millihertz sources, bridging the frequency gap between LIGO and NANOGrav. Unique sources detectable in the millihertz-GW sky by LISA are EMRIs.

This thesis focuses on developing models of gravitational waves produced by EMRIs, which form when a stellar-mass compact object (the secondary with mass μ) is captured into a strong-gravity orbit around a supermassive black hole (the primary with mass M) in a galactic center. Supermassive black holes reside in galactic centers while a large population of stellar-mass compact objects, including black holes and neutron stars, are dispersed throughout the entire galaxy. Mechanisms such as two-body relaxation and dynamical friction can scatter the stellar-mass objects close enough to the supermassive black hole to generate GWs, causing them to enter progressively tighter orbits governed by GW emission. GW emission depletes the energy of such systems, causing orbits to tighten during the inspiral phase and culminate in a plunge event, when the secondary black hole merges with the primary one.

EMRIs undergo thousands to millions of orbits in the LISA band; the extreme mass ratio means that inspiral is slow, and many cycles are spent in the strong field region of the larger black hole. Observations of EMRIs will therefore provide exquisitely precise measurements of supermassive black hole masses and spins with a fractional precision of 10^{-4}–10^{-6}, surpassing current LVK and X-ray observations [22]. With ten EMRI observations, the slope of the supermassive black hole mass function is expected to be determined precisely near $10^6 M\odot$, helping to disentangle the co-evolution of massive black holes with their host galaxies [23]. Due to their high mass ratios ($\varepsilon = \mu/M \sim 10^{-7}$–$10^{-4}$), EMRIs robustly test predictions of the theory of general relativity (GR) in the strong-field regime [24]. The multipolar structure of black holes will be measured at the subpercent level; any deviation from GR will thus be compelling evidence for new fundamental physics. Finally, due to sky localizations of a few square degrees, combined with cosmic distance measurements with better than 10% error, EMRIs have the potential to sharply constrain the value of the Hubble constant [22].

To summarize, a few open astrophysics problems that gravitational waves from EMRIs will address include: *How well does general relativity describe the strong-field regime near the horizon of black holes? What are the precise characteristics of massive black holes? What are the dynamics of compact objects in the vicinity of supermassive black holes?* Another motivation for studying EMRIs is that the large mass ratio simplifies the equations of motion, yielding tractable, semi-analytic solutions via perturbation theory. These perturbation theory models of EMRI motion can be compared to numerical simulations and extrapolated to smaller mass ratios, offering insights into the dynamics of generic binaries.

1.2.2 Black hole perturbation theory

We can only unlock the full potential of EMRI observations by developing gravitational waveform models that both accurately capture strong gravity effects near black holes and resolve the disparate length and time scales inherent to the EMRI system. Building such models is only possible using black hole perturbation theory, where we treat the secondary as a "test object" which minimally perturbs the primary to leading order. The EMRI's small mass ratio ε means we can treat the binary as the Kerr solution for a rotating black hole [19] plus a perturbation characterizing the smaller body. Fig. 1.3 displays a schematic of an extreme mass-ratio black hole binary system with mass ratio $\varepsilon = \mu/M$.

At leading order in ε, the small body's four-momentum p^α obeys the geodesic equation,

$$\frac{Dp^\alpha}{d\tau} = 0 \,, \tag{1.1}$$

where $D/d\tau$ is the covariant derivative along the orbit and τ is proper time. Post-geodesic effects, which can be modeled by adding a forcing term to the right-hand side,

$$\frac{Dp^\alpha}{d\tau} = f^\alpha \,, \tag{1.2}$$

describe physics beyond the leading "free fall" of a body. Schematically, we can write the spacetime metric of a large mass-ratio binary as

$$g^{\rm bin}_{\mu\nu} = g_{\mu\nu} + \underbrace{h^{(1)}_{\mu\nu}}_{\mathcal{O}(\varepsilon)} + \underbrace{h^{(2)}_{\mu\nu}}_{\mathcal{O}(\varepsilon^2)} + \mathcal{O}(\varepsilon^3) \,. \tag{1.3}$$

Here, $g^{\rm bin}_{\mu\nu}$ is the metric describing the binary system, and $g_{\mu\nu}$ is the "background" metric, describing its largest member. The contributions $h^{(1)}_{\mu\nu}$ and $h^{(2)}_{\mu\nu}$ are first- and second-order perturbations arising from the binary's smaller member. If the metric was unperturbed, so that we described the binary's spacetime as just of the background, $g^{\rm bin}_{\mu\nu} = g_{\mu\nu}$, then the trajectory of a non-spinning body would be given by the geodesic equation in the background $g_{\mu\nu}$ (see Sec. 2.1). The trajectory of a spinning body in this spacetime would be given by the Mathisson-Papapetrou equations, discussed in detail in Sec. 2.2. Including the metric perturbations $h^{(n)}_{\mu\nu}$ introduces self-force effects into the dynamics and leads to the decay of the orbit due to gravitational radiation reaction.

Therefore, post-geodesic corrections include the gravitational self-force, which is the interaction of an object with its own perturbation to the spacetime, and the spin-curvature force, due to the coupling between the secondary object's spin with the background spacetime curvature. In the adiabatic regime—characterized by slow GW emission—the trajectory evolves smoothly between geodesic orbits which gradually tighten due to GW emission. Adiabatic evolution is driven at leading order by the first-order dissipative self-force; the most important corrections to adiabatic evolution, called "post-adiabatic terms," include contributions from the secondary spin, the conservative first-order self-force, and the dissipative second-order self-force.

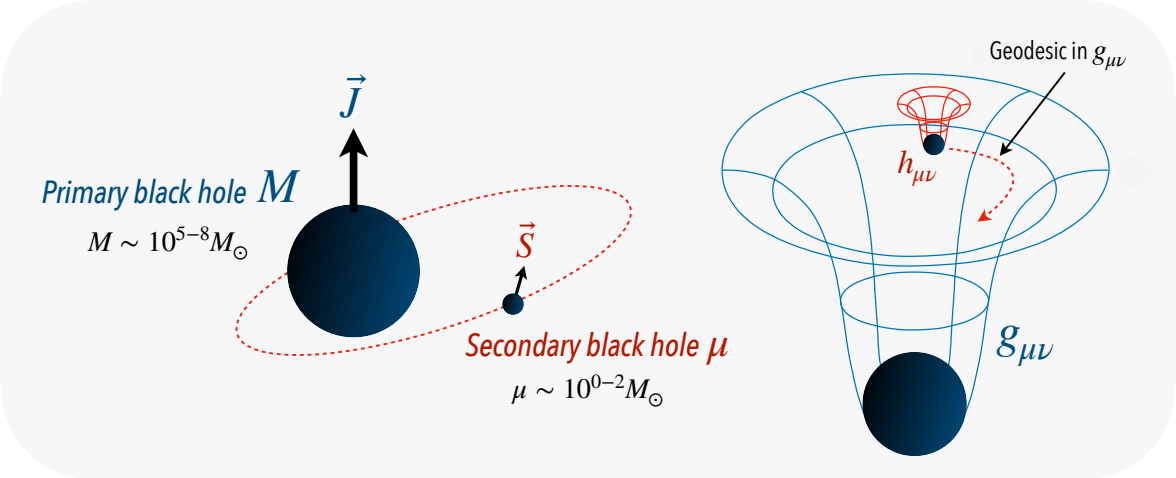

Figure 1.3: *Left.* Binary black hole system with a large mass ratio; M and μ label the masses, and $\vec{J}$ and $\vec{S}$ label the spins of the primary and secondary black holes respectively. *Right.* The spacetime metric of the primary black hole is $g_{\mu\nu}$ and $h_{\mu\nu}$ is the correction to the metric due to the secondary black hole. At lowest order, the secondary black hole follows a geodesic of the $g_{\mu\nu}$ metric.

1.3 Drivers of inspiral evolution

1.3.1 Post-geodesic corrections

Accurate EMRI modeling for measuring black hole parameters[1] with LISA necessitates the inclusion of post-geodesic corrections, which encompass backreaction from gravitational-wave emission and drive the inspiral. Additional corrections, including the spin-curvature force, arise if the secondary black hole possesses intrinsic angular momentum viz., secondary spin.

We can write the force on the right-hand side of Eq. (1.2) as

$$f^\alpha = \underbrace{f^{(1)\alpha}}_{\mathcal{O}(\varepsilon)} + \underbrace{f^{(2)\alpha}}_{\mathcal{O}(\varepsilon^2)} + \mathcal{O}(\varepsilon^3) \,. \tag{1.4}$$

The first-order term $f^{(1)\alpha}$ arises from $h^{(1)}_{\mu\nu}$ as well as the spin-curvature force, while $f^{(2)\alpha}$ is due to $h^{(2)}_{\mu\nu}$. Explictly, we have

$$f^{(1)\alpha} = f^{(1)\alpha}_{\rm mono} + f^\alpha_{\rm SCF} \,, \tag{1.5}$$

$$f^{(2)\alpha} = f^{(2)\alpha}_{\rm mono} + f^\alpha_{\rm dipole} \,, \tag{1.6}$$

where $f^\alpha_{\rm SCF}$ is the spin-curvature force, and $f^{(1)\alpha}_{\rm mono}$, $f^{(2)\alpha}_{\rm mono}$, and $f^\alpha_{\rm dipole}$ are contributions to the self-force. If the small body is a compact object, higher multipoles can generally be neglected, meaning that the pole-dipole approximation is used and the body is described entirely by its mass μ and spin S. The subscript "mono" denotes that the force is due to the

[1]For a list of physical parameters describing an EMRI model and estimates for the accuracy of parameter inference, see Ref. [25].

mass of the small body (the body's mass monopole); the subscript "dipole" denotes that the force is due to the spin of the small body (the body's mass current dipole). Here we provide an overview of different forcing effects, including those which are not part of the analyses presented in this thesis.

Many of these terms can also be broken into dissipative and conservative contributions. For example, the first-order self force can be usefully written

$$f^{(1)\alpha}_{\rm mono} = f^{(1)\alpha}_{\rm diss} + f^{(1)\alpha}_{\rm cons} \ . \tag{1.7}$$

The dissipative contribution, $f^{(1)\alpha}_{\rm diss}$, includes the leading radiation reaction and secular decay of the orbit; the conservative part of this force, $f^{(1)\alpha}_{\rm cons}$, describes forcing terms which perturb orbital elements without secular change to the orbit. Dissipative terms change sign under time reversal; conservative forces are time reversal symmetric. Although the self force contains both dissipative and conservative pieces, the spin-curvature force as described by the Mathisson-Papapetrou equations is conservative. For the purposes of the following discussion, it will be useful to divide the other forcing terms similarly, although it must be noted that it is somewhat tricky to split some of the second-order forcing terms into dissipative and conservative pieces:

$$f^{(2)\alpha}_{\rm mono} = f^{(2)\alpha}_{\rm diss} + f^{(2)\alpha}_{\rm cons} \ , \tag{1.8}$$

$$f^{\alpha}_{\rm dipole} = f^{\alpha}_{\rm dipole,diss} + f^{\alpha}_{\rm dipole,cons} \ . \tag{1.9}$$

1.3.2 Adiabatic approximation and post-1-adiabatic terms

In this work, we study very large mass ratio inspirals for which the time scale of orbital evolution is significantly longer than the time scale for individual orbits. This enables us to use an *adiabatic approximation*, which treats the inspiral as an orbit whose elements are secularly decaying due to GW backreaction. The adiabatic approximation neglects the conservative self force, but provides a framework that allows us to identify post-adiabatic corrections to the leading adiabatic evolution. To build an inspiral in this framework, we break the first-order dissipative self force into an orbit-averaged adiabatic part $f^{\alpha}_{\rm ad}$ plus oscillations about this average, $f^{\alpha}_{\rm oscil}$:

$$f^{(1)\alpha}_{\rm diss} = f^{\alpha}_{\rm ad} + f^{\alpha}_{\rm oscil} \ , \tag{1.10}$$

where

$$f^{\alpha}_{\rm ad} = \langle f^{(1)\alpha}_{\rm diss} \rangle \ , \quad f^{\alpha}_{\rm oscil} = f^{(1)\alpha}_{\rm diss} - \langle f^{(1)\alpha}_{\rm diss} \rangle \ . \tag{1.11}$$

The angle brackets denote a particular average over the orbit; see Eq. (1.4) of Ref. [26] for a precise definition of this average. A similar decomposition into orbit-averaged and oscillating pieces can be applied to other forcing terms. This decomposition introduces a two-time-scale expansion, separating orbit-averaged quantities which evolve slowly, on the system's radiation-reaction timescale, from those which oscillate rapidly, on the system's orbital timescale. This expansion provides an excellent framework for computing the contributions of rapidly oscillating perturbations to the phase of the gravitational waveform as well as the slowly evolving secular contributions [27].

Neglecting the issue of resonances (moments in the inspiral when two of the frequencies are in a small integer ratio, which complicates the averaging needed to define $f_{\rm ad}$ [27]–[30]), the influence of each of the post-geodesic forces on the phase of the waveform takes the form

$$\Phi = \underbrace{\varphi_0 \varepsilon^{-1}}_{\text{adiabatic: } f^\alpha_{\rm ad}} + \underbrace{\varphi_1 \varepsilon^{0}}_{\substack{\text{post-1-adiabatic: } f^\alpha_{\rm SCF} + \\ f^\alpha_{\rm oscil} + f^{(1)\alpha}_{\rm cons} + \langle f^{(2)\alpha}_{\rm diss}\rangle + \langle f^\alpha_{\rm dipole,diss}\rangle}} + \dots \,, \tag{1.12}$$

where the φ coefficients are dimensionless and do not depend on ε. The leading-order contribution to inspiral phase arises from the adiabatic, first-order force term $f^\alpha_{\rm ad}$. Neglecting resonances, the most important sub-leading terms come from post-1-adiabatic order forces, which phase counting analyses have shown must be included in order for the waveform to be accurate enough to match phase with LISA sources (e.g., to serve as "detection templates" [27]). The post-1-adiabatic order contribution to the inspiral phase comes from the oscillatory part of the dissipative first-order force $f^\alpha_{\rm oscil}$, the conservative part of the first-order self force $\langle f^{(1)\alpha}_{\rm cons}\rangle$, the orbit-averaged dissipative part of the second-order self force, and the spin-curvature force.

The $f^\alpha_{\rm SCF}$ and $\langle f^\alpha_{\rm dipole,diss}\rangle$ terms in the post-1-adiabatic piece of the gravitational-wave phase (1.12) arise due to the spin of the secondary black hole. These two contributions to the EMRI waveform are shown graphically in Fig. 1.4. First, the *kinematics* of the orbit changes due to the conservative spin-curvature force, given by the Mathisson-Papapetrou-Dixon equations [31]–[33]; we focus on this in Chapters 3 and 4. This corresponds to the $f^\alpha_{\rm SCF}$ contribution to the post-1-adiabatic term of the GW phase in Eq. (1.12). In addition, there is a correction to the *GW fluxes* of an orbiting small body due to the dipole term in the stress-energy tensor $T_{\mu\nu}$; we discuss this in Chapter 6. This corresponds to the $f^\alpha_{\rm dipole,diss}$ contribution to the post-1-adiabatic term of the GW phase in Eq. (1.12). The perturbed orbital kinematics must be combined with GW fluxes to generate a gravitational-radiation-driven inspiral; we compute inspirals which include spin-curvature force and point-particle gravitational wave fluxes in Chapter 5.

The flowchart at the bottom of Fig. 1.4 breaks down the steps associated with each calculation. The top row of the flowchart shows the steps associated with characterizing spinning-body orbits and their frequencies, while the bottom row displays the steps required to compute spinning-particle gravitational wave fluxes. Combining these two pieces together yields a complete accounting of spinning-secondary effects in extreme mass-ratio inspiral trajectories (the dark blue box in the bottom right corner of Fig. 1.4).

1.4 Past work on spinning-body motion near black holes

A great deal of work, both numerical and analytic, has gone into developing models for the dynamics of and gravitational waves produced by systems containing spinning members. Two limiting approaches have been used extensively for analytic modeling of such systems: the post-Newtonian PN approximation, formally good when members of the binary are widely separated and orbital speeds are small compared to light, and the extreme mass-ratio limit described in Sec. 1.2.2. The effective-one-body (EOB) framework synthesizes elements from

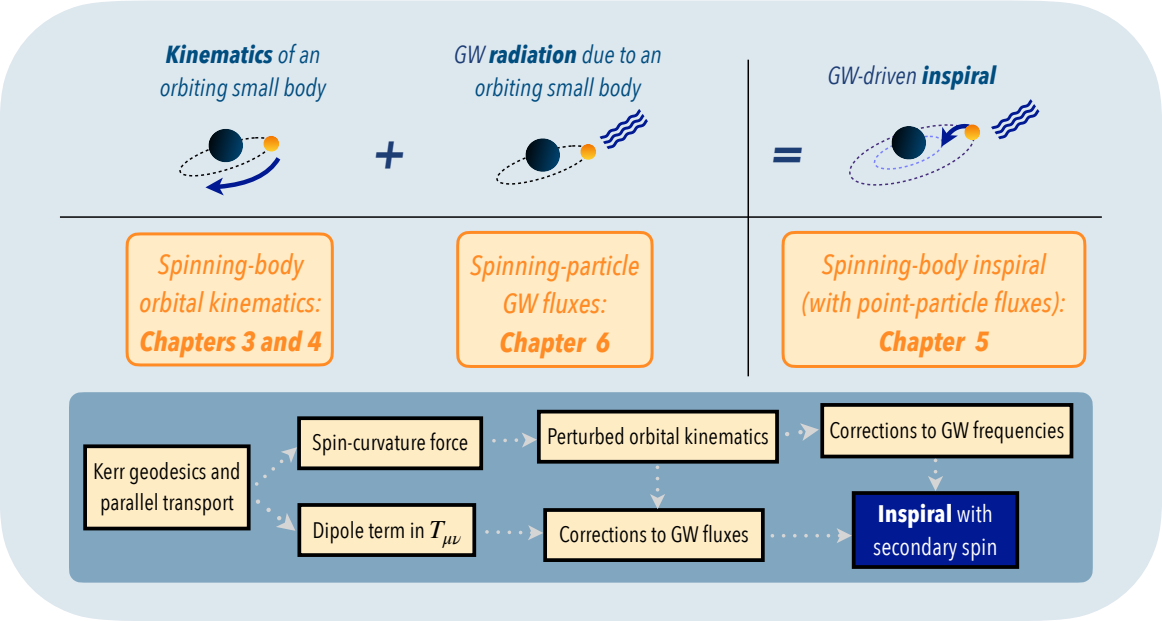

Figure 1.4: *Top:* Schematic of the different spinning-secondary contributions to large-mass ratio gravitational-wave driven trajectories. The orange text labels which thesis chapters describe the calculation of corresponding contributions. *Bottom:* Flowchart outlining the steps associated with the calculation of the different spinning secondary contributions to the inspiral trajectory.

post-Newtonian, extreme-mass-ratio, and numerical relativity results in order to construct a useful prescription for modeling inspirals across a wide parameter space.

1.4.1 Review: Orbital motion of spinning bodies

The dynamics of comparable mass binaries with spinning components has been explored in many post-Newtonian studies [34]–[40]; complementary to this, binaries with spinning members have been investigated extensively in numerical relativity simulations [41]–[46]. Considerable work has also been undertaken to develop EOB models that include spin and quantify their reliability [47]–[53]; a comparison of spinning effective one body Hamiltonians can be found in Ref. [54]. In addition, studies of the relativistic three-body problem correspond to the spinning two-body problem in certain regimes. For example, in hierarchical triple systems, there can be a correspondence between the orbital angular momentum of the so-called "inner" binary (a two-body system which itself orbits a massive black hole) and the spin of a test body. This correspondence holds if the separation of the inner binary is much smaller than the curvature scale associated with the black hole about which the inner binary orbits [55].

A number of studies have examined the motion of spinning bodies orbiting black holes. Many of these studies have focused either on numerical treatment of the Papapetrou equations (for example, Refs. [56]–[58]), or on constrained orbital geometries such as nearly circular or nearly equatorial orbits. For example, Ref. [59] finds analytic expressions for

the radial, meridional, and spin precession frequencies, including terms quadratic in spin for the limit of nearly circular, nearly equatorial orbits (see in particular Sec. IV B of [59]). Treating the system to first order in the small body's spin has astrophysical relevance in the context of EMRIs. A scheme of this type was outlined in Ref. [60] and elucidated further in Refs. [61], [62]. Spinning-body orbits have been computed to first order in spin using similar frameworks in Refs. [63]–[65]. A useful effective potential approach presented in Refs. [66]–[68] describes equatorial orbits when the spin of the small body is aligned with the orbit. This method has been employed to compute corrections to orbital frequencies and explore resonance effects for equatorial orbits [69]–[71]. Corrections to the innermost stable circular orbit (ISCO) location of spinning-body motion have also been calculated [72]–[77].

Another thread to this research is the use of a canonical Hamiltonian framework to describe the motion of a spinning body [78]. An explicit Hamiltonian for was presented to linear order in spin in Ref. [79], and later extended to quadratic order by Vines et al. [80]. This canonical Hamiltonian picture provides the basis for certain spinning EOB models [81], [82]. Witzany et al. presented an overview of Hamiltonian formulations of spinning-body motion in Ref. [83]. A Hamilton-Jacobi formulation of spinning-body motion, which exploits the separability of parallel transport in order to determine the turning points analytically, is also known and can be used to compute corrections to the orbital frequencies [84]. This analysis shows that the equations of motion "almost" separate — the librational motion in the radial and polar directions is coupled only by the way in which the libration region varies over an orbit. As such, Witzany shows that the equations of motion are amenable to computing important quantities such as frequencies associated with the orbits of spinning bodies.

Post-Newtonian analyses long ago indicated that spinning binaries exhibit chaotic dynamics [85]–[87]. The integrability of eccentric, spinning back hole binaries up to second post-Newtonian order was demonstrated in Ref. [39], with action angle variables presented explicitly in Ref. [40]. In the extreme mass ratio limit, numerical studies in both Schwarzschild [88] and Kerr [89], [90] backgrounds found evidence for chaotic motion. Witzany's linear-in-spin Hamilton-Jacabi analysis indicates that terms beyond linear in spin are necessary in order for orbits to exhibit chaos [84], and numerical studies have shown that prolonged resonances leading to chaotic motion can be attributed to terms that are quadratic in spin [91]. Recently, it has been shown that a Carter-like integral exists up to second-order in the small body's spin for a test body possessing exactly the spin-induced quadrupole moment expected for a Kerr black hole [92], [93].

1.4.2 Review: Gravitational radiation from spinning bodies

The first-order, orbit-averaged adiabatic self force, $f^{\alpha}_{\rm ad} \equiv \langle f^{(1)\alpha}_{\rm diss} \rangle$, acts to evolve the conserved quantities describing an orbit. The rates of change of these quantities (often called "fluxes") can be inferred by computing how the orbiting body perturbs the curvature of the binary spacetime. Most importantly, computing the adiabatic contribution only requires knowledge of the curvature perturbation at null infinity and on the large black hole's event horizon; we do not need these quantities at the orbit itself [94], [95]. These fluxes, and thus knowledge of how to evolve conserved orbital quantities, can be evaluated along generic orbits around

a Kerr black hole to obtain corresponding adiabatic inspirals and waveforms [26], [96]–[99].

The full first-order self force, including pieces that we neglect in our analysis, have been calculated on bound orbits around a Kerr black hole [100], [101] and used to generate non-spinning body inspirals [102]–[104]. Second-order self-force calculations of $f^{(2)\alpha}_{\rm mono}$ are just beginning to be applied to astrophysically interesting situations. Work to date has focused on computing this force in the Schwarzschild spacetime [105]–[107]. Detailed comparisons of effective-one-body waveforms with second-order self-force results have been undertaken [108], [109]. This already provides important constraining information which has been exploited to refine the description of binaries in the effective one-body approach [110].

The spin-curvature force $f^{\alpha}_{\rm SCF}$ is entirely conservative and given by the Mathisson-Papapetrou equations discussed in Sec. 2.2. It has been proven that the motion of a spinning body under the conservative piece of the self-force is Hamiltonian to first order in mass and spin; the explicit form of this Hamiltonian was also obtained, which will likely be useful for EMRI waveform calculations [111]. Inspirals along generic orbits around a non-rotating black hole including both the spin-curvature force as well as the first-order conservative and oscillating dissipative pieces of the self-force were computed in Ref. [112]. The impact of different spin supplementary conditions on gravitational wave fluxes has been explored for both Schwarzschild [113] and Kerr [114] black holes. It is crucial to understand and quantify the effect a small body's spin has on the dynamics of black hole orbits and the gravitational waves produced in spinning-body EMRI systems. The measurability of the secondary spin and its influence on EMRI parameter estimation has been assessed in previous studies [115]–[118].

For a spinning body orbiting a Kerr black hole, it is possible to construct the dissipative part of $f^{\alpha}_{\rm dipole}$, which enters at post-1-adiabatic order, from the time-averaged energy and angular momentum fluxes computed at infinity and at the black hole horizon [119]. Quasi-circular equatorial orbits with the spin of the small body aligned with the orbit provide a useful limit that has been studied extensively, and is often used to verify new methods for calculating gravitational wave fluxes. The fluxes have been evaluated for circular orbits of spinning bodies in both Schwarzschild [113], [120] and Kerr spacetimes [117], [121]–[123], as well as for eccentric equatorial orbits with aligned spin [67], [124] and quasi-circular orbits with misaligned spin [125]. Skoupý and Lukes-Gerakopoulos used these fluxes to compute the adiabatic inspiral of a spinning body in the equatorial plane of a Kerr black hole [126]. A study of the effect of a spinning secondary on the self force in a Schwarzschild background with aligned spin and a circular orbit was conducted by Mathews and collaborators [127]. Very recently, the asymptotic fluxes for generic spinning body orbits were computed for the first time [128]; part of this analysis is discussed in Chapter 6 of this thesis.

1.5 Overview of this thesis

The goal of this thesis is to characterize the role of secondary spin in the large mass-ratio limit of the general relativistic two-body problem, with the aim of precisely modeling gravitational wave signals produced by EMRIs. In particular, this thesis uses black hole perturbation theory to study the influence of the spin of the secondary black hole on (1) binary dynamics and (2) gravitational radiation. The remaining chapters comprise a technical introduction, sev-

eral published papers, preliminary results from ongoing work, and final conclusions. Much of the subsequent chapters rely on a shared theoretical background, which I outline in Chapter 2. All of the work in this thesis is theoretical, with a mixture of analytic and numerical analysis. The work in Chapters 3, 4, 5, and 6 is original and my own. Collaborators are acknowledged at the beginning of each chapter. In specific cases, we compare our work to existing results in the literature and clearly indicate where we conduct these comparisons.

Chapter 3 presents results that were originally published in the paper *Precisely computing bound orbits of spinning bodies around black holes. I. General framework and results for nearly equatorial orbits* [Drummond & Hughes, 2022a] [129]. In this paper, we describe a method for precisely computing bound orbits of spinning bodies about black holes. Exploiting the fact that in the large mass-ratio limit spinning-body orbits are close to geodesics (in a sense that can be made precise) and using closed-form results describing the precession of the small body's spin along black hole orbits, we develop a frequency-domain formulation of the motion which can be solved very precisely. We examine a range of orbits with this formulation, focusing on orbits which are eccentric and nearly equatorial, but for which the small body's spin is arbitrarily oriented. Chapter 4 is based on the companion paper for Chapter 3, *Precisely computing bound orbits of spinning bodies around black holes. II. Generic orbits* [Drummond & Hughes, 2022b] [130]. In this paper, we apply our formulation to the fully generic case—orbits which are inclined and eccentric, with the small body's spin arbitrarily oriented.

Chapter 5 presents results that were originally published in the paper *Extreme mass-ratio inspiral and waveforms for a spinning body into a Kerr black hole via osculating geodesics and near-identity transformations* [Drummond et al., 2024] [131]. In this paper, we use an osculating geodesic integrator, which treats the worldline as evolution through a sequence of geodesic orbits, as well as near-identity (averaging) transformations, which eliminate dependence on orbital phases, allowing for very fast computation of generic spinning-body inspirals. The resulting inspirals and waveforms include all critical dynamical effects which govern such systems (orbit and precession frequencies, inspiral, strong-field gravitational-wave amplitudes), and as such form an effective first model for the inspiral of spinning bodies into Kerr black holes. We emphasize that at present, this calculation is not self-consistent, since we neglect effects which enter at the same order as effects we include. However, the analysis demonstrates that the impact of spin-curvature forces can be incorporated into extreme mass-ratio inspiral waveform tools with relative ease, making it possible to augment these models with this important aspect of source physics.

Chapter 6 focuses on the computation of gravitational-wave fluxes for spinning particles orbiting black holes. This chapter contains parts of the paper *Asymptotic gravitational-wave fluxes from a spinning test body on generic orbits around a Kerr black hole* [Skoupý et al., 2023] [128], as well as presenting the methodology for an approximation scheme to compute GW fluxes. Chapter 7 provides a summary of the work presented in the thesis as well as plans for future work.

Chapter 2

Technical background

In this chapter, I present a brief discussion of technical material relevant to the rest of the thesis. In Sec. 2.1, I review properties of geodesics of the Kerr metric, which describe rotating black hole spacetimes in vacuum. Section 2.2 discusses spinning-body orbits in curved spacetimes, while Section 2.3 describes the calculation of the leading order terms in adiabatic radiation-reaction using the Teukolksy formalism.

2.1 Geodesics in Kerr spacetime

Because we describe orbits of spinning bodies as perturbations of the orbits of non-spinning bodies, we begin by briefly reviewing the properties of Kerr geodesics. This content has been discussed at great length elsewhere [132]–[141]; here we provide a brief synopsis in order for the thesis to be self-contained, and to introduce important notation and conventions.

2.1.1 Kerr metric and constants of motion

The metric for a Kerr black hole with mass M and spin parameter a in Boyer-Lindquist coordinates t, r, θ, ϕ [142] reads

$$\begin{aligned} ds^2 = &-\left(1-\frac{2r}{\Sigma}\right)dt^2 + \frac{\Sigma}{\Delta}\,dr^2 - \frac{4Mar\sin^2\theta}{\Sigma}dt\,d\phi + \Sigma\,d\theta^2 \\ &+ \frac{\left(r^2+a^2\right)^2 - a^2\Delta\sin^2\theta}{\Sigma}\sin^2\theta\,d\phi^2, \end{aligned} \tag{2.1}$$

where

$$\Delta = r^2 - 2Mr + a^2\,, \qquad \Sigma = r^2 + a^2\cos^2\theta\,. \tag{2.2}$$

(Here and throughout we use geometrized units, with $G = 1 = c$.)

Four constants of motion characterize Kerr geodesics. The first is the rest mass μ of the orbiting body. It is determined by requiring $\hat{p}^\alpha = \mu\hat{u}^\alpha$ (where $\hat{p}^\alpha$ is the geodesic's 4-momentum, and $\hat{u}^\alpha$ its 4-velocity; we use the hat accent to denote quantities defined along geodesics) and by requiring the norm of the 4-velocity to be -1. The Kerr metric (2.1) is independent of the coordinates t and ϕ, implying that the spacetime possesses two Killing

vectors ξ_t^α and ξ_ϕ^α, corresponding to time translation and axial symmetries respectively. These Killing vectors yield two more constants of the motion, the energy per unit mass $\hat{E}$ and axial angular momentum per unit mass $\hat{L}_z$:

$$\hat{E} = -\xi_t^\alpha \hat{u}_\mu = -\hat{u}_t \ , \tag{2.3}$$

$$\hat{L}_z = \xi_\phi^\alpha \hat{u}_\mu = \hat{u}_\phi \ . \tag{2.4}$$

Note that we have normalized these quantities by the mass μ of the orbiting body.

The Kerr metric also admits an anti-symmetric Killing-Yano tensor [143], given by [125]

$$\mathcal{F}_{\mu\nu} = a\cos\theta\left(\bar{e}^1_\mu \bar{e}^0_\nu - \bar{e}^0_\mu \bar{e}^1_\nu\right) + r\left(\bar{e}^2_\mu \bar{e}^3_\nu - \bar{e}^3_\mu \bar{e}^2_\nu\right) \ , \tag{2.5}$$

where

$$\bar{e}^0_\mu = \left[\sqrt{\frac{\Delta}{\Sigma}}, 0, 0, -a\sin^2\theta\sqrt{\frac{\Delta}{\Sigma}}\right] , \tag{2.6}$$

$$\bar{e}^1_\mu = \left[0, \sqrt{\frac{\Sigma}{\Delta}}, 0, 0\right] , \tag{2.7}$$

$$\bar{e}^2_\mu = \left[0, 0, \sqrt{\Sigma}, 0\right] , \tag{2.8}$$

$$\bar{e}^3_\mu = \left[-\frac{a\sin\theta}{\sqrt{\Sigma}}, 0, 0, \frac{(r^2+a^2)\sin\theta}{\sqrt{\Sigma}}\right] . \tag{2.9}$$

This tensor has the defining property

$$\nabla_\gamma \mathcal{F}_{\alpha\beta} + \nabla_\beta \mathcal{F}_{\alpha\gamma} = 0 \ . \tag{2.10}$$

Let us define the vector

$$\hat{\mathcal{L}}^\nu = \mathcal{F}^{\mu\nu}\hat{u}_\mu \ . \tag{2.11}$$

We will call this the orbital angular momentum 4-vector, since it has the dimensions of orbital angular momentum (per unit mass of the orbiting body), and reduces to the orbital angular momentum in the Schwarzschild limit.

Notice that in Refs. [84] and [144], this vector is defined with the index contracted on the second index of $\mathcal{F}^{\mu\nu}$. Because of the Killing-Yano tensor's antisymmetry, this results in an overall sign difference. With the definition (2.11), equatorial orbits have $\hat{\mathcal{L}}^\theta \propto -\hat{L}_z$. This is a sensible correspondence, since (by right-hand rule) one expects the angular momentum of a prograde equatorial orbit (for which $\hat{L}_z > 0$) to point opposite to the direction of increasing polar angle θ. We have found that this sign swap is needed to establish correspondence between our results and important examples of past literature. In particular, past work which examined equatorial orbits of bodies with spin aligned with the large black hole's spin and with the orbital angular momentum typically designate the small body's spin as pointing along the "z direction." This correspondence requires the "z direction" (i.e., parallel to the large black hole's spin) to point in the direction of decreasing θ at the equatorial plane.

From the antisymmetry of $\mathcal{F}^{\mu\nu}$ we see that

$$\hat{\mathcal{L}}^\mu \hat{u}_\mu = 0 \ . \tag{2.12}$$

Further, using Eq. (2.10), it is straightforward to show that $\hat{\mathcal{L}}^\mu$ is parallel-transported along geodesics:

$$\frac{D\hat{\mathcal{L}}^\beta}{d\tau} \equiv \hat{u}^\alpha \nabla_\alpha \hat{\mathcal{L}}^\beta = 0 \,. \tag{2.13}$$

It is also not hard to show that the square of this vector

$$\hat{K} = \hat{\mathcal{L}}^\mu \hat{\mathcal{L}}_\mu \tag{2.14}$$

is conserved, i.e. that

$$\frac{D\hat{K}}{d\tau} \equiv \hat{u}^\alpha \nabla_\alpha \hat{K} = 0 \,. \tag{2.15}$$

Carter [145] first demonstrated the existence of a fourth conserved constant for Kerr geodesic motion. This constant arises from a Killing tensor $K_{\mu\nu}$, which can be thought of as the "square" of $\mathcal{F}_{\mu\nu}$,

$$K_{\mu\nu} = \mathcal{F}_{\mu\alpha}\mathcal{F}_\nu{}^\alpha \,. \tag{2.16}$$

The corresponding constant

$$\hat{K} = K_{\alpha\beta}\hat{u}^\alpha \hat{u}^\beta \tag{2.17}$$

is identical to the $\hat{K}$ defined in (2.14), and is usually called the "Carter constant." For many analyses, it is particularly convenient to combine $\hat{K}$, $\hat{E}$, and $\hat{L}_z$ into a related conserved quantity $\hat{Q}$ given by

$$\hat{Q} = \hat{K} - \left(\hat{L}_z - a\hat{E}\right)^2 \tag{2.18}$$

$$= \hat{p}_\theta^2 + a^2 \cos^2\hat{\theta}\left(1 - \hat{E}^2\right) + \cot^2\hat{\theta}\,\hat{L}_z^2 \,. \tag{2.19}$$

Confusingly, $\hat{Q}$ is also often called the Carter constant; we will use both $\hat{K}$ and $\hat{Q}$ from time to time in our analysis. The constant $\hat{Q}$ is particularly useful for discussing geodesics, so we focus on this version of the Carter constant in the remainder of this section.

2.1.2 4-velocities, turning points, and parameterization

Carter first showed that the existence of these conserved quantities permits the geodesic equations to be separated in Boyer-Lindquist coordinates [145]. These separated equations are given by

$$\Sigma^2\left(\frac{d\hat{r}}{d\tau}\right)^2 = [\hat{E}(\hat{r}^2+a^2) - a\hat{L}_z]^2 - \Delta[\hat{r}^2 + (\hat{L}_z - a\hat{E})^2 + \hat{Q}] \equiv R(\hat{r}) \,, \tag{2.20}$$

$$\Sigma^2\left(\frac{d\hat{\theta}}{d\tau}\right)^2 = \hat{Q} - \cot^2\hat{\theta}\hat{L}_z^2 - a^2\cos^2\hat{\theta}(1-\hat{E}^2) \equiv \Theta(\hat{\theta}) \,, \tag{2.21}$$

$$\Sigma\frac{d\hat{\phi}}{d\tau} = \csc^2\hat{\theta}\hat{L}_z + a\hat{E}\left(\frac{\hat{r}^2+a^2}{\Delta} - 1\right) - \frac{a^2\hat{L}_z}{\Delta} \equiv \Phi(\hat{r},\hat{\theta}) \,, \tag{2.22}$$

$$\Sigma\frac{d\hat{t}}{d\tau} = \hat{E}\left(\frac{(\hat{r}^2+a^2)^2}{\Delta} - a^2\sin^2\hat{\theta}\right) + a\hat{L}_z\left(1 - \frac{\hat{r}^2+a^2}{\Delta}\right) \equiv T(\hat{r},\hat{\theta}) \,. \tag{2.23}$$

Because these are evaluated strictly along geodesic orbits, we parameterize them using the coordinates $(\hat{r}, \hat{\theta}, \hat{\phi}, \hat{t})$ of such an orbit. Equations (2.20) – (2.23) are parameterized using proper time τ along the orbit. As written, these equations are not completely separated: the factor $\Sigma = \hat{r}^2 + a^2 \cos^2 \hat{\theta}$ couples the radial and polar motions. By introducing a new time parameter λ, commonly called "Mino time" and defined by $d\lambda = d\tau/\Sigma$ [94], the radial and polar equations of motion decouple, yielding

$$\left(\frac{d\hat{r}}{d\lambda}\right)^2 = R(\hat{r}) \ , \qquad \left(\frac{d\hat{\theta}}{d\lambda}\right)^2 = \Theta(\hat{\theta}) \ ,$$
$$\frac{d\hat{\phi}}{d\lambda} = \Phi(\hat{r}, \hat{\theta}) \ , \qquad \frac{d\hat{t}}{d\lambda} = T(\hat{r}, \hat{\theta}) \ . \tag{2.24}$$

Mino-time λ is a very convenient parameterization for describing the strong-field dynamics of Kerr black hole orbits. By using $d\hat{t}/d\lambda$, it is not difficult to convert from λ to Boyer-Lindquist time t, which naturally describes quantities as measured by a distant observer.

To understand the turning points of bound geodesics and the parameterization that we use, begin by carefully examining the functions $R(\hat{r})$ and $\Theta(\hat{\theta})$. For bound orbits, $R(\hat{r})$ can be written

$$R(\hat{r}) = (1 - \hat{E}^2)(r_1 - \hat{r})(\hat{r} - r_2)(\hat{r} - r_3)(\hat{r} - r_4) \ , \tag{2.25}$$

where the roots are ordered such that $r_4 \leq r_3 \leq r_2 \leq \hat{r} \leq r_1$. The roots r_1 and r_2 are turning points of the motion. Likewise, $\Theta(\hat{\theta})$ can be written

$$\Theta(\hat{\theta}) = \frac{a^2}{\sin^2 \hat{\theta}} \left(1 - \hat{E}^2\right) \left(z_+^2 - \cos^2 \hat{\theta}\right) \left(z_-^2 - \cos^2 \hat{\theta}\right) \ , \tag{2.26}$$

where we have introduced $\hat{z} \equiv \cos \hat{\theta}$. These roots are ordered such that $0 \leq z_- \leq 1 \leq z_+$; turning points of the motion occur where $\hat{z} = z_-$. This occurs when $\hat{\theta} = \theta_-$ and $\hat{\theta} = \pi - \theta_-$, defined by $\cos \theta_- = z_-$.

Bound geodesics are thus confined to a torus, bounded in radius by $r_2 \leq \hat{r} \leq r_1$ and in polar angle by $\theta_- \leq \hat{\theta} \leq (\pi - \theta_-)$. We can build these bounds into the orbiting body's motion by defining

$$\hat{r} = \frac{pM}{1 + e \cos \hat{\chi}_r} \ , \tag{2.27}$$
$$\cos \hat{\theta} = \sin I \cos \hat{\chi}_\theta \ . \tag{2.28}$$

The angles $\hat{\chi}_r$ and $\hat{\chi}_\theta$ are relativistic generalizations of the "true anomaly" angles often used in Newtonian orbital dynamics; these angles increase monotonically over an orbit. The parameters p and e are the orbit's semi-latus rectum and eccentricity, respectively; in the Newtonian limit, they correspond to the equivalent parameters which define a Keplerian ellipse. By inspection, one can see that

$$r_1 = \frac{pM}{1 - e} \ , \qquad r_2 = \frac{pM}{1 + e} \ . \tag{2.29}$$

The angle I defines the inclination of the orbit; it is related to the angle θ_- according to

$$I = \pi/2 - \mathrm{sgn}(\hat{L}_z)\theta_- \ . \tag{2.30}$$

This angle automatically encodes a notion of prograde ($\hat{L}_z > 0$, $I < 90°$) and retrograde ($\hat{L}_z < 0$, $I > 90°$) orbits. Equatorial orbits ($\theta_- = 90°$) have $I = 0°$ (prograde) or $I = 180°$ (retrograde). Throughout this thesis, we will also use $x_I \equiv \cos I$.

Up to initial conditions, an orbit can be specified by either the set of constants of the motion ($\hat{E}$, $\hat{L}_z$, $\hat{Q}$) or the quantities (p, e, I) which determine the orbit's geometry (being careful to choose values which do not go inside the "last stable orbit," the locus of parameter space inside which bound orbits are unstable and rapidly plunge into the black hole; see [146] for discussion). In this analysis, we use (p, e, I), and then use expressions given in Refs. [139], [144] (see also App. A of Ref. [147]) to determine $\hat{E}$, $\hat{L}_z$, and $\hat{Q}$. Once these parameters are known, we can use closed-form expressions for the solutions to the geodesic equations (2.20–2.23), formulated in terms of elliptic functions [139]. We also use solutions for bound geodesic trajectories as functions of Mino-time, $\hat{r}(\lambda)$ and $\hat{z}(\lambda)$, using the simplified form given by van de Meent [144]. Formulae for computing geodesic trajectories are implemented in the `KerrGeodesics` *Mathematica* package of the Black Hole Perturbation Toolkit (hereafter "the Toolkit") [148].

2.2 The motion of a spinning body

Strictly speaking, geodesics describe only the motion of zero-mass point particles. Any mass deforms the spacetime, pushing its trajectory away from the geodesic; any structure beyond a point can couple to spacetime curvature, also pushing its trajectory away from the geodesic. The leading example of such structure is the body's spin. We now consider the orbital motion of a pointlike body endowed with spin angular momentum.

2.2.1 Spin-curvature coupling

A small spinning body moving in a curved spacetime precesses as it moves along its trajectory, and couples to the curvature of the background spacetime. The equations governing this precession and motion are known as the Mathisson-Papapetrou equations [31]–[33], [149], and are given by

$$\frac{Dp^\alpha}{d\tau} = -\frac{1}{2} R^\alpha{}_{\nu\lambda\sigma} u^\nu S^{\lambda\sigma} \,, \tag{2.31}$$

$$\frac{DS^{\alpha\beta}}{d\tau} = p^\alpha u^\beta - p^\beta u^\alpha \,. \tag{2.32}$$

In these equations, the operator $D/d\tau$ denotes a covariant derivative along the small body's worldline, $R^\alpha{}_{\nu\lambda\sigma}$ is the Riemann curvature of the spacetime in which the small body orbits, $S^{\lambda\sigma}$ is the small body's spin tensor (about which we say more below), p^α is the small body's 4-momentum, and $u^\nu = dx^\nu/d\tau$ is its 4-velocity. In general, a spinning body's 4-momentum and 4-velocity are not parallel to each other, but are related by

$$p^\alpha = \mu u^\alpha - u_\gamma \frac{DS^{\alpha\gamma}}{d\tau} \,. \tag{2.33}$$

Including additional structure on the small body leads to more complicated equations of motion. For example, the small body's quadrupole moment couples to the gradient of curvature [150]–[152] and introduces additional torque terms [153]. The Mathisson-Papapetrou equations represent the "pole-dipole" approximation, in which the small body is treated as a monopolar point mass supplemented with a dipolar spin.

For each spacetime Killing vector ξ^α there is a constant of motion along the spinning body's worldline given by

$$\mathcal{C} = p_\alpha \xi^\alpha - \frac{1}{2} S^{\alpha\beta} \nabla_\beta \xi_\alpha \, . \tag{2.34}$$

Using this, one finds that the conserved energy and axial angular momentum per unit mass for a spinning body moving in a Kerr spacetime are given by

$$E^S = -u_t + \frac{1}{2\mu} S^{\alpha\beta} \partial_\beta g_{t\alpha}, \tag{2.35}$$

$$L_z^S = u_\phi - \frac{1}{2\mu} S^{\alpha\beta} \partial_\beta g_{\phi\alpha}. \tag{2.36}$$

There is no Carter constant for a spinning body, though (as we discuss below) there is a generalization of the Carter constant which is conserved to linear order in the small body's spin.

2.2.2 Spin supplementary conditions

Equations (2.31) and (2.32) do not completely specify the evolution of all degrees of freedom in the orbit of a spinning body; we must impose an additional constraint in order to close the system of equations. This constraint is called the Spin Supplementary Condition (SSC), and can be regarded as fixing internal degrees of freedom associated with the extended structure of the small body. In the non-relativistic limit, the center of mass can be identified as the natural place for the worldline to pass through the extended body. However, the location of the center of mass is observer dependent in relativistic dynamics. The role of the SSC is thus to select one of the infinite choices of worldlines passing through the small body. Since there is in general no natural choice for the worldline, the SSC is intrinsically arbitrary. Excellent discussion of the physical meaning of the SSC can be found in Ref. [154]; comparisons of different SSCs and investigation of their equivalence can be found in Refs. [155]–[159].

An SSC commonly used in studies of gravitational wave sources is due to Tulczyjew [160], and is given by

$$p_\alpha S^{\alpha\beta} = 0 \, . \tag{2.37}$$

Using (2.37), we find the relationship between the four-velocity and the four-momentum (2.33) is now given by

$$u^\mu = \frac{\mathcal{M}}{\mu^2} \left(p^\mu + \frac{2 S^{\mu\nu} R_{\nu\rho\sigma\tau} p^\rho S^{\sigma\tau}}{4\mu^2 + R_{\alpha\beta\gamma\delta} S^{\alpha\beta} S^{\gamma\delta}} \right) \, , \tag{2.38}$$

where

$$\mu \equiv \sqrt{-p_\alpha p^\alpha} \, , \tag{2.39}$$

$$\mathcal{M} \equiv -p_\alpha u^\alpha \, . \tag{2.40}$$

These relationships tell us that $p^\alpha = \mu u^\alpha + \mathcal{O}(S^2)$, and $\mu = \mathcal{M} + \mathcal{O}(S^2)$, a result we will exploit shortly.

The spin tensor is antisymmetric, which facilitates defining the spin vector [156]

$$S^\mu = -\frac{1}{2\mu}\epsilon^{\mu\nu}{}_{\alpha\beta}p_\nu S^{\alpha\beta}, \tag{2.41}$$

where

$$\epsilon_{\alpha\beta\gamma\delta} = \sqrt{-g}[\alpha\beta\gamma\delta] \tag{2.42}$$

and where $\sqrt{-g}$ is the metric determinant, reducing to $\Sigma\sin\theta$ for Kerr, and $[\alpha\beta\gamma\delta]$ is the totally antisymmetric symbol. By combining these results, one can show that the magnitude of the spin is another constant of the motion, given by

$$S^2 = S^\alpha S_\alpha = \frac{1}{2}S_{\alpha\beta}S^{\alpha\beta}\ . \tag{2.43}$$

2.2.3 Leading order in small body's spin

The magnitude S of the small body's spin can be defined using a dimensionless spin parameter s:

$$S = s\mu^2\ . \tag{2.44}$$

If the small body is itself a Kerr black hole, then $0 \leq s \leq 1$, which tells us that $S \leq \mu^2$. Note that two dimensionless secondary spin parameters are commonly used in the literature. The other, used for example in [124], [126], is:

$$\sigma = \frac{S}{\mu M}\ , \tag{2.45}$$

and satisfies $0 \leq \sigma \leq \mu/M$. A virtue of this form is that σ is of order the mass ratio ε, which can facilitate comparing the magnitude of various terms in our analysis.

Linear-in-spin effects are thus effectively quadratic in the system's mass ratio, affecting a system's dynamics at the same formal order as important self force effects [161]–[163]. The next order in spin scales with the fourth power of the system's mass ratio, practically negligible at extreme mass ratios. A linear-in-spin analysis is thus formally interesting as well as of astrophysical relevance. As such, we focus on the linear-in-spin limit, neglecting terms in all of our equations that are $\mathcal{O}(S^2)$ or higher.

In this limit, the Matthisson-Papapetrou equations (2.31) – (2.32) and the Tulczyjew SSC (2.37) take a particularly useful form. Revisiting various relations in Secs. 2.2.1 and 2.2.2 but dropping all terms beyond linear in S, Eq. (2.33) becomes

$$p^\alpha = \mu u^\alpha\ . \tag{2.46}$$

The orbit's 4-velocity and 4-momentum are parallel at this order. With this, the Mathisson-Papapetrou equations can be written

$$\frac{Du^\alpha}{d\tau} = -\frac{1}{2\mu}R^\alpha{}_{\nu\lambda\sigma}u^\nu S^{\lambda\sigma}\ , \tag{2.47}$$

$$\frac{DS^{\alpha\beta}}{d\tau} = 0\ . \tag{2.48}$$

The second of these equations tells us that the spin tensor is parallel transported along the worldline at this order.

Linearizing in S, Eq. (2.41) becomes

$$S^{\mu} = -\frac{1}{2}\epsilon^{\mu\nu}{}_{\alpha\beta}\hat{u}_{\nu}S^{\alpha\beta} \ , \tag{2.49}$$

or equivalently,

$$S^{\alpha\beta} = \epsilon^{\alpha\beta\mu\nu}\hat{u}_{\mu}S_{\nu} \ . \tag{2.50}$$

Using these linear-in-spin forms, the SSC (2.37) becomes

$$\hat{u}_{\alpha}S^{\alpha\beta} = 0 \ , \tag{2.51}$$

or

$$\hat{u}_{\alpha}S^{\alpha} = 0 \ . \tag{2.52}$$

Equation (2.52) helps us understand the meaning of the SSC, at least in a linear-in-spin analysis: it tells us that in a freely-falling frame that moves with the geodesic whose 4-velocity is $\hat{u}^{\alpha}$, the small body's spin is purely spatial. Combining Eqs. (2.48) and (2.50), we find

$$\frac{DS^{\mu}}{d\tau} = 0 \ , \tag{2.53}$$

so the spin vector is also parallel transported along the worldline at this order.

2.2.4 Parallel transport in Kerr

Since the small body's spin vector is parallel transported along its orbit, as described by Eq. (2.53), let us examine such parallel transport in detail. Past work [164] showed how to build a solution describing this transport using a frequency-domain expansion, demonstrating that an additional frequency emerges which characterizes the timescale associated with the spin's precession. Van de Meent [144] has since then produced an elegant closed-form tetrad-based solution for describing the parallel transport of vectors along Kerr geodesics, following methods first developed Marck [165]–[167]; see also work by Bini and collaborators, which explores and clarifies the geometrical properties of Marck's procedure [150], [168], [169], as well as Mashhoon and collaborators [63], [170]. Following Ref. [144], we summarize the procedure for constructing this tetrad and describe how to use it to describe a spinning body moving along its orbit.

We write the tetrad $\{e_{0\alpha}(\lambda), \tilde{e}_{1\alpha}(\lambda), \tilde{e}_{2\alpha}(\lambda), e_{3\alpha}(\lambda)\}$. Take its first leg, $e_{0\alpha}(\lambda)$, to be the geodesic's 4-velocity; take its last leg, $e_{3\alpha}(\lambda)$, to be the (normalized) orbital angular momentum 4-vector defined in Eq. (2.11). Our tetrad so far consists of the vectors

$$e_{0\alpha}(\lambda) = \hat{u}_{\alpha}(\lambda) \ , \qquad e_{3\alpha}(\lambda) = \frac{1}{\sqrt{\hat{K}}}\hat{\mathcal{L}}_{\alpha}(\lambda) \ , \tag{2.54}$$

where $\hat{\mathcal{L}}_{\alpha}(\lambda)$ is the orbital angular momentum 4-vector along the geodesic with 4-velocity $\hat{u}_{\alpha}(\lambda)$. By the properties of $\hat{u}^{\alpha}(\lambda)$, $\hat{\mathcal{L}}^{\alpha}(\lambda)$, and $\hat{K}$, these tetrad legs are orthogonal to each other and parallel transported along $\hat{u}^{\alpha}(\lambda)$. We then construct $\tilde{e}_{1\alpha}(\lambda)$ and $\tilde{e}_{2\alpha}(\lambda)$ by choosing

two vectors which lie in the plane orthogonal to $e_{0\alpha}(\lambda)$ and $e_{3\alpha}(\lambda)$; see Ref. [144], Eqs. (50) and (51), for explicit formulas.

The resulting tetrad is in general not parallel transported. However, by defining

$$e_{1\alpha}(\lambda) = \cos\psi_p(\lambda)\,\tilde{e}_{1\alpha}(\lambda) + \sin\psi_p(\lambda)\,\tilde{e}_{2\alpha}(\lambda) \tag{2.55}$$

$$e_{2\alpha}(\lambda) = -\sin\psi_p(\lambda)\,\tilde{e}_{1\alpha}(\lambda) + \cos\psi_p(\lambda)\,\tilde{e}_{2\alpha}(\lambda) \tag{2.56}$$

and requiring that the precession phase $\psi_p(\lambda)$ satisfies

$$\frac{d\psi_p}{d\lambda} = \sqrt{\hat{K}}\left(\frac{(r^2+a^2)\hat{E} - a\hat{L}_z}{\hat{K}+r^2} + a\frac{\hat{L}_z - a(1-z^2)\hat{E}}{\hat{K}-a^2z^2}\right) \tag{2.57}$$

we obtain a tetrad $\{e_{0\alpha}(\lambda), e_{1\alpha}(\lambda), e_{2\alpha}(\lambda), e_{3\alpha}(\lambda)\}$ that is parallel transported along the geodesic [144], [165], [166]. Van de Meent further finds a closed form solution to Eq. (2.57) of the form

$$\psi_p(\lambda) = \Upsilon_s\lambda + \psi_r(\hat{\Upsilon}_r\lambda) + \psi_\theta(\hat{\Upsilon}_\theta\lambda)\ , \tag{2.58}$$

where Υ_s (denoted Υ_ψ in Ref. [144]) is the frequency (conjugate to Mino-time) describing the precession of this tetrad along the orbit, and $\hat{\Upsilon}_{r/\theta}$ are the radial/polar frequencies of the orbit conjugate to Mino-time. The functions $\psi_r(\hat{\Upsilon}_r\lambda)$ and $\psi_\theta(\hat{\Upsilon}_\theta\lambda)$ are phases associated with the orbit's radial and polar motions. We define the Mino-time precession period as $\Lambda_s = 2\pi/\Upsilon_s$. Code for computing these tetrad legs is implemented as part of the `KerrGeodesics` package in the Toolkit [148].

This solution makes setting the spin of the small body easy: We write the small body's spin vector

$$S_\alpha = S^0 e_{0\alpha}(\lambda) + S^1 e_{1\alpha}(\lambda) + S^2 e_{2\alpha}(\lambda) + S^3 e_{3\alpha}(\lambda)\ , \tag{2.59}$$

where $\{S^0, S^1, S^2, S^3\}$ are all constants with the dimension of angular momentum. The requirement that $\hat{u}^\alpha S_\alpha = 0$ means that $S^0 = 0$ for all configurations. A component $S^3 \equiv S_\parallel$ denotes a component of the small body's spin parallel or antiparallel to the orbital angular momentum, normal to the orbital plane; S^1 and S^2 define components perpendicular to the orbital angular momentum, in the orbital plane. A spin vector with $S^1 = S^2 = 0$ does not precess, and so its motion has no frequency components at harmonics of the spin-precession frequency Υ_s. By contrast, when S^1 or S^2 are non-zero, the small body's spin precesses over an orbit, and harmonics of the frequency Υ_s appear in a frequency-domain description of the small body's orbit.

This allows us to express S_α in terms of the parallel and perpendicular spin components of the small-body's non-dimensional spin parameter s:

$$S_\alpha = \mu^2\left(s_\perp\cos\phi_s\, e_{1\alpha} + s_\perp\sin\phi_s\, e_{2\alpha} + s_\parallel\, e_{3\alpha}\right)\ , \tag{2.60}$$

where $s = \sqrt{s_\perp^2 + s_\parallel^2}$, and ϕ_s describes the orientation of the spin vector components. The small body's spin vector will precess only when S^1 or S^2 are non-vanishing.

2.2.5 Spinning-body orbits

We now briefly survey some of the key differences between spinning-body and geodesic orbits; Chapters 3 and 4 as well as Refs. [84], [171], [172] provide more details. Spinning-body orbits are qualitatively different from geodesic ones. If the body's spin is misaligned from the orbit, then its orientation precesses, with a Mino-time frequency Υ_s characterizing this precession; the body's orbital plane likewise precesses at this frequency. This precession appears in the equations of motion as a variation in the bounds of both the polar and radial libration regions. Indeed, one finds that the radial and polar motions for a spinning body do not separate when parameterized in Mino time as they do for geodesics [84], [171], [172]. Finally, a body's spin also shifts the orbital frequencies relative to the orbital frequencies associated with geodesic orbits. The well-understood frequencies $\Omega_{r,\theta,\phi}$ which characterize geodesic orbits are each shifted by an amount $\propto s_{\parallel}$, the component of the smaller body's spin parallel to its angular momentum.

We first consider equatorial orbits with aligned spin: $s = s_{\parallel}$, $s_{\perp} = 0$. Spinning-body and geodesic orbits are quite similar in this case: motion is constrained to the plane $\theta = \pi/2$, and the radial motion is confined to an interval $r_2 \leq r \leq r_1$, where r_2 and r_1 are constants. We show examples of equatorial non-spinning and spinning-body orbits with the same initial conditions in panel (a) of Fig. 2.1. Differences emerge because the trajectories have different frequencies associated with both their radial and axial motions.

Qualitative differences become noticeable when $s_{\perp} \neq 0$. When the small body's spin vector is misaligned, it precesses and the spinning body's orbit oscillates by an amount $\mathcal{O}(S)$ out of the equatorial plane. For these "nearly equatorial" orbits, the radial motion remains constrained to the range $r_2 \leq r \leq r_1$, but the polar libration range is modified, with $\theta = \pi/2 + \delta\vartheta_S$. The orbital plane precesses in response to the small body's spin precession, adjusting the turning points of the polar motion depending on the spin precession phase ψ_s. This can be seen in panel (b) of Fig. 2.1: the orange (non-spinning) worldline is confined to the equatorial plane, while the blue (spinning-body) worldline oscillates about the equatorial plane.

Fully generic spinning-body orbits have eccentricity, are inclined with respect to the equatorial plane, and have an arbitrarily oriented small-body spin. Functions evaluated along generic orbits have structure at harmonics of three frequencies: radial Ω_r, polar Ω_θ, and spin-precessional Ω_s. We can use this to write functions evaluated along an orbit as a Fourier expansion of the form

$$f[r,\theta,S^{\mu}] = \sum_{j=-1}^{1}\sum_{k,n=-\infty}^{\infty} f_{jkn} e^{-ij\Omega_s t} e^{-in\Omega_r t} e^{-ik\Omega_\theta t} \,, \tag{2.61}$$

where S^{μ} is the small-body's spin vector. Note the different index ranges in this sum: there are only three harmonics of the spin frequency Ω_s, while in principle an infinite set of both polar and radial harmonics are present. (In practice, these sums converge over a finite range, though one must study the system carefully to determine an appropriate truncation point [172].)

The coupling of radial, polar and spin-precessional motions for generic spinning-body orbits causes the positions of the radial turning points to depend on θ and the spin-precession

phase ψ_s. Similarly, the polar turning points depend on radial position and ψ_s, as derived in Ref. [84]. Panel (c) of Fig. 2.1 shows a generic geodesic (in orange) and spinning-body trajectory (in blue) with the same initial conditions. The opacity of the curves increases as time advances; this illustrates how the trajectories diverge at late times, as the opacity increases.

2.3 Adiabatic radiation-reaction via Teukolsky formalism

We infer the impact of the leading-order adiabatic self force by computing GWs and the associated rates of change of the orbital integrals E, L_z, and Q using the Teukolsky equation [173]. See Ref. [26] for a detailed discussion of the methods we use; we provide a brief overview here.

The Teukolsky equation computes perturbations to the Weyl Newman-Penrose curvature scalar ψ_4, defined as

$$\psi_4 = -C_{\alpha\beta\gamma\delta} n^\alpha \bar{m}^\beta n^\gamma \bar{m}^\delta \,, \tag{2.62}$$

where $C_{\alpha\beta\gamma\delta}$ is the Weyl curvature tensor and n^α and $\bar{m}^\alpha$ are legs of the Newman-Penrose null tetrad $(l^\mu, n^\mu, m^\mu, \overline{m}^\mu)$ defined as [174]:

$$l^\mu = \left(\frac{r^2+a^2}{\Delta}, 1, 0, \frac{a}{\Delta}\right) , \tag{2.63a}$$

$$n^\mu = \frac{1}{2\Sigma}\left(\varpi^2, -\Delta, 0, a\right) \,, \tag{2.63b}$$

$$m^\mu = \frac{\sqrt{1-z^2}}{\sqrt{2}\bar{\zeta}}\left(ia, 0, -1, \frac{i}{1-z^2}\right) \,, \tag{2.63c}$$

$$\overline{m}^\mu = \frac{\sqrt{1-z^2}}{\sqrt{2}\zeta}\left(-ia, 0, -1, -\frac{i}{1-z^2}\right) \tag{2.63d}$$

with

$$\zeta = r - iaz \quad \text{and} \quad \varpi^2 = r^2 + a^2 \,.$$

Teukolsky derived the equation governing ψ_4 [173],

$$ {}_{-2}\mathcal{O}\ {}_{-2}\Psi = 4\pi\Sigma T \,, \tag{2.64}$$

where ${}_{-2}\Psi = \zeta^4\psi_4$, ${}_{-2}\mathcal{O}$ is a second order partial differential operator, and T is a source term. Note that we have specialized to spin-weight $s=-2$, a particularly convenient choice for studies of gravitational radiation. The forms for other spin weights, as well as the explicit form of the source term, are given in Ref. [173].

2.3.1 Solving the Teukolsky equation in the frequency domain

We solve Eq. (2.64) in the frequency domain, writing ψ_4 in a Fourier and multipolar expansion

$$\psi_4 = \frac{1}{\zeta^4}\int_\infty^\infty d\omega \sum_{l=2}^\infty \sum_{m=-l}^\infty R_{lm}(r;\omega) S_{lm}(\varphi; a\omega) e^{i[m\varphi - \omega(t-t_0)]} \,. \tag{2.65}$$

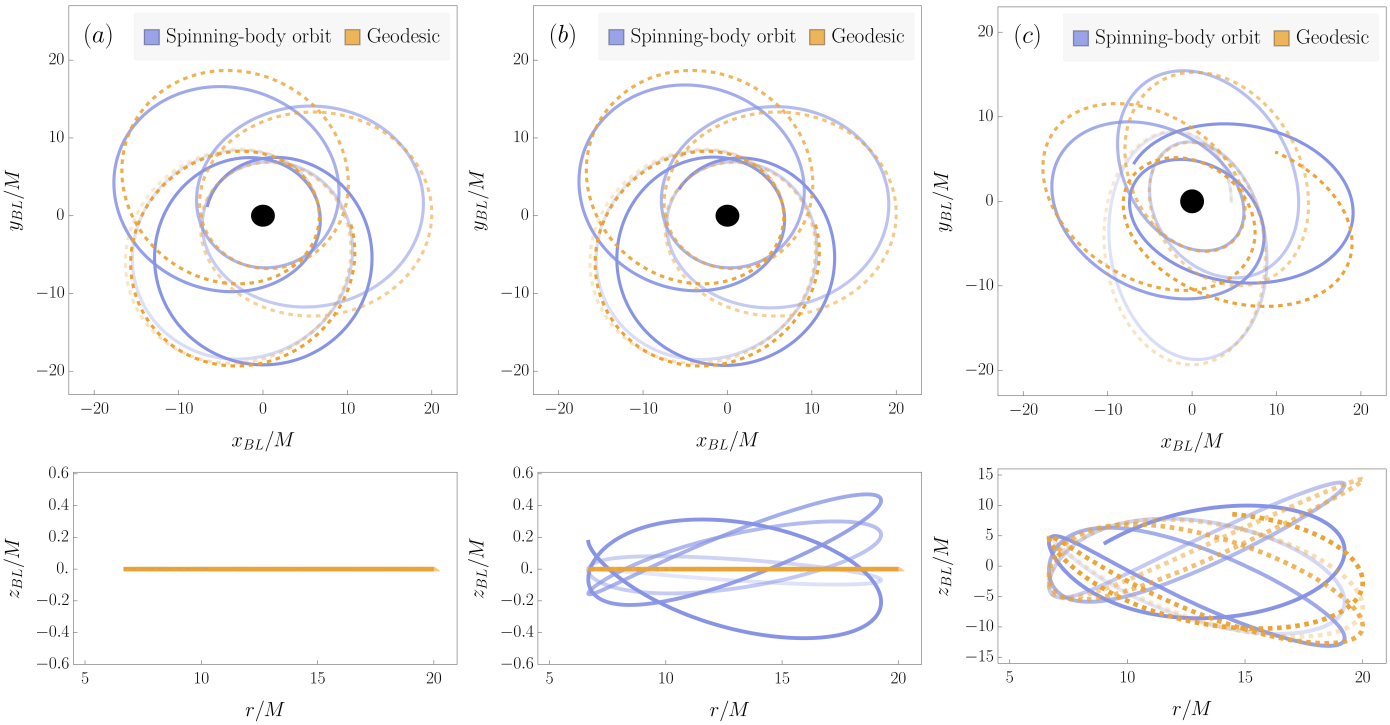

Figure 2.1: Comparison of spinning-body (blue) and geodesic (orange) orbit trajectories. Within each column, the trajectories shown have the same initial conditions. The top row shows x_{BL}-y_{BL} trajectories; the bottom shows trajectories in r-z_{BL}. (The coordinates x_{BL}, y_{BL}, z_{BL} are Cartesian-like representations of the Boyer-Lindquist coordinates: $x_{BL} = r\sin\theta\cos\phi$, etc.) Increasing opacity of the trajectory curves denotes increasing time. Panel (a) shows equatorial trajectories; for the blue (spinning-body) trajectory, the spin of the small body is aligned with the spin of the larger black hole. The major difference in the trajectories in this case is the dephasing that occurs because spin-curvature coupling changes the timescales associated with orbital motions. Panel (b) shows the same geodesic orbit as panel (a) but the spinning-body trajectory corresponds to a small body with its spin misaligned with its orbit. Notice that the in-plane motion is similar to what we find in panel (a), at least over the time interval shown here, though the motion acquires an out-of-plane motion that is entirely absent from the geodesic case. Note also the different scales used for the out-of-plane motion, versus the in-plane and radial motion: the out-of-plane motion is smaller by a factor ~ 30. Panel (c) shows generic orbits for both cases. In all panels, the parameters used are $a = 0.7M$, $p = 10$, $e = 0.5$, $\varepsilon = 0.1$, and $s = 1$. In panels (b) and (c), we put $s_{\parallel} = 0.9s$ and $\phi_s = \pi/2$; in panel (c), we further put $x_I = 0.6967$. Here and in many of the other plots, we have used a much less extreme mass ratio than is appropriate for these techniques in order to magnify the effect of spin-curvature coupling physics.

The function $S_{lm}(\vartheta, a\omega)$ introduced here is a spheroidal harmonic of spin-weight -2; the field ψ_4 so computed is evaluated at the event $(t,\, r,\, \vartheta,\, \varphi)$. This decomposition separates Eq. (2.64) into a pair of ordinary differential equations governing the spheroidal harmonic and governing the radial dependence $R_{lm}(r, \omega)$.

As discussed at some length in Ref. [26], computing adiabatic inspirals requires knowledge only of ψ_4 in the limits $r \to \infty$ and $r \to r_+ = M + \sqrt{M^2 - a^2}$. The GW strain far from the source is related to ψ_4 by

$$\psi_4 = \frac{1}{2}\frac{d^2}{dt^2}(h_+ - ih_\times) \text{ as } r \to \infty \,. \tag{2.66}$$

By exploiting the Teukolsky-Starobinsky identities [175], we can also obtain all the information we need about the secondary's impact on the spacetime for our adiabatic analysis by examining ψ_4 at the event horizon, $r \to r_+$.

Identities make it possible to compute fluxes at the horizon using ψ_4. The solutions to the Teukolsky equation allow us to construct the rates of change of E, L_z, and Q from GW backreaction and radiation absorbed by the horizon. A key point for us is that the radial dependence behaves asymptotically as

$$R_{lm}(r, \omega) \to Z^{\infty}_{lm\omega} r^3 e^{i\omega r_*} \,, \qquad r \to \infty \,, \tag{2.67}$$

$$R_{lm}(r, \omega) \to Z^{\rm H}_{lm\omega} \Delta e^{-i(\omega - m\Omega_H) r_*} \,, \quad r \to r_+ \,. \tag{2.68}$$

Here the frequency $\Omega_H = a/(2Mr_+)$ is the rotation frequency of the horizon, and r^* is the tortoise coordinate

$$r_*(r) = r + \frac{Mr_+}{\sqrt{M^2 - a^2}} \ln\left(\frac{r - r_+}{2M}\right) - \frac{Mr_-}{\sqrt{M^2 - a^2}} \ln\left(\frac{r - r_-}{2M}\right) \,, \tag{2.69}$$

where $r_- = M - \sqrt{M^2 - a^2}$.

For bound black hole orbits, the frequency ω in Eq. (2.65) has support only at discrete harmonics:

$$\omega \to \omega_{mkn} = m\Omega_\phi + k\Omega_\theta + n\Omega_r \,, \tag{2.70}$$

where Ω_x is the frequency associated with a complete cycle of the orbit's motion in coordinate x. Using this, the amplitudes $Z^{\infty,{\rm H}}_{lm\omega}$ can be further decomposed,

$$Z^{\infty,{\rm H}}_{lm\omega} = \sum_{k=-\infty}^{\infty} \sum_{n=-\infty}^{\infty} Z^{\infty,{\rm H}}_{lmkn} \delta(\omega - \omega_{mkn}) \,. \tag{2.71}$$

See Ref. [26] for all the details of this harmonic decomposition.

2.3.2 Rates of change of E, L_z and Q

The coefficients $Z^{\infty,{\rm H}}_{lmkn}$ contain all the information we need to build adiabatic inspirals and waveforms. From these coefficients, we compute the rates of change dE/dt, dL_z/dt, dQ/dt for

each geodesic in the osculating sequence. Each of these quantities break into a contribution from the fields at $r \to \infty$ and at $r \to r_+$. The energy fluxes dE/dt are given by [175]:

$$\left(\frac{dE}{dt}\right)^{\infty} = \sum_{lmkn} \frac{|Z^{\infty}_{lmkn}|^2}{4\pi\omega^2_{mkn}} , \tag{2.72}$$

$$\left(\frac{dE}{dt}\right)^{\rm H} = \sum_{lmkn} \frac{\alpha_{lmkn} \left|Z^{\rm H}_{lmkn}\right|^2}{4\pi\omega^2_{mkn}} . \tag{2.73}$$

The factor α_{lmkn} appears quite a lot when examining quantities which are evaluated on the event horizon, and is given by

$$\alpha_{lmkn} = \frac{256(2Mr_+)^5(\omega_{mkn} - m\Omega_{\rm H})[(\omega_{mkn} - m\Omega_{\rm H})^2 + 4\epsilon^2][(\omega_{mkn} - m\Omega_{\rm H})^2 + 16\epsilon^2]\omega^3_{mkn}}{|C_{lmkn}|^2} . \tag{2.74}$$

The factors $|C_{lmkn}|^2$ and ϵ are in turn given by

$$\begin{aligned} |C_{lmkn}|^2 &= [(\lambda^2_{lmkn} + 2)^2 + 4am\omega_{mkn} - 4a^2\omega^2_{mkn}](\lambda^2_{lmkn} + 36am\omega_{mkn} - 36a^2\omega^2_{mkn}) \\ &+ (2\lambda_{lmkn} + 3)(96a^2\omega^2_{mkn} - 48am\omega_{mkn}) + 144\omega^2_{mkn}(M^2 - a^2) , \end{aligned} \tag{2.75}$$

$$\epsilon = \frac{\sqrt{M^2 - a^2}}{4Mr_+} . \tag{2.76}$$

The angular momentum fluxes dL_z/dt are [175]:

$$\left(\frac{dL_z}{dt}\right)^{\infty} = \sum_{lmkn} \frac{m\,|Z^{\infty}_{lmkn}|^2}{4\pi\omega^3_{mkn}} , \tag{2.77}$$

$$\left(\frac{dL_z}{dt}\right)^{\rm H} = \sum_{lmkn} \frac{\alpha_{lmkn} m \left|Z^{\rm H}_{lmkn}\right|^2}{4\pi\omega^3_{mkn}} . \tag{2.78}$$

The Carter constant "fluxes"[1] dQ/dt are computed by averaging the dissipative self force on a geodesic [176], and are given by

$$\left(\frac{dQ}{dt}\right)^{\infty} = \sum_{lmkn} |Z^{\infty}_{lmkn}|^2 \frac{\mathcal{L}_{mkn} + k\Upsilon_\theta}{2\pi\omega^3_{mkn}} , \tag{2.79}$$

$$\left(\frac{dQ}{dt}\right)^{\rm H} = \sum_{lmkn} \alpha_{lmkn} \left|Z^{\rm H}_{lmkn}\right|^2 \frac{\mathcal{L}_{mkn} + k\Upsilon_\theta}{2\pi\omega^3_{mkn}} , \tag{2.80}$$

where

$$\mathcal{L}_{mkn} = m\langle\cot^2\theta\rangle L_z - a^2\omega_{mkn}\langle\cos^2\theta\rangle E . \tag{2.81}$$

[1]Strictly speaking, dQ/dt is not a flux since one cannot isolate a contribution of the rate of change of Q by only examining the GWs emitted from a system. Equations (2.79) and (2.80) instead involve quantities from the radiation field combined with averaged properties of the orbit. It is common to call dQ/dt a flux nonetheless, since it enters the adiabatic backreaction analysis identically to the true fluxes dE/dt and dL_z/dt.

The expressions $\langle \cot^2\theta \rangle$ and $\langle \cos^2\theta \rangle$ in Eq. (2.81) denote $\cot^2\theta$ and $\cos^2\theta$ averaged over an orbit using

$$\langle f_\theta(\theta) \rangle = \frac{1}{\Lambda_\theta} \int_0^{\Lambda_\theta} f_\theta[\theta(\lambda)]\, d\lambda \,. \tag{2.82}$$

To evolve from geodesic to geodesic in the osculating sequence, we impose a balance law:

$$\left(\frac{d\mathcal{C}}{dt}\right)^{\rm orbit} = -\left(\frac{d\mathcal{C}}{dt}\right)^{\infty} - \left(\frac{d\mathcal{C}}{dt}\right)^{\rm H} \tag{2.83}$$

for each $\mathcal{C} \in (E, L_z, Q)$. This balance is equivalent to computing the orbit-averaged, leading-order self force. Using these to evolve from geodesic to geodesic in the osculating sequence builds the adiabatic inspiral.

2.3.3 Multi-voice gravitational waveforms

To build the gravitational waveform associated with this inspiral, we begin by examining Eq. (2.65) in the limit $r \to \infty$. Using Eqs. (2.67) and (2.71) in this limit, (2.65) yields the following result for ψ_4 along the inspiral:

$$\psi_4(t^{\rm i}) = \frac{1}{r} \sum_{lmkn} Z^{\infty}_{lmkn}(t^{\rm i}) S_{lm}\left[\vartheta, a\omega_{mkn}(t^{\rm i})\right] e^{i\left[m\varphi - \Phi_{mkn}(t^{\rm i})\right]} \,. \tag{2.84}$$

Notice that the asymptotic amplitude Z^{∞}_{lmkn} and the mode frequency ω_{mkn} have become functions of the inspiral time $t^{\rm i}$. We have also replaced the mode frequency times t with the integrated mode phase:

$$\Phi_{mkn}(t^{\rm i}) = \int_{t_0}^{t^{\rm i}} \omega_{mkn}(t')dt' \,. \tag{2.85}$$

Combining this with Eq. (2.66) allows us to read out the gravitational waveform generated along the inspiral:

$$\begin{aligned} h(t^{\rm i}) &\equiv h_+(t^{\rm i}) - i h_\times(t^{\rm i}) \\ &= \frac{1}{r} \sum_{lmkn} A_{lmkn}(t^{\rm i}) S_{lm}[\varphi; a\omega_{mkn}(t^{\rm i})] e^{i[m\varphi - \Phi_{mkn}(t^{\rm i})]} \,, \end{aligned} \tag{2.86}$$

where

$$A_{lmkn}(t^{\rm i}) = -\frac{2 Z^{\infty}_{lmkn}(t^{\rm i})}{\omega^2_{mkn}(t^{\rm i})} \,. \tag{2.87}$$

Further discussion and detailed justification of various steps introduced in this section is given in Ref. [26].

Chapter 3

Precisely computing bound orbits of spinning bodies around black holes I: General framework and results for nearly equatorial orbits

This chapter is based on work previously published in Physical Review D (Drummond & Hughes 2022a) [171], written in collaboration with Scott A. Hughes.

3.1 Introduction and motivation

In this chapter, we examine the force that arises due to the coupling of the background curvature with the spin of the small body, the spin-curvature force f^α_S. The equation governing the small body's motion becomes

$$\frac{Dp^\alpha}{d\tau} = f^\alpha_S \equiv -\frac{1}{2} R^\alpha{}_{\nu\lambda\sigma} u^\nu S^{\lambda\sigma} \,. \tag{3.1}$$

This is one of the Mathisson-Papapetrou equations, as was discussed in detail in Sec. 2.2. Here $R^\alpha{}_{\nu\lambda\sigma}$ is the Riemann curvature tensor of the background spacetime, and u^ν is the 4-velocity associated with the smaller body's orbital motion. The tensor $S^{\lambda\sigma}$ describes the spin of the orbiting body. If that body is a Kerr black hole, $S^{\lambda\sigma} \propto s\mu^2$ where s is a dimensionless spin parameter with $s \leq 1$. The spin-curvature force thus affects the orbiting body's motion at next-to-leading-order in mass ratio, just like many important self force effects [161]–[163].

3.1.1 Synopsis of our formulation

In the subsequent analysis, we examine orbits under the influence of the spin-curvature force f^α_S. Because our focus is on extreme mass-ratio systems, we truncate all spin effects at leading order in the small body's spin. Under the assumption that the small body is itself a Kerr black hole (an astrophysically plausible assumption for EMRI systems), the small body's spin has a magnitude that scales with its mass squared. Terms beyond linear in spin

thus scale very steeply with the system's mass ratio. At this order, a closed-form description of the spin precession is known [177], amounting to parallel transport of a vector along a Kerr geodesic. With the precessional dynamics of the small body's spin in hand, we can straightforwardly compute the spin-curvature force. From this, we find the spinning-body trajectory $[r(t), \theta(t), \phi(t)]$ consistent with the spin-curvature force by solving Eq. (3.1).

Following Ref. [177], we characterize the small body's spin using a set of quantities $\{S^1, S^2, S^3\}$ which represent the components of its spin vector projected onto three legs of a tetrad used in the closed-form analysis of its precession (see Sec. 2.2.4). (A fourth component S^0, corresponding to the remaining leg of the tetrad, is constrained to be zero by the spin supplementary condition discussed in Sec. 2.2.2.) We write its magnitude $S = \sqrt{S_\parallel^2 + S_\perp^2}$, where $S_\parallel = S^3$ describes the component normal to the orbital plane, and $S_\perp = \sqrt{(S^1)^2 + (S^2)^2}$ describes its magnitude within this plane. If $S_\perp \neq 0$, then components of the spin vector oscillate in the orbital plane with a frequency Ω_s, describing a precession of the spin vector along its orbit; this frequency is described in more detail in Sec. 2.2.4, and computed in Ref. [177]. At leading order in spin, the quantities $S_\perp$ and $S_\parallel$ (and thus S) are constants of motion along the spinning body's orbit.

Because we consider the small body's spin to be a small parameter, the spinning-body orbits we examine are "close to" geodesic orbits (in a sense made more precise later). We begin our discussion of spinning-body orbits by examining how we parameterize bound Kerr geodesics. The radial motion of bound geodesics is typically described using a semi-latus rectum p and an eccentricity e, such that the orbit oscillates between apoastron at $r_1 = pM/(1-e)$ and periastron at $r_2 = pM/(1+e)$. The polar angle θ of a bound orbit oscillates such that $-\sin I \leq \cos\theta \leq \sin I$. Using these bounds, we write these motions

$$\hat{r} = \frac{pM}{1 + e\cos\hat{\chi}_r} \,, \quad \cos\hat{\theta} = \sin I \cos\hat{\chi}_\theta \,. \tag{3.2}$$

Here and throughout this chapter, we use a "hat" accent (e.g. $\hat{r}$) to denote a quantity which is evaluated on a geodesic. The definitions (3.2) introduce the angles $\hat{\chi}_r$ and $\hat{\chi}_\theta$, which are generalizations of "true anomaly" angles often used in discussions of orbits in Newtonian gravity. The libration range of the geodesics does not change over an orbit, so that p, e and I are all constants of motion. Geodesics can be equivalently characterized by another set of constants of motion: $\hat{E}$, $\hat{L}_z$ and $\hat{Q}$, which denote a geodesic's energy, axial angular momentum and Carter constant respectively. These quantities are discussed in more detail in Sec. 2.1.

Spinning-body orbits cannot in general be parameterized in the same way as geodesics using Eq. (3.2). For the "nearly equatorial" cases that we consider in this chapter, we find the following parameterization robustly describes these orbits:

$$r = \frac{pM}{1 + e\cos\chi_r} \,, \quad \theta = \frac{\pi}{2} + \delta\vartheta_S \,. \tag{3.3}$$

This radial motion has turning points at $r = pM/(1 \pm e)$, exactly as for geodesic orbits. However, the anomaly angle χ_r is not the same as the anomaly angle $\hat{\chi}_r$ which describes geodesic motion. We elaborate on the difference between these angles in Sec. 3.4. The polar angle deviates from the equatorial plane by $\delta\vartheta_S$, a quantity with an amplitude $\mathcal{O}(S_\perp)$ which

oscillates at harmonics of the frequency Ω_s. If $S_\perp = 0$, so that the small body's spin is aligned or anti-aligned with the orbital angular momentum, then $\delta\vartheta_S = 0$. Aligned and anti-aligned orbits can be purely equatorial.

For generic orbits, we find that the libration regions in both r and θ must be modified to include oscillations at precession frequency Ω_s. We defer the details of how this is handled to Chapter 4, which examines generic orbits of spinning bodies with generic spin-orbit configuration.

3.1.2 Organization of this chapter

In the remainder of this chapter, we present our method for precisely computing bound orbits of spinning bodies orbiting black holes. In Sec. 3.2.1, we present a frequency-domain description of motion in a Kerr spacetime that is particularly useful in our examination of spinning-body orbits and in Sec. 3.2.2 we present the framework for describing the leading-order in spin deviation from a geodesic trajectory.

We begin our detailed study of bound spinning-body motion by examining several simple cases. In Sec. 3.3, we examine orbits which are circular and either equatorial or nearly equatorial, for which we can obtain closed form analytic solutions. This simple case allows us to establish the general principles of the framework we use throughout the chapter, as well as to compare with previously known results. We present the circular, nearly equatorial case in detail and for general black hole spin. In Sec. 3.4, we extend these circular cases by expanding in eccentricity in order to study slightly eccentric, nearly equatorial orbits. For general Kerr, we develop closed-form solutions to first order in eccentricity. We also present these solutions to second order in eccentricity for the Schwarzschild limit.

Finally, in Sec. 3.5, we use a frequency-domain treatment to compute orbits with arbitrary eccentricity and with the small body's spin arbitrarily oriented. The frequency-domain expansion allows us to examine orbits with arbitrary eccentricity, provided we include enough harmonics in our expansion. We calculate how the spin-curvature coupling shifts the orbital frequencies Ω_r and Ω_ϕ from their geodesic expectations (using the fact that the parameterization for nearly equatorial spinning-body orbits is very similar to the parameterization of equatorial geodesic orbits), as well as how the coupling shifts the constants of motion E^S, L_z^S and Q^S.

Section 3.6 concludes with a summary of our results, and an outline of plans for future work that uses the orbits of spinning bodies. We also briefly remark on results we present in Chapter 4, which describes how to extend this framework to model fully generic orbits (i.e., orbits of arbitrary eccentricity and inclination) with generic orientation of the small body's spin.

3.2 Spinning body motion in the frequency domain

3.2.1 Frequency-domain description of non-spinning bodies

Bound Kerr geodesics are triperiodic, with three frequencies describing their radial, polar, and azimuthal motions. Denote by $\hat{\Lambda}_r$, $\hat{\Lambda}_\theta$, and $\hat{\Lambda}_\phi$ the radial, polar, and axial Mino-time

periods (i.e., the interval of Mino time it takes for the orbit to move from r_1 to r_2 back to r_1; the interval to move from θ_- to $\pi - \theta_-$ back to θ_-; and the interval to move through 2π radians of axial angle). Denote by $\hat{\Upsilon}_r$, $\hat{\Upsilon}_\theta$, and $\hat{\Upsilon}_\phi$ the corresponding frequencies, with $\hat{\Upsilon}_x = 2\pi/\hat{\Lambda}_x$. First derived in this form in Ref. [135], we used closed-form expressions for these quantities given in Ref. [139], and coded into the `KerrGeodesics` package of the Toolkit [148].

From these Mino-time expressions, we can find their Boyer-Lindquist coordinate-time analogues using a factor $\hat{\Gamma}$ which is the orbit-averaged factor relating an interval of Mino-time λ to an element of coordinate time t. Let $\hat{T}_x$ be the coordinate time orbital period for motion in coordinate x, and let $\hat{\Omega}_x = 2\pi/\hat{T}_x$ be the corresponding frequency. Then,

$$\hat{\Omega}_{r,\theta,\phi} = \frac{\hat{\Upsilon}_{r,\theta,\phi}}{\hat{\Gamma}} , \qquad \hat{T}_{r,\theta,\phi} = \hat{\Gamma}\,\hat{\Lambda}_{r,\theta,\phi} . \tag{3.4}$$

Expressions for $\hat{\Gamma}$ (and thus for $\hat{\Omega}_{r,\theta,\phi}$) are also provided in Ref. [139] and encoded in the `KerrGeodesics` package of the Toolkit [148]

The Mino-time frequencies are particularly useful for our purposes because they make possible Fourier expansions of functions evaluated along Kerr orbits. Let $f(\lambda) = f\left[\hat{r}(\lambda), \hat{\theta}(\lambda)\right]$ be a function of $\hat{r}(\lambda)$ and $\hat{\theta}(\lambda)$. As shown in Ref. [135], we can write

$$f = \sum_{k=-\infty}^{\infty} \sum_{n=-\infty}^{\infty} f_{kn} e^{-i\left(k\hat{\Upsilon}_\theta + n\hat{\Upsilon}_r\right)\lambda} , \tag{3.5}$$

where the Fourier coefficient f_{kn} is given by

$$f_{kn} = \frac{1}{\hat{\Lambda}_r\hat{\Lambda}_\theta} \int_0^{\hat{\Lambda}_r} \int_0^{\hat{\Lambda}_\theta} f\left[\hat{r}(\lambda_r), \hat{\theta}(\lambda_\theta)\right] e^{ik\hat{\Upsilon}_\theta\lambda_\theta} e^{in\hat{\Upsilon}_r\lambda_r} d\lambda_\theta d\lambda_r . \tag{3.6}$$

The component f_{00} represents the orbit-average of the function $f[\hat{r}(\lambda), \hat{\theta}(\lambda)]$. It's worth noting that the quantities $\hat{\Upsilon}_\phi$ and $\hat{\Gamma}$ are orbit averages of the functions $\Phi(\hat{r}, \hat{\theta})$ and $T(\hat{r}, \hat{\theta})$ defined in Eq. (2.24):

$$\hat{\Upsilon}_\phi = \frac{1}{\hat{\Lambda}_r\hat{\Lambda}_\theta} \int_0^{\hat{\Lambda}_r} \int_0^{\hat{\Lambda}_\theta} \Phi[\hat{r}(\lambda_r), \hat{\theta}(\lambda_\theta)] d\lambda_r\, d\lambda_\theta , \tag{3.7}$$

$$\hat{\Gamma} = \frac{1}{\hat{\Lambda}_r\hat{\Lambda}_\theta} \int_0^{\hat{\Lambda}_r} \int_0^{\hat{\Lambda}_\theta} T[\hat{r}(\lambda_r), \hat{\theta}(\lambda_\theta)] d\lambda_r\, d\lambda_\theta . \tag{3.8}$$

We will use a variant of these definitions to compute Υ_ϕ and Γ along orbits of spinning bodies.

3.2.2 Spin deviation from geodesic trajectory

As argued in Sec. 2.2.3, our focus is on computing orbits to linear order in the small body's spin. For the configurations that we study, the spin is a small parameter, and these trajectories can be regarded as perturbative deviations from bound Kerr geodesics. We discuss

the nature of an orbit's "spin shift" in detail later as we analyze specific orbit and spin configurations. In general, the small body's trajectory can be written in the form

$$x^\alpha(\lambda) = \hat{x}^\alpha(\lambda) + \delta x^\alpha_S(\lambda) \ , \tag{3.9}$$

where $\hat{x}^\alpha(\lambda)$ is the coordinate-space trajectory of an appropriately chosen geodesic, and $\delta x^\alpha_S(\lambda)$ is the $\mathcal{O}(S)$ shift due to the spin. Similarly, we write the small body's 4-velocity

$$u^\alpha = \hat{u}^\alpha + u^\alpha_S \ , \tag{3.10}$$

where $\hat{u}^\alpha$ solves the geodesic equation, and $u^\alpha_S = \mathcal{O}(S)$.

One important point to note is that $\hat{x}^\alpha(\lambda)$ will in general have different periods than $x^\alpha(\lambda)$: the periods $\Lambda_{r,\theta,\phi}$ which characterize bound orbits of spinning bodies differ from the geodesic periods $\hat{\Lambda}_{r,\theta,\phi}$ by $\mathcal{O}(S)$. As such, a naive definition of δx^α_S necessarily contain unbounded, secularly growing terms. Such terms ruin the perturbative expansion that we use.

As such, we do not use the explicit form Eq. (3.9) directly when we compute spinning-body orbits in Secs. 3.4 and 3.5. We instead characterize these orbits using amplitude-phase variables. Doing so, the frequency shift is incorporated into the parameterization; see Eq. (3.72) or (3.137) and nearby text. Once we have solved for the frequency shift and phase variables, we can then compute δx^α_S. These quantities are particularly useful for finding the concomitant "spin shifts" to constants of motion, which we describe below. In Appendix A.1, we provide the explicit form of δx^α_S in terms of variables that we use in this work, as well as further discussion of the secular terms.

As the orbit evolves, we must preserve the norm of its 4-velocity. Using Eq. (3.10), demanding that $\hat{u}^\alpha \hat{u}_\alpha = -1$, and enforcing $u^\alpha u_\alpha = -1$ yields the constraint

$$\hat{u}^\alpha u^S_\alpha + \hat{u}_\alpha u^\alpha_S = 0 \ . \tag{3.11}$$

Writing $u_\alpha = g_{\alpha\beta} u^\beta$, and noting that $g_{\alpha\beta}$ is evaluated along the spinning-body orbits for which $r = \hat{r} + \delta r_S$ and $\theta = \hat{\theta} + \delta\vartheta_S$, the spin-corrected covariant 4-velocity has the form

$$u^S_\alpha = g_{\alpha\beta} u^\beta_S + \delta r_S \partial_r g_{\alpha\beta} \hat{u}^\beta + \delta\theta_S \partial_\theta g_{\alpha\beta} \hat{u}^\beta \ . \tag{3.12}$$

This allows us to write constraint (3.11) entirely in terms of the contravariant spin-correction to the 4-velocity, viz.,

$$2 g_{\alpha\beta} \hat{u}^\alpha u^\beta_S + \delta r_S \partial_r g_{\alpha\beta} \hat{u}^\alpha \hat{u}^\beta + \delta\theta_S \partial_\theta g_{\alpha\beta} \hat{u}^\alpha \hat{u}^\beta = 0 \ . \tag{3.13}$$

We use this constraint throughout our analysis. We also define the leading order in spin corrections to the energy δE^S and axial angular momentum δL^S_z due to the spin using (2.35) and (2.36):

$$E^S = \hat{E} + \delta E^S \ , \tag{3.14}$$

$$L^S_z = \hat{L}_z + \delta L^S_z \ . \tag{3.15}$$

As mentioned in Sec. 2.2.1, an analogue to the Carter constant is preserved at linear order in spin. Normalizing by the orbiting body's rest mass squared, it is given by [153]

$$K^S = K_{\alpha\beta} u^\alpha u^\beta + \delta\mathcal{C}^S, \tag{3.16}$$

where

$$\delta\mathcal{C}^S = -\frac{2}{\mu}\hat{u}^\mu S^{\rho\sigma}\left(\mathcal{F}^\nu{}_\sigma \nabla_\nu \mathcal{F}_{\mu\rho} - \mathcal{F}_\mu{}^\nu \nabla_\nu \mathcal{F}_{\rho\sigma}\right) . \tag{3.17}$$

We define the first order in spin correction to K by

$$K^S = \hat{K} + \delta K^S , \tag{3.18}$$

where $\hat{K}$ is the Carter constant along the geodesic whose 4-velocity is $\hat{u}^\alpha$, and δK^S is $\mathcal{O}(S)$. Combining Eqs. (3.9), (3.10) and (3.16) with the definition (3.18) and truncating at linear order in S, we find

$$\delta K^S = 2K_{\alpha\beta}\hat{u}^\alpha u_S^\beta + \delta r_S \partial_r K_{\alpha\beta}\hat{u}^\alpha\hat{u}^\beta + \delta\theta_S \partial_\theta K_{\alpha\beta}\hat{u}^\alpha\hat{u}^\beta + \delta\mathcal{C}^S . \tag{3.19}$$

The first line of Eq. (3.19) includes two terms which are due to the shift of the small body's orbit that we find when examining spinning-body orbits. Applying Eq. (2.18), we then find the first-order shift in Q:

$$\delta Q^S = \delta K^S - 2(\hat{L}_z - a\hat{E})(\delta L_z^S - a\delta E^S) . \tag{3.20}$$

For nearly equatorial orbits with polar motion defined by $\theta = \pi/2 + \delta\vartheta_S$ in Eq. (3.3), $\delta\vartheta_S$ and $\delta\theta_S$ may be used interchangeably (which we do throughout this chapter). However, in general, $\delta\vartheta_S$ corresponds only to the corrections to the *libration region* of the polar motion, while $\delta\theta_S$ denotes the entire spin-perturbation associated with θ, as defined in Eq. (3.9). This distinction becomes important in the analysis in Chapter 4,

3.2.3 General characteristics of spinning-body orbits

In the remainder of this chapter, we examine several examples of the orbits of spinning bodies about Kerr black holes. Before exploring these specific cases in detail, we briefly lay out and summarize general characteristics of the orbits that we find.

Consider first an orbit that would be equatorial if the orbiting body were non-spinning. If this body's spin is normal to the equatorial plane (i.e., parallel or antiparallel to both the orbital angular momentum and the large black hole's spin), then its orbit is quite simple. Just as in the geodesic case, we can use the parameterization $r = pM/(1 + e\cos\chi_r)$. The radial turning points are fixed for the duration of the orbit at $pM/(1 \pm e)$, and the orbit's dynamics maps onto a true anomaly angle χ_r. This true anomaly differs from the true anomaly that describes geodesics, $\hat{\chi}_r$; details of this difference are presented in Sec. 3.4. The orbit's radial frequency is shifted compared to the geodesic by an amount $\mathcal{O}(S)$; we write the radial frequency $\Upsilon_r = \hat{\Upsilon}_r + \Upsilon_r^S$. This case is discussed in quantitative detail in Secs. 3.4.3 and 3.5.1, with the special case of circular equatorial orbits presented in Sec. 3.3.1.

Consider next such an orbit but with the spin misaligned with respect to the orbital plane. This misalignment introduces $\mathcal{O}(S)$ oscillations centered about the equatorial plane:

The polar motion acquires a correction $\delta\vartheta_S$ whose Fourier expansion is at harmonics of the spin frequency Υ_s and the radial frequency $\Upsilon_r = \hat{\Upsilon}_r + \Upsilon_r^S$. The radial motion, however, remains exactly as it was in the spin-aligned case. We discuss this case in detail in Secs. 3.4.2 and 3.5.2; an explicit analytic solution for circular, nearly equatorial motion is calculated in Sec. 3.3.2.

We focus on these equatorial and nearly equatorial cases in this chapter. For orbits that are not "nearly equatorial", the parameterization becomes rather more complicated. In particular, the "geodesic-like" parameterization of the nearly equatorial case must be modified, adding a spin-induced contribution to the orbit's libration region in both the radial and polar motions. This holds even if the spin-vector is aligned with the orbital angular momentum. We discuss these more complicated cases in Chapter 4.

3.3 Spinning-body orbits I: Circular, nearly equatorial orbits

We begin our study of spinning-body orbits by examining several simple cases for which we can find closed-form, fully analytic solutions. These cases allow us to introduce the main principles we use to describe and parameterize our solutions, and provide limiting examples which can be compared against other results in the literature. We begin with the simplest possible orbit: a circular orbit of radius r, confined to the equatorial plane ($I = 0°$ or $I = 180°$).

Many of the results we find are derived in Ref. [125], which focuses on circular orbits of spinning bodies, as well as elsewhere in the literature. The results we present in Sec. 3.3.1 can also be obtained using the effective potential derived in Ref. [67] (see also Refs. [66] and [68]). To facilitate the comparison to this literature, we discuss the method of Ref. [67] in detail in Appendix A.2.

3.3.1 Aligned spin

Start with the small body spin parallel or antiparallel to the orbit: we set the spin components $S^1 = S^2 = 0$, and set $S^3 = s_\parallel \mu^2$, with $-1 \leq s_\parallel \leq 1$. The small body's spin is parallel to the orbit if $s_\parallel > 0$, and antiparallel if $s_\parallel < 0$. The geodesic integrals of motion are

$$\hat{E} = \frac{1 - 2v^2 \pm qv^3}{\sqrt{1 - 3v^2 \pm 2qv^3}} , \tag{3.21}$$

$$\hat{L}_z = \pm\sqrt{rM}\frac{1 \mp 2qv^3 + q^2v^4}{\sqrt{1 - 3v^2 \pm 2qv^3}} , \tag{3.22}$$

$$\hat{Q} = 0 . \tag{3.23}$$

We have introduced $v = \sqrt{M/r}$ (equivalently $r = M/v^2$) and $q = a/M$. Where there is a choice, the upper sign is for prograde orbits ($I = 0°$) and the lower is for retrograde ($I = 180°$). The small body's background 4-velocity is given by $\hat{u}_\alpha = (-\hat{E}, 0, 0, \hat{L}_z)$.

The small body's spin 4-vector is given by

$$S_\alpha = s_\parallel \mu^2 e_{3\alpha} = (0, 0, \mp r s_\parallel \mu^2, 0) \ . \tag{3.24}$$

This result comes from the fact that for an equatorial circular orbit [144],

$$\begin{aligned} e_{3\alpha} &= \left(0, 0, -r\frac{(\hat{L}_z - a\hat{E})}{|\hat{L}_z - a\hat{E}|}, 0\right) \\ &= (0, 0, \mp r, 0) \ . \end{aligned} \tag{3.25}$$

If the orbit is prograde and $s_\parallel > 0$, or the orbit is retrograde and $s_\parallel < 0$, then the small body's spin points in the direction of decreasing θ; vice versa if $s_\parallel$ and the orbit have the opposite signs and orientations.

Let us examine (2.47) for this case. Using Eq. (3.10), we start by expanding the covariant derivative:

$$\begin{aligned} \frac{Du^\alpha}{d\tau} &= (\hat{u}^\beta + u_S^\beta)\nabla_\beta\,(\hat{u}^\alpha + u_S^\alpha) \\ &= \frac{d\hat{u}^\alpha}{d\tau} + \frac{du_S^\alpha}{d\tau} + \Gamma^\alpha{}_{\beta\gamma}\hat{u}^\beta\hat{u}^\gamma + 2\Gamma^\alpha{}_{\beta\gamma}\hat{u}^\beta u_S^\gamma + \mathcal{O}(S^2) \\ &= \frac{du_S^\alpha}{d\tau} + 2\Gamma^\alpha{}_{\beta\gamma}\hat{u}^\beta u_S^\gamma \ . \end{aligned} \tag{3.26}$$

Here, $\Gamma^\alpha{}_{\beta\gamma}$ is the Christoffel connection for the Kerr geometry evaluated along the orbit. In going from the second line to the third line, we used the fact that $\hat{u}^\alpha$ solves the geodesic equation, and we linearized in S. We also used the fact that, for this orbit, the spinning body remains confined to the equatorial plane $\theta = \pi/2$ at radius r. For the misaligned case we consider next, the orbit oscillates in the polar direction, and there is a correction term that involves $\partial_\theta \Gamma^\alpha{}_{\beta\gamma}$.

Requiring the spinning body's orbit to be circular and equatorial means that

$$u_S^r = u_S^\theta = 0 \ . \tag{3.27}$$

Further, the requirement that $u_S^\alpha \hat{u}_\alpha = 0$ tells us that

$$u_S^t = \frac{\hat{L}_z}{\hat{E}} u_S^\phi \ . \tag{3.28}$$

The only unique component we must determine is thus u_S^ϕ. Note that we must have $du_S^\phi/d\tau = 0$. If we observe the system in a frame that co-rotates with the orbit, it appears static; the symmetries of the spin-curvature coupling in this case do not introduce any dynamics.

Combining Eqs. (2.53) and (3.26) with $u_S^r = u_S^\theta = 0 = du_S^\phi/d\tau$, we find the equation which governs the spin correction to the small body's orbital velocity is given by

$$2\Gamma^r{}_{\beta\gamma}\hat{u}^\beta u_S^\gamma = -\frac{1}{2\mu} R^r{}_{\nu\lambda\sigma}\hat{u}^\nu S^{\lambda\sigma} \ ; \tag{3.29}$$

all other components of this equation vanish. Expanding the right-hand and left-hand sides of (3.29), we find

$$2\Gamma^{r}{}_{\beta\gamma}\hat{u}^{\beta}u_S^{\gamma} = \mp\frac{2v\sqrt{1-3v^2\pm 2qv^3}(1-2v^2+q^2v^4)u_S^{\phi}}{1-2v^2\pm qv^3}\,, \tag{3.30}$$

$$-\frac{1}{2\mu}R^{r}{}_{\nu\lambda\sigma}\hat{u}^{\nu}S^{\lambda\sigma} = \frac{3s_{\parallel}\mu}{M^2}\frac{v^7(1\mp qv)(1-2v^2+q^2v^4)}{1-3v^2\pm 2qv^3}\,. \tag{3.31}$$

Using this to evaluate Eq. (3.29) yields

$$u_S^{\phi} = \mp\frac{3s_{\parallel}\mu}{2M^2}\frac{v^6(1\mp qv)(1-2v^2\pm qv^3)}{(1-3v^2\pm 2qv^3)^{3/2}}\,. \tag{3.32}$$

Using Eq. (3.28), this in turn yields a simple result for u_S^t.

An observationally important aspect of this solution is its influence on the system's orbital frequency. Using

$$\Omega_{\phi} = \frac{u^{\phi}}{u^t} = \frac{\hat{u}^{\phi}+u_S^{\phi}}{\hat{u}^t+u_S^t}\,, \tag{3.33}$$

expanding in S, using $\hat{\Omega}_{\phi} = \hat{u}^{\phi}/\hat{u}^t$, and finally defining $\Omega_{\phi} = \hat{\Omega}_{\phi}+\delta\Omega_{\phi}$, we find the correction to the frequency due to the spin-curvature force:

$$\delta\Omega_{\phi} = \hat{\Omega}_{\phi}\left(\frac{u_S^{\phi}}{\hat{u}^{\phi}} - \frac{u_S^t}{\hat{u}^t}\right)\,. \tag{3.34}$$

For circular and equatorial orbits,

$$\hat{\Omega}_{\phi} = \pm\frac{v^3}{M(1\pm qv^3)}\,. \tag{3.35}$$

Combining these various results, we find the shift to the axial frequency:

$$\delta\Omega_{\phi} = \mp\frac{3s_{\parallel}}{2M}\frac{\mu}{M}\frac{(1\mp qv)}{(1\pm qv^3)^2}v^6\,. \tag{3.36}$$

This agrees exactly with Eq. (4.26) in Ref. [125].

The orbiting body's energy, axial angular momentum, and Carter constant are also shifted. Combining Eqs. (2.35), (2.36), (3.14), and (3.15) with the results in this section and using Eqs. (3.19) and (3.20), we find

$$\delta E^S = -\frac{s_{\parallel}}{2}\frac{\mu}{M}\frac{(1\mp qv)(1\mp 4q^3+3q^2v^4)}{(1-3v^2\pm 2qv^3)^{3/2}}v^5\,, \tag{3.37}$$

$$\delta L_z^S = \pm\frac{s_{\parallel}\mu}{2}\frac{(2-13v^2+18v^4)\pm 3q(3-7v^2)v^3+2q^2(1+2v^2)v^6\pm q^3(3-7v^2)v^7+3q^4v^{10}}{(1-3v^2\pm 2qv^3)^{3/2}}\,, \tag{3.38}$$

$$\delta K^S = s_{\parallel}\mu\frac{(2-13v^2+18v^4)\mp 2qv(2-17v^2+28v^4)-q^2v^4(17-45v^2)\mp 6q^3v^7-3q^4v^8}{v(1-3v^2\pm 2qv^3)^2}\,, \tag{3.39}$$

$$\delta Q^S = \mp 2s_{\parallel}\mu a\,. \tag{3.40}$$

These expressions for the conserved quantities δE^S and δL_z^S match exactly with Eqs. (A.19) and (A.20) derived using the alternative approach outlined in Appendix A.2. It is interesting that there is a non-zero δQ^S even though there is no change to the polar motion of the small body in this case. We note that Witzany has provided a modified definition of δQ^S (see text near Eq. (48) of Ref. [84]) such that it is zero for cases in which there is no polar motion; we are likely to adopt this definition in future work. In any case, our result agrees with that reported in Ref. [125], after translating the somewhat different notation.

3.3.2 Misaligned spin

Now consider the small body's spin misaligned from the orbit. The background 4-velocity and integrals of motion are identical to those used in Sec. 3.3.1, but the small body's spin becomes

$$S_\alpha = \mu^2 \left(s_\perp \cos\phi_s \, e_{1\alpha} + s_\perp \sin\phi_s \, e_{2\alpha} + s_\parallel \, e_{3\alpha} \right) . \tag{3.41}$$

We have broken the spin into a component parallel to the orbital angular momentum (out of the orbital plane) with magnitude $s_\parallel$, and into components normal to the orbital angular momentum (in the orbital plane) with magnitude $s_\perp$. The angle ϕ_s describes the orientation of the spin components normal to the orbit. Setting $s = \sqrt{s_\perp^2 + s_\parallel^2}$, we require $0 \leq s \leq 1$.

Using (2.55) and (2.56), Eq. (3.41) can be rewritten

$$S_\alpha = \mu^2 \left[s_\perp \Big(\cos(\phi_s + \psi_p) \tilde{e}_{1\alpha} + \sin(\phi_s + \psi_p) \tilde{e}_{2\alpha} \Big) + s_\parallel e_{3\alpha} \right] , \tag{3.42}$$

where ψ_p is the precession phase, which grows with time. The tetrad leg $e_{3\alpha}$ is the same as in Sec. 3.3.1. Continuing to use the parameterization $q \equiv a/M$, $v = \sqrt{M/r}$, the tetrad legs $\tilde{e}_{1\alpha}$ and $\tilde{e}_{2\alpha}$ are given by

$$\tilde{e}_{1\alpha} = \left(0, \frac{1}{\sqrt{1 - 2v^2 + a^2 v^4}}, 0, 0 \right) , \tag{3.43}$$

$$\tilde{e}_{2\alpha} = \left(v \sqrt{\frac{1 - 2v^2 + q^2 v^4}{1 - 3v^2 \pm 2qv^3}}, 0, 0, \mp r(1 \pm qv^3) \sqrt{\frac{1 - 2v^2 + q^2 v^4}{1 - 3v^2 \pm 2qv^3}} \right) . \tag{3.44}$$

For circular and equatorial orbits, the precession phase ψ_p can be written as functions of Mino-time λ, proper time τ, or Boyer-Lindquist time t:

$$\psi_p = \Upsilon_s \lambda = \omega_s \tau = \Omega_s t , \tag{3.45}$$

with

$$\Upsilon_s = \sqrt{rM} = M/v , \qquad \omega_s = \sqrt{M/r^3} = v^3/M ,$$
$$\Omega_s = \omega_s \frac{\sqrt{1 - 3v^2 \pm 2qv^3}}{(1 \pm qv^3)} . \tag{3.46}$$

This limiting form for Υ_s was found in Ref. [164], and is confirmed by the general expression derived in Ref. [144]. The factor Σ which converts from Mino-time frequencies to proper-time frequencies takes the constant value r^2 for circular and equatorial orbits; likewise, the factor

$$\Gamma = r^2 \frac{1 \pm qv^3}{\sqrt{1 - 3v^2 \pm 2qv^3}} \tag{3.47}$$

which converts between Mino-time frequencies and coordinate-time quantities is constant for circular and equatorial orbits.

To proceed, we again examine Eq. (2.47) and use Eq. (3.3), i.e., $\theta = \pi/2 + \delta\vartheta_S$, with $\delta\vartheta_S = \mathcal{O}(S)$. Expanding the covariant derivative yields a slightly different result as compared to what we found in the aligned case:

$$\begin{aligned}
\frac{Du^\alpha}{d\tau} &= (\hat{u}^\beta + u_S^\beta)\nabla_\beta\,(\hat{u}^\alpha + u_S^\alpha) \\
&= \frac{d\hat{u}^\alpha}{d\tau} + \frac{du_S^\alpha}{d\tau} + \Gamma^\alpha{}_{\beta\gamma}\hat{u}^\beta\hat{u}^\gamma + \delta\vartheta_S\partial_\theta\Gamma^\alpha{}_{\beta\gamma}\hat{u}^\beta\hat{u}^\gamma + 2\Gamma^\alpha{}_{\beta\gamma}\hat{u}^\beta u_S^\gamma + \mathcal{O}(S^2) \\
&= \frac{du_S^\alpha}{d\tau} + \delta\vartheta_S\partial_\theta\Gamma^\alpha{}_{\beta\gamma}\hat{u}^\beta\hat{u}^\gamma + 2\Gamma^\alpha{}_{\beta\gamma}\hat{u}^\beta u_S^\gamma\,.
\end{aligned} \tag{3.48}$$

The misaligned spin causes the small body to oscillate about the equatorial plane by $\delta\vartheta_S$. This shifts the connection term at $\mathcal{O}(S)$, leading to the term in $\partial_\theta\Gamma^\alpha{}_{\beta\gamma}$.

Expanding the covariant derivatives and Riemann components of Eq. (2.47) for this case, making use of Eq. (3.48) we find

$$\frac{du_S^r}{d\tau} \pm \frac{2v(1 - 2v^2 + q^2v^4)\sqrt{1 - 3v^2 \pm 2qv^3}}{1 - 2v^2 \pm qv^3} u_S^\phi = \frac{3s_\parallel\mu}{M^2}\frac{v^7(1 \mp qv)(1 - 2v^2 + q^2v^4)}{1 - 3v^2 \pm 2qv^3}\,, \tag{3.49}$$

$$\frac{du_S^\phi}{d\tau} + \frac{2v^5(1 - 2v^2 \pm qv^3)}{M^2(1 - 2v^2 + q^2v^4)\sqrt{1 - 3v^2 \pm 2qv^3}} u_S^r = 0\,, \tag{3.50}$$

for the equations governing u_S^r and u_S^ϕ. Notice that these equations do not couple to the precessing orbit's polar motion. Notice also that since $\hat{u}^r = \hat{u}^\theta = 0$, Eq. (3.28) holds for the misaligned case, and we do not need a separate equation governing u_S^t.

We require the orbit to remain circular, so we put $u_S^r = 0 = du_S^r/d\tau$. This allows us to immediately solve Eq. (3.49):

$$u_S^\phi = \mp\frac{3s_\parallel\mu}{2M^2}\frac{v^6(1 \mp qv)(1 - 2v^2 \pm qv^3)}{(1 - 3v^2 \pm 2qv^3)^{3/2}}\,. \tag{3.51}$$

Since this does not vary with time, Eq. (3.50) is also satisfied. Equation (3.51) is identical to the result we found in the spin-aligned case, Eq. (3.32). Our solution for u_S^t is likewise identical to its aligned counterpart. From this it follows that Eq. (3.36) describes the change to the orbital frequency in this case as well.

The polar motion for this misaligned case requires more attention. As stated above, we put $\theta = \pi/2 + \delta\vartheta_S$, where $\delta\vartheta_S$ denotes the spin-induced polar motion about the equatorial

plane. Because $\hat{u}^\theta = 0$, we put $u^\theta = u^\theta_S = d\delta\vartheta_S/d\tau$. The polar component of Eq. (2.47) thus becomes

$$\frac{d^2\delta\vartheta_S}{d\tau^2} + \frac{v^6}{M^2}\frac{(1 \mp 4qv^3 + 3q^2v^4)}{(1 - 3v^2 \pm 2qv^3)}\delta\vartheta_S = -\frac{3s_\perp\mu}{M^3}\frac{v^9(1 \mp qv)\sqrt{1 - 2v^2 + q^2v^4}}{1 - 3v^2 \pm 2qv^3}\cos(\phi_s + \psi_p) \ . \tag{3.52}$$

The coefficient of $\delta\vartheta_S$ on the left-hand side of Eq. (3.52) is the square of the polar proper-time frequency for circular equatorial geodesic orbits, which we denote ω_θ. The solution to Eq. (3.52) has the form

$$\delta\vartheta_S = A(\tau)\sin(\omega_\theta\tau) + B(\tau)\cos(\omega_\theta\tau) \ , \tag{3.53}$$

where

$$\omega_\theta = \frac{v^3}{M}\sqrt{\frac{1 \mp 4qv^3 + 3q^2v^4}{1 - 3v^2 \pm 2qv^3}} \ , \tag{3.54}$$

and where $A(\tau)$ and $B(\tau)$ are given by

$$\begin{aligned} A(\tau) = c_1 &- \frac{3s_\perp\mu}{2M^2}\frac{v^6(1 \mp qv)}{\sqrt{1 - 3v^2 \pm 2qv^3}}\sqrt{\frac{1 - 2v^2 + q^2v^4}{1 \mp 4qv^3 + 3q^2v^4}} \\ &\times \left[\frac{\sin(\phi_s + (\omega_s - \omega_\theta)\tau)}{\omega_s - \omega_\theta} + \frac{\sin(\phi_s + (\omega_s + \omega_\theta)\tau)}{\omega_s + \omega_\theta}\right] \ , \end{aligned} \tag{3.55}$$

$$\begin{aligned} B(\tau) = c_2 &+ \frac{3s_\perp\mu}{2M^2}\frac{v^6(1 \mp qv)}{\sqrt{1 - 3v^2 \pm 2qv^3}}\sqrt{\frac{1 - 2v^2 + q^2v^4}{1 \mp 4qv^3 + 3q^2v^4}} \\ &\times \left[\frac{\cos(\phi_s + (\omega_s - \omega_\theta)\tau)}{\omega_s - \omega_\theta} - \frac{\cos(\phi_s + (\omega_s + \omega_\theta)\tau)}{\omega_s + \omega_\theta}\right] \ . \end{aligned} \tag{3.56}$$

The constants c_1 and c_2 must be determined by matching to the initial conditions $\delta\vartheta_S|_{\tau=0}$ and $u^\theta_S|_{\tau=0}$. The precession of the small body's spin as it orbits the black hole causes the orbital plane to likewise precess. Note that the frequency combination $\omega_s - \omega_\theta$ never passes through zero anywhere over the domain of allowed orbits. As such, the functions $A(\tau)$ and $B(\tau)$ defined in Eqs. (3.55) and (3.56) are well behaved everywhere.

The changes to the integrals of motion we find are identical to those in the aligned case, Eqs. (3.37) – (3.40). The fact that the changes δE^S and δL^S_z are identical is consistent with other patterns that this analysis uncovered. However, the fact that δQ^S is identical — in particular, that δQ^S is insensitive to $s_\perp$ — is somewhat surprising, since the small body does in fact move in the polar direction when the spin and orbit are misaligned. The precession of the smaller body's spin nonetheless keeps the orbit equatorial on average, which appears to be sufficient for Q to take its equatorial value. This again is consistent with results found in Ref. [125].

3.4 Spinning-body orbits II: Slightly eccentric, nearly equatorial orbits

Slightly eccentric equatorial orbits are simple enough that, by expanding in both eccentricity e and spin s, we can develop and present mostly closed-form results for this case. In our discussion below, we show leading-order results, $\mathcal{O}(e,s)$, for orbits of bodies with general spin orientation in the Kerr spacetime. We go to higher order, $\mathcal{O}(e^2,s)$ for Schwarzschild only, confining ourselves to the case of small body spin aligned with the orbit. Though no issue of principle prevents us from developing a more generic analysis at higher order, the formulas describing Kerr orbits become cumbersome as we go to higher order in e. As we will see below, our leading-order analysis is sufficient for us to understand the impact of misaligned spin on spinning-body orbital dynamics.

The results in the aligned spin section, Sec. 3.4.3, can be obtained using an alternative method we describe in Appendix A.2. This method is discussed in Refs. [66]–[68], and involves using conserved quantities E^S, L_z^S, μ^2 and S^2 to develop an effective potential for the radial motion.

3.4.1 General principles

In this section and in what follows, we switch from using proper time τ to Mino time λ for our parameterization of these orbits. This switch is not necessary for equatorial or nearly equatorial orbits, but will be necessary for the generic cases that we study in the next chapter. Using this parameterization now allows us to set up the calculation in this framework, and to examine the form of the solutions which emerge in this relatively simple limit.

The governing equation for the orbits is Eq. (2.47), which we repeat here and use to define the spin-curvature force f_S^α:

$$\frac{Du^\alpha}{d\tau} = -\frac{1}{2\mu} R^\alpha{}_{\nu\lambda\sigma} u^\nu S^{\lambda\sigma} \equiv f_S^\alpha/\mu \,. \tag{3.57}$$

Expanding the covariant derivative, this becomes

$$\frac{du^\alpha}{d\tau} + \Gamma^\alpha{}_{\beta\gamma} u^\beta u^\gamma = f_S^\alpha/\mu \,, \tag{3.58}$$

where $\Gamma^\alpha{}_{\beta\gamma}$ is the Christoffel connection for the Kerr spacetime, evaluated along the orbit.

Let us define

$$U^\alpha \equiv \frac{dx^\alpha}{d\lambda} = \Sigma u^\alpha \,; \tag{3.59}$$

this follows from $u^\alpha = dx^\alpha/d\tau$, as well as the definition of Mino-time: $d/d\lambda = \Sigma d/d\tau$. From (3.59), it follows that

$$\frac{du^\alpha}{d\lambda} = \frac{1}{\Sigma}\frac{dU^\alpha}{d\lambda} - \frac{U^\alpha}{\Sigma^2}\frac{d\Sigma}{d\lambda} \,. \tag{3.60}$$

Next multiply (3.58) by Σ^2. Doing so and using Eq. (3.60), we put the equation which governs spinning-body orbits into the form

$$\frac{dU^\alpha}{d\lambda} - \frac{U^\alpha}{\Sigma}\frac{d\Sigma}{d\lambda} + \Gamma^\alpha{}_{\beta\gamma} U^\beta U^\gamma = \Sigma^2 f_S^\alpha/\mu \,. \tag{3.61}$$

Note that in general,

$$\frac{d\Sigma}{d\lambda} = 2r\,U^r - 2a^2\cos\theta\sin\theta\,U^\theta\ . \tag{3.62}$$

For the equatorial and nearly equatorial orbits which are our focus in this section, the second term in (3.62) is $\mathcal{O}(S^2)$, which we neglect. The factor $(1/\Sigma)d\Sigma/d\lambda$ in Eq. (3.61) becomes $2U^r/r$.

For misaligned orbits, the orbiting body oscillates about the equatorial plane, just as we discussed for the circular misaligned case in Sec. 3.3.2. Setting the polar angle to $\theta = \pi/2 + \delta\vartheta_S$, with $\delta\vartheta_S = \mathcal{O}(S)$, the connection term in Eq. (3.61) becomes

$$\Gamma^\alpha{}_{\beta\gamma}U^\beta U^\gamma = (\Gamma^\alpha{}_{\beta\gamma})_{\theta=\pi/2}\,U^\beta U^\gamma + \delta\vartheta_S\,(\partial_\theta\Gamma^\alpha{}_{\beta\gamma})_{\theta=\pi/2}\,\hat{U}^\beta\hat{U}^\gamma\ . \tag{3.63}$$

Notice that it is the geodesic 4-velocity $\hat{U}^\beta$ that appears in the term with the derivative of the connection. Because $\delta\vartheta_S$ is itself $\mathcal{O}(S)$, contributions from the non-geodesic parts of U^β enter this term at $\mathcal{O}(S^2)$ or higher.

Let us write the small body's spin in the form

$$S_\alpha = \mu^2\left[s_\perp\Big(\cos(\phi_s+\psi_p)\tilde{e}_{1\alpha} + \sin(\phi_s+\psi_p)\tilde{e}_{2\alpha}\Big) + s_\parallel e_{3\alpha}\right]\ , \tag{3.64}$$

$$= \big(s_\perp\mu^2\sigma_t, s_\perp\mu^2\sigma_r, \mp s_\parallel\mu^2 r, s_\perp\mu^2\sigma_\phi\big)\ . \tag{3.65}$$

Both the precession phase ψ_p and the tetrad elements $\tilde{e}_{1\alpha}$ and $\tilde{e}_{2\alpha}$ are more complicated than they were in the circular limit; we defer discussion of their detailed forms until they are needed later in our analysis. The form (3.65) is a useful rewriting of (3.64); the components $\sigma_{t,r,\phi}$ can be read out of $\tilde{e}_{1\alpha}$ and $\tilde{e}_{2\alpha}$.

With everything in place, it is now not difficult to evaluate all the terms appearing in Eq. (3.61) and write out the equations governing the small body's 4-velocity U^α. First, we write out the equations for U^r, U^t and U^ϕ.

$$\begin{aligned}\frac{dU^t}{d\lambda} &- \frac{2U^r\left[(r^3-3Mr^2+a^2(r-M))\,U^r + aM(3r^2+a^2)U^\phi\right]}{r^2\Delta}\\ &= \frac{3s_\parallel\mu(\hat{L}_z - a\hat{E})M(r^2+a^2)\hat{U}^r}{r^2\Delta}\ ,\end{aligned} \tag{3.66}$$

$$\begin{aligned}\frac{dU^r}{d\lambda} &+ \frac{\Delta\left[M(U^t - aU^\phi)^2 - r^3(U^\phi)^2\right]}{r^4} - \frac{(2r^2-3Mr-a^2)(U^r)^2}{r\Delta}\\ &= \frac{3s_\parallel\mu(\hat{L}_z - a\hat{E})M\left[\hat{E}(r^2+a^2) - a\hat{L}_z\right]}{r^2}\ ,\end{aligned} \tag{3.67}$$

$$\frac{dU^\phi}{d\lambda} + \frac{2U^r\left[aMU^r + (r^3-2Mr^2-a^2M)U^\phi\right]}{r^2\Delta} = \frac{3as_\parallel\mu(\hat{L}_z - a\hat{E})M\hat{U}^r}{r^2\Delta}\ . \tag{3.68}$$

No term involving $\delta\vartheta_S$ enters these equations at $\mathcal{O}(S)$. Indeed, note that the equations for U^t, U^r, and U^ϕ are completely independent of U^θ at this order. We can therefore solve $U^{t,r,\phi}$ independently from our solution for U^θ.

It is worth remarking that Eqs. (3.66) and (3.68) turn out to simplify further by converting them to equations for u_t and u_ϕ. Doing so using by converting from $U^{t,\phi}$ to $u^{t,\phi}$, lowering an index, and then using $u_t = -\hat{E} + u_t^S$, $u_\phi = \hat{L}_z + u_\phi^S$, where $u_{t,\phi}^S = \mathcal{O}(S)$, we find

$$\frac{du_t^S}{d\lambda} = -\frac{3s_\parallel \mu(\hat{L}_z - a\hat{E})M\hat{U}^r}{r^4} \,, \tag{3.69}$$

$$\frac{du_\phi^S}{d\lambda} = \frac{3as_\parallel \mu(\hat{L}_z - a\hat{E})M\hat{U}^r}{r^4} \,. \tag{3.70}$$

Solving Eqs. (3.69) and (3.70) is equivalent to solving (3.66) and (3.68), respectively.

Finally, the equation we find for U^θ is

$$\begin{aligned}&\frac{dU^\theta}{d\lambda} + \frac{2a^4 r\hat{E}^2 - 4a^3 r\hat{E}\hat{L}_z + (r-2M)r^3\hat{L}_z^2 + a^2(2r^3\hat{E}^2 + 2r\hat{L}_z^2 - (\hat{U}^r)^2)}{r^2\Delta}\delta\vartheta_S \\ &= -\frac{3s_\perp \mu(\hat{L}_z - a\hat{E})M}{r^3\Delta}\left(\sigma_t(r^2+a^2)\hat{U}^r + \sigma_r\left[\hat{E}(r^2+a^2) - a\hat{L}_z\right]\Delta + \sigma_\phi a\hat{U}^r\right) \,,\end{aligned} \tag{3.71}$$

Notice that $dU^\theta/d\lambda$ only couples to $s_\perp$, and $dU^{t,r,\phi}/d\lambda$ only couple to $s_\parallel$. Notice further that we have not yet introduced an expansion in eccentricity. This means that for *all* nearly equatorial orbits, the small body's motion in the equatorial plane is totally decoupled from its out-of-plane dynamics.

For equatorial and nearly equatorial orbits, we take the small body to move on a trajectory whose radial motion is given by

$$r = \frac{pM}{1 + e\cos\chi_r} \,. \tag{3.72}$$

We introduce here the orbit's the semi-latus rectum p and eccentricity e, as well as the radial true anomaly χ_r. This anomaly can be written

$$\chi_r = w_r + \delta\chi_r \,, \tag{3.73}$$

where w_r is the radial *mean anomaly*. The difference between the radial mean and true anomalies, $\delta\chi_r$, is an oscillatory function whose mean value is zero. In the Mino-time parameterization, $w_r = \Upsilon_r\lambda$.

As discussed in Sec. 2.1, the parameterization (3.72) is used extensively in studies of geodesic motion. As we will show, it works perfectly for nearly equatorial orbits of spinning bodies as well. This form does not work so well for generic orbits of spinning bodies; for general orbit inclination, we need to allow the radial libration region to oscillate as the orbit precesses. This case is discussed in Chapter 4.

We now solve for the orbit by introducing simultaneous expansions in the small body's spin and the orbit's eccentricity e. By requiring that Eqs. (3.66) – (3.68) hold order by order, we construct a full solution for the orbit of the small body's motion to that order in our expansion.

3.4.2 Leading order in eccentricity

We begin by considering Kerr orbits at $\mathcal{O}(e,s)$. In this limit, it suffices to put $\chi_r = w_r = \Upsilon_r\lambda = (\hat{\Upsilon}_r + \Upsilon_r^S)\lambda$. [Although there is a linear-in-eccentricity correction to χ_r, its impact on the small body's motion enters at $\mathcal{O}(e^2)$.]

To first order in e, the radial motion of the small body is thus given by

$$r = pM\left(1 - e\cos w_r\right) = pM\left[1 - \frac{e}{2}\left(e^{iw_r} + e^{-iw_r}\right)\right] \ . \tag{3.74}$$

The second form proves to be particularly useful for our purposes.

Our goal is to compute how the spin-curvature interaction affects all of the important parameters of our system. Just as in our study of circular and equatorial orbits, we assume that the constants of the motion take the form $\mathcal{X}^S = \hat{\mathcal{X}} + \delta\mathcal{X}^S$ (with $\mathcal{X} \in [E, L_z, K, Q]$), and that

$$\Upsilon_r = \hat{\Upsilon}_r + \Upsilon_r^S \ , \tag{3.75}$$

$$\Upsilon_\phi = \hat{\Upsilon}_\phi + \Upsilon_\phi^S \ , \tag{3.76}$$

$$\Gamma = \hat{\Gamma} + \Gamma^S \ . \tag{3.77}$$

First consider just the leading-order geodesic motion. The integrals of motion are

$$\hat{E} = \frac{1 - 2v^2 \pm qv^3}{\sqrt{1 - 3v^2 \pm 2qv^3}} + \mathcal{O}(e^2) \ , \tag{3.78}$$

$$\hat{L}_z = \pm\frac{M}{v}\sqrt{\frac{1 \mp 2qv^3 + q^2v^4}{1 - 3v^2 \pm 2qv^3}} + \mathcal{O}(e^2) \ , \tag{3.79}$$

$$\hat{Q} = 0 \ . \tag{3.80}$$

As before, $q \equiv a/M$, but now we have $v = \sqrt{1/p}$. We also have

$$\hat{\Upsilon}_r = \frac{M}{v}\sqrt{\frac{1 - 6v^2 \pm 8qv^3 - 3q^2v^4}{1 - 3v^2 \pm 2qv^3}} + \mathcal{O}(e^2) \ , \tag{3.81}$$

$$\hat{\Upsilon}_\phi = \pm\frac{M}{v}\sqrt{\frac{1}{1 - 3v^2 \pm 2qv^3}} + \mathcal{O}(e^2) \ , \tag{3.82}$$

$$\hat{\Gamma} = \frac{M^2(1 \pm qv^3)}{v^4\sqrt{1 - 3v^2 \pm 2qv^3}} + \mathcal{O}(e^2) \ . \tag{3.83}$$

Let us first consider the components which describe the in-plane orbital motion, $U^{t,r,\phi}$. We write these components

$$U^t = U^t_0 + s_\parallel e\left(U^t_{-1}e^{iw_r} + U^t_{+1}e^{-iw_r}\right) \ , \tag{3.84}$$

$$U^\phi = U^\phi_0 + s_\parallel e\left(U^\phi_{-1}e^{iw_r} + U^\phi_{+1}e^{-iw_r}\right) \ , \tag{3.85}$$

$$U^r = \frac{dr}{d\lambda} = -\frac{iepM}{2}\left(\hat{\Upsilon}_r + \Upsilon_r^S\right)\left(e^{iw_r} - e^{-iw_r}\right) \ . \tag{3.86}$$

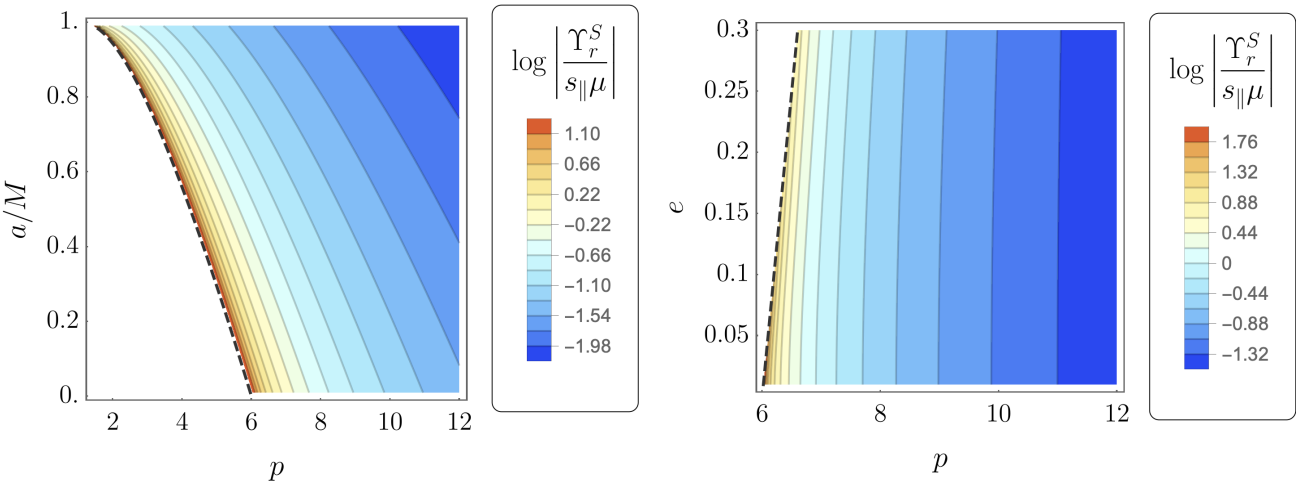

Figure 3.1: Example of the spin contribution Υ_r^S to the radial Mino-time frequency Υ_r. Left panel shows Υ_r^S to leading order in e as a function of semi-latus rectum p and spin parameter a for prograde orbits ($I = 0°$); see Eq. (3.91). Right panel shows Υ_r^S to second-order in e for Schwarzschild black hole orbits ($a = 0$) as a function of p and e. In both cases, the last stable orbit is indicated by the black dashed line.

In our assumed form of U^r, we used the fact that for small eccentricity equatorial orbits, $dw_r/d\lambda = \hat{\Upsilon}_r + \Upsilon_r^S$.

We next insert Eqs. (3.84), (3.85), and (3.86) into Eqs. (3.66), (3.67), and (3.68), also enforcing the constraint (3.11) in order to solve to each order in s and e. This exercise yields

$$\Gamma \equiv U_0^t = \frac{M^2(1 \pm qv^3)}{v^4\sqrt{1 - 3v^2 \pm 2qv^3}} \mp \left(\frac{3s_\parallel \mu}{2}\right) \frac{Mv(1 \mp qv)(1 \mp 2qv^3 + q^2v^4)}{(1 - 3v^2 \pm 2qv^3)^{3/2}} \,, \tag{3.87}$$

$$U_{-1}^t = U_{+1}^t = \mp \left(\frac{3s_\parallel \mu}{2}\right) \frac{qMv^4(1 \mp qv)^2(1 \mp 2qv^3 + q^2v^4)}{(1 - 2v^2 + q^2v^4)(1 - 3v^2 \pm 2qv^3)^{3/2}} \,, \tag{3.88}$$

$$\Upsilon_\phi \equiv U_0^\phi = \pm\frac{M}{v}\sqrt{\frac{1}{1 - 3v^2 \pm 2qv^3}} - \left(\frac{3s_\parallel \mu}{2}\right) \frac{v^2(1 \mp qv)(1 - 2v^2 \pm qv^3)}{(1 - 3v^2 \pm 2qv^3)^{3/2}} \,, \tag{3.89}$$

$$U_{-1}^\phi = U_{+1}^\phi = -\left(\frac{3s_\parallel \mu}{2}\right) \frac{qv^5(1 - 2v^2 \pm qv^3)}{(1 - 2v^2 + q^2v^4)(1 - 3v^2 \pm 2qv^3)^{3/2}} \,, \tag{3.90}$$

$$\Upsilon_r^S = \left(\frac{3s_\parallel \mu}{2}\right) \frac{v^2(1 \mp qv)\,(1 - 2v^2 \mp qv^3(5 - 14v^2) + 5v^4q^2(1 - 4v^2) \pm 7q^3v^7)}{(1 - 3v^2 \pm 2qv^3)^{3/2}\sqrt{1 - 6v^2 \pm 8qv^3 - 3q^2v^4}} \,. \tag{3.91}$$

Eq. (3.91) matches with the expression Eq. (A.41) derived using the exact-in-e approach discussed in Appendix A.2. The integrals of the motion for these orbits are identical to those what we found in the circular case, Eqs. (3.37) – (3.40), but with $v = \sqrt{1/p}$. The left panel of Figure 3.1 displays how Υ_r^S depends on a according to Eq. (3.91). Notice that the axial frequency Υ_ϕ and quantity Γ, which converts from Mino-time frequencies to coordinate-time frequencies, are obtained by orbit averaging U^ϕ and U^t respectively. Hence, Γ is the same as U_0^t, given in Eq. (3.87), and Υ_ϕ is the same as U_0^ϕ in Eq. (3.89).

Turn now to the out-of-plane motion. To make progress here, we first must more completely describe the tetrad elements. They take the form

$$\tilde{e}_{1\alpha} = \tilde{e}^0_{1\alpha} + e\,\tilde{e}^1_{1\alpha} \,, \tag{3.92}$$
$$\tilde{e}_{2\alpha} = \tilde{e}^0_{2\alpha} + e\,\tilde{e}^1_{2\alpha} \,. \tag{3.93}$$

The terms $\tilde{e}^0_{1\alpha}$ and $\tilde{e}^0_{2\alpha}$ are exactly as defined in Eqs. (3.43) and (3.44), but with $v = \sqrt{1/p}$ rather than $v = \sqrt{M/r}$. The eccentricity corrections are given by

$$\tilde{e}^1_{1\alpha} = \left(-\frac{v^2}{M}\zeta\hat{\Upsilon}_r \sin w_r, \frac{v^2(1-q^2v^2)}{(1-2v^2+q^2v^4)^{3/2}} \cos w_r, 0, qv^2\zeta\hat{\Upsilon}_r \sin w_r \right) \,, \tag{3.94}$$
$$\tilde{e}^1_{2\alpha} = \left(v\zeta \cos w_r, -\frac{v^3(1\mp qv)}{(1-2v^2-q^2v^4)^{3/2}}\hat{\Upsilon}_r \sin w_r, 0, pM(1\mp qv^3)\zeta\cos w_r \right) \,, \tag{3.95}$$

where

$$\zeta = \sqrt{\frac{1-3v^2\pm 2qv^3}{1-2v^2+q^2v^4}} \,. \tag{3.96}$$

We used $dw_r/d\lambda = \hat{\Upsilon}_r$ rather than $dw_r/d\lambda = \Upsilon_r = \hat{\Upsilon}_r + \Upsilon^S_r$ because these tetrad elements are used to build the spin vector S_α; any contribution from Υ^S_r is at $\mathcal{O}(S^2)$.

To complete our description of the out-of-plane motion, we first note that because $\hat{U}^\theta = 0$

$$U^\theta = \Sigma u^\theta = \Sigma \frac{d\delta\vartheta_S}{d\tau} = \frac{d\delta\vartheta_S}{d\lambda} \,, \tag{3.97}$$

and so

$$\frac{dU^\theta}{d\lambda} = \frac{d^2\delta\vartheta_S}{d\lambda^2} \,. \tag{3.98}$$

Using this in Eq. (3.71), along with Eqs. (3.78), (3.79), and (3.86) for $\hat{E}$, $\hat{L}_z$, and $\hat{U}^r$, and finally using Eqs. (3.94) and (3.95) to work out the components σ_t, σ_r, and σ_ϕ yields

$$\frac{d^2\delta\vartheta_S}{d\lambda^2} + \Upsilon^2_\theta \delta\vartheta_S = F^\theta_S(\lambda) \,, \tag{3.99}$$

where

$$\Upsilon_\theta = \frac{M}{v}\sqrt{\frac{1\mp 4qv^3+3q^2v^4}{1-3v^2\pm 2qv^3}}, \tag{3.100}$$

is the Mino-time polar frequency for nearly equatorial circular orbits, and where the forcing term is given by

$$\begin{aligned} F^\theta_S(\lambda) &= 3s_\perp \mu M \left[\mp \frac{v(1\mp qv)\left[1-2v^2+q^2v^4+e\left(1-v^2\mp 2qv^3+2q^2v^4\right)\cos w_r\right]}{(1-3v^2\pm 2qv^3)\sqrt{1-2v^2+q^2v^4}} \cos(\phi_s+\psi_p) \right] \\ &\equiv 3s_\perp \mu M(\alpha_1 + e\alpha_2 \cos w_r)\cos(\phi_s+\psi_p) \,. \end{aligned} \tag{3.101}$$

For notational convenience, we have introduced

$$\alpha_1 = \mp \frac{v(1 \mp qv)\sqrt{1 - 2v^2 + q^2v^4}}{(1 - 3v^2 \pm 2qv^3)} \ , \tag{3.102}$$

$$\alpha_2 = \mp \frac{v(1 \mp qv)(1 - v^2 \mp 2qv^3 + 2q^2v^4)}{(1 - 3v^2 \pm 2qv^3)\sqrt{1 - 2v^2 + q^2v^4}} \ . \tag{3.103}$$

For eccentric equatorial orbits, the precession phase takes the form

$$\psi_p = \Upsilon_s \lambda + \psi_r \ , \tag{3.104}$$

where

$$\Upsilon_s = M\sqrt{p} + \mathcal{O}(e^2) = \frac{M}{v} + \mathcal{O}(e^2) \ , \tag{3.105}$$

and where ψ_r is a contribution to the precession phase that varies along the orbit's radial motion. Van de Meent [144] provides a general expression for ψ_r; for small eccentricity, this expression reduces to

$$\begin{aligned} \psi_r &= -\frac{2ev^2(1 \mp qv)^2}{(1 - 2v^2 + q^2v^4)} \sqrt{\frac{1 - 3v^2 \pm 2qv^3}{1 - 6v^2 \pm 8qv^3 - 3q^2v^4}} \sin w_r \\ &\equiv e\varpi(q, v) \sin w_r \ . \end{aligned} \tag{3.106}$$

Note that $\psi_r \propto ev^2$, and so by definition ψ_r is a small quantity in the small eccentricity limit. This allows us to usefully expand $\cos(\phi_s + \psi_p)$:

$$\begin{aligned} \cos(\phi_s + \psi_p) &= \cos(\phi_s + \Upsilon_s \lambda + e\varpi \sin w_r) \\ &= \cos(\phi_s + \Upsilon_s \lambda) \cos(e\varpi \sin w_r) - \sin(\phi_s + \Upsilon_s \lambda) \sin(e\varpi \sin w_r) \\ &\simeq \cos(\phi_s + \Upsilon_s \lambda) - e\varpi \sin w_r \sin(\phi_s + \Upsilon_s \lambda) \ . \end{aligned} \tag{3.107}$$

Combining Eqs. (3.101) and (3.107), and then linearizing in e yields

$$F_S^\theta(\lambda) = 3s_\perp \mu M \Big\{ \alpha_1 \cos(\phi_s + \Upsilon_s \lambda) + e \Big[\alpha_2 \cos w_r \cos(\phi_s + \Upsilon_s \lambda) - \alpha_1 \varpi \sin w_r \sin(\phi_s + \Upsilon_s \lambda) \Big] \Big\} \ . \tag{3.108}$$

As in Sec. 3.3.2, we use variation of constants to solve Eq. (3.99), yielding

$$\delta\vartheta_S = A(\lambda) \cos(\Upsilon_\theta \lambda) + B(\lambda) \sin(\Upsilon_\theta \lambda) \ , \tag{3.109}$$

where

$$A(\lambda) = c_1 - \frac{3\mu M s_\perp}{8\Upsilon_\theta}\left[\frac{4\alpha_1\cos(\lambda(\Upsilon_s-\Upsilon_\theta))}{\Upsilon_s-\Upsilon_\theta} - \frac{4\alpha_1\cos(\lambda(\Upsilon_\theta+\Upsilon_s))}{\Upsilon_\theta+\Upsilon_s}\right.$$
$$+ \frac{2e(\alpha_2-\alpha_1\varpi)\cos(\lambda(-\Upsilon_\theta+\Upsilon_r-\Upsilon_s))}{-\Upsilon_\theta+\hat{\Upsilon}_r-\Upsilon_s} + \frac{2e(\alpha_2+\alpha_1\varpi)\cos(\lambda(-\Upsilon_\theta+\Upsilon_r+\Upsilon_s))}{-\Upsilon_\theta+\hat{\Upsilon}_r+\Upsilon_s}$$
$$\left. - \frac{2e(\alpha_2-\alpha_1\varpi)\cos(\lambda(\Upsilon_\theta+\Upsilon_r-\Upsilon_s))}{\Upsilon_\theta+\hat{\Upsilon}_r-\Upsilon_s} - \frac{2e(\alpha_2+\alpha_1\varpi)\cos(\lambda(\Upsilon_\theta+\Upsilon_r+\Upsilon_s))}{\Upsilon_\theta+\hat{\Upsilon}_r+\Upsilon_s}\right], \tag{3.110}$$

$$B(\lambda) = c_2 + \frac{3\mu M s_\perp}{8\Upsilon_\theta}\left[\frac{4\alpha_1\sin(\lambda(\Upsilon_s-\Upsilon_\theta))}{\Upsilon_s-\Upsilon_\theta} + \frac{4\alpha_1\sin(\lambda(\Upsilon_\theta+\Upsilon_s))}{\Upsilon_\theta+\Upsilon_s}\right.$$
$$+ \frac{2e(\alpha_2-\alpha_1\varpi)\sin(\lambda(-\Upsilon_\theta+\Upsilon_r-\Upsilon_s))}{-\Upsilon_\theta+\hat{\Upsilon}_r-\Upsilon_s} + \frac{2e(\alpha_2+\alpha_1\varpi)\sin(\lambda(-\Upsilon_\theta+\Upsilon_r+\Upsilon_s))}{-\Upsilon_\theta+\hat{\Upsilon}_r+\Upsilon_s}$$
$$\left. + \frac{2e(\alpha_2-\alpha_1\varpi)\sin(\lambda(\Upsilon_\theta+\Upsilon_r-\Upsilon_s))}{\Upsilon_\theta+\hat{\Upsilon}_r-\Upsilon_s} + \frac{2e(\alpha_2+\alpha_1\varpi)\sin(\lambda(\Upsilon_\theta+\Upsilon_r+\Upsilon_s))}{\Upsilon_\theta+\hat{\Upsilon}_r+\Upsilon_s}\right]. \tag{3.111}$$

We have put $\phi_s = 0$ here for simplicity. Notice that the total radial frequency Υ_r appears inside the sine and cosine functions, but the *geodesic* radial frequency $\hat{\Upsilon}_r$ appears outside these functions in these solutions. This is because $A(\lambda)$ and $B(\lambda)$ are used to build the $\mathcal{O}(S)$ out of plane precessional motion of the small body, and $\Upsilon_r = \hat{\Upsilon}_r + \mathcal{O}(S)$. Using Υ_r instead of $\hat{\Upsilon}_r$ outside of the sines and cosines would affect the solution at $\mathcal{O}(S^2)$, and we neglect terms at this order.

It is important to note that the combination $\hat{\Upsilon}_r + \Upsilon_s - \Upsilon_\theta$ can pass through zero. For example, when $a = 0$, this occurs for orbits that have $v = \sqrt{(2\sqrt{3}-3)/3}$, for which $p \simeq 6.464$; for $a = M$, this occurs for orbits that have $v = (1/2)(\pm 1/\sqrt{3} + \sqrt{1/3 + 2/\sqrt{3}}$, for which $p \simeq 1.238$ (prograde) and $p \simeq 9.690$ (retrograde). The general case smoothly connects these limiting forms as a function of a. At least naively, Eq. (3.110) appears to be poorly behaved at such "resonant" orbits, with certain terms diverging as this combination of frequencies passes through zero. It is not difficult to show, however, that the combination $\alpha_2 + \alpha_1\varpi$ passes through zero at exactly the same orbits for which $\hat{\Upsilon}_r + \Upsilon_s = \Upsilon_\theta$. Such resonances thus have no dynamical impact on the system. This is consistent with recent work [84], [91] which shows that spinning body orbits are integrable at leading order in the smaller body's spin.

Equations (3.109), (3.110) and (3.111) show that the out-of-plane motion of the small body depends on $s_\perp$, is uncoupled from the in-plane motion, and is periodic, with structure at harmonics of the precession frequency Υ_s, the radial frequency Υ_r, and the polar frequency Υ_θ. As we consider more general configurations, we expect qualitatively similar behavior. We thus design our algorithm for describing the small body's orbital motion in the general case in order to capture such behavior.

3.4.3 Next order in eccentricity

As our final "simple" case, we examine equatorial and eccentric orbits to second order in eccentricity. To keep the expressions relatively simple, we do this only for orbits of Schwarzschild black holes, and only examine the spin-aligned case. As we saw for the equatorial and nearly equatorial orbits discussed in the previous section, non-aligned small body spin decouples from all components of the body's orbit except the out-of-plane motion component U^θ, which is itself decoupled from the aligned spin and from all other components of the orbital motion. Focusing on the Schwarzschild limit of aligned spin orbits will be sufficient for us to develop a strategy for solving for this motion to high precision for more generic cases.

The two most important changes versus our previous analyses are that it will turn out we need to know many quantities describing geodesics to *fourth* order in e in order to compute corrections to the orbits of spinning bodies; and, we need a more complete accounting for the difference between the true anomaly χ_r and the mean anomaly $w_r \equiv \Upsilon_r \lambda$. The need to go to fourth order in e may be somewhat surprising. The reason is that the radial velocity introduces a factor e; certain terms in the analysis which scale with $\hat{U}^r \hat{U}_r$ or $\hat{U}^r U_r^S$ have their order in eccentricity "boosted" by a factor of e^2.

To describe the true anomaly, we generalize a functional form that is well known from studies of Keplerian orbits, writing

$$\begin{aligned}\chi_r &= w_r + \left[e\left(\beta_{11} + \beta_{11}^S\right) + e^3\left(\beta_{31} + \beta_{31}^S\right)\right]\sin w_r \\ &\quad + e^2\left(\beta_{22} + \beta_{22}^S\right)\sin 2w_r + e^3\left(\beta_{33} + \beta_{33}^S\right)\sin 3w_r \\ &\equiv w_r + \delta\hat{\chi}_r + \delta\chi_r^S \ .\end{aligned} \tag{3.112}$$

The quantity $\delta\hat{\chi}_r$ stands for all the oscillatory geodesic terms (i.e., the terms with β_{ab}) that take us from the mean anomaly to the true anomaly. The quantity $\delta\chi_r^S$ stands for the equivalent terms which arise from spin-curvature coupling (the terms with β_{ab}^S).

Other quantities we need are the integrals of the motion and the radial frequency:

$$\hat{E} = \frac{1-2v^2}{\sqrt{1-3v^2}} + \frac{e^2v^2}{2}\frac{(1-4v^2)^2}{(1-2v^2)(1-3v^2)^{3/2}} + \frac{e^4v^4}{8}\frac{(1-4v^2)^2(3-8v^2)}{(1-2v^2)^3(1-3v^2)^{5/2}} \ , \tag{3.113}$$

$$\hat{L}_z = M\sqrt{p}\left(\frac{1}{\sqrt{1-3v^2}} + \frac{e^2v^2}{2}\frac{1}{(1-3v^2)^{3/2}} + \frac{3e^4v^4}{8}\frac{1}{(1-3v^2)^{5/2}}\right) \ , \tag{3.114}$$

$$\begin{aligned}\hat{\Upsilon}_r = M\sqrt{p}\Bigg(&\sqrt{\frac{1-6v^2}{1-3v^2}} + \frac{e^2v^2}{4}\frac{(1-9v^2)(2-9v^2)}{(1-3v^2)^{3/2}(1-6v^2)^{3/2}} \\ &+ \frac{3e^4v^4}{64}\frac{[8-25v^2(1-3v^2)(8-49v^2+147v^4)]}{(1-3v^2)^{5/2}(1-6v^2)^{7/2}}\Bigg) \ .\end{aligned} \tag{3.115}$$

The right panel of Figure 3.1 shows how Υ_r^S depends on e according to Eq. (3.115).

The true anomaly (3.112), coupled with the form $r = p/(1 + e\cos\chi_r)$, suffices to fully describe the radial motion. Turn next to the small body's motion in t and ϕ. We parameterize

this motion using the 4-velocity components

$$u_t = -\hat{E} + u_t^S \ ,$$
$$u_\phi = \hat{L}_z + u_\phi^S \ . \tag{3.116}$$

Raising the index and multiplying by $\Sigma = r^2$, these components can be easily converted to the forms $U^{t,\phi}$. We assume that the spin corrections to these 4-velocity components take the form

$$u_t^S = \sum_{n=-3}^{3} u_{t,n}^s e^{-inw_r} \ , \quad u_\phi^S = \sum_{n=-3}^{3} u_{\phi,n}^s e^{-inw_r} \ . \tag{3.117}$$

We generically find that $u^s_{(t,\phi),n} \propto e^{|n|}$. We find that we don't have enough information to pin down these components for $|n| > 3$; presumably we need to describe the geodesic motion to higher order in order to do this.

We solve for the various unknown quantities we have introduced by enforcing Eqs. (3.66) – (3.68) and the constraint (3.11), and then gathering terms in spin and eccentricity. Terms at order $(s_\parallel)^0$ are geodesic, and can be used to find the coefficients which make $\delta\hat{\chi}_r$, defined in Eq. (3.112):

$$\beta_{11} = -\frac{v^2}{1-6v^2} \ , \tag{3.118}$$
$$\beta_{22} = \frac{v^4}{8(1-6v^2)^2} \ , \tag{3.119}$$
$$\beta_{31} = -\frac{19v^6}{16(1-6v^2)^3} \ , \tag{3.120}$$
$$\beta_{33} = -\frac{v^6}{48(1-6v^2)^3} \ . \tag{3.121}$$

Turn now to various aspects of the solution at order $s_\parallel$. First, we find the following coefficients which define $\delta\chi_r^S$:

$$\beta_{11}^S = \frac{s_\parallel \mu}{M} v^3 \frac{(1-2v^2)}{(1-6v^2)^2} \ , \tag{3.122}$$
$$\beta_{22}^S = -\frac{s_\parallel \mu}{4M} \frac{v^5(1-2v^2)}{(1-6v^2)^3} \ , \tag{3.123}$$
$$\beta_{31}^S = \frac{s_\parallel \mu}{16M} \frac{v^7(25+156v^2-924v^4)}{(1-2v^2)(1-6v^2)^4} \ , \tag{3.124}$$
$$\beta_{33}^S = \frac{s_\parallel \mu}{16M} \frac{v^7(1-2v^2)}{(1-6v^2)^4} \ . \tag{3.125}$$

We next find the terms which define u_ϕ^S and u_t^S:

$$u_\phi^S = -s_\parallel \mu \left(\frac{3v^2}{2} \frac{(1-2v^2)}{(1-3v^2)^{3/2}} + e^2 \frac{v^2}{4} \frac{(2-5v^2-16v^4+48v^6)}{(1-2v^2)(1-3v^2)^{5/2}} \right) , \tag{3.126}$$

$$\begin{aligned} u_t^S = \frac{s_\parallel \mu}{M} \Bigg(& \frac{3v^5}{2} \frac{(1-2v^2)}{(1-3v^2)^{3/2}} + \frac{3ev^5 \cos w_r}{(1-3v^2)1/2} \\ & + \frac{e^2 v^5}{4} \frac{[2-25v^2+126v^4+234v^6+6(1-3v^2)^2(1-7v^2)\cos 2w_r]}{(1-6v^2)(1-3v^2)^{5/2}} \\ & + \frac{e^3 v^5}{8} \frac{\cos w_r \, [4-24v^2-81v^4+459v^6+(4-84v^2+513v^4-891v^6)\cos 2w_r]}{(1-6v^2)^2(1-3v^2)^{3/2}} \Bigg) . \end{aligned} \tag{3.127}$$

Finally, we compute the shift to the radial frequency due to spin-curvature coupling:

$$\Upsilon_r^S = \frac{3 s_\parallel \mu}{2} \left(\frac{v^2(1-2v^2)}{(1-3v^2)^{3/2}\sqrt{1-6v^2}} - \frac{e^2 v^2}{12} \frac{(4-106v^2+985v^4-4275v^6+8928v^8-7452v^{10})}{(1-2v^2)(1-3v^2)^{5/2}(1-6v^2)^{5/2}} \right) . \tag{3.128}$$

Neglecting the terms in e^2, this is consistent with the result we found previously, Eq. (3.91) in the limit $q \to 0$. In addition, Eq. (3.91) agrees exactly with the Υ_S^r in Eq. (A.36) obtained using the approach presented in Ref. [67]; see Appendix A.2 for details of this comparison.

Several other important quantities can be derived from what we computed here. Two that are particularly important are the axial frequency Υ_ϕ, and the quantity Γ which converts from Mino-time frequencies and periods to coordinate-time frequencies and periods. As discussed in Sec. 3.2.1, the axial frequency Υ_ϕ is the orbit average of U^ϕ:

$$\Upsilon_\phi = \frac{1}{2\pi} \int_0^{2\pi} U^\phi(w_r) dw_r . \tag{3.129}$$

Using $U^\phi = \Sigma g^{\phi\phi} u_\phi$, we find

$$\Upsilon_\phi = \frac{M}{v\sqrt{1-3v^2}} \left(1 + \frac{e^2 v^2}{2(1-3v^2)} - \frac{3 s_\parallel v^3}{2} \frac{1-2v^2}{1-3v^2} - \frac{s_\parallel e^2 v^3}{4} \frac{(2-5v^2-16v^4+48v^6)}{(1-2v^2)(1-3v^2)^2} \right) . \tag{3.130}$$

Likewise, Γ is found by orbit averaging $U^t = \Sigma g^{tt} u_t$:

$$\begin{aligned} \Gamma = \frac{M^2}{v^4\sqrt{1-3v^2}} \Bigg(& 1 + \frac{e^2}{2} \frac{(3-38v^2+148v^4-186v^6)}{(1-11v^2+36v^4-36v^6)} \\ & - \frac{3 s_\parallel v^5}{2} \frac{1}{(1-3v^2)} + \frac{s_\parallel e^2 v^3}{4} \frac{(4-43v^2+160v^4-186v^6-144v^8+216v^{10})}{(1-2v^2)(1-3v^2)^2(1-6v^2)^2} \Bigg) . \end{aligned} \tag{3.131}$$

With these quantities in hand, it is straightforward to compute $\Omega_{r,\phi} = \Upsilon_{r,\phi}/\Gamma$. Finally, the shifts to the conserved integrals due to the spin-curvature interaction become.

$$\delta E^S = -\frac{s_\parallel \mu v^5}{2M(1-3v^2)^{3/2}} \left(1 - e^2 \frac{(4-15v^2)}{2(1-3v^2)} \right) , \tag{3.132}$$

$$\delta L_z^S = \frac{s_\parallel \mu (2-13v^2+18v^4)}{2(1-3v^2)^{3/2}} \left(1 - \frac{e^2 v^4}{2} \frac{(17-96v^2+144v^4)}{(1-2v^2)^2(1-3v^2)(2-9v^2)} \right) . \tag{3.133}$$

All of these quantities agree with Eqs. (A.26) and (A.27) which were obtained using the exact-in-eccentricity approach outlined in Appendix A.2.

3.5 Spinning-body orbits III: Frequency-domain treatment

We now consider nearly equatorial orbits with *arbitrary* eccentricity, using a frequency-domain treatment of the spinning body's motion. As described in Sec. 2.2.4, the spin of the small body introduces the precession frequency Υ_s into the analysis. The small body also shifts the orbital frequencies by an amount $\mathcal{O}(S)$ which we denote Υ_r^S and Υ_θ^S. Functions evaluated on a spinning body's orbit can thus be written as a Mino-time Fourier expansion in terms of frequencies $\Upsilon_r = \hat{\Upsilon}_r + \Upsilon_r^S$, $\Upsilon_\theta = \hat{\Upsilon}_\theta + \Upsilon_\theta^S$ and Υ_s:

$$f(\lambda) = \sum_{j=-1}^{1} \sum_{n,k=-\infty}^{\infty} f_{jnk} e^{-ij\Upsilon_s \lambda} e^{-in(\hat{\Upsilon}_r + \Upsilon_r^S)\lambda} e^{-ik(\hat{\Upsilon}_\theta + \Upsilon_\theta^S)\lambda} \,. \tag{3.134}$$

The Fourier coefficient f_{jnk} is given by

$$f_{jnk} = \frac{1}{\Lambda_r \Lambda_\theta \Lambda_s} \int_0^{\Lambda_r} \int_0^{\Lambda_\theta} \int_0^{\Lambda_s} f\left(\lambda_r, \lambda_\theta, \lambda_s\right) e^{ij\Upsilon_s \lambda_s} e^{in(\hat{\Upsilon}_r + \Upsilon_r^S)\lambda_r} e^{ik(\hat{\Upsilon}_\theta + \Upsilon_\theta^S)\lambda_\theta} d\lambda_\theta d\lambda_r d\lambda_s \,, \tag{3.135}$$

where $\Lambda_{r,\theta,s} = 2\pi/\Upsilon_{r,\theta,s}$. By writing all relevant quantities as expansions of this form, we can compute the properties of spinning-body orbits to arbitrary precision, and develop a natural way of computing the frequency shifts Υ_r^S and Υ_θ^S. As written, Eq. (3.134) is appropriate for generic spinning-body orbits. In this analysis, we examine orbits of arbitrary eccentricity that are equatorial or nearly equatorial; the generic case is developed and presented in Chapter 4.

3.5.1 Aligned spin

We first consider eccentric orbits with the spin of the small body aligned with the orbit. The orbit's geometry in this case is exactly as in Sec. 3.4.3, but we now allow for arbitrary eccentricity. In this case, only radial oscillations are present in the motion, so all orbits can be described using expansions of the form

$$f(\lambda) = \sum_{n=-\infty}^{\infty} f_n e^{-in(\hat{\Upsilon}_r + \Upsilon_r^S)\lambda} \,. \tag{3.136}$$

To evaluate these expressions, we truncate the Fourier expansion at a finite value $n_{\max}$. In Fig. 3.2, we examine the convergence of important properties of the orbit as we increase $n_{\max}$. These residuals are computed by comparing our frequency-domain expansion for these quantities with an alternate method which is exact in eccentricity, but only applies to the spin-aligned case. This method, which is based on that described by Saijo et al. (Ref. [67]) is described in detail in Appendix A.2. Our results indicate that we can accurately handle large eccentricities (up to at least $e \sim 0.8$) by increasing $n_{\max}$, though larger e requires larger values of $n_{\max}$ in order to meet a prescribed level of truncation error.

As described in Sec. 3.4.1, we parameterize the radial motion as

$$r = \frac{pM}{1 + e\cos\chi_r} \,. \tag{3.137}$$

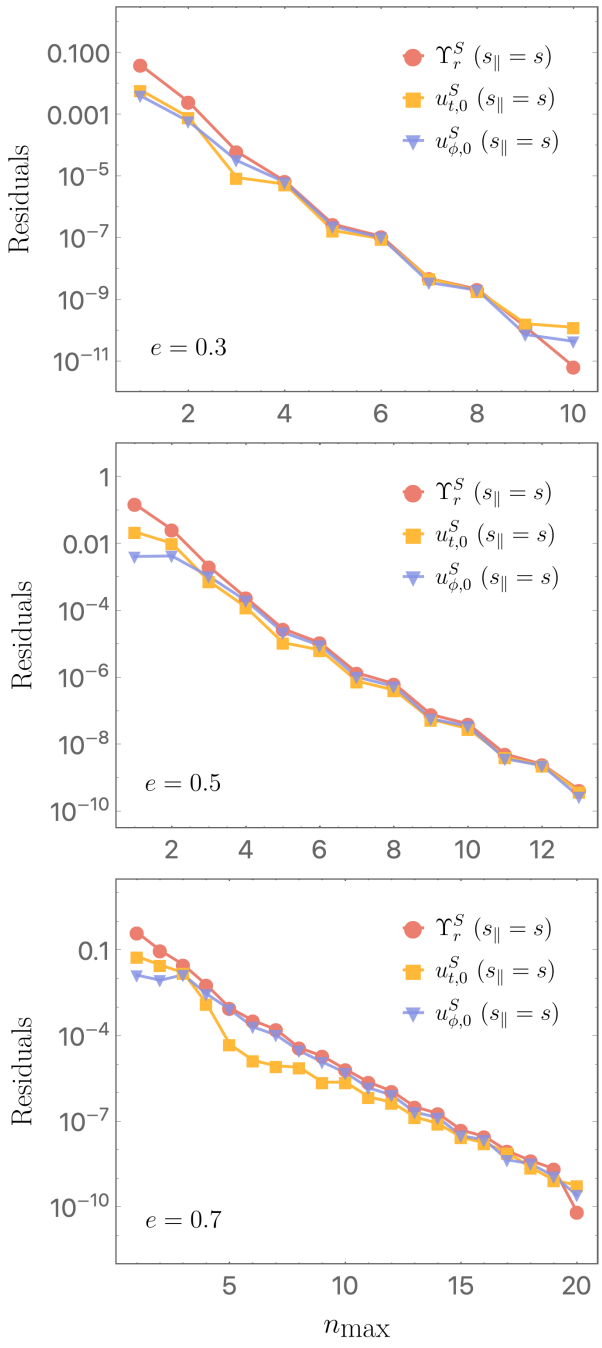

Figure 3.2: Plot of residuals versus $n_{\max}$ with $s_\parallel = s$ for $u_{t,0}^S$ (orange), $u_{\phi,0}^S$ (blue), Υ_r^S (red). These residuals are computed by comparing our frequency-domain expansion to results found using an approach which, for the spin-aligned case, is exact in eccentricity; see Ref. [67] and Appendix A.2 for detailed discussion. Top panel shows $e = 0.3$; middle is $e = 0.5$; and bottom is $e = 0.7$. In all cases, the large black hole has spin parameter $a = 0.9M$, and the orbit has $p = 10$ and $I = 0°$.

This form guarantees that the motion is constrained to the interval $p/(1+e) \leq r \leq p/(1-e)$. As in Eq. (3.73), we write the true anomaly χ_r in Eq. (3.137) as

$$\chi_r = w_r + \delta\chi_r \,, \tag{3.138}$$

where w_r is the mean anomaly and $\delta\chi_r$ is an oscillating contribution to χ_r. The oscillating contribution in turn has a piece associated with geodesic motion, $\delta\hat{\chi}_r$, and another piece that arises from spin-curvature coupling $\delta\chi_r^S = \mathcal{O}(S)$,

$$\delta\chi_r = \delta\hat{\chi}_r + \delta\chi_r^S \,. \tag{3.139}$$

The mean anomaly also has geodesic and spin-curvature contributions:

$$w_r = \left(\hat{\Upsilon}_r + \Upsilon_r^S\right)\lambda \,, \tag{3.140}$$

where Υ_r^S is the $\mathcal{O}(S)$-correction to the radial Mino-time frequency. It is useful to write the true anomaly angles $\delta\hat{\chi}_r$ and $\delta\chi_r^S$ as Fourier expansions[1],

$$\delta\hat{\chi}_r = \sum_{n=-\infty}^{\infty} \delta\hat{\chi}_{r,n} e^{-inw_r} \,, \tag{3.141}$$

$$\delta\chi_r^S = \sum_{n=-\infty}^{\infty} \delta\chi_{r,n}^S e^{-inw_r} \,. \tag{3.142}$$

We set $\chi_{r,0}^S = 0$; this amounts to a choice of initial true anomaly. Note that the geodesic Fourier coefficients $\delta\hat{\chi}_{r,n}$ are known, as described in Sec. 2.1. Observe, however, that w_r includes the frequency correction Υ_r^S, meaning that $w_r + \delta\hat{\chi}_r$, with $\delta\hat{\chi}_r$ given by Eq. (3.141), is *not* the same as the true anomaly for the corresponding geodesic orbit with the same radial turning points. We treat the non-oscillating part of the spinning body's true anomaly as almost identical to the non-oscillating part of the true anomaly belonging to the geodesic with the same turning points, differing only by an appropriate shift to the orbit's frequency. This cures a pathology associated with the fact that the rate at which the mean anomaly accumulates for geodesic orbits differs at $\mathcal{O}(S)$ from the rate at which it accumulates for spinning-body orbits. This issue is described in more detail in Appendix A.1.

As in Eq. (3.116), we define the $\mathcal{O}(S)$-corrections to the temporal and axial components of the 4-velocity by

$$u_t = -\hat{E} + u_t^S \,, \qquad u_\phi = \hat{L}_z + u_\phi^S \,, \tag{3.143}$$

where u_t^S and u_ϕ^S can also be written as Fourier expansions,

$$u_t^S = \sum_{n=-\infty}^{\infty} u_{t,n}^S e^{-inw_r} \,, \tag{3.144}$$

$$u_\phi^S = \sum_{n=-\infty}^{\infty} u_{\phi,n}^S e^{-inw_r} \,. \tag{3.145}$$

[1]Note that if the function we are Fourier expanding already has a subscript, we use a comma to denote the specific Fourier mode. For example, $\delta\hat{\chi}_{r,1}$ is the $n = 1$ harmonic of function $\delta\hat{\chi}_r$.

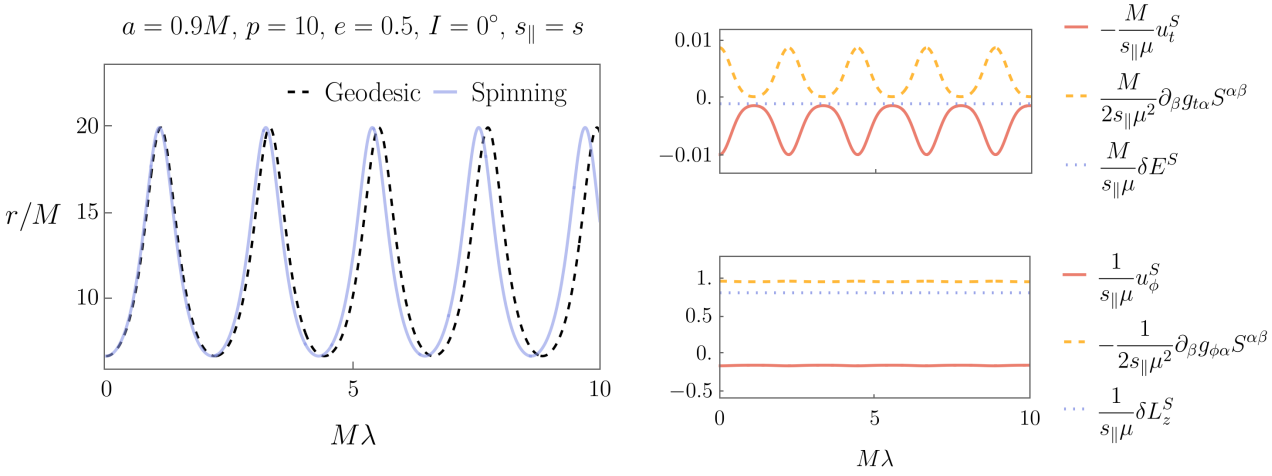

Figure 3.3: Example of radial motion for an aligned, spinning body in an equatorial orbit of a Kerr black hole ($a = 0.9M$). Left panel shows r versus λ for a geodesic (black dashed) and for a spinning-body orbit (blue solid). These orbits share radial turning points, corresponding to semi-latus rectum $p = 10M$, eccentricity $e = 0.5$. Top right panel shows the spinning body's $-u_t^S$ (red), $\partial_\beta g_{t\alpha} S^{\alpha\beta}/(2\mu)$ (orange), and δE^S (blue) versus λ. Bottom right panel shows the spinning body's u_ϕ^S (red), $-\partial_\beta g_{\phi\alpha} S^{\alpha\beta}/(2\mu)$ (orange), δL_z^S (blue) versus λ. Notice that the shifts in the integrals of motion E and L_z are constants, even though the terms which contribute to them oscillate. (The oscillations in the terms which contribute to δL_z^S are so small they can barely be seen on this plot.) In all cases, the Fourier expansions have been taken to $n_{\max} = 8$; for the left panel, we have used $\mu s/M = 0.5$.

We divide both u_t^S and u_ϕ^S into a piece that is constant, and a piece that oscillates:

$$u_t^S = u_{t,0}^S + \delta u_t^S(\lambda) \ , \quad u_\phi^S = u_{\phi,0}^S + \delta u_\phi^S(\lambda) \ . \tag{3.146}$$

We can solve for the oscillating pieces using the t- and ϕ- components of Eq. (2.47). Combining the axial and temporal components yields two equations of the form

$$\frac{du_\phi^S}{d\lambda} = \mathcal{R}_\phi \ , \quad \frac{du_t^S}{d\lambda} = \mathcal{R}_t \ , \tag{3.147}$$

where $\mathcal{R}_\phi$ and $\mathcal{R}_t$ are functions of known geodesic quantities. For the equatorial and nearly equatorial cases, Eqs. (3.147) are equivalent to Eqs. (3.69) – (3.70), and we can read out the functions $\mathcal{R}_\phi$ and $\mathcal{R}_t$ from there. The equations in (3.147) allow us to immediately solve for δu_t^S and δu_ϕ^S. The constants $u_{t,0}^S$ and $u_{\phi,0}^S$ are determined by the system's initial conditions; as described below, we solve for these quantities along with the other unknowns, $\delta\chi_r^S$ and Υ_r^S.

To make further progress, we insert Eqs. (3.137) and (3.143) into Eq. (2.47) and linearize in spin. By gathering in terms of unknown quantities, the radial component of Eq. (2.47) has the form

$$\mathcal{F}_r \frac{d^2\delta\chi_r^S}{d\lambda^2} + \mathcal{G}_r \frac{d\delta\chi_r^S}{d\lambda} + \mathcal{H}_r \delta\chi_r^S + \mathcal{I}_{1r}\Upsilon_r^S + \mathcal{I}_2 u_{t,0}^S + \mathcal{I}_3 u_{\phi,0}^S + \mathcal{J} = 0 \ . \tag{3.148}$$

In this equation, we have gathered all the terms and functional behavior which are known (i.e., they depend on the behavior of the geodesic with p and e) into the functions $\mathcal{F}_r$, $\mathcal{G}_r$, $\mathcal{H}_r$, $\mathcal{I}_{1r}$, $\mathcal{I}_2$, $\mathcal{I}_3$ and $\mathcal{J}$. The explicit expressions for these functions in the Schwarzschild spacetime can be found in Appendix A.3.1. For Kerr, the expressions become rather unwieldy. We include a *Mathematica* notebook in the supplementary material which computes the expressions for $a \neq 0$. Note that we solved for δu_t^S and δu_ϕ^S when we solve (3.147); these functions are incorporated into $\mathcal{J}$.

We also use $u^\alpha u_\alpha = -1$ linearized in spin [i.e., Eq. (3.11)], as an additional constraint. This yields an equation of the form

$$\mathcal{K}_r \frac{d\delta\chi_r^S}{d\lambda} + \mathcal{M}_r \delta\chi_r^S + \mathcal{N}_{1r}\Upsilon_r^S + \mathcal{N}_2 u_{t,0}^S + \mathcal{N}_3 u_{\phi,0}^S + \mathcal{P} = 0 \ , \tag{3.149}$$

where $\mathcal{K}_r$, $\mathcal{M}_r$, $\mathcal{N}_{1r}$, $\mathcal{N}_2$, $\mathcal{N}_3$ and $\mathcal{P}$ are again all functions[2] of known quantities, and are listed in Appendix A.3.1 for Schwarzschild (with the Kerr versions included in supplemental material). The solutions for δu_t^S and δu_ϕ^S are here incorporated into the function $\mathcal{P}$.

To solve for the unknown aspects of the spinning body's orbit, we write $\mathcal{F}_r$, $\mathcal{G}_r$, $\mathcal{H}_r$, $\mathcal{I}_{1r}$, $\mathcal{I}_2$, $\mathcal{I}_3$, $\mathcal{J}$, $\mathcal{K}_r$, $\mathcal{M}_r$, $\mathcal{N}_{1r}$, $\mathcal{N}_2$, $\mathcal{N}_3$ and $\mathcal{P}$ as Fourier expansions of the form shown in Eq. (3.136). We insert these expansions, along with Eq. (3.142), into Eqs. (3.148) and (3.149). Evaluating Eqs. (3.148) and (3.149) in the frequency domain, we turn this differential equation into a system of linear equations which can be expressed in the form

$$\mathbf{M} \cdot \mathbf{v} + \mathbf{c} = 0 \ , \tag{3.150}$$

[2]The functions $\mathcal{F}_r$, $\mathcal{G}_r$, etc. follow a mostly alphabetic sequence; however, we skip the letter $\mathcal{L}$ in our scheme to avoid confusion with the angular momentum 4-vector defined in Eq. (2.11).

where $\mathbf{M}$ is a matrix whose entries are related to the Fourier expansions of several of the functions appearing in Eqs. (3.148) and (3.149), and where $\mathbf{c}$ is a column vector whose entries are related to the Fourier expansion of the functions $\mathcal{J}$ and $\mathcal{P}$. The entries of the column vector $\mathbf{v}$ are the problem's various unknown quantities, such as the spin-induced shift in the radial frequency Υ_r^S. As an illustration of this equation's form, we have written out the explicit form of $\mathbf{M}$, $\mathbf{v}$, and $\mathbf{c}$ in Appendix A.3.2 for $n_{\max} = 1$. Note that this value of $n_{\max}$ is far too small to achieve numerical convergence, and is used only for illustrative purposes. The matrix equation is ungainly when written out for realistic values of $n_{\max}$, though it poses no difficulties for numerical analysis. We then solve this system of linear equations for the unknown variables $\delta\chi_r^S$, Υ_r^S, $u_{\phi,0}^S$ and $u_{t,0}^S$. This yields a complete solution for the motion of the spinning body to first order in spin.

When the small body's spin is aligned with the orbit, an alternative method based on Ref. [67] allows us to calculate Υ_r^S exactly as a function of eccentricity; this method is described in detail in Appendix A.2. Figure 3.2 shows how Υ_r^S, $u_{\phi,0}^S$ and $u_{t,0}^S$ converge to the exact result as we increase the value of $n_{\max}$. For higher eccentricities, we need to include more harmonics (use a larger value of $n_{\max}$) in order for the solution to converge to the same level of accuracy as the lower eccentricity orbit. For example, for an eccentricity of $e = 0.7$ (bottom panel of Fig. 3.2) we need $n_{\max} = 20$ to obtain the same discrepancy between the exact and frequency-domain result as for $e = 0.3$ (top panel of Fig. 3.2) with $n_{\max} = 9$.

An example of an aligned spinning body's equatorial orbit is shown in the left panel of Fig. 3.3. The geodesic orbit with the same radial turning points is overplotted for comparison. Notice the two ways in which the spinning body's radial motion differs from that of the geodesic. First, the radial frequency is shifted by Υ_r^S. This effect can be very clearly seen in Fig. 3.3. Second, the shape of the orbit is modified due to the impact of the oscillatory term in the true anomaly $\delta\chi_r^S$. This effect is quite a bit smaller, and is not obvious in the figure for this choice of parameters.

In the right panel of Fig. 3.3, we show u_t^S and u_ϕ^S, as well as corrections to the spinning body's energy δE^S and axial angular momentum δL_z^S [using Eqs. (3.14) and (3.15)]. As expected, the oscillations in $\partial_\beta g_{t\alpha} S^{\alpha\beta}/(2\mu)$ and $\partial_\beta g_{\phi\alpha} S^{\alpha\beta}/(2\mu)$ precisely cancel oscillations in δu_t^S and δu_ϕ^S; upon summing, δE^S and δL_z^S are indeed constant. The values for the spinning body's energy and axial angular momentum match those obtained using the alternative approach described in Appendix A.2; see App. A.2.2 in particular.

3.5.2 Misaligned spin

We now consider eccentric, nearly equatorial orbits, allowing the spin of the small body to have arbitrary orientation. As we saw in Secs. 3.3.1, 3.4.3 and 3.5.1, if the spin of the small body is aligned with the orbit, the motion remains in the equatorial plane. However, if the spin of the test body is misaligned, the spin vector precesses, as described in Secs. 3.3.2 and 3.4.2. The spin precession introduces the frequency Υ_s into the motion. Orbital quantities can then be described using expansions of the form

$$f(\lambda) = \sum_{j=-1}^{1} \sum_{n=-\infty}^{\infty} f_{jn} e^{-ij\Upsilon_s \lambda} e^{-in(\hat{\Upsilon}_r + \Upsilon_r^S)\lambda} \,. \tag{3.151}$$

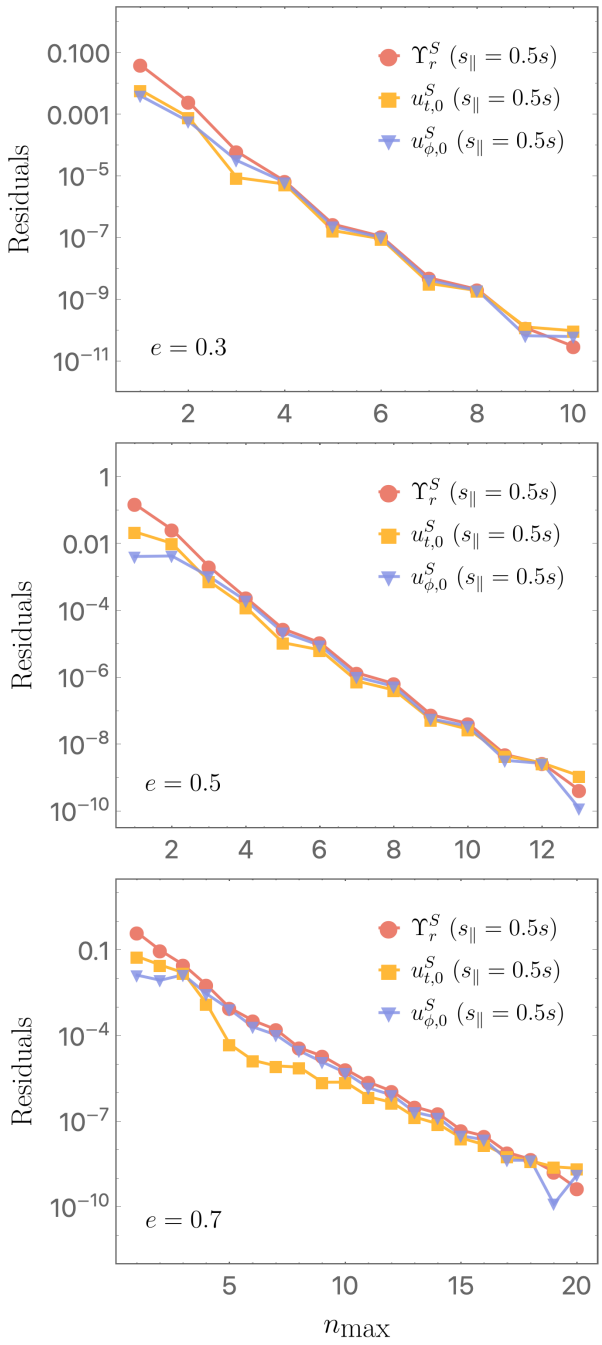

Figure 3.4: Plot of residuals versus $n_{\max}$ for a nearly equatorial orbit of a misaligned spinning body. The body's spin in this case has $s_\parallel = 0.5s$, $s_\perp = \sqrt{3}s/2$. We show residuals for $u_{t,0}^S$ (orange), $u_{\phi,0}^S$ (blue), Υ_r^S (red). To compute these residuals, we use the fact that the equations for this case are identical to the equations for the spin-aligned case, but substituting $s_\parallel$ for the small body's spin s. Because of this, the exact-in-eccentricity solution (described in Ref. [67] and Appendix A.2) that describes aligned orbits can be used to compute the quantities which describe the radial part of misaligned spinning body's orbit, provided we use only the parallel component $s_\parallel$ all of the relevant expressions. As in Fig. 3.2, top panel shows $e = 0.3$, middle shows $e = 0.5$, and bottom is $e = 0.7$. In all cases, the large black hole has spin parameter $a = 0.9M$, and the orbit has $p = 10$ and $I = 0°$.

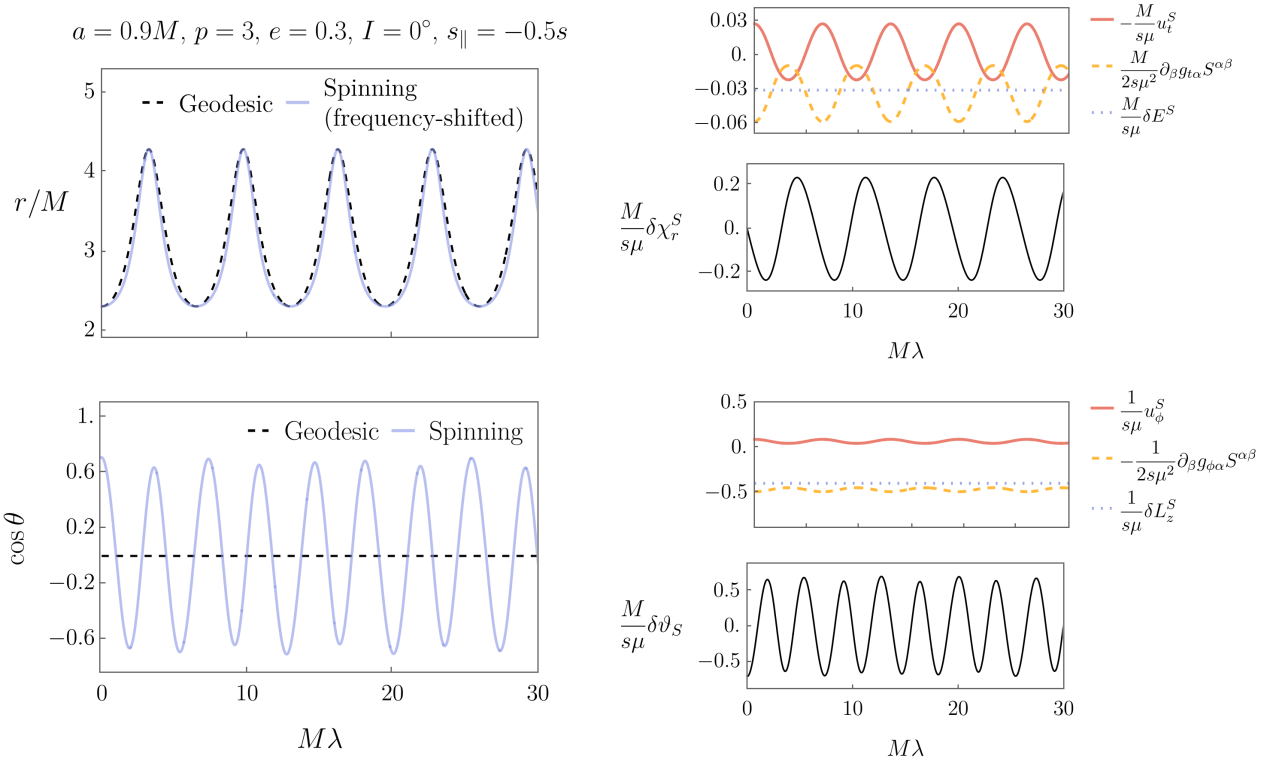

Figure 3.5: Example of the motion of a nearly equatorial prograde ($I = 0°$) orbit for a non-aligned spinning test body around a Kerr black hole with $a = 0.9M$. Top left panel shows r versus λ for a geodesic (black dashed) and a spinning test body (blue solid) orbit. These orbits share radial turning points, corresponding to $p = 3M$, $e = 0.3$. Note that, in the left two panels, we have used an unphysically high spin $\mu s/M = 1$ in order make the spin-curvature effects clearly visible. Also note that for making this plot, the spinning-body orbit has been shifted slightly: its radial frequency $\Upsilon_r = \hat{\Upsilon}_r + \Upsilon_r^S$ has been replaced with $\hat{\Upsilon}_r$. This is done so that in the plot the geodesic and the spinning-body orbit pass through their radial turning points at the same times, which helps to illustrate differences in their motion between each turning point. Bottom left panel shows $\cos\theta$ versus λ for a geodesic (black dashed) and the spinning-body (blue solid) orbit. Top right shows $-u_t^S$ (red), $\partial_\beta g_{t\alpha}S^{\alpha\beta}/(2\mu)$ (orange), and δE^S (blue), as well as $\delta\chi_r^S$ (black), all versus λ. Finally, the bottom right panel shows u_ϕ^S (red), $-\partial_\beta g_{\phi\alpha}S^{\alpha\beta}/(2\mu)$ (orange), and δL_z^S (blue), as well as $\delta\vartheta_S$ (black), all versus λ. Notice that the spin-induced shifts to the integrals of motion E and L_z are constants, although each such term has contributions that oscillate. In making these plots, we have used $s_\parallel = -0.5s$, $\phi_s = 0$ and $n_{\max} = 5$. In the two left panels, we have used $\mu s/M = 1$.

Note that in the expansion (3.151) we do not include harmonics at frequency Υ_θ. Such harmonics can in principle be present, as we saw in Eqs. (3.109), (3.110), and (3.111). In the present analysis, we have only considered initial conditions such that the amplitude of the Υ_θ harmonics are suppressed. In Chapter 4, we examine motion governed by the completely general form (3.134); the motion in this case has harmonics of all three frequencies are present.

The spin precession induces out-of-plane motion, which we describe by introducing the new variable $\delta\vartheta_S$, as in Secs. 3.3.2 and 3.4.2. The orbit can therefore be parameterized by

$$r = \frac{pM}{1 + e\cos\left(w_r + \delta\hat{\chi}_r + \delta\chi_r^S\right)} , \tag{3.152}$$

$$\theta = \frac{\pi}{2} + \delta\vartheta_S . \tag{3.153}$$

The spin contribution to the radial anomaly angle, $\delta\chi_r^S$, consists of purely radial oscillations,

$$\delta\chi_r^S = \sum_{n=-\infty}^{\infty} \delta\chi_{r,n}^S e^{-inw_r} ; \tag{3.154}$$

the Fourier expansion for $\delta\vartheta_S$ depends in addition on the frequency Υ_s,

$$\delta\vartheta_S = \sum_{j=-1}^{1}\sum_{n=-\infty}^{\infty} \delta\vartheta_{S,jn} e^{-inw_r} e^{-ijw_s} . \tag{3.155}$$

We have introduced $w_s = \Upsilon_s\lambda$. For the nearly equatorial case, non-trivial polar motion $\delta\vartheta_S$ emerges, varying with the spin precession frequency Υ_s. As mentioned above, we do not include harmonics at frequency Υ_θ in the expansion (3.155); this case will be presented in Chapter 4.

Figure 3.2 displays the convergence of an orbit with aligned spin, while Figure 3.4 shows the convergence of an orbit with misaligned spin, where both orbits have the same radial turning points. We call the discrepancy between the exact result and our value for a certain $n_{\max}$ the "residuals". These residuals are normalized by the exact value of the quantity we are computing, so the values for Υ_r^S, $u_{t,0}^S$ and $u_{\phi,0}^S$ are directly comparable. As $n_{\max}$ increases, the residuals decrease and approach closer to the true value, as expected. The convergence trend is identical for both the aligned and misaligned cases, except for the highest value of $n_{\max}$ for each of the different eccentricities. At this point, the working precision of the calculation is insufficient and the computation breaks down due to rounding error.

As in Sec. 3.5.1, we write the axial and temporal components of the 4-velocity in the form Eq. (3.146) and use Eq. (3.147) to find δu_ϕ^S and δu_t^S. We insert Eqs. (3.152), (3.153) and (3.143) into Eq. (2.47) and linearize in spin. Similarly to Sec. 3.5.1, the radial component of Eq. (2.47) has the form

$$\mathcal{F}_r\frac{d^2\delta\chi_r^S}{d\lambda^2} + \mathcal{G}_r\frac{d\delta\chi_r^S}{d\lambda} + \mathcal{G}_\vartheta\frac{d\delta\vartheta_S}{d\lambda} + \mathcal{H}_r\delta\chi_r^S + \mathcal{H}_\vartheta\delta\vartheta_S + \mathcal{I}_{1r}\Upsilon_r^S + \mathcal{I}_2 u_{t,0}^S + \mathcal{I}_3 u_{\phi,0}^S + \mathcal{J} = 0 , \tag{3.156}$$

where $\mathcal{F}_r$, $\mathcal{G}_r$, $\mathcal{G}_\vartheta$, $\mathcal{H}_r$, $\mathcal{H}_\vartheta$, $\mathcal{I}_{1r}$, $\mathcal{I}_2$, $\mathcal{I}_3$ and $\mathcal{J}$ are all functions of known quantities. For nearly equatorial orbits, $\mathcal{G}_\vartheta = \mathcal{H}_\vartheta = 0$. This is not the case for generic orbit geometry, which we discuss in Chapter 4; we include these functions in Eq. (3.156) in order to lay out the structure we need for the generic case.

When the small body's spin is misaligned with the orbit, the body's motion takes it out of the equatorial plane. This requires us to include the θ-component of Eq. (2.47) in our analysis. We linearize this equation in spin, yielding

$$\mathcal{Q}_\vartheta \frac{d^2\delta\vartheta_S}{d\lambda^2} + \mathcal{S}_r \frac{d\delta\chi_r^S}{d\lambda} + \mathcal{S}_\vartheta \frac{d\delta\vartheta_S}{d\lambda} + \mathcal{T}_r\delta\chi_r^S + \mathcal{T}_\vartheta\delta\vartheta_S + \mathcal{U}_{1r}\Upsilon_r^S + \mathcal{U}_2 u_{t,0}^S + \mathcal{U}_3 u_{\phi,0}^S + \mathcal{V} = 0\,. \tag{3.157}$$

In (3.157), the functions $\mathcal{Q}_\vartheta$, $\mathcal{S}_r$, $\mathcal{S}_\vartheta$, $\mathcal{T}_r$, $\mathcal{T}_\vartheta$, $\mathcal{U}_{1r}$ $\mathcal{U}_2$, $\mathcal{U}_3$ and $\mathcal{V}$ all depend on known quantities. For nearly equatorial orbits, $\mathcal{S}_r = \mathcal{S}_\vartheta = \mathcal{T}_r = \mathcal{U}_{1r} = \mathcal{U}_2 = \mathcal{U}_3 = 0$. This is not the case for the more generic orbits which we discuss in Chapter 4. As in our discussion of the spin-aligned case, we use $u^\alpha u_\alpha = -1$ to obtain a linear-in-spin constraint which we write

$$\mathcal{K}_r \frac{d\delta\chi_r^S}{d\lambda} + \mathcal{K}_\vartheta \frac{d\delta\vartheta_S}{d\lambda} + \mathcal{M}_r\delta\chi_r^S + \mathcal{M}_\vartheta\delta\vartheta_S + \mathcal{N}_{1r}\Upsilon_r^S + \mathcal{N}_2 u_{t,0}^S + \mathcal{N}_3 u_{\phi,0}^S + \mathcal{P} = 0\,. \tag{3.158}$$

Here, $\mathcal{K}_r$, $\mathcal{K}_\vartheta$, $\mathcal{M}_r$, $\mathcal{M}_\vartheta$, $\mathcal{N}_{1r}$,$\mathcal{N}_2$, $\mathcal{N}_3$ and $\mathcal{P}$ are again all functions of known quantities. For nearly equatorial orbits, $\mathcal{K}_\vartheta = \mathcal{M}_\vartheta = 0$. We list the Schwarzschild limit of all these functions in App. A.3.1, and include Kerr versions in our supplementary material.

We can now write $\mathcal{F}_r$, $\mathcal{G}_r$, $\mathcal{G}_\vartheta$, $\mathcal{H}_r$, $\mathcal{H}_\vartheta$, $\mathcal{I}_{1r}$, $\mathcal{I}_2$, $\mathcal{I}_3$, $\mathcal{J}$, $\mathcal{Q}_\vartheta$, $\mathcal{S}_r$, $\mathcal{S}_\vartheta$, $\mathcal{T}_r$, $\mathcal{T}_\vartheta$, $\mathcal{U}_{1r}$, $\mathcal{U}_2$, $\mathcal{U}_3$, $\mathcal{V}$, $\mathcal{K}_r$, $\mathcal{K}_\vartheta$, $\mathcal{M}_r$, $\mathcal{M}_\vartheta$, $\mathcal{N}_{1r}$, $\mathcal{N}_2$, $\mathcal{N}_3$ and $\mathcal{P}$ as Fourier expansions of the form given in Eq. (3.151). We insert these expansions, along with Eqs. (3.154) and (3.155), into Eqs. (3.156), (3.157) and (3.158). This turns these differential equations into linear algebraic ones; as in our discussion of aligned orbits in Sec. 3.5.1, we gather terms into matrix form, and then solve for the for the unknown variables $\delta\chi_r^S$, $\delta\vartheta_S$, Υ_r^S, $u_{t,0}^S$ and $u_{\phi,0}^S$. Further details about the matrix system corresponding to Eq. (3.157) are provided in Appendix A.3.2 and the explicit solution given for $n_{\max} = 1$. As discussed in Secs. 3.3.2 and 3.4.2, when the small body's spin is misaligned from the orbit, qualitatively distinct behaviour arises due to the spin's precession.

In the left panel of Fig. 3.5, we show r and θ for a small body with misaligned spin; an equatorial geodesic with the same radial turning points is overplotted for comparison. The form of $\delta\chi_r^S$ and $\delta\vartheta_S$ for this orbit is shown in the right panels of Fig. 3.5. As in Sec. 3.5.1, there are two main ways in which the radial motion of the spinning body differs from that of the geodesic with the same turning points: the radial frequency is shifted, and the shape of the orbit is modified by $\delta\chi_r^S$. We have actually hidden the first effect by shifting the spinning-body orbit's radial frequency — the solid curve in Fig. 3.5 is a spinning-body orbit with the radial frequency $\Upsilon_r = \hat{\Upsilon}_r + \Upsilon_r^S$ replaced with $\hat{\Upsilon}_r$. This allows us to more clearly show the impact of the shifted radial anomaly oscillation $\delta\chi_r^S$ — notice that the shifted geodesic sometimes moves faster, and sometimes slower, than the spinning-body orbit with which it is plotted. The frequency shift Υ_r^S is exactly the same as for the equivalent aligned case except with s replaced by $s_\parallel$. The harmonic content of $\cos\theta$ is more complicated, exhibiting a beat between Υ_r and Υ_s. We also plot u_t^S and u_ϕ^S alongside the corrections to the spinning body's energy δE^S and orbital angular momentum δL_z^S in the right panels of Fig. 3.5.

3.6 Summary and future work

In this work, we have studied equatorial and nearly equatorial orbits of spinning bodies around black holes in detail. Such orbits reduce to equatorial ones when the orbiting body is non-spinning. When the spin is aligned with the orbit, the motion is confined to the equatorial plane. When the spin vector is misaligned, it precesses with Mino-time frequency Υ_s, and the motion acquires a polar oscillation $\delta\vartheta_S$ whose magnitude is $\mathcal{O}(S)$. The solution in this case appears to diverge on "resonances," orbits for which the radial and spin frequencies combine to be commensurate with the polar oscillation frequency: $\hat{\Upsilon}_r + \Upsilon_s = \Upsilon_\theta$. In fact, the amplitude of the driving force vanishes at such frequencies, and the system is well behaved, in keeping with past work which demonstrated that nothing "interesting" happens during spin-orbit resonances at least when considering the motion to leading order in spin [84], [91]. Sections 3.3 and 3.4 presented analytic descriptions of nearly equatorial orbits that are circular and slightly eccentric respectively. In Sec. 3.5, we introduced a frequency-domain description of nearly equatorial orbits with arbitrary eccentricity.

In Chapter 4, we use this frequency-domain approach to describe completely generic orbits — orbits that are both inclined and eccentric, with the small body's spin arbitrarily oriented. It is worth remarking that, for the nearly equatorial orbits we consider here, spinning-body orbits share the same radial turning points as some equatorial geodesic orbit. For the nearly equatorial case, this "reference geodesic" which shares the orbit's turning points serves as a particularly convenient point of comparison in analyzing the spinning body's orbit. This analysis becomes more complicated in the generic case, for which neither the polar nor the radial libration ranges coincide in general with those of a geodesic. We can nonetheless define a "reference geodesic" whose turning points coincide with the spinning body's orbit in an orbit-averaged sense; details are given in Chapter 4. We use this framework to compute corrections arising from the small body's spin to the orbital frequencies Υ_r and Υ_θ for generic orbits in Chapter 4. In addition, we present a detailed comparison between our approach and the methods presented in Ref. [84] for the case of equatorial, spin-aligned orbits in Appendix B.2.

Results in Ref. [164] suggest that the behavior near resonance of terms which are quadratic in spin plays a critical role in the emergence of chaotic motion via the KAM theorem. This is supported by Ref. [91] which contains a detailed numerical study of the growth of resonances and chaos for spinning-body motion in a Schwarzschild spacetime. By using the techniques discussed here to provide a very accurate formulation of the linear-in-spin aspect of spinning-body orbits, we plan to extend work in Ref. [164] by investigating the behaviour of the quadratic in spin terms in the frequency domain. We hope this may clarify the precise manner in which nonlinear terms in the spinning-body equations of motion push such orbits from integrable to chaotic behavior in a Kerr background.

Another avenue for future work is to incorporate secondary spin into gravitational waveform models. An osculating geodesic integrator [178], [179] can be used to generate spinning-body worldlines. Any perturbed system of the form $Dp^\alpha/d\tau = \delta f^\alpha$ can be described using an osculating geodesic framework, so long as δf^α is sufficiently small. In the EMRI limit we are interested in, both the spin-curvature force f_S^α and the self-force effects are small, so it should be possible to fold both into a forcing term and build a spinning-body inspi-

ral. Such a framework has been developed for Schwarzschild orbits, and is presented in Ref. [112]; we hope to use a similar approach to model completely generic spinning-body Kerr inspirals. Ultimately, one hopes to build a fully self consistent self-force driven inspiral, and it is encouraging that the first steps have been taken in this direction [180].

Chapter 4

Precisely computing bound orbits of spinning bodies around black holes II: Generic orbits

This chapter is based on work previously published in Physical Review D (Drummond & Hughes 2022b) [172], written in collaboration with Scott A. Hughes.

4.1 Introduction and motivation

This work is a continuation of Chapter 3, which lays out the general framework that we use but presents results only for equatorial or nearly equatorial orbits ("nearly equatorial" meaning they would be equatorial if the small body were not spinning, but can oscillate by $\mathcal{O}(S)$ out of the equatorial plane due to spin precession effects). In this paper, we present results for orbits of spinning bodies around black holes with completely generic orbital configurations and spin orientations.

4.1.1 Synopsis of our frequency-domain description

We use a frequency-domain framework to compute the orbits of spinning bodies. Bound Kerr geodesics naturally lend themselves to this type of treatment as they are characterized by the three coordinate-time frequencies $\hat{\Omega}_r$, $\hat{\Omega}_\theta$ and $\hat{\Omega}_\phi$ related to radial, polar, and axial motions respectively. This triperiodicity allows for a frequency-domain description of functions which are computed along Kerr orbits:

$$f[\hat{r}(t),\hat{\theta}(t)] = \sum_{kn} f_{kn} e^{-in\hat{\Omega}_r t} e^{-ik\hat{\Omega}_\theta t} \,, \tag{4.1}$$

where f_{kn} are Fourier expansion coefficients. Notice that the function f we use to illustrate this expansion depends on the orbit's radial coordinate r and polar coordinate θ. This is common for many relevant functions in our analysis; because the Kerr spacetime is axisymmetric, the coordinate ϕ often does not enter the analysis. Notice also we write certain quantities in (4.1) using a "hat" accent, e.g. $\hat{r}(t)$ or $\hat{\Omega}_r$. Throughout this paper, we use this

accent to denote a quantity which corresponds to a geodesic orbit. A slight modification to the formulation (4.1) allows us to characterize the properties of spinning-body orbits, as was observed in Ref. [164]. We describe our frequency-domain formulation in detail in Sec. 4.3.1.

The spin of the small body injects additional harmonic structure into the orbit — spin precession introduces a new frequency [144], which we label Ω_s. In addition, the spin of the small body changes the orbital frequencies. Let us denote the changes relative to an appropriately defined geodesic by Ω_r^S and Ω_θ^S. Quantities expanded along a spinning body's orbit, such as the spin-curvature force f_S^α, can be written as a Fourier expansion in terms of frequencies $\Omega_r = \hat{\Omega}_r + \Omega_r^S$, $\Omega_\theta = \hat{\Omega}_\theta + \Omega_\theta^S$, and Ω_s:

$$f[r(t), \theta(t), S^\mu(t)] = \sum_{jkn} f_{jkn} e^{-ij\Omega_s t} e^{-in\Omega_r t} e^{-ik\Omega_\theta t} \ . \tag{4.2}$$

Here S^μ is a 4-vector which describes the spin of the small body. Note that the radial and polar indices n and k both range from $-\infty$ to ∞; the spin harmonic index j only varies over the range $j \in [-1, 0, 1]$. As with the geodesic expansion (4.1), the frequency-domain expansion (4.2) provides useful machinery for characterizing properties associated with spinning-body orbits.

We find it convenient to associate each spinning-body orbit with a "reference" geodesic. We thus begin by discussing the parameterization we use for geodesic orbits. Up to initial conditions, a geodesic is characterized by its semi-latus rectum p, its eccentricity e and an inclination angle I. In terms of these parameters, a geodesic's radial and polar motion are parameterized by

$$\hat{r} = \frac{pM}{1 + e\cos\hat{\chi}_r} \ , \quad \cos\hat{\theta} = \sin I \cos\hat{\chi}_\theta \ , \tag{4.3}$$

where the angles $\hat{\chi}_r$ and $\hat{\chi}_\theta$ are relativistic versions of "true anomaly" angles used in Keplerian orbital dynamics. Notice that the radial motion oscillates between periapsis at $pM/(1+e)$ and apoapsis at $pM/(1-e)$; the polar motion oscillates such that $-\sin I \leq \cos\theta \leq \sin I$.

Spinning-body orbits have a more ornate structure than geodesics, and in most cases cannot be parameterized in exactly this manner. An exception is the limit of equatorial orbits in which the small body's spin is aligned with the normal to the orbital plane. In that case, we set $I = 0°$ or $180°$, and we find we can parameterize the orbit such that it has the same turning points $pM/(1 \pm e)$ as a geodesic orbit. Note that the motion between turning points differs, however, thanks to the spin-curvature force; see detailed discussion in Secs. 3.4 and 3.5, especially discussion near Eqs. (5.16), (5.54), and (6.4).

If the small body's spin is misaligned with the orbit, or the orbit is inclined with respect to the equatorial plane, the libration region varies along the orbit. These variations couple the radial, polar, and spin precessional motions, complicating the equations of motion, and preventing them from fully separating. Despite the complications of the libration region's variation, we can constrain the "purely radial" motion — the aspects of the motion which only have harmonics in Ω_r — to lie between $pM/(1+e)$ and $pM/(1-e)$. We can likewise constrain the "purely polar" motion, which only has harmonics in Ω_θ, to lie between $-\sin I$ and $\sin I$. In this sense, we parameterize the spinning-body orbits with respect to a reference geodesic which has radial and polar turning points precisely at $pM/(1 \pm e)$ and $\pm\sin I$. We

then compute shifts to important properties of the orbit relative to this reference geodesic. For example, for spinning-body orbits confined entirely to the equatorial plane, we compute shifts to the orbital frequencies relative to geodesic orbits with the same radial turning points; this case is discussed in detail in the previous chapter (Chapter 3). In this chapter, we further elucidate how reference geodesics are characterized briefly in Sec. 4.2.1, and in much greater detail in Sec. 4.3.1. In Appendix B.1, we discuss different definitions of reference geodesics (i.e., geodesics "close to" a corresponding spinning-body orbit) that have been used in the literature.

4.1.2 Organization of this chapter

In Sec. 4.2.1, we describe spinning-body orbits qualitatively. This description is then made quantitative as we outline the small-spin perturbative approach (Secs. 4.2.2) and computational framework (Sec. 4.2.3) that we use to calculate the orbits.

In Sec. 4.3, we use a frequency-domain treatment to compute generic orbits, which are both inclined and eccentric, and for which the small body's spin is arbitrarily oriented. We outline the general principles of the frequency-domain description in Sec. 4.3.1. In Secs. 4.3.2 and 4.3.2, we focus specifically on spinning-body orbits that are "nearly circular," with aligned spins discussed in Sec. 4.3.2 and misaligned spins discussed in Sec. 4.3.2. Nearly circular orbits have an associated reference geodesic that is circular; the orbits have a Boyer-Lindquist coordinate radius that is constant modulo a small variation of $\mathcal{O}(S)$. In Sec. 4.3.2, we consider the fully generic case, with both arbitrary eccentricities and inclinations. We conclude in Sec. 4.4 by summarizing our results and outlining plans for related future research. In Appendix B.2, we compare our results with an alternative method for computing these frequency shifts presented in Ref. [84].

As in the previous chapter, quite a few of the functions which enter into this analysis are extremely lengthy. Both because this makes them difficult to read and because the likelihood of introducing errors when typesetting them is high, we provide the explicit formulas for these expressions using a *Mathematica* notebook included with this paper's Supplementary Material [181], rather than writing the expressions out in this thesis.

4.2 Generic spinning-body orbits: general principles

In this analysis, we formulate the motion of a spinning body in terms of a nearby "reference" geodesic orbit. We begin our discussion of spinning-body motion by presenting a qualitative overview of their orbits and the parameterizations used to describe them (Sec. 4.2.1). In Sec. 4.2.2, we then discuss spin-induced deviations to geodesic trajectories and orbital quantities. In Sec. 4.2.3, we present the mathematical framework we use to compute spinning-body orbits.

4.2.1 Characteristics of spinning-body orbits

Spinning-body orbits generally tend to be qualitatively distinct from geodesic orbits. The most obvious difference is the introduction of harmonics at frequency Υ_s, which appear when

$s_\perp \neq 0$ due to the precession of the spin vector. However, even when $s_\perp = 0$ so that there is no spin precession, the libration range can vary over the course of the orbit due to harmonics of both Υ_r and Υ_θ. Unlike the geodesic orbits given in Eqs. (2.24), the radial and polar motions of a spinning body do not fully separate thanks to their coupling via the variations in orbit's libration region. Instead, the radial turning points are functions of θ and ψ_p, while the polar turning points are functions of r and ψ_p; see Ref. [84] for explicit analytic expressions for turning point corrections.

Because bound geodesics have turning points that are fixed for the duration of the orbit, we cannot in general find a geodesic with the same turning points as a given spinning-body orbit. We find, however, that aspects of the motion which are totally described by harmonics of the radial frequency Ω_r do in fact have fixed radial turning points; we call this the "purely radial" portion of the orbit. Likewise, aspects of the motion which are totally described by harmonics of the polar frequency Ω_θ have fixed polar turning points; we call this the "purely polar" orbital motion. With this in mind, we define the reference geodesic as the geodesic that has the same radial turning points as the purely radial part of the spinning-body orbit, and that has the same polar turning points as the purely polar part of that orbit. Aspects of the motion which cannot be written as purely radial or purely polar describe variations in the orbit's turning points, and are incorporated into functions which combine the radial, polar, and precessional frequencies. Section 4.3.1 expands on this idea, providing computational detail; see also Appendix B.1 for discussion of alternative mappings between geodesic and spinning-body orbits used in the literature.

The simplest case is an equatorial orbit with aligned spin, so that $s_\perp = 0$. In this case, an orbit's radial and polar motion can be parameterized as

$$r = \frac{pM}{1 + e\cos\chi_r}\,, \quad \theta = \frac{\pi}{2}\,. \tag{4.4}$$

This constrains the radial motion to the interval $p/(1+e) \leq r \leq p/(1-e)$, exactly as for geodesic motion. Note, however, that the true anomaly angle χ_r for the spinning-body orbit is not the same as the geodesic true anomaly $\hat{\chi}_r$: there is a shift in the radial frequency from $\hat{\Upsilon}_r$ to $\Upsilon_r = \hat{\Upsilon}_r + \Upsilon_r^S$, as well as a shift to an oscillating contribution to this angle.

For misaligned spin, with $s_\perp \neq 0$, the spin vector precesses and truly equatorial orbits do not exist. However, we can find "nearly equatorial" orbits which oscillate $\mathcal{O}(S)$ out of the equatorial plane. For the nearly equatorial orbits, we can still parameterize the radial motion in the same way as a geodesic, but there are adjustments to the polar libration range due to the spin precession. The turning points of the polar motion then depend on the spin precession phase ψ_p. We write nearly equatorial orbits in the form

$$r = \frac{pM}{1 + e\cos\chi_r}\,, \quad \theta = \frac{\pi}{2} + \delta\vartheta_S\,, \tag{4.5}$$

where the angle $\delta\vartheta_S$ describes the $\mathcal{O}(S)$ librations in polar angle. We investigate these orbits in detail in Chapter 3.

Spinning-body orbits which are inclined with respect to the equatorial plane cannot be parameterized in the same way as geodesics even when $s_\perp = 0$. Inclined orbits with aligned spin (i.e., with $s_\perp = 0$) that are $\mathcal{O}(S)$ away from circular — "nearly circular" orbits — can

be parameterized using

$$r = pM + \delta\, \text{r}_S \,, \tag{4.6}$$
$$\cos\theta = \sin I \cos\chi_\theta \,. \tag{4.7}$$

The polar motion in this parameterization is the same as that for an inclined geodesic orbit (bearing in mind that the true anomaly angle χ_θ differs from the true anomaly $\hat{\chi}_\theta$ that describes a geodesic), but the radial motion includes a function $\delta\, \text{r}_S$ which accounts for oscillations in the radial libration region due to spin-curvature coupling. This form is discussed in detail in Section 4.3.2.

For nearly circular orbits with misaligned spin, the radial turning points depends on both θ and ψ_p; the polar turning points depend on r and ψ_p. The orbits in this case are described by

$$r = pM + \delta\, \text{r}_S \,, \tag{4.8}$$
$$\cos\theta = \sin I \cos\chi_\theta + \delta\, \text{z}_S \,. \tag{4.9}$$

The function $\delta\, \text{z}_S$ accounts for variations in the $\cos\theta$ libration region. This parameterization can be written as a variation in polar angle:

$$\delta\, \text{z}_S = -\delta\vartheta_S \sqrt{1 - \sin^2 I \cos^2\chi_\theta} \,. \tag{4.10}$$

This relationship is most useful for nearly equatorial orbits which have $\sin I = 0$, for which $\delta\, \text{z}_S = -\delta\vartheta_S$. Circular, inclined orbits with misaligned spin are discussed in detail in Sec. 4.3.2.

Finally, in the fully generic case when the orbit is eccentric and inclined with arbitrarily oriented spin, the parameterization we use has the form

$$r = \frac{pM}{1 + e\cos\chi_r} + \delta\, \text{r}_S \,, \tag{4.11}$$
$$\cos\theta = \sin I \cos\chi_\theta + \delta\, \text{z}_S \,. \tag{4.12}$$

This case is discussed in detail in Sec. 4.3.2.

4.2.2 Perturbative framework for the motion of spinning bodies

In Eq. (2.44), we defined a dimensionless spin parameter s which satisfies $0 \leq s \leq 1$ if the small body is itself a Kerr black hole. The magnitude of the small body's spin is then $S \leq \mu^2$, and so linear-in-spin effects are quadratic in the system's mass ratio. In what follows, we neglect terms in our equations that are $\mathcal{O}(S^2)$ or higher, as such terms are negligible for the extreme mass ratio systems we are interested in.

With a linear-in-spin analysis in mind, it is possible to write the small body's trajectory as

$$x^\alpha(\lambda) = \hat{x}^\alpha(\lambda) + \delta x^\alpha_S(\lambda) \,. \tag{4.13}$$

Here, $\hat{x}^\alpha(\lambda)$ is the trajectory of a geodesic, and $\delta x^\alpha_S(\lambda)$ is the $\mathcal{O}(S)$-deviation from the geodesic trajectory due to the spin of the small body. Similarly, as defined in Eq. (3.10), we can write

$$u^\alpha = \hat{u}^\alpha + u^\alpha_S \ . \tag{4.14}$$

As discussed in Sec. 3.2.2, we do not directly use the form Eq. (4.13) when we evaluate spinning-body orbits in Sec. 4.3. We instead parameterize spinning-body orbits using amplitude-phase variables, where the frequency shift is incorporated into the parameterization; see Eqs. (4.37) – (4.38) and surrounding text. These variables are either periodic or constant and do not contain secularly growing terms; they can be described using Fourier expansions as outlined in Sec. 4.3.1. Once we have solved for the frequency shifts and other unknowns, it is then possible to compute radial and polar spin corrections δr_S and $\delta\theta_S$, whose explicit forms in terms of the amplitude-phase variables are given by Eqs. (4.55) and (4.56). One of our goals is to compute corrections relative to geodesic motion of important quantities associated with the orbit. Such quantities include the constants of motion, which we write in the form

$$\mathcal{X}^S = \hat{\mathcal{X}} + \delta\mathcal{X}^S \ , \tag{4.15}$$

where $\mathcal{X} \in [E, L_z, K, Q]$. Here $\hat{\mathcal{X}}$ is the quantity associated with the reference geodesic and $\delta\mathcal{X}^S$ is the correction required when we include the spin of the orbiting body. Explicitly, the leading-order-in-spin corrections to the energy δE^S and axial angular momentum δL^S_z are defined by

$$E^S = \hat{E} + \delta E^S \ , \ L^S_z = \hat{L}_z + \delta L^S_z \ . \tag{4.16}$$

where E^S and L^S_z are given by Eqs. (2.35) and (2.36). Similarly, the first order in spin correction to K is defined by

$$K^S = \hat{K} + \delta K^S \ , \tag{4.17}$$

where

$$\delta K^S = 2K_{\alpha\beta}\hat{u}^\alpha u^\beta_S + \delta r_S \partial_r K_{\alpha\beta}\hat{u}^\alpha\hat{u}^\beta + \delta\theta_S\partial_\theta K_{\alpha\beta}\hat{u}^\alpha\hat{u}^\beta + \delta\mathcal{C}^S \ . \tag{4.18}$$

and where $\delta\mathcal{C}^S$ is given by Eq. (3.17). Finally, using Eq. (2.18), we can obtain the first-order shift in Q:

$$\delta Q^S = \delta K^S - 2(\hat{L}_z - a\hat{E})(\delta L^S_z - a\delta E^S) \ . \tag{4.19}$$

The spin of the small body also introduces corrections to the fundamental frequencies of the orbit, which we write in the form

$$\Upsilon_x = \hat{\Upsilon}_x + \Upsilon^S_x \ , \quad \Gamma = \hat{\Gamma} + \Gamma^S \ , \tag{4.20}$$

where $x \in [r, \theta, \phi]$. As discussed in Sec. 2.2.4, the spin of the small body also introduces the spin-precession frequency Υ_s into the motion, meaning that orbits of spinning bodies can generally be described using Mino-time Fourier expansions with harmonics of frequencies $\hat{\Upsilon}_r + \Upsilon^S_r$, $\hat{\Upsilon}_\theta + \Upsilon^S_\theta$ and Υ_s. This frequency-domain approach is what we will use in Sec. 4.3 to compute properties of spinning-body orbits.

4.2.3 Computing spinning-body orbits

We now outline the explicit mathematical framework we use to compute the modification to the small body's trajectory arising from the spin-curvature interaction. Eq. (2.47) is the governing equation for the spinning-body orbits discussed in this work. We repeat this equation below:

$$\frac{Du^\alpha}{d\tau} = -\frac{1}{2\mu} R^\alpha{}_{\nu\lambda\sigma} u^\nu S^{\lambda\sigma} \equiv f_S^\alpha/\mu \,. \tag{4.21}$$

We define the right-hand side of this equation to be the spin-curvature force f_S^α. When we expand the covariant derivative, we have

$$\frac{du^\alpha}{d\tau} + \Gamma^\alpha{}_{\beta\gamma} u^\beta u^\gamma = f_S^\alpha/\mu \,, \tag{4.22}$$

where $\Gamma^\alpha{}_{\beta\gamma}$ is the Christoffel connection for the Kerr spacetime. We find it convenient to perform all our calculations in Mino-time, so we define

$$U^\alpha \equiv \frac{dx^\alpha}{d\lambda} = \Sigma u^\alpha \,, \tag{4.23}$$

where the 4-velocity is $u^\alpha = dx^\alpha/d\tau$ and Mino-time is defined by $d/d\lambda = \Sigma d/d\tau$. Now that we have defined U^α by Eq. (4.23), we multiply Eq. (4.22) by Σ^2, yielding

$$\frac{dU^\alpha}{d\lambda} + \Pi^\alpha = F_S^\alpha/\mu \,, \tag{4.24}$$

where

$$F_S^\alpha \equiv \Sigma^2 f_S^\alpha \,, \quad \Pi^\alpha \equiv -\frac{U^\alpha}{\Sigma}\frac{d\Sigma}{d\lambda} + \Gamma^\alpha{}_{\beta\gamma} U^\beta U^\gamma \,. \tag{4.25}$$

Consider Eq. (4.24) component by component. We start with the axial and temporal components of the 4-velocity. Begin by writing u_t and u_ϕ as

$$u_t = -\hat{E} + u_t^S, \qquad u_\phi = \hat{L}_z + u_\phi^S, \tag{4.26}$$

where $u_{t,\phi}^S = \mathcal{O}(S)$. Combining the axial and temporal components of Eq. (2.47) yields two equations of the form

$$\frac{du_\phi^S}{d\lambda} = \mathcal{R}_\phi \,, \quad \frac{du_t^S}{d\lambda} = \mathcal{R}_t \,, \tag{4.27}$$

where $\mathcal{R}_\phi$ and $\mathcal{R}_t$ are functions of known geodesic quantities. For the case of nearly equatorial orbits, these functions are given in Eqs. (3.69) and (3.70) of the previous chapter; for the general case, they are among the functions which we include in the supplementary *Mathematica* notebook which accompanies the published version of this chapter [172]. Using Eqs. (4.27), we can then solve for u_t^S and u_ϕ^S.

Turn next to the radial and polar components of Eq. (4.24), which we write

$$\frac{d^2 r}{d\lambda^2} + \Pi^r = F_S^r \,, \tag{4.28}$$

$$\frac{d^2\theta}{d\lambda^2} + \Pi^\theta = F_S^\theta \,. \tag{4.29}$$

We solve Eqs. (4.28) and (4.29) by linearizing in spin and expanding in the frequency domain. In addition, we preserve the norm of the 4-velocity along the orbit, requiring that

$$u^\alpha u_\alpha = -1 \, . \tag{4.30}$$

We linearize Eq. (4.30) in spin, and expand in the frequency domain. Our full frequency-domain treatment of spinning-body orbits is discussed in detail in Sec. 4.3.

4.3 Generic spinning-body orbits: Frequency-domain treatment

We now compute spinning-body orbits which have arbitrary eccentricity and inclination, using a frequency-domain treatment of the spinning body's motion. In Chapter 3, we described equatorial and nearly equatorial spinning-body orbits in detail. In that work, we used essentially the same frequency-domain techniques to study equatorial (aligned spin) and nearly equatorial (misaligned spin) orbits with arbitrary eccentricity. We now extend this technique to encompass orbits that have any orbital inclination, not only those that are within polar angles $\mathcal{O}(S)$ of the equatorial plane.

4.3.1 Frequency-domain description

Writing quantities defined on a spinning body's orbit in expansions of the form

$$f(\lambda) = \sum_{j=-1}^{1} \sum_{n,k=-\infty}^{\infty} f_{jnk} e^{-i(j\Upsilon_s + n\Upsilon_r + k\Upsilon_\theta)\lambda} \, , \tag{4.31}$$

allows us to compute orbits to a high level of precision. The Fourier coefficient f_{jnk} is defined by

$$\begin{aligned} f_{jnk} = \frac{1}{\Lambda_r \Lambda_\theta \Lambda_s} \int_0^{\Lambda_r} \int_0^{\Lambda_\theta} \int_0^{\Lambda_s} f(\lambda_r, \lambda_\theta, \lambda_s) \\ \times e^{i(j\Upsilon_s \lambda_s + n\Upsilon_r \lambda_r + k\Upsilon_\theta \lambda_\theta)} \, d\lambda_r d\lambda_\theta d\lambda_s \, . \end{aligned} \tag{4.32}$$

The techniques we describe below allow us to precisely compute a spinning body's orbital frequencies Υ_r and Υ_θ for fully generic orbits. As discussed and defined in Eq. (4.20), we treat these frequencies as "spin shifted" relative to the the radial and polar frequencies of a reference geodesic, writing $\Upsilon_r = \hat{\Upsilon}_r + \Upsilon_r^S$ and $\Upsilon_\theta = \hat{\Upsilon}_\theta + \Upsilon_\theta^S$.

Generalities

We first examine the t and ϕ components of the 4-velocity. The frequency-domain expansion allows us to solve the axial and temporal components of Eq. (2.47), which we write explicitly

in the form shown in Eqs. (4.27). To do this, we expand u_t^S and u_ϕ^S as[1]:

$$u_t^S = \sum_{j=-1}^{1} \sum_{n,k=-\infty}^{\infty} u_{t,jnk}^S e^{-i(j\Upsilon_s + n\Upsilon_r + k\Upsilon_\theta)\lambda} , \tag{4.33}$$

$$u_\phi^S = \sum_{j=-1}^{1} \sum_{n,k=-\infty}^{\infty} u_{\phi,jnk}^S e^{-i(j\Upsilon_s + n\Upsilon_r + k\Upsilon_\theta)\lambda} . \tag{4.34}$$

We split u_t^S into a constant $u_{t,0}^S$ plus an oscillatory contribution $\delta u_t^S(\lambda)$:

$$u_t^S = u_{t,0}^S + \delta u_t^S(\lambda) . \tag{4.35}$$

We divide u_ϕ^S in the same way:

$$u_\phi^S = u_{\phi,0}^S + \delta u_\phi^S(\lambda) \tag{4.36}$$

Using Eqs. (4.27), we can immediately solve for δu_t^S and δu_ϕ^S.

We also use a frequency-domain description to solve the radial and polar Eqs. (4.28) – (4.29). As described in Sec. 4.2.1, generic orbits can be parameterized by

$$r = \frac{pM}{1 + e\cos\chi_r} + \delta \mathscr{r}_S , \tag{4.37}$$

$$\cos\theta = \sin I \cos\chi_\theta + \delta \mathscr{z}_S . \tag{4.38}$$

We break the radial true anomaly χ_r in Eq. (4.37) into a mean anomaly $w_r = \Upsilon_r \lambda$ and oscillating contributions $\delta\chi_r$; we break up the the polar true anomaly χ_θ in Eq. (4.38) similarly, using $w_\theta = \Upsilon_\theta \lambda$:

$$\chi_r = w_r + \delta\chi_r , \quad \chi_\theta = w_\theta + \delta\chi_\theta . \tag{4.39}$$

The mean anomalies have geodesic and spin-curvature pieces,

$$w_r = \left(\hat{\Upsilon}_r + \Upsilon_r^S\right)\lambda , \quad w_\theta = \left(\hat{\Upsilon}_\theta + \Upsilon_\theta^S\right)\lambda , \tag{4.40}$$

where Υ_r^S is the contribution to the radial Mino-time frequency arising from spin-curvature coupling, and Υ_θ^S is the analogous contribution to the polar Mino-time frequency. The oscillating contributions likewise have one piece that arises from geodesic motion $\delta\hat{\chi}_x$ and another associated with spin-curvature coupling $\delta\chi_x^S$, where $x \in [r, \theta]$:

$$\delta\chi_r = \delta\hat{\chi}_r(w_r) + \delta\chi_r^S , \quad \delta\chi_\theta = \delta\hat{\chi}_\theta(w_\theta) + \delta\chi_\theta^S . \tag{4.41}$$

In Eq. (4.41), the Fourier coefficients of $\delta\hat{\chi}_r(w_r)$ and $\delta\hat{\chi}_\theta(w_\theta)$ are identical to those used to describe the anomaly angle of a geodesic orbit with parameters p, e and I in Eqs. (2.27) and

[1]Note that if the function we are Fourier expanding already has a subscript, we use a comma to denote the specific Fourier mode. For example, $u_{t,1,0,-1}^S$ is the $j = 1$, $n = 0$, $k = -1$ harmonic of function u_t^S.

(2.28):

$$\delta\hat{\chi}_r(w_r) = \sum_{n=-\infty}^{\infty} \delta\hat{\chi}_{r,n} e^{-inw_r} \,, \tag{4.42}$$

$$\delta\hat{\chi}_\theta(w_\theta) = \sum_{k=-\infty}^{\infty} \delta\hat{\chi}_{\theta,k} e^{-ikw_\theta} \,. \tag{4.43}$$

Note, however, that the phases w_r and w_θ are not the same as those for the geodesic orbit with corresponding values of (p, e, I), due to the presence of Υ_r^S and Υ_θ^S in Eq. (4.40). The spin-corrections to the fundamental frequencies are built into our parameterization of spinning-body orbits. We explicitly include the w_r and w_θ arguments in Eq. (4.41) to emphasize this.

Reference geodesics

As we have discussed, we cannot in general constrain the radial or polar motion of spinning body orbits to lie between two fixed turning points as we can for bound geodesics. However, we can constrain the purely radial motion (aspects of the motion that only involve harmonics of Υ_r) and the purely polar motion (with only harmonics in Υ_θ) to lie within the radial and polar turning points of a given geodesic orbit. In our approach, we parameterize an orbit by selecting a geodesic with parameters (p, e, I), as well as an initial spin-vector orientation. The purely radial motion of the spinning body's motion is then confined to the region $pM/(1+e) \leq r \leq pM/(1-e)$, and its purely polar is confined to $-\sin I \leq \cos\theta \leq \sin I$. We call the geodesic with parameters (p, e, I) in this picture the "reference geodesic." We briefly introduced this concept in Sec. 4.2.1. Note that there are alternative mappings between geodesics and spinning bodies that have been used in the literature; see Appendix B.1 for further discussion.

We write $\delta\chi_r^S$ and $\delta\chi_\theta^S$ as Fourier expansions,

$$\delta\chi_r^S = \sum_{n=-\infty}^{\infty} \delta\chi_{r,n}^S e^{-inw_r} \,, \tag{4.44}$$

$$\delta\chi_\theta^S = \sum_{k=-\infty}^{\infty} \delta\chi_{\theta,k}^S e^{-ikw_\theta} \,. \tag{4.45}$$

Note that because $\delta\chi_r^S$ and $\delta\chi_\theta^S$ both have average values of zero (they represent oscillatory contributions to the χ_r^S and χ_θ^S, we set $\delta\chi_{r,0}^S = 0$ and $\delta\chi_{\theta,0}^S = 0$). Notice that the expansion for $\delta\chi_r^S$ in Eq. (4.44) consists purely harmonics at the radial frequency; $\delta\chi_\theta^S$ in Eq. (4.45) likewise consists purely of harmonics at the polar frequency. In this way, we have constrained the purely radial motion to the interval $p/(1+e) \leq r \leq p/(1-e)$ and purely polar motion to the interval $-\sin I \leq \cos\theta \leq \sin I$.

The remaining dynamics, consisting of motion that is neither purely radial nor purely polar, describes how the libration regions varies, and is mapped onto the quantities $\delta\,\text{ż}_S$ and $\delta\,\text{ż}_S$. We expand these quantities using generic Fourier expansions of the form shown in Eq.

(4.31):

$$\delta \mathscr{r}_S = \sum_{j=-1}^{1} \sum_{n,k=-\infty}^{\infty} \delta \mathscr{r}_{S,jnk} e^{-i(jw_s + nw_r + kw_\theta)} \,, \tag{4.46}$$

$$\delta \mathscr{z}_S = \sum_{j=-1}^{1} \sum_{n,k=-\infty}^{\infty} \delta \mathscr{z}_{S,jnk} e^{-i(jw_s + nw_r + kw_\theta)} \,, \tag{4.47}$$

where $w_s = \Upsilon_s \lambda$. Notice that harmonics of all three frequencies — radial, polar, and spin precession — are present in these expansions. When we evaluate Eq. (4.46), we require that k and j cannot both be zero; otherwise, that contribution would represent a purely radial dynamic, which we have constrained to be in the anomaly angle χ_r. Likewise, when we evaluate Eq. (4.47), we require that n and j cannot both be zero, since the purely polar dynamics is entirely contained in χ_θ.

In summary, the anomaly angles $\delta\chi_r^S$ and $\delta\chi_\theta^S$ control the shape of the orbit while keeping the turning points unchanged relative to the reference geodesic orbit, whereas $\delta \mathscr{r}_S$ and $\delta \mathscr{z}_S$ affect the position of the turning points and introduce spin precession effects into the dynamics. In the nearly equatorial case ($I = 0$), we find $\delta \mathscr{z}_S = -\delta\theta_S$; in the nearly circular case ($e = 0$), we have $\delta \mathscr{r}_S = \delta r_S$.

Deviation of a spinning body's orbit from its reference geodesic

Once we expand the anomaly variables χ_r and χ_θ as discussed in Sec. 4.3.1, a generic orbit's radial and polar motion as described by Eqs. (4.37) and (4.38) can be written in the form

$$r(\lambda) = \frac{pM}{1 + e\cos(w_r + \delta\hat{\chi}_r(w_r) + \delta\chi_r^S)} + \delta \mathscr{r}_S \,, \tag{4.48}$$

$$\cos\theta(\lambda) = \sin(I)\cos\big(w_\theta + \delta\hat{\chi}_\theta(w_\theta) + \delta\chi_\theta^S\big) + \delta \mathscr{z}_S \,. \tag{4.49}$$

Here, $\delta\hat{\chi}_r(w_r)$, $\delta\chi_r^S$ and $\delta \mathscr{r}_S$ are given by Eqs. (4.42), (4.44) and (4.46); the analogous quantities for the polar motion $\delta\hat{\chi}_\theta(w_\theta)$, $\delta\chi_\theta^S$, and $\delta \mathscr{z}_S$ are given by Eqs. (4.43), (4.45) and (4.47). Notice that the functions $\delta\hat{\chi}_r(w_r)$ and $\delta\hat{\chi}_\theta(w_\theta)$ have as their arguments w_r and w_θ, whose forms are given in Eq. (4.40). These functions are exactly the oscillating contributions to the anomaly angles that one computes for geodesic orbits, but with their frequencies shifted to remain phase-locked with spinning-body orbits. For geodesics, their arguments would be $\hat{w}_r = \hat{\Upsilon}_r\lambda$ and $\hat{w}_\theta = \hat{\Upsilon}_\theta\lambda$.

In Sec. 4.2.2, we defined the deviation from the geodesic trajectory induced by the spin of the small body by writing $x^\alpha(\lambda)$ as

$$\delta x_S^\alpha(\lambda) = x^\alpha(\lambda) - \hat{x}^\alpha(\lambda) \,, \tag{4.50}$$

where $\hat{x}^\alpha(\lambda)$ is a geodesic orbit. Using the reference geodesic in this equation, $\hat{r}$ and $\hat{\theta}$ are given by

$$\hat{r}(\lambda) = \frac{pM}{1 + e\cos\left(\hat{w}_r + \delta\hat{\chi}_r(\hat{w}_r)\right)} \,, \tag{4.51}$$

$$\cos\hat{\theta}(\lambda) = \sin I\cos\left(\hat{w}_\theta + \delta\hat{\chi}_\theta(\hat{w}_\theta)\right) \,. \tag{4.52}$$

Here we use the purely geodesic forms

$$\delta\hat{\chi}_r(\hat{w}_r) = \sum_{n=-\infty}^{\infty} \delta\hat{\chi}_{r,n} e^{-in\hat{w}_r\lambda} \,, \tag{4.53}$$

$$\delta\hat{\chi}_\theta(\hat{w}_\theta) = \sum_{k=-\infty}^{\infty} \delta\hat{\chi}_{\theta,k} e^{-ik\hat{w}_\theta\lambda} \,. \tag{4.54}$$

Combining the definition (4.50) with our solutions for the spinning body's motion, Eqs. (4.48) and (4.49), and for the reference geodesic, Eqs. (4.51) and (4.52), we find

$$\begin{aligned}\delta r_S(\lambda) = epM &\frac{\Upsilon_r^S \lambda \left(1 - i\sum_n n\delta\hat{\chi}_{r,n} e^{-in\hat{w}_r}\right) + \delta\chi_r^S(w_r)}{\left[1 + e\cos\left(\hat{w}_r + \delta\hat{\chi}_r(\hat{w}_r)\right)\right]^2} \\ &\times \sin\left(\hat{w}_r + \delta\hat{\chi}_r(\hat{w}_r)\right) + \delta\,\text{ɾ}_S \,,\end{aligned} \tag{4.55}$$

$$\begin{aligned}\delta\theta_S(\lambda) = \Upsilon_r^S \lambda &\left(1 - i\sum_k k\delta\hat{\chi}_{\theta,k} e^{-ik\hat{w}_\theta}\right) + \delta\chi_\theta^S(w_\theta) \\ &- \frac{\delta\,\text{ɿ}_S}{\sin I \sin\left(\hat{w}_\theta + \delta\hat{\chi}_\theta(\hat{w}_\theta)\right)} \,,\end{aligned} \tag{4.56}$$

where we have used the fact that $\Upsilon_r^S = \mathcal{O}(S)$. Notice that both $\delta r_S(\lambda)$ and $\delta\theta_S(\lambda)$ show secular growth. This is because of the difference in frequencies between the geodesic $\hat{x}^\alpha(\lambda)$ and spinning-body $x^\alpha(\lambda)$ orbits. The presence of these secularly growing terms means that, as defined, $\delta r_S(\lambda)$ and $\delta\theta_S(\lambda)$ cannot easily be studied using a frequency-domain treatment [182].

To address this, consider a slightly modified version of this definition:

$$\delta x^\alpha_{S,\text{shift}}(\lambda) = x^\alpha(\lambda) - \hat{x}^\alpha_{\text{shift}}(\lambda) \,. \tag{4.57}$$

This deviation is defined versus a *frequency-shifted* formulation of the geodesic motion:

$$\hat{r}_{\text{shift}}(\lambda) = \frac{pM}{1 + e\cos\left(w_r + \delta\hat{\chi}_r(w_r)\right)} \,, \tag{4.58}$$

$$\cos\hat{\theta}_{\text{shift}}(\lambda) = \sin I\cos\left(w_\theta + \delta\hat{\chi}_\theta(w_\theta)\right) \,. \tag{4.59}$$

Equations (4.58) and (4.59) describe a trajectory that is identical to the reference geodesic, but with all periodic features oscillating at the frequency associated with the spinning body's orbit. The deviation from this shifted geodesic is given by

$$\delta r_{S,\text{shift}}(\lambda) = epM\frac{\delta\chi_r^S(w_r)\sin\left[w_r + \delta\hat{\chi}_r(w_r)\right]}{\left(1 + e\cos\left[w_r + \delta\hat{\chi}_r(w_r)\right]\right)^2} + \delta\,\text{ɾ}_S \,, \tag{4.60}$$

$$\delta\theta_{S,\text{shift}} = \delta\chi_\theta^S(w_\theta) - \frac{\delta\,\text{ɿ}_S}{\sin I\sin\left(\hat{w}_\theta + \delta\hat{\chi}_\theta(\hat{w}_\theta)\right)} \,. \tag{4.61}$$

We discuss a variant of Eq. (4.60) which does not include the libration shift $\delta\,\text{ɾ}_S$ in Appendix A.1. These modified offsets from the reference geodesic do not exhibit any secular growth, and can be nicely described using this chapter's frequency-domain expansions.

Coordinate-time quantities

We can use our spinning-body solutions for u_ϕ to compute the Mino-time ϕ-frequency Υ_ϕ, using

$$\Upsilon^S_\phi = U^\phi_{S,000} \ , \tag{4.62}$$

where

$$U^\phi_{S,000} = \frac{1}{\Lambda_r\Lambda_\theta\Lambda_s}\int_0^{\Lambda_r}\int_0^{\Lambda_\theta}\int_0^{\Lambda_s} U^\phi_S \, d\lambda_r d\lambda_\theta d\lambda_s \ ; \tag{4.63}$$

we remind the reader that $U^\phi \equiv d\phi/d\lambda$. Similarly, we can calculate the spin-correction to Γ which denotes the average rate of accumulation of coordinate-time t per unit Mino-time using

$$\Gamma^S = U^t_{S,000} \ , \tag{4.64}$$

where

$$U^t_{S,000} = \frac{1}{\Lambda_r\Lambda_\theta\Lambda_s}\int_0^{\Lambda_r}\int_0^{\Lambda_\theta}\int_0^{\Lambda_s} U^t_S \, d\lambda_r d\lambda_\theta d\lambda_s \ . \tag{4.65}$$

Once we have the correction to Γ, we can convert any of the Mino-time frequencies into coordinate-time frequencies. Observing that

$$\hat{\Omega}_k + \Omega^S_k = \frac{\hat{\Upsilon}_k + \Upsilon^S_k}{\hat{\Gamma} + \Gamma^S} \tag{4.66}$$

for $k \in (r, \theta, \phi)$, we see that shifts to the coordinate-time frequencies are given by

$$\Omega^S_k = \hat{\Omega}_k\left(\frac{\Upsilon^S_k}{\hat{\Upsilon}_k} - \frac{\Gamma^S}{\hat{\Gamma}}\right) \tag{4.67}$$

to linear order in the small body's spin.

4.3.2 Results

Nearly circular orbits: Aligned spin

We now discuss spinning-body orbits that are $\mathcal{O}(S)$ away from being circular — nearly circular orbits. We outline how we compute the first-order in spin contribution to the polar Mino-time frequency Υ^S_θ using a frequency-domain description for the motion.

We consider a circular inclined reference geodesic, with the spin vector of the small body aligned with the orbit. In this case, orbits can be described using expansions of the form

$$f(\lambda) = \sum_{k=-\infty}^{\infty} f_k e^{-ikw_\theta} \ . \tag{4.68}$$

In order to evaluate these expressions, we truncate the Fourier expansion at a finite value; for the expansion above, we truncate the series at $k_{\rm max}$. By truncating this Fourier expansion at an appropriately large $k_{\rm max}$, we can compute orbits with an arbitrarily high inclination.

As described in Sec. 4.2.1, we use a parameterization to describe the motion in θ which resembles the form typically used to describe geodesic orbits, as in Eq. (2.28). In addition to

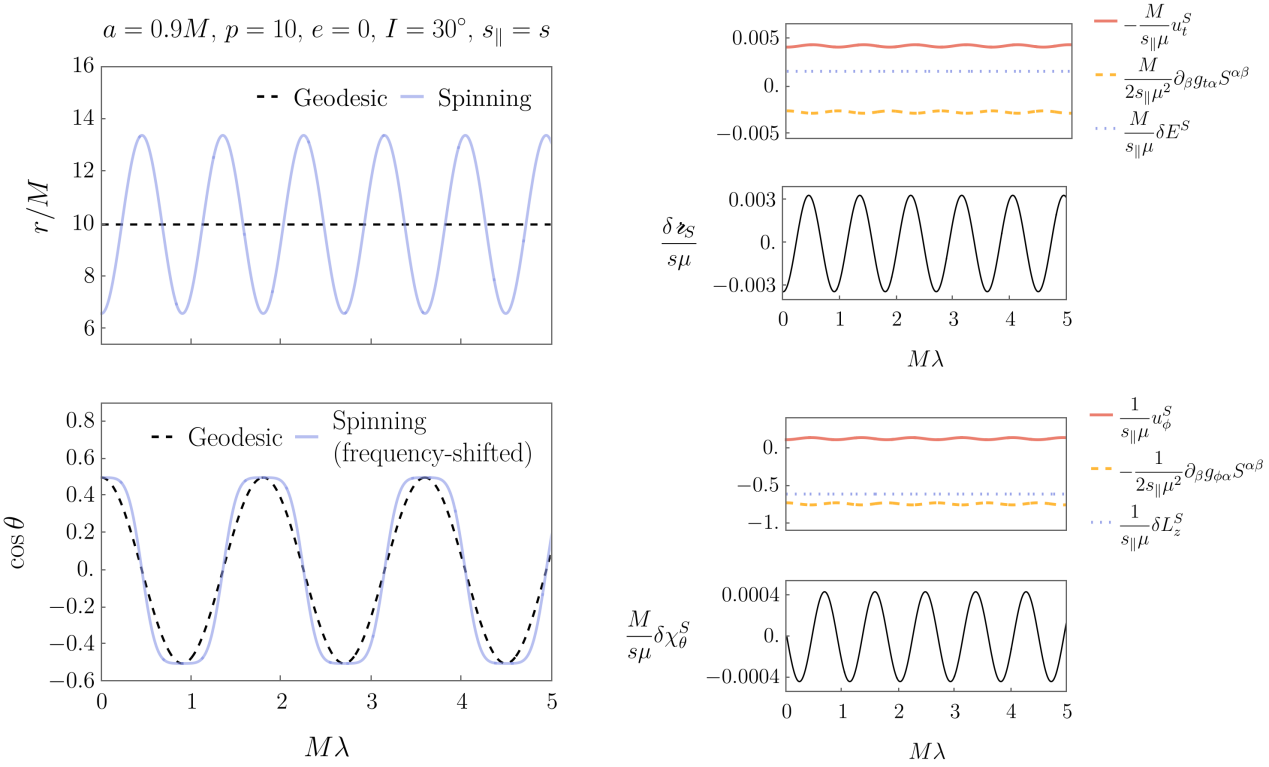

Figure 4.1: Example of the motion of a nearly circular orbit for an aligned spinning test body around a Kerr black hole with $a = 0.9M$. Top left panel shows r versus λ for a geodesic (black dashed) and a spinning test body (blue solid) orbit. The radial reference geodesic is circular, with $p = 10$, $e = 0$. Bottom left panel shows $\cos\theta$ versus λ for a geodesic (black dashed) and a spinning test body (blue solid) orbit. These orbits share polar turning points, corresponding to $I = 30°$. Note that, in the left two panels, we have used an unphysically high spin $\mu s/M = 10^3$ in order make the spin-curvature effects clearly visible. Also note that the spinning-body orbit has been shifted slightly: its polar frequency $\Upsilon_\theta = \hat{\Upsilon}_\theta + \Upsilon_\theta^S$ has been replaced with $\hat{\Upsilon}_\theta$. This is done so that the geodesic and the spinning-body orbit pass through their polar turning points at the same times, which helps to illustrate differences in their motion between each turning point. Top right shows $-u_t^S$ (red), $\partial_\beta g_{t\alpha}S^{\alpha\beta}/2\mu$ (orange), δE^S (blue) as well as $\delta \mathscr{C}_S$ (black), all versus λ. Finally, the bottom right panel shows u_ϕ^S (red), $-\partial_\beta g_{\phi\alpha}S^{\alpha\beta}/2\mu$ (orange), δL_z^S (blue) as well as $\delta\chi_\theta^S$ (black), all versus λ. Notice that the spin-induced shifts to the integrals of motion E and L_z are constants, although each such term has contributions that oscillate. In making these plots, we have used $s = s_\parallel$ and $k_{\max} = 6$.

this, we must account for the fact that the spin of the test body induces oscillations about pM, the radius of the circular reference geodesic. We thus parameterize the orbit as

$$r = pM + \delta\, \text{r}_S \ , \tag{4.69}$$

$$\cos\theta = \sin I \cos\left(w_\theta + \delta\hat{\chi}_\theta(w_\theta) + \delta\chi^S_\theta\right) \ . \tag{4.70}$$

The functions $\delta\chi^S_\theta$ and $\delta\, \text{r}_S$ are described by purely polar oscillations in this case:

$$\delta\chi^S_\theta = \sum_{k=-\infty}^{\infty} \delta\chi^S_{\theta,k} e^{-ikw_\theta} \ , \tag{4.71}$$

$$\delta\, \text{r}_S = \sum_{k=-\infty}^{\infty} \delta\, \text{r}_{S,k} e^{-ikw_\theta} \ . \tag{4.72}$$

We insert Eqs. (4.69), (4.70) and (4.26) into (4.28) – (4.29) and linearize in spin. The first-order-in-spin piece of Eq. (4.28) becomes

$$\mathcal{F}_\text{r}\frac{d^2\delta\, \text{r}_S}{d\lambda^2} + \mathcal{G}_\text{r}\frac{d\delta\, \text{r}_S}{d\lambda} + \mathcal{G}_\theta\frac{d\delta\chi^S_\theta}{d\lambda} + \mathcal{H}_\text{r}\delta\, \text{r}_S + \mathcal{H}_\theta\delta\chi^S_\theta + \mathcal{I}_{1\theta}\Upsilon^S_\theta + \mathcal{I}_2 u^S_{t,0} + \mathcal{I}_3 u^S_{\phi,0} + \mathcal{J} = 0 \ , \tag{4.73}$$

where $\mathcal{F}_\text{r}$, $\mathcal{G}_\text{r}$, $\mathcal{G}_\theta$, $\mathcal{H}_\text{r}$, $\mathcal{H}_\theta$, $\mathcal{I}_{1\theta}$, $\mathcal{I}_2$, $\mathcal{I}_3$ and $\mathcal{J}$ are all functions of known quantities evaluated on geodesics. We now consider the first-order-in-spin piece of Eq. (4.29), which becomes

$$\mathcal{Q}_\theta\frac{d^2\delta\chi^S_\theta}{d\lambda^2} + \mathcal{S}_\text{r}\frac{d\delta\, \text{r}_S}{d\lambda} + \mathcal{S}_\theta\frac{d\delta\chi^S_\theta}{d\lambda} + \mathcal{T}_\text{r}\delta\, \text{r}_S + \mathcal{T}_\theta\delta\chi^S_\theta + \mathcal{U}_{1\theta}\Upsilon^S_\theta + \mathcal{U}_2 u^S_{t,0} + \mathcal{U}_3 u^S_{\phi,0} + \mathcal{V} = 0 \ , \tag{4.74}$$

where $\mathcal{Q}_\theta$, $\mathcal{S}_\text{r}$, $\mathcal{S}_\theta$, $\mathcal{T}_\text{r}$, $\mathcal{T}_\theta$, $\mathcal{U}_{1\theta}$, $\mathcal{U}_2$, $\mathcal{U}_3$ and $\mathcal{V}$ are all functions of known quantities on geodesics. Third, we use the constraint $u^\alpha u_\alpha = -1$ to obtain a linearized equation of the form

$$\mathcal{K}_\text{r}\frac{d\delta\, \text{r}_S}{d\lambda} + \mathcal{K}_\theta\frac{d\delta\chi^S_\theta}{d\lambda} + \mathcal{M}_\text{r}\delta\, \text{r}_S + \mathcal{M}_\theta\delta\chi^S_\theta + \mathcal{N}_{1\theta}\Upsilon^S_\theta + \mathcal{N}_2 u^S_{t,0} + \mathcal{N}_3 u^S_{\phi,0} + \mathcal{P} = 0 \ , \tag{4.75}$$

where $\mathcal{K}_\text{r}$, $\mathcal{K}_\theta$, $\mathcal{M}_\text{r}$, $\mathcal{M}_\theta$, $\mathcal{N}_{1\theta}$, $\mathcal{N}_2$, $\mathcal{N}_3$ and $\mathcal{P}$ are again all functions[2] of known quantities on geodesics.

We write the functions $\mathcal{F}_\text{r}$, $\mathcal{G}_\text{r}$, $\mathcal{G}_\theta$, $\mathcal{H}_\text{r}$, $\mathcal{H}_\theta$, $\mathcal{I}_{1\theta}$, $\mathcal{I}_2$, $\mathcal{I}_3$, $\mathcal{J}$, $\mathcal{Q}_\theta$, $\mathcal{S}_\text{r}$, $\mathcal{S}_\theta$, $\mathcal{T}_\text{r}$, $\mathcal{T}_\theta$, $\mathcal{U}_{1\theta}$, $\mathcal{U}_2$, $\mathcal{U}_3$, $\mathcal{V}$, $\mathcal{K}_\text{r}$, $\mathcal{K}_\theta$, $\mathcal{M}_\text{r}$, $\mathcal{M}_\theta$, $\mathcal{N}_{1\theta}$, $\mathcal{N}_2$, $\mathcal{N}_3$ and $\mathcal{P}$ as Fourier expansions of the form (4.68). The explicit forms for many of these expressions in the limiting case of nearly equatorial Schwarzschild orbits ($a = 0$) can be found in Appendix A.3.1. For the general case, we provide expressions using the *Mathematica* notebook in the Supplemental Material associated with the published version of this chapter [181]. Some of the general expressions are very lengthy (hundreds of terms long) and could likely be simplified with some effort; we present them in a companion Mathematica notebook for convenience and completeness.

We insert these expansions along with (4.71) and (4.72) into (4.73), (4.74) and (4.75). We then solve for the unknown variables $\delta\, \text{r}_S$, $\delta\chi^S_\theta$, Υ^S_θ u^S_t and u^S_ϕ.

[2]The functions $\mathcal{F}_\text{r}$, $\mathcal{G}_\text{r}$, etc. follow a mostly alphabetic sequence; however, we skip the letter $\mathcal{L}$ in our scheme to avoid confusion with the angular momentum 4-vector defined in Eq. (2.11).

In the left-hand panels of Fig. 4.1, we show r and θ for a circular, inclined, spin-aligned orbit; r and θ for the corresponding reference geodesic orbit are overplotted. The period associated with the spinning-body orbit's polar motion is shifted so that it remains phase-locked with the geodesic orbit. The right-hand panels of Fig. 4.1 show $\delta\,\text{r}_S$ and $\delta\chi^S_\theta$ for the spinning-body orbit. We also plot u^S_t and u^S_ϕ alongside the spin contributions to the orbit's energy and axial angular momentum, δE^S and δL^S_z. Notice that the spinning-body orbit we obtain is not circular; this can be seen in the top left panel of Fig. 4.1, where the effect is exaggerated so that the oscillations in r are clearly visible. In Chapter 3, we perturbed about an equatorial reference geodesic and obtained a spinning-body orbit that did not lie in the equatorial plane; here we perturb about a circular reference geodesic, yielding a corresponding spinning-body orbit that is not circular. In contrast to the behavior we saw in Chapter 3, we cannot attribute this behavior only to spin precession, since we see this effect even when the spin vector is aligned.

In Fig. 4.2, we see how Υ_θ, $u^S_{t,0}$ and $u^S_{\phi,0}$ converge to their true values in the case of nearly circular, inclined orbits. We define "residuals" here to mean the difference between the value of the quantity computed at successive $k_{\max}$'s, rather than a direct comparison with an exact value (as they were defined in Chapter 3). As expected, the residuals generally decrease as $k_{\max}$ increases. However, the pattern of convergence isn't strictly monotonic; the residuals tend to tick upwards for odd values of $k_{\max}$.

Nearly circular orbits: Misaligned spin

We now consider nearly circular inclined orbits with the spin of the test body misaligned from the orbit (i.e., circular orbits $s_\perp \neq 0$). Taking into account the effect of spin precession, many orbital quantities can be described using frequency-domain expansions of the form

$$f(\lambda) = \sum_{j=-1}^{1}\sum_{k=-\infty}^{\infty} f_{jk} e^{-i(jw_s + kw_\theta)} \,. \tag{4.76}$$

As described in Sec. 4.2.1, the parameterization of the orbit in this case has the form

$$r = pM + \delta\,\text{r}_S \,, \tag{4.77}$$

$$\cos\theta = \sin I \cos\left(w_\theta + \delta\hat{\chi}_\theta(w_\theta) + \delta\chi^S_\theta\right) + \delta\,\text{z}_S \,. \tag{4.78}$$

Compared to the parameterization in Sec. 4.3.2, there is a new term $\delta\,\text{z}_S$ which adjusts the polar turning points relative to the reference geodesic. The libration variations $\delta\,\text{r}_S$ and $\delta\,\text{z}_S$ depend on both Υ_θ and Υ_s, while $\delta\chi^S_\theta$ only has oscillations at harmonics of Υ_θ:

$$\delta\chi^S_\theta = \sum_{k=-\infty}^{\infty} \delta\chi^S_{\theta,k} e^{-ikw_\theta} \,, \tag{4.79}$$

$$\delta\,\text{r}_S = \sum_{j=-1}^{1}\sum_{k=-\infty}^{\infty} \delta\,\text{r}_{S,jk} e^{-i(kw_\theta + jw_s)} \,, \tag{4.80}$$

$$\delta\,\text{z}_S = \sum_{j=-1}^{1}\sum_{k=-\infty}^{\infty} \delta\,\text{z}_{S,jk} e^{-i(kw_\theta + jw_s)} \,, \tag{4.81}$$

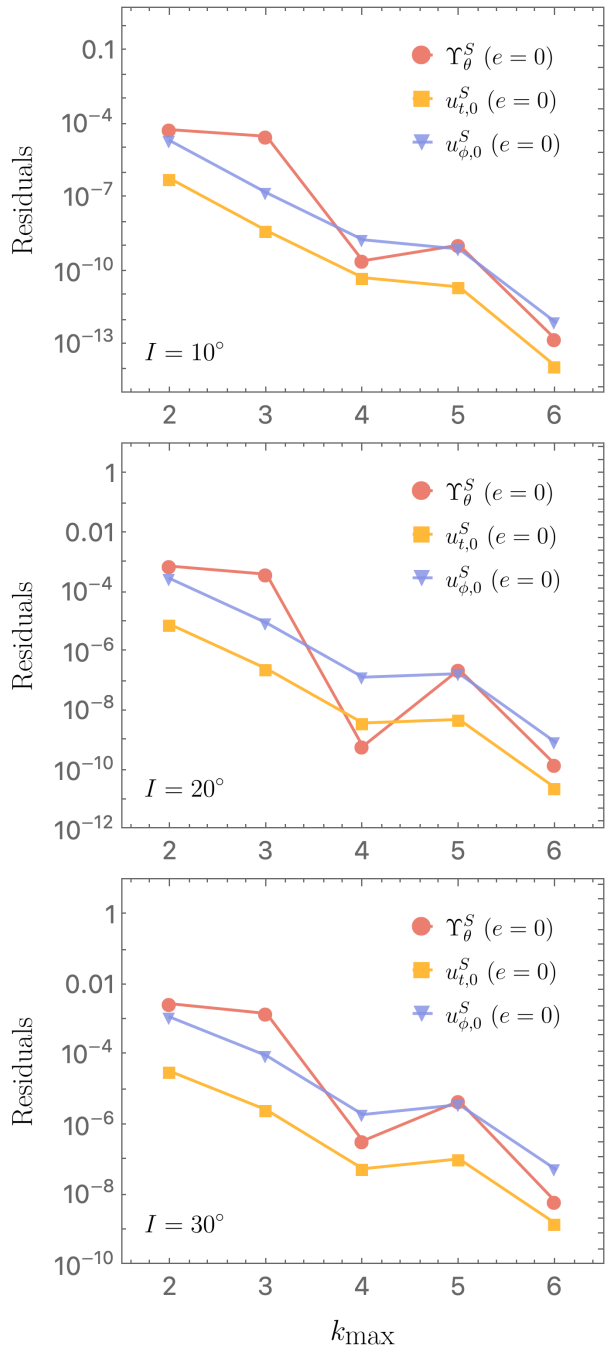

Figure 4.2: Plot of residuals versus $k_{\max}$ for a nearly circular ($e = 0$) orbit of an aligned ($s_\parallel = s$) spinning body. We plot Υ^S_θ, $u^S_{t,0}$, $u^S_{\phi,0}$ using red circular, orange square and blue triangular markers respectively. To compute these residuals, we evaluate the change between subsequent values of $k_{\max}$ for each of the quantities plotted. Top panel shows $I = 10°$; middle shows $I = 20°$; and bottom shows $I = 30°$. In all cases, the large black hole has spin parameter $a = 0.9M$, and the orbit has $p = 10$.

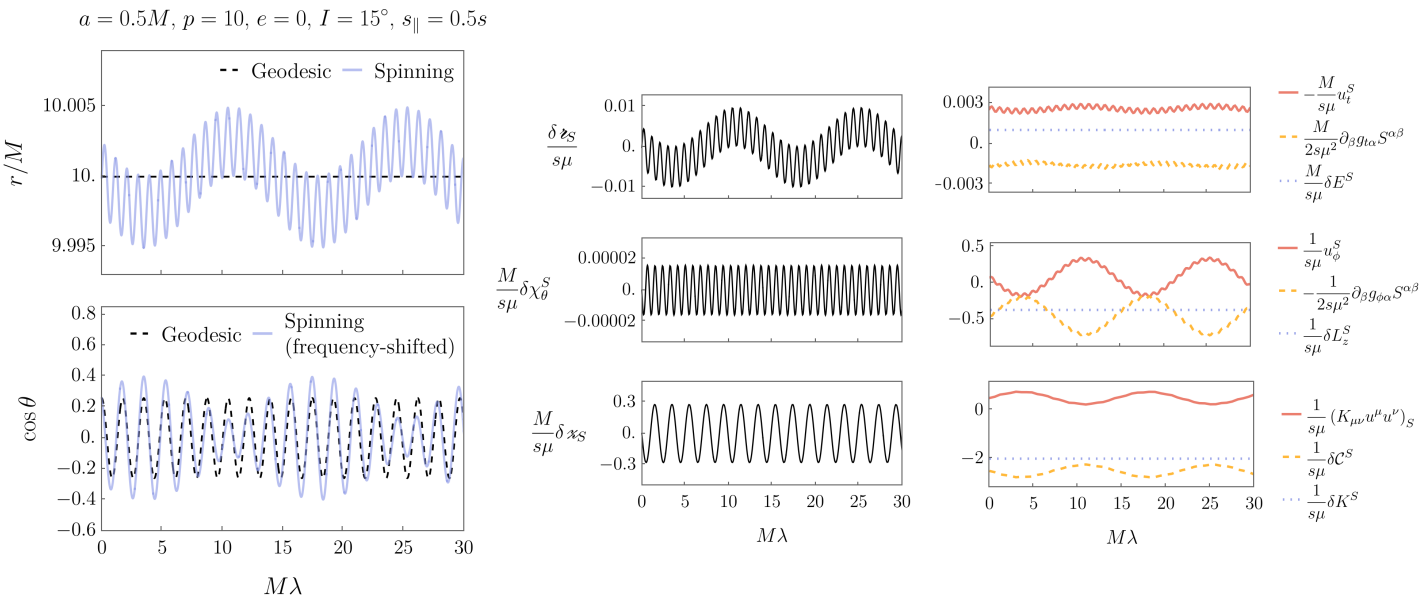

Figure 4.3: Example of the motion of a nearly circular orbit for a non-aligned spinning test body around a Kerr black hole with $a = 0.5M$. Top left panel shows r versus λ for a geodesic (black dashed) and a spinning test body (blue solid) orbit. The radial reference geodesic is circular, with $p = 10$, $e = 0$. Bottom left panel shows $\cos\theta$ versus λ for a geodesic (black dashed) and a spinning test body (blue solid) orbit. The polar reference geodesic has $I = 15°$. Note that, in the two left panels, we have used an unphysically high spin $\mu s/M = 0.5$ in order make the spin-curvature effects clearly visible. Also note that for making this plot, the spinning-body orbit has been shifted slightly: its polar frequency $\Upsilon_\theta = \hat{\Upsilon}_\theta + \Upsilon^S_\theta$ has been replaced with $\hat{\Upsilon}_\theta$. This is done so that in the plot the geodesic and the spinning-body orbit pass through their polar turning points at the same times, which helps to illustrate differences in their motion between each turning point. Middle column shows $\delta\varkappa_S$, $\delta\chi^S_\theta$ and $\delta\varkappa_S$, all versus λ and all drawn with black solid lines. Top right panel shows $-u^S_t$ (red), $\partial_\beta g_{t\alpha}S^{\alpha\beta}/2\mu$ (orange), δE^S (blue), all versus λ. Middle right panel shows u^S_ϕ (red), $-\partial_\beta g_{\phi\alpha}S^{\alpha\beta}/2\mu$ (orange), δL^S_z (blue), all versus λ. Finally, bottom right panel shows $(K_{\mu\nu}u^\mu u^\nu)_S$ (red), $\delta\mathcal{C}^S$ (orange), δK^S (blue), all versus λ. Notice that the spin-induced shifts to the integrals of motion E, L_z and K are constants, although each such term has contributions that oscillate. In making these plots, we have used $s_\parallel = s/2$, $s_\perp = \sqrt{3}s/2$, $\phi_s = \pi/2$ and $k_{\max} = 3$.

where, in the last line, j cannot equal zero. We then follow the same procedure as described for nearly circular inclined orbits with aligned spin to convert the time-domain expressions into a linear algebraic system in the frequency domain, but now including the term $\delta \varkappa_S$ in the equations.

We insert equations (4.77), (4.78) and (4.26) into (4.28) – (4.29) and linearize in spin. Eq. (4.28) can be written

$$\mathcal{F}_\varrho \frac{d^2\delta\varrho_S}{d\lambda^2} + \mathcal{G}_\varrho \frac{d\delta\varrho_S}{d\lambda} + \mathcal{G}_\theta \frac{d\delta\chi_\theta^S}{d\lambda} + \mathcal{G}_\varkappa \frac{d\delta\varkappa_S}{d\lambda} + \mathcal{H}_\varrho \delta\varrho_S + \mathcal{H}_\theta \delta\chi_\theta^S + \mathcal{H}_\varkappa \delta\varkappa_S + \mathcal{I}_{1\theta}\Upsilon_\theta^S + \mathcal{I}_2 u_{t,0}^S + \mathcal{I}_3 u_{\phi,0}^S + \mathcal{J} = 0 \,, \tag{4.82}$$

where $\mathcal{F}_\varrho$, $\mathcal{G}_\varrho$, $\mathcal{G}_\theta$, $\mathcal{G}_\varkappa$, $\mathcal{H}_\varrho$, $\mathcal{H}_\theta$, $\mathcal{H}_\varkappa$, $\mathcal{I}_{1\theta}$, $\mathcal{I}_2$, $\mathcal{I}_3$ and $\mathcal{J}$ are all functions of known quantities evaluated on geodesics. Similarly, we can write Eq. (4.29) in the form

$$\mathcal{Q}_\theta \frac{d^2\delta\chi_\theta^S}{d\lambda^2} + \mathcal{Q}_\varkappa \frac{d^2\delta\varkappa_S}{d\lambda^2} + \mathcal{S}_\varrho \frac{d\delta\varrho_S}{d\lambda} + \mathcal{S}_\theta \frac{d\delta\chi_\theta^S}{d\lambda} + \mathcal{S}_\varkappa \frac{d\delta\varkappa_S}{d\lambda} + \mathcal{T}_\varrho \delta\varrho_S + \mathcal{T}_\theta \delta\chi_\theta^S + \mathcal{T}_\varkappa \delta\varkappa_S + \mathcal{U}_{1\theta}\Upsilon_\theta^S + \mathcal{U}_2 u_{t,0}^S + \mathcal{U}_3 u_{\phi,0}^S + \mathcal{V} = 0 \,, \tag{4.83}$$

where $\mathcal{Q}_\theta$, $\mathcal{Q}_\varkappa$, $\mathcal{S}_\varrho$, $\mathcal{S}_\theta$, $\mathcal{S}_\varkappa$, $\mathcal{T}_\varrho$, $\mathcal{T}_\theta$, $\mathcal{T}_\varkappa$, $\mathcal{U}_{1\theta}$, $\mathcal{U}_2$, $\mathcal{U}_3$ and $\mathcal{V}$ are all functions of known quantities evaluated on geodesics. We again also use $u^\alpha u_\alpha = -1$, yielding

$$\mathcal{K}_\varrho \frac{d\delta\varrho_S}{d\lambda} + \mathcal{K}_\theta \frac{d\delta\chi_\theta^S}{d\lambda} + \mathcal{K}_\varkappa \frac{d\delta\varkappa_S}{d\lambda} + \mathcal{M}_\varrho \delta\varrho_S + \mathcal{M}_\theta \delta\chi_\theta^S + \mathcal{M}_\varkappa \delta\varkappa_S + \mathcal{N}_{1\theta}\Upsilon_\theta^S + \mathcal{N}_2 u_{t,0}^S + \mathcal{N}_3 u_{\phi,0}^S + \mathcal{P} = 0 \,, \tag{4.84}$$

where $\mathcal{K}_\varrho$, $\mathcal{K}_\theta$, $\mathcal{K}_\varkappa$, $\mathcal{M}_\varrho$, $\mathcal{M}_\theta$, $\mathcal{M}_\varkappa$, $\mathcal{N}_{1\theta}$, $\mathcal{N}_2$, $\mathcal{N}_3$ and $\mathcal{P}$ are again all functions of known quantities evaluated on geodesics.

We describe $\mathcal{F}_\varrho$, $\mathcal{G}_\varrho$, $\mathcal{G}_\theta$, $\mathcal{G}_\varkappa$, $\mathcal{H}_\varrho$, $\mathcal{H}_\theta$, $\mathcal{H}_\varkappa$, $\mathcal{I}_{1\theta}$, $\mathcal{I}_2$, $\mathcal{I}_3$, $\mathcal{J}$, $\mathcal{Q}_\theta$, $\mathcal{Q}_\varkappa$, $\mathcal{S}_\varrho$, $\mathcal{S}_\theta$, $\mathcal{S}_\varkappa$, $\mathcal{T}_\varrho$, $\mathcal{T}_\theta$, $\mathcal{T}_\varkappa$, $\mathcal{U}_{1\theta}$, $\mathcal{U}_2$, $\mathcal{U}_3$, $\mathcal{V}$, $\mathcal{K}_\varrho$, $\mathcal{K}_\theta$, $\mathcal{K}_\varkappa$, $\mathcal{M}_\varrho$, $\mathcal{M}_\theta$, $\mathcal{M}_\varkappa$, $\mathcal{N}_{1\theta}$, $\mathcal{N}_2$, $\mathcal{N}_3$ and $\mathcal{P}$ using Fourier expansions of the form (4.76). We provide the full expressions for these functions in the *Mathematica* notebook in the Supplemental Material accompanying the article corresponding to this chapter [181]. We insert these expansions along with (4.79), (4.80) and (4.81), into (4.82), (4.83) and (4.84). We then solve for the unknown variables $\delta\varrho_S$, $\delta\chi_\theta^S$, $\delta\varkappa_S$, Υ_θ^S, u_t^S and u_ϕ^S.

In the left-hand panels of Fig. 4.3, we show r and θ for a misaligned nearly circular spinning-body orbit, with the circular inclined reference geodesic overplotted for reference. As in Fig. 4.1, the spinning-body orbit's polar frequency is shifted so that it remains phase-locked with the geodesic orbit. The form of $\delta\varrho_S$, $\delta\chi_\theta^S$ and $\delta\varkappa_S$ for this orbit are shown in the right panels of Fig. 4.3. As in Fig. 4.1, we plot u_t^S and u_ϕ^S as well as the corrections to the spinning body's orbital energy δE^S and axial angular momentum δL_z^S in the right panels of Fig. 4.3.

In the bottom right panel of Fig. 4.3, we show the spin-correction to the Carter constant K. We plot the first-order in spin correction to the term $K_{\mu\nu}u^\mu u^\nu$ and the quantity $\delta\mathcal{C}^S$ which is defined in (3.17), giving us the overall first-order correction to K denoted δK^S. For equatorial reference geodesics, δQ^S has the simple form $2as_\parallel$, as was discussed in Chapter 3. In this case, when the orbit is inclined and the spin vector is precessing, we find that the first-order in spin correction to $K_{\mu\nu}u^\mu u^\nu$ is no longer constant. The oscillations in this quantity precisely cancel oscillations in $\delta\mathcal{C}^S$, yielding constant values for δK^S and δQ^S.

Generic orbits

We finally examine generic orbits of spinning test bodies. We use the following Fourier expansion

$$f(\lambda) = \sum_{n,k=-\infty}^{\infty} \sum_{j=-1}^{1} f_{jnk} e^{-i(jw_s + nw_r + kw_\theta)} \tag{4.85}$$

for the various quantities we must evaluate. To evaluate these expressions, we truncate the Fourier expansion at a finite value; for the expansion above, we truncate the radial series at $n_{\max}$ and the polar series at $k_{\max}$. By truncating this Fourier expansion at an appropriately large $n_{\max}$ and $k_{\max}$, we can compute orbits with an arbitrarily high eccentricity and inclination.

In general, the radial and polar motions are coupled and consequently orbits of spinning bodies have radial and polar turning points that vary over the course of the orbit. This means that positions of the radial turning points depend on θ and likewise the polar turning points depend on the radial position of the body, as explicitly shown in Ref. [84]. In addition, the turning points depend on the precession phase ψ_p defined in equation (2.58). Therefore, as in Eqs. (4.37) – (4.38), we include the terms $\delta\, \text{z}_S$ and $\delta\, \text{z}_S$ in our parameterization to capture the modification to the libration range, yielding

$$r = \frac{pM}{1 + e\cos\left(w_r + \delta\hat{\chi}_r(w_r) + \delta\chi_r^S\right)} + \delta\, \text{z}_S \ , \tag{4.86}$$

$$\cos\theta = \sin I \cos\left(w_\theta + \delta\hat{\chi}_\theta(w_\theta) + \delta\chi_\theta^S\right) + \delta\, \text{z}_S \ . \tag{4.87}$$

As described in Sec. 4.3.1, the true anomaly angles $\delta\chi_r^S$ and $\delta\chi_\theta^S$ contained inside the arguments of the cosines in Eqs. (6.30) and (6.31) consist of purely radial and purely polar oscillations respectively:

$$\delta\chi_r^S = \sum_{n=-\infty}^{\infty} \delta\chi_{r,n}^S e^{-inw_r} \ , \tag{4.88}$$

$$\delta\chi_\theta^S = \sum_{k=-\infty}^{\infty} \delta\chi_{\theta,k}^S e^{-ikw_\theta} \ . \tag{4.89}$$

Motion that is not purely radial or purely polar is subsumed into the functions $\delta\, \text{z}_S$ and $\delta\, \text{z}_S$. These quantities are written as Fourier expansions of the form (4.85). For the radial libration variation,

$$\delta\, \text{z}_S = \sum_{j=-1}^{1} \sum_{n,k=-\infty}^{\infty} \delta\, \text{z}_{S,jnk} e^{-i(nw_r + kw_\theta + jw_s)} \ , \tag{4.90}$$

where k and j cannot both be zero; for the polar libration variation,

$$\delta\, \text{z}_S = \sum_{j=-1}^{1} \sum_{n,k=-\infty}^{\infty} \delta\, \text{z}_{S,,jnk} e^{-i(nw_r + kw_\theta + jw_s)} \ , \tag{4.91}$$

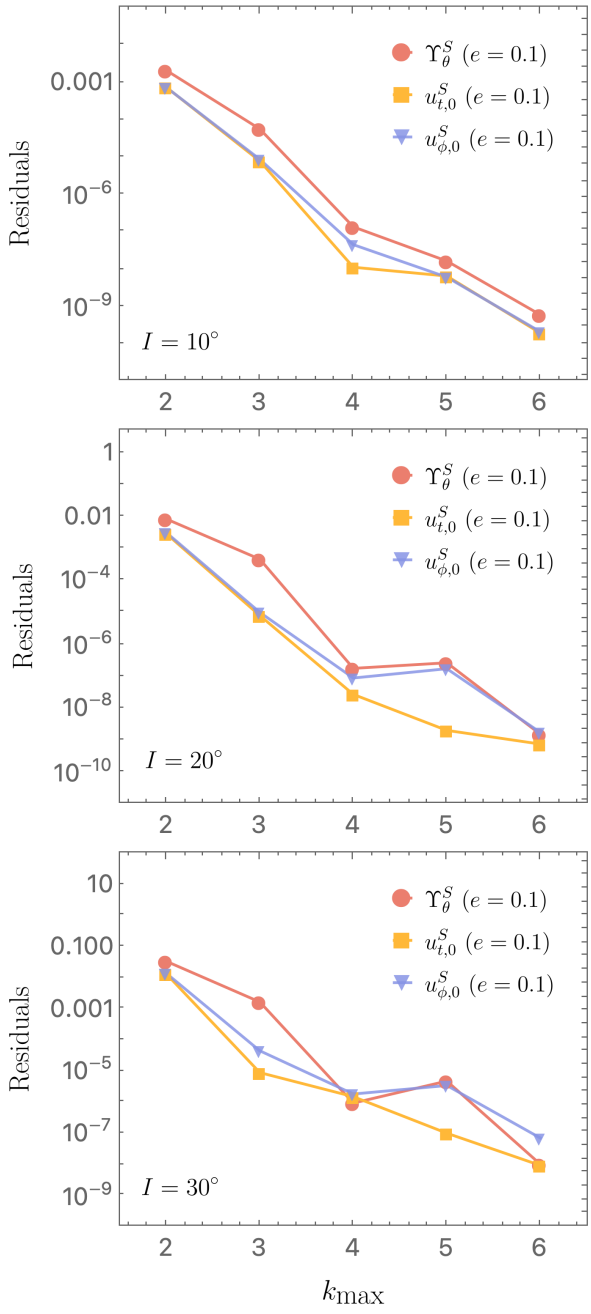

Figure 4.4: Plot of residuals versus $k_{\max}$ for a generic ($e = 0.1$) orbit of an aligned ($s_\parallel = s$) spinning body. We plot Υ^S_θ, $u^S_{t,0}$, $u^S_{\phi,0}$ using red circular, orange square and blue triangular markers respectively. As in Fig. 4.2, we compute the residuals by evaluating the change between subsequent values of $k_{\max}$ for each of the quantities plotted. Top panel shows $I = 10°$; middle shows $I = 20°$; and bottom shows $I = 30°$. In all cases, $n_{\max} = k_{\max}$, the large black hole has spin parameter $a = 0.9M$, and the orbit has $p = 10$.

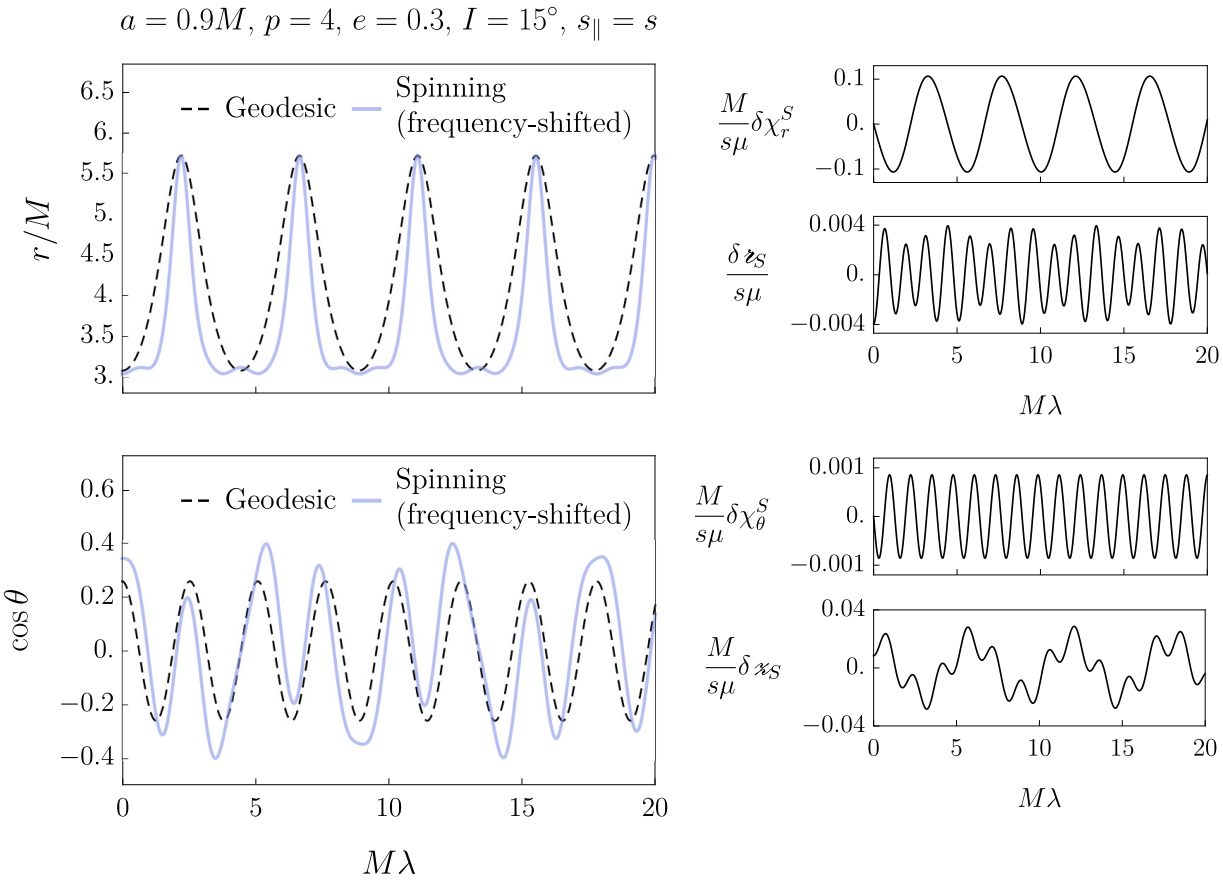

Figure 4.5: Example of generic orbit motion for an aligned spinning test body around a Kerr black hole with $a = 0.9M$. Top left panel shows r versus λ for a geodesic (black dashed) and a spinning test body (blue solid) orbit. The radial reference geodesic has $p = 4$, $e = 0.3$. Note that, in the two left panels, we have used an unphysically high spin $\mu s/M = 10$ in order make the spin-curvature effects clearly visible. Also note that the spinning-body orbit has been shifted slightly: its radial frequency $\Upsilon_r = \hat{\Upsilon}_r + \Upsilon_r^S$ has been replaced with $\hat{\Upsilon}_r$ and its polar frequency $\Upsilon_\theta = \hat{\Upsilon}_\theta + \Upsilon_\theta^S$ has been replaced with $\hat{\Upsilon}_\theta$. This is done so that in the plot the geodesic and the spinning-body orbit remain phase-locked, which helps to illustrate differences in their motion between each turning point. Bottom left panel shows $\cos\theta$ versus λ for a geodesic (black dashed) and a spinning test body (blue solid) orbit. The polar reference geodesic has $I = 15°$. Again, note that for making this plot, the spinning-body orbit has been shifted slightly: its polar frequency $\Upsilon_\theta = \hat{\Upsilon}_\theta + \Upsilon_\theta^S$ has been replaced with $\hat{\Upsilon}_\theta$ for the same reason described above. The right column shows $\delta\chi_r^S$, $\delta\,\text{ɛ}_S$, $\delta\chi_\theta^S$ and $\delta\,\text{ϰ}_S$, all versus λ and all drawn using black solid lines. In making these plots, we have used $s_\parallel = s$ and $n_{\max} = k_{\max} = 3$.

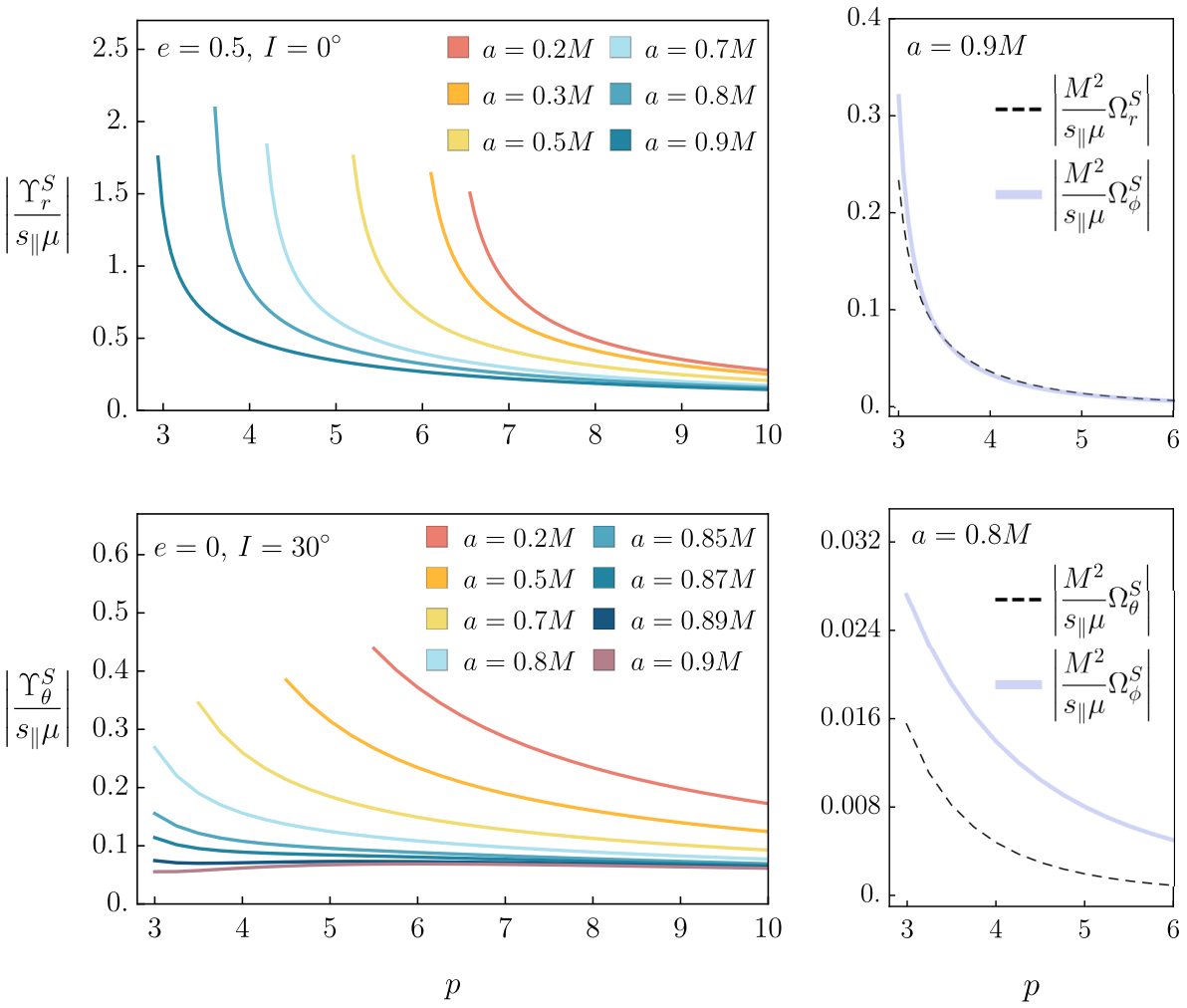

Figure 4.6: Example of the spin contributions Υ_r^S and Υ_θ^S to the radial and polar Mino-time frequencies Υ_r and Υ_θ, as well as spin contributions Ω_r^S and Ω_θ^S to the radial and polar coordinate-time frequencies Ω_r and Ω_θ. Top left panel shows Υ_r^S versus p with $e = 0.5$ and $I = 0°$ for different values of a. Bottom left panel shows Υ_θ^S versus p with $e = 0$ and $I = 30°$ for different values of a. Top right panel shows Ω_r^S (black dashed) and Ω_ϕ^S (blue solid) versus p with $a = 0.9M$, $e = 0.5$ and $I = 0°$. Bottom right panel shows Ω_θ^S (black dashed) and Ω_ϕ^S (blue solid) versus p with $a = 0.8M$, $e = 0$ and $I = 30°$. In making these plots, we have used $n_{\rm max} = k_{\rm max} = 5$.

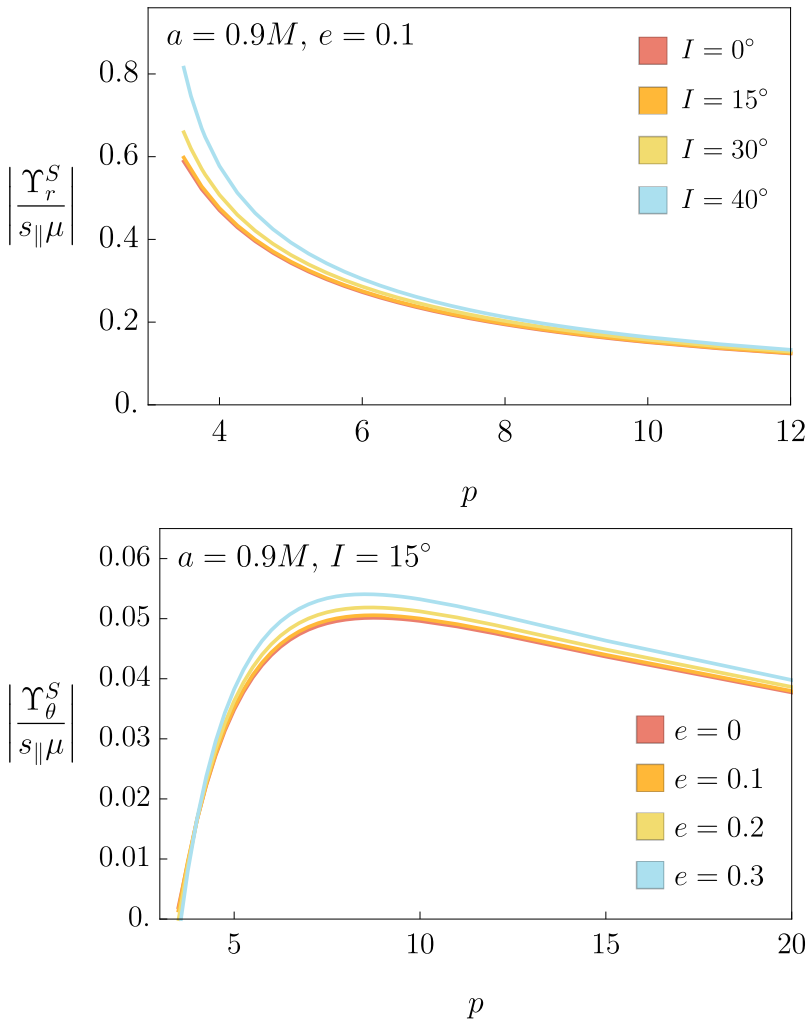

Figure 4.7: Example of the spin contributions Υ_r^S and Υ_θ^S to the radial and polar Mino-time frequencies Υ_r and Υ_θ. Top panel shows Υ_r^S versus p with $e = 0.1$ for $I = 0°$ (red), $I = 15°$ (orange), $I = 30°$ (yellow) and $I = 40°$ (blue). Bottom panel shows Υ_θ^S versus p with $I = 15°$ for $e = 0$ (red), $e = 0.1$ (orange), $e = 0.2$ (yellow) and $e = 0.3$ (blue). In making these plots, we have used $a = 0.9M$ and $s_\parallel = s$. In making these plots, we have used $n_{\rm max} = k_{\rm max} = 3$.

where n and j cannot both be zero.

We insert equations (6.30), (6.31) and (4.26) into (4.28) – (4.29) and linearize in spin. The radial equation (4.28) now has the form

$$\mathcal{F}_r\frac{d^2\delta\chi_r^S}{d\lambda^2}+\mathcal{F}_{\text{ɤ}}\frac{d^2\delta\,\text{ɤ}_S}{d\lambda^2}+\mathcal{G}_r\frac{d\delta\chi_r^S}{d\lambda}+\mathcal{G}_{\text{ɤ}}\frac{d\delta\,\text{ɤ}_S}{d\lambda}+\mathcal{G}_\theta\frac{d\delta\chi_\theta^S}{d\lambda}+\mathcal{G}_{\text{ϰ}}\frac{d\delta\,\text{ϰ}_S}{d\lambda}+H_r\delta\chi_r^S+\mathcal{H}_{\text{ɤ}}\delta\,\text{ɤ}_S$$
$$+\mathcal{H}_\theta\delta\chi_\theta^S+\mathcal{H}_{\text{ϰ}}\delta\,\text{ϰ}_S+\mathcal{I}_{1r}\Upsilon_r^S+\mathcal{I}_{1\theta}\Upsilon_\theta^S+\mathcal{I}_2u_{t,0}^S+\mathcal{I}_3u_{\phi,0}^S+\mathcal{J}=0\,. \quad (4.92)$$

As we have seen in earlier expressions, the quantities $\mathcal{F}_r$, $\mathcal{F}_{\text{ɤ}}$, $\mathcal{G}_r$, $\mathcal{G}_{\text{ɤ}}$, $\mathcal{G}_\theta$, $\mathcal{G}_{\text{ϰ}}$, $\mathcal{H}_r$, $\mathcal{H}_{\text{ɤ}}$, $\mathcal{H}_\theta$, $\mathcal{H}_{\text{ϰ}}$, $\mathcal{I}_{1r}$, $\mathcal{I}_{1\theta}$, $\mathcal{I}_2$, $\mathcal{I}_3$ and $\mathcal{J}$ are all functions of known quantities evaluated on geodesics. Eq. (4.29) becomes

$$\mathcal{Q}_\theta\frac{d^2\delta\chi_\theta^S}{d\lambda^2}+\mathcal{Q}_{\text{ϰ}}\frac{d^2\delta\,\text{ϰ}_S}{d\lambda^2}+S_r\frac{d\delta\chi_r^S}{d\lambda}+\mathcal{S}_{\text{ɤ}}\frac{d\delta\,\text{ɤ}_S}{d\lambda}+\mathcal{S}_\theta\frac{d\delta\chi_\theta^S}{d\lambda}+\mathcal{S}_{\text{ϰ}}\frac{d\delta\,\text{ϰ}_S}{d\lambda}+\mathcal{T}_r\delta\chi_r^S+\mathcal{T}_{\text{ɤ}}\delta\,\text{ɤ}_S$$
$$+\mathcal{T}_\theta\delta\chi_\theta^S+\mathcal{T}_{\text{ϰ}}\delta\,\text{ϰ}_S+\mathcal{U}_{1r}\Upsilon_r^S+\mathcal{U}_{1\theta}\Upsilon_\theta^S+\mathcal{U}_2u_{t,0}^S+\mathcal{U}_3u_{\phi,0}^S+\mathcal{V}=0\,, \quad (4.93)$$

where $\mathcal{Q}_\theta$, $\mathcal{Q}_{\text{ϰ}}$, S_r, $\mathcal{S}_{\text{ɤ}}$, $\mathcal{S}_\theta$, $\mathcal{S}_{\text{ϰ}}$, $\mathcal{T}_r$, $\mathcal{T}_{\text{ɤ}}$, $\mathcal{T}_\theta$, $\mathcal{T}_{\text{ϰ}}$, $\mathcal{U}_{1r}$, $\mathcal{U}_{1\theta}$, $\mathcal{U}_2$, $\mathcal{U}_3$ and $\mathcal{V}$ are all functions of known quantities evaluated on geodesics. We also use $u^\alpha u_\alpha=-1$ to obtain

$$\mathcal{K}_r\frac{d\delta\chi_r^S}{d\lambda}+\mathcal{K}_{\text{ɤ}}\frac{d\delta\,\text{ɤ}_S}{d\lambda}+\mathcal{K}_\theta\frac{d\delta\chi_\theta^S}{d\lambda}+\mathcal{K}_{\text{ϰ}}\frac{d\delta\,\text{ϰ}_S}{d\lambda}+\mathcal{M}_r\delta\chi_r^S+\mathcal{M}_{\text{ɤ}}\delta\,\text{ɤ}_S+\mathcal{M}_\theta\delta\chi_\theta^S+\mathcal{M}_{\text{ϰ}}\delta\,\text{ϰ}_S$$
$$+\mathcal{N}_{1r}\Upsilon_r^S+\mathcal{N}_{1\theta}\Upsilon_\theta^S+\mathcal{N}_2u_{t,0}^S+\mathcal{N}_3u_{\phi,0}^S+\mathcal{P}=0\,, \quad (4.94)$$

where $\mathcal{K}_r$, $\mathcal{K}_{\text{ɤ}}$, $\mathcal{K}_\theta$, $\mathcal{K}_{\text{ϰ}}$, $\mathcal{M}_r$, $\mathcal{M}_{\text{ɤ}}$, $\mathcal{M}_\theta$, $\mathcal{M}_{\text{ϰ}}$, $\mathcal{N}_{1r}$, $\mathcal{N}_{1\theta}$, $\mathcal{N}_2$, $\mathcal{N}_3$ and $\mathcal{P}$ are again all known functions evaluated on geodesics.

We describe $\mathcal{F}_r$, $\mathcal{F}_{\text{ɤ}}$, $\mathcal{G}_r$, $\mathcal{G}_{\text{ɤ}}$, $\mathcal{G}_\theta$, $\mathcal{G}_{\text{ϰ}}$, $\mathcal{H}_r$, $\mathcal{H}_{\text{ɤ}}$, $\mathcal{H}_\theta$, $\mathcal{H}_{\text{ϰ}}$, $\mathcal{I}_{1r}$, $\mathcal{I}_{1\theta}$, $\mathcal{I}_2$, $\mathcal{I}_3$, $\mathcal{J}$, $\mathcal{Q}_\theta$, $\mathcal{Q}_{\text{ϰ}}$, S_r, $\mathcal{S}_{\text{ɤ}}$, $\mathcal{S}_\theta$, $\mathcal{S}_{\text{ϰ}}$, $\mathcal{T}_r$, $\mathcal{T}_{\text{ɤ}}$, $\mathcal{T}_\theta$, $\mathcal{T}_{\text{ϰ}}$, $\mathcal{U}_{1r}$, $\mathcal{U}_{1\theta}$, $\mathcal{U}_2$, $\mathcal{U}_3$, $\mathcal{V}$, $\mathcal{K}_r$, $\mathcal{K}_{\text{ɤ}}$, $\mathcal{K}_\theta$, $\mathcal{K}_{\text{ϰ}}$, $\mathcal{M}_r$, $\mathcal{M}_{\text{ɤ}}$, $\mathcal{M}_\theta$, $\mathcal{M}_{\text{ϰ}}$, $\mathcal{N}_{1r}$, $\mathcal{N}_{1\theta}$, $\mathcal{N}_2$, $\mathcal{N}_3$, and $\mathcal{P}$ using Fourier expansions of the form (4.85). We provide full expressions for these functions in the *Mathematica* notebook in the Supplemental Material for this paper [181]. We insert these expansions along with (4.88), (4.89), (6.33) and (6.34) into (4.92), (4.93) and (4.94). We then solve for the unknown variables $\delta\chi_r^S$, $\delta\,\text{ɤ}_S$, $\delta\chi_\theta^S$, $\delta\,\text{ϰ}_S$, Υ_r^S, Υ_θ^S, u_t^S and u_ϕ^S. This frequency-domain approach therefore naturally allows us to compute the first-order-in-spin corrections to the orbital frequencies Υ_r^S and Υ_θ^S for totally generic orbits of spinning particles.

In Fig. 4.4, we see how Υ_θ converges to its true values as $n_{\max}$ and $k_{\max}$ increase for a reference geodesic that is both inclined and eccentric. In Sec. 4.3.2, the convergence of Υ_θ for nearly circular ($e=0$) orbits is plotted in Fig. 4.2. At all inclinations, at $n_{\max}=2$, the residuals are smaller for the $e=0$ reference orbit than for the slightly eccentric $e=0.1$ reference orbit. For the smallest inclination $I=10^\circ$ (top panel), this difference holds for all $n_{\max}$; the quantities corresponding to a reference geodesic that is both eccentric and inclined (Fig. 4.4) all converge slower than those corresponding to a reference geodesic that is nearly circular and inclined (Fig. 4.2). However, as the inclination is increased, the difference in the rate of convergence between the eccentric and circular cases decreases. At the highest inclination, $I=30^\circ$, they converge at roughly the same rate.

Fig. 4.5 shows an example of r and θ for a generic spinning-body orbit, in addition to the functions $\delta\chi_r^S$, $\delta\chi_\theta^S$, $\delta\,\text{ɤ}_S$ and $\delta\,\text{ϰ}_S$ which go into constructing the orbit's r and θ. In the

two left-hand panels of Fig. 4.5, the reference geodesic orbit associated with this spinning-body orbit is overplotted with a dotted black curve; both the radial and polar frequencies associated with the spinning-body orbit are shifted so that it remains phase-locked with the geodesic reference orbit. In addition, $\mu s/M$ has been chosen to have an unphysically large value of 10 in order to clearly show the effect of spin-curvature coupling on the shape of the orbit.

Figure 4.6 shows how Υ_r^S varies with p for nearly equatorial eccentric orbits, and likewise how Υ_θ^S varies with p for nearly circular inclined orbits. Notice that the spin corrections to the polar Mino-time frequencies Υ_θ^S (bottom left panel) have a different dependence on p compared to the radial Mino-time frequencies Υ_r^S (top left panel). For all spins, we see that the radial correction Υ_r^S increases rapidly near the last stable orbit (LSO). For small values of a, the behavior of Υ_θ^S is similar, increasing as orbits approach the LSO, albeit with a shallower slope. However, for large a ($a > 0.8M$), a different trend emerges. For $a = 0.85M$ and $a = 0.87M$ the curve flattens, with a slight uptick as it approaches the LSO; for $a = 0.89M$ and $a = 0.9M$, the curve reaches a maximum and begins to trend downwards very close to the LSO, as can be seen in the bottom left panel of Fig. 4.6. The dependence of the frequency corrections on a is fairly similar for both Υ_r^S and Υ_θ^S: In both cases, at fixed p, the frequency correction is larger for the smaller value of a. Fig. 4.6 displays coordinate-time frequency corrections Ω_r, Ω_θ and Ω_ϕ for an equatorial orbit (top right panel) and an inclined orbit (bottom right panel).

Fig. 4.7 shows how the corrections to the radial Υ_r^S and polar Υ_θ^S Mino-time frequencies vary with p, e and I when the reference geodesic is both inclined and eccentric. In Fig. 4.7, we see similar trends to those in Fig. 4.6. In the bottom panel of Fig. 4.7, Υ_θ^S increases with decreasing p until it reaches a maximum and then begins to decrease as p approaches the LSO. Increasing the eccentricity of the orbit shifts the maximum Υ_θ^S to a higher value. In the top panel of Fig. 4.7, Υ_r^S increases with decreasing p. Increasing the inclination angle of the orbit leads to a more rapid increase in Υ_r^S as p approaches the LSO.

4.4 Summary and future work

In this chapter, we present a frequency-domain approach for precisely computing the orbits of spinning bodies. This extends the work presented in Chapter 3 by considering completely generic orbits with arbitrarily oriented spin, going beyond the equatorial and nearly equatorial orbits discussed previously. In Sec. 4.2, we outline our perturbative approach to studying spinning-body dynamics both qualitatively and quantitatively, and in Sec. 4.3.1, we describe how we compute spinning-body orbits in the frequency-domain. In Sec. 4.3.2, we discuss the results we obtain using frequency-domain methods; in particular, we compute the corrections to the radial Υ_r^S and polar Υ_θ^S frequencies due to the spin of the orbiting body.

There are several future avenues we plan to explore related to this work. First, we aim to study the role played by nonlinear-in-spin terms near resonance in pushing the spinning-body dynamics from integrable to chaotic via the KAM theorem; this would extend the preliminary investigation in Ref. [164]. Second, we are working on incorporating secondary spin into gravitational waveform models using an osculating geodesic scheme [178], [179]. For example, this method has already been applied to produce spinning-body inspirals for

a Schwarzschild background in Ref. [112]. Our goal is to build a framework for completely generic adiabatic inspirals of spinning bodies.

In addition, we aim to systematically explore and present the orbital frequencies obtained in this work. First, we want to explicitly demonstrate that the frequencies obtained in Ref. [84] are entirely equivalent to those presented in this work. We explicitly show the equivalence of the two approaches for the equatorial spin-aligned case in App. B.2 and we intend to extend this comparison to include frequencies associated with completely generic orbits. Second, we plan to compare with Post-Newtonian results based on the analysis in Refs. [39] and [40] as another validity check of our results. A catalog of these frequencies and how they vary with the parameters describing orbits and the small body's spin orientation is likely to be of use as waveform models for large mass ratio systems are developed and incorporated in gravitational-wave measurement pipelines.

Chapter 5

Extreme mass-ratio inspiral and waveforms for a spinning body into a Kerr black hole via osculating geodesics and near-identity transformations

This chapter is based on work previously published in Physical Review D (Drummond, Lynch, Hanselman, Becker & Hughes, 2024) [131], written in collaboration with Philip Lynch, Alexandra G. Hanselman, Devin R. Becker and Scott A. Hughes.

5.1 Introduction and motivation

The goal of the work that we present here is to show how one can augment adiabatic waveforms to include one particular post-adiabatic effect, the spin-curvature force. We emphasize strongly that our analysis does *not* develop a self-consistent waveform model: we explicitly leave out effects which enter at the same order as the spin-curvature force, but which must be included to have a complete accounting of post-adiabatic effects at this order. Our goal instead is to show how one can combine data and methods that currently exist in order to make inspirals of spinning bodies into Kerr black holes, and to make the waveforms corresponding to such inspirals.

The particular model we develop in this paper treats inspiral as a sequence of geodesic orbits, evolving from geodesic to geodesic under the combined influence of the spin-curvature force and the orbit-averaged self force. This allows us to develop an EMRI model that incorporates the most important qualitative dynamics (four distinct orbit and precession frequencies, as well as strong-field backreaction), and to make a waveform that includes these effects. Other approaches to developing such inspirals would require input that, at present, is not yet ready to be used. For example, one might imagine treating the inspiral worldline as a sequence of spinning-body orbits (following the prescription laid out in Chapters 3 and 4), then evolving through the sequence by computing the orbit-averaged backreaction at each orbit. Although we have a good prescription describing such orbits, we do not yet have large data sets which describe backreaction and wave amplitudes from these orbits (although

the first calculations describing such data have been performed [128]). Indeed, it is not yet fully understood how to compute orbit-averaged backreaction on such orbits (see concluding discussion in Ref. [128]).

The model we construct and present here is arguably the best that can be done for making spinning body inspiral with tools and data that exist right now. We propose it as a first tool that can augment existing methods for making adiabatic inspirals and waveforms. When applied to fast EMRI waveform methods (presently being extended to cover the Kerr parameter space), these waveforms will be useful for science studies assessing the importance of secondary spin for generic spinning-body inspiral. These waveforms will also serve as a benchmark against which later models can be compared as fast and effective methods for incorporating other post-adiabatic effects become broadly available.

Near-identity transformations (NITs) play a crucial role in our waveform construction procedure. Modeling EMRIs with NITs introduces an averaging that significantly reduces computational cost by eliminating the evaluation of forcing terms multiple times per orbit cycle. Previous works had applied this technique to eccentric Schwarzschild inspirals [104], [183] and Kerr inspirals with eccentricity [101], orbital inclination [184], and both [185]. This work marks the first time that effects from the spinning secondary have been folded into this scheme.

5.2 Organization and notation of this chapter

We here provide an outline of the chapter's organization, as well as a summary of the conventions and notation we use throughout. It is worth emphasizing that much of our analysis is based on bringing together techniques that have been presented at length elsewhere. As such, several sections of this paper present just a high-level synopsis of these methods. Several appendices provide detail needed to flesh out the calculations, and summarize material that is presented at length in the references which develop these methods.

Because our analysis is built on bound orbits around Kerr black holes, we briefly review the properties of these orbits in Sec. 5.3. We begin with the geodesic orbits of non-spinning bodies and their parameterization in 5.3.1, and summarize the properties of spinning body orbits in 5.3.2. In Sec. 5.3.3, we discuss why we choose to anchor our analysis to the properties of geodesic orbits, rather than using spinning-body orbits as our main tool. We discuss at some length the rationale behind this choice, and why it will be useful as a complementary approach when future data allow us to use spinning-body orbits for broader studies than is possible right now.

In Sec. 5.4, we briefly describe the osculating geodesic (abbreviated "OG") framework which underlies our inspiral analysis, describing how to map a worldline to a set of geodesics with evolving elements. We lay out the detailed equations we evolve to generate spinning body inspirals in the Appendix C.2. In Sec. 5.4.1, we show how to describe spinning-body orbits as forced geodesics, explicitly demonstrating that this approach yields orbits equivalent to those developed using the frequency-domain method of Chapters 3 and 4. We describe how we incorporate the leading adiabatic backreaction in Sec. 5.4.2.

In Sec. 5.5, we describe the mathematical scheme underlying the near-identity averaging transformation (abbreviated "NIT") in detail. The osculating geodesic (OG) method,

although accurate, becomes increasingly computationally expensive as the number of cycles in an inspiral grows, scaling inversely with the system's mass ratio. The NIT procedure used in Sec. 5.5 introduces an averaging transformation that reduces computational cost while maintaining modeling accuracy. We compare the NIT and OG methods to assess their computational efficiency in modeling EMRIs and benchmark the accuracy of the NIT calculation.

We outline the notation used in this section in Sec. 5.5.1, then discuss Mino-time and Boyer-Lindquist-time formulations of NITs in Secs. 5.5.2 and 5.5.3 respectively. We then present the full set of averaged equations of motion for the specific forcing terms studied in this work in Sec. 5.5.4. We discuss the details of our NIT implementation in Sec. 5.5.5. Additional background and details on the NIT are presented in Appendix C.3, and some important details for how we match the OG and NIT calculations in Appendix C.4.

We present results describing spinning body inspirals in Sec. 5.6, and their associated GWs in Sec. 5.7. We first look at examples of generic (inclined and eccentric) inspirals with aligned secondary spin in Sec. 5.6.1, and then generalize to arbitrarily oriented spin in Sec. 5.6.2. We comment that our study of generic inspiral is presently limited by the paucity of data available describing generic strong-field adiabatic radiation reaction. Though work continues to generate additional such data, we have confined ourselves to the $a = 0.7M$ generic orbit data set that was used in Ref. [26].

We begin our discussion of waveforms from spinning body inspirals by briefly reviewing in Sec. 5.7.1 the general principles used to compute waveforms; greater detail can be found in Ref. [26]. We then examine in Sec. 5.7.2 the waveforms which correspond to the inspirals presented in Sec. 5.6. Of particular physical interest is a comparison of waveforms with and without spinning secondary effects, showing the observable imprint that secondary spin has on the waveform. On a pragmatic level from the standpoint of computations, we also compare waveforms produced with the OG technique versus those using the NIT to generate the trajectory. We show that these waveforms differ very little, though the NIT produces waveforms significantly more quickly.

Throughout this chapter, we use the (fairly standard) convention that lowercase Greek indices on vectors and tensors denote spacetime coordinate indices. Latin indices are used on certain quantities to designate elements of a set that holds parameters which describe orbital elements: capital Latin indices are used for seven-element sets, used for the parameters of OGs; lowercase Latin indices are used for two-, three-, and four-element sets, describing the properties of orbits.

5.3 Bound orbits of Kerr black holes

In our analysis, we approximate inspiral by a sequence of bound orbits, evolving from orbit to orbit under the influence of orbit-averaged GW backreaction. We use GW amplitudes computed at each orbit to describe contributions to the waveform from this inspiral. To set this up, we briefly review the properties of the orbits we use. Additional important technical details have been presented in depth in 2, as well as other papers, such as Refs. [26], [101], [139], [144], [186], so we confine this discussion to a high-level synopsis sufficient to lay out the notation and details we need for the analysis in this chapter.

5.3.1 Orbits of non-spinning bodies

Bound Kerr geodesics can be described using several time parameterizations. The radial and polar motions can both be described using a quasi-Keplerian description, mapping the oscillatory coordinate motion to orbit anomaly angles which increase monotonically with time. We begin by noting that bound geodesic orbits around a Kerr black hole are contained within a torus that lies in the radius range $r_2 \leq r \leq r_1$ and in the polar angle range $\theta_1 \leq \theta \leq (\pi - \theta_1)$. It is very useful to remap the radii r_2 and r_1 using

$$r_1 = \frac{pM}{1-e} , \qquad r_2 = \frac{pM}{1+e} . \tag{5.1}$$

We have introduced p, the orbit's semi-latus rectum, and e, its eccentricity. A geodesic orbit's bounds are then totally set by choosing the parameters p, e, and θ_1. Those parameters can be remapped to integrals of the motion $\hat{E}$ (energy), $\hat{L}_z$ (axial angular momentum), and $\hat{Q}$ (Carter constant) which are related to the spacetime's Killing vectors and Killing tensor, and are conserved along any geodesic. An alternate form of the Carter constant, $\hat{K} \equiv \hat{Q} + (\hat{L}_z - a\hat{E})^2$ is also useful. (The "hat" accents indicate that these conserved quantities are defined on geodesics.) See Refs. [132], [139] for further discussion.

We build the bounds on the radial motion into our parameterization by defining

$$r = \frac{pM}{1 + e\cos\chi_r} . \tag{5.2}$$

The angle χ_r is a relativistic analog of the true anomaly angle commonly used to describe orbital dynamics in Newtonian gravity. We define[1] $\chi_r = \chi_r^F + \chi_r^S$. The "$F$" superscript signifies that χ_r^F evolves on fast timescales, related to the orbital motion; the "S" tells us that χ_r^S evolves on slow timescales, related to the backreaction. For geodesics (i.e., in the absence of forcing terms), χ_r^S is a constant, corresponding to the initial radial phase. We later allow χ_r^S to change with time, accounting for its slow evolution under a perturbing force; see discussion in App. C.2.

The function $R(r)$ defined in Eq. (2.20) is a quartic with four roots ordered such that $r_4 \leq r_3 \leq r_2 \leq r \leq r_1$. For a bound orbit, the roots r_1 and r_2 are the physical turning points of the motion, discussed above; the roots r_3 and r_4 depend in a straightforward way on the orbit parameters p, e, and x_I (see, e.g., Ref. [139] for a form that is commonly used). From the form (2.20), we can write

$$R(r) = (1 - \hat{E}^2)(r_1 - r)(r - r_2)(r - r_3)(r - r_4) , \tag{5.3}$$

where $\hat{E}$ is the orbit's energy introduced above. It is convenient to introduce parameters p_3 and p_4 such that

$$r_3 = \frac{p_3 M}{1-e} , \qquad r_4 = \frac{p_4 M}{1+e} . \tag{5.4}$$

Using this, we write the radial component of the geodesic equation (2.20) as a differential equation for χ_r [187]:

[1] The angle χ_r^S we use in this analysis is equivalent to χ_{r0} in Ref. [26]. In [179], ψ_0 is used to denote the initial radial phase, and is equivalent to our χ_r^S, modulo a minus sign.

$$\frac{d\chi_r}{d\lambda} = \frac{M\sqrt{1-\hat{E}^2}\left[(p-p_3)-e(p+p_3\cos\chi_r)\right]^{1/2}\left[(p-p_4)+e(p-p_4\cos\chi_r)\right]^{1/2}}{1-e^2}$$
$$\equiv X_r^F(\chi_r)\ . \tag{5.5}$$

Remapping the oscillatory radial dynamics onto the monotonically evolving angle χ_r makes the bounded nature of geodesic motion explicit, allowing for straightforward numerical handling of the radial turning points.

Turn now to the polar motion. Defining $z \equiv \cos\theta$, we can write the function $\Theta(\theta)$ from Eq. (**??**) (see also Eq. (2.21)) in terms of roots $0 \leq z_1 \leq 1 \leq z_2$ [144]:

$$\Theta(\theta) = \frac{z_1^2 - z^2}{1-z^2}\left(z_2^2 - a^2(1-\hat{E}^2)z^2\right)\ . \tag{5.6}$$

This form, taken from Ref. [144], has the advantage that it allows for straightforward evaluation in the $a \to 0$ limit. Turning points of the polar motion occur where $z = z_1$, corresponding to when $\theta = \theta_1$ and $\theta = \pi - \theta_1$. The second polar root z_2, given by Eq. (15) in Ref. [144], is not actually reached by physical orbits (it generally corresponds to $\cos\theta > 1$). We define the inclination angle I as

$$I = \pi/2 - \mathrm{sgn}(\hat{L}_z)\theta_1\ ; \tag{5.7}$$

$I = 0$ corresponds to prograde equatorial orbits, $I = 180^\circ$ to retrograde equatorial, and orbital properties vary smoothly between these extremes. We put $x_I \equiv \cos I$, from which we see that $z_1 = \sqrt{1-x_I^2}$. This allows us to parameterize our polar motion as

$$\cos\theta = \sqrt{1-x_I^2}\cos\chi_\theta = \sin I\cos\chi_\theta\ , \tag{5.8}$$

where χ_θ is another relativistic generalization of the "true anomaly" angle used in Newtonian orbital dynamics. As we did for the radial motion, we define[2] $\chi_\theta = \chi_\theta^F + \chi_\theta^S$, breaking this anomaly angle into "fast" and "slow" terms. In the absence of forcing terms, χ_θ^S is a constant, the initial polar phase. In the osculating element framework (see App. C.2), we promote χ_θ^S to a time-varying quantity. Combining the various reparameterizations with the polar geodesic equation (2.21) yields an equation governing χ_θ [144], [187]:

$$\frac{d\chi_\theta}{d\lambda} = \sqrt{z_2^2 - a^2(1-\hat{E}^2)(1-x_I^2)\cos^2\chi_\theta}$$
$$\equiv X_\theta^F(\chi_\theta)\ . \tag{5.9}$$

Bound Kerr geodesics are triperiodic, and can be characterized with frequencies describing the orbit's radial, polar, and axial behavior: the frequencies $\hat{\Upsilon}_{r,\theta,\phi}$ describe an orbit's radial, polar, and axial frequencies per unit Mino time, and $\hat{\Omega}_{r,\theta,\phi}$ describe these frequencies per unit Boyer-Lindquist coordinate time. The Mino-time and coordinate-time frequencies

[2]The angle χ_θ^S is equivalent to $\chi_{\theta 0}$ used in Ref. [26]. In [179], χ_0 is used to denote the initial polar phase, and is equivalent to χ_θ^S in this analysis, modulo a minus sign.

are related by a factor $\hat{\Upsilon}_t$ that describes[3] how much coordinate time accumulates, on average, per unit Mino time along the orbit: $\hat{\Omega}_{r,\theta,\phi} = \hat{\Upsilon}_{r,\theta,\phi}/\hat{\Upsilon}_t$. The inverse of these frequencies, times 2π, gives the Mino- and coordinate-time periods:

$$\hat{\Lambda}_{\phi,\theta,r} = \frac{2\pi}{\hat{\Upsilon}_{\phi,\theta,r}} , \tag{5.10}$$

$$\hat{T}_{\phi,\theta,r} = \frac{2\pi}{\hat{\Omega}_{\phi,\theta,r}} . \tag{5.11}$$

As in our discussion of the constants of motion $\hat{E}$, $\hat{L}_z$, and $\hat{Q}$, the hat accents indicate that these quantities are evaluated on geodesics. See Ref. [139] for formulas describing these frequencies, periods, and the factor $\hat{\Upsilon}_t$.

An action-angle parametrization of geodesic motion is useful for the construction of near-identity transformations in Sec. 5.5. In this formulation, the Mino-time action angles q_r and q_z are chosen as the orbital phases describing the motion in r and z respectively; explicit formulas connecting these angles to motion in their associated coordinate are given in Refs. [139], [144], and are coded into the `KerrGeodesics` package of the Toolkit [148]. We denote by $P_i = \{p, e, x_I\}$ the set of orbital elements. In this form, the geodesic equations of motion are given by

$$\frac{dP_j}{d\lambda} = 0 , \tag{5.12}$$

$$\frac{dq_{r,z}}{d\lambda} = \hat{\Upsilon}_{r,z}(\vec{P}) . \tag{5.13}$$

(Note that $\hat{\Upsilon}_z = \hat{\Upsilon}_\theta$; the period of a complete cycle in θ is identical that of a complete cycle in $z = \cos\theta$.) In other words, for geodesics the elements $\vec{P}$ are constants of motion and the right-hand side of Eq. (5.13) is an orbital frequency determined by $\vec{P}$. As such, the orbital phases[4] have solutions $q_{z,r} = \hat{\Upsilon}_{r,z}\lambda + q^S_{r,z}$, where $q^S_{r,z}$ is the value of that phase when $\lambda = 0$. These phases will evolve on the slow timescale when certain post-geodesic forces are introduced.

Up to initial conditions, a geodesic orbit can be specified by "principal orbital elements." These are either the constants of motion ($\hat{E}$, $\hat{L}_z$, $\hat{Q}$) or the parameters (p, e, x_I) describing the geometry of the orbit. We can convert between ($\hat{E}$, $\hat{L}_z$, $\hat{Q}$) and (p, e, x_I) using mappings given in Refs. [26], [139], [144]. The initial conditions of the orbit are specified by "positional orbital elements" which are (χ^S_r, χ^S_θ, ϕ_0, t_0) in the quasi-Keplerian case and (q^S_r, q^S_z, ϕ_0, t_0) in the action-angle case. In order to find the geodesic trajectories for a particular set of orbital elements $\{p, e, x_I, \chi^S_r, \chi^S_\theta, \phi_0, t_0\}$ or $\{p, e, x_I, q^S_r, q^S_z, \phi_0, t_0\}$, we need only solve differential equations for the radial and polar phases χ_r and χ_θ, i.e., Eqs. (5.5) and (5.9); or for q_r and q_θ, i.e., Eqs. (5.13).

[3] This factor is labeled $\hat{\Gamma}$ in many references [26], [96], [139], [187], to reflect the fact that it represents a conversion between two different notions of time, rather than being related to a periodic aspect of orbital motion. It is however labeled $\hat{\Upsilon}_t$ in much of the NIT literature, and we follow that convention here.

[4] Note that the orbital phases $q_{r,z}$ are identical to the "mean anomaly angles" $w_{r,\theta}$ used in Chapters 3 and 4.

5.3.2 Orbits of spinning bodies

The geodesic orbits discussed above describe the motion of a pointlike body freely falling in spacetime. These equations of motion fundamentally derive from the equation of parallel transport for a freely falling body's 4-momentum:

$$\frac{Dp^\mu}{d\tau} = 0 \ . \tag{5.14}$$

If the body is not pointlike but has some extended structure, this structure will couple to the spacetime in which it moves, changing its trajectory. This coupling can be incorporated into the framework describing the body's motion by replacing the right-hand side of (5.14) with a forcing term reflecting how the body's structure couples to spacetime.

The simplest example of such coupling structure is the body's spin angular momentum. The equation of motion in this case becomes [32], [33], [149]

$$\frac{Dp^\mu}{d\tau} = -\frac{1}{2} R^\mu{}_{\nu\lambda\sigma} u^\nu S^{\lambda\sigma} \ . \tag{5.15}$$

The right-hand side of this equation is the spin-curvature force.

For extreme mass ratio systems, it makes sense to linearize in the spin of the smaller body: taking the smaller body to be a Kerr black hole, terms linear in spin enter the forcing equations at order μ^2, so terms quadratic in spin enter at order μ^4. Linearizing, the equations discussed above simplify to

$$\frac{Du^\mu}{d\tau} = -\frac{1}{2\mu} R^\mu{}_{\nu\lambda\sigma} u^\nu S^{\lambda\sigma} \ , \tag{5.16}$$

$$\frac{DS^\mu}{d\tau} = 0 \ , \tag{5.17}$$

$$u_\mu S^\mu = 0 \ . \tag{5.18}$$

Witzany has proven that these linearized equations can be cast as a Hamiltonian system [84], [188], and thus that the spin-curvature force is conservative. A consequence of this is that the linearized equations admit bound orbits. These orbits can be characterized by energy E, axial angular momentum L_z, and an analog of either the Carter constant Q or $K \equiv Q + (L_z - aE)^2$, much like geodesic orbits[5], though offset from the geodesic values by an amount that is proportional to the secondary spin S. (Note that we do not write these quantities with hat accents, emphasizing that they are offset from their geodesic analogs.) Likewise, these orbits have frequencies $(\Omega_r, \Omega_\theta, \Omega_\phi)$ describing their coordinate motions which differ from the geodesic values by an amount scaling with S. They also have a "precession frequency" Ω_s which describes the precession of the spin.

Chapters 3 and 4 describe in detail how to construct orbits of spinning bodies using a frequency domain technique to solve the linearized equations (5.16)–(5.18). For our purposes,

[5]It is worth emphasizing that the quantities E and L_z can be defined for motion under the complete set of Papapetrou equations, but analogs of Q and K can be found only when these equations are linearized in spin [153]. It has recently been shown that analogs of Q and K can be found for the full equations if one includes the next multipole order in the analysis (the secondary's quadrupole moment), though only if that quadrupole moment takes the values appropriate for a Kerr black hole. See Ref. [93] for further discussion.

a key point is that the resulting motion is similar to geodesic motion, and we can adapt the quasi-Keplerian formulation to describe these orbits. For example, in the general case, the radial and polar motions can be written

$$r = \frac{pM}{1 + e\cos\chi_r} + \delta\,\mathscr{r}_S \,, \tag{5.19}$$

$$\cos\theta = \sin I \cos\chi_\theta + \delta\,\mathscr{z}_S \,. \tag{5.20}$$

These expressions resemble the forms used for geodesic motion, with a few key differences. The anomaly angles χ_r and χ_θ used for spinning-body orbits differ from the angles used to describe geodesics:

$$\chi_r = \chi_r^{\rm SG} + \delta\chi_r^S \,, \quad \chi_\theta = \chi_\theta^{\rm SG} + \delta\chi_\theta^S \,. \tag{5.21}$$

The quantities $\chi_{r,\theta}^{\rm SG}$ are identical to the anomaly angles used for geodesics, but expanded in a Mino-time Fourier series and with the geodesic frequencies $\hat{\Upsilon}_{r,\theta}$ shifted to the frequencies $\Upsilon_{r,\theta}$ appropriate for spinning-body orbits (the superscript "SG" stands for "shifted geodesic"). The terms $\delta\chi_{r,\theta}^S$ are $O(S)$ shifts to the anomaly angles. See Chapters 3 and 4 for details and further discussion. The libration regions for spinning-body orbits also differ from those of geodesics; this difference is encoded in the functions $\delta\,\mathscr{r}_S$ and $\delta\,\mathscr{z}_S$ introduced in Eqs. (5.19) and (5.20). These functions are both $O(S)$, and are both periodic in harmonics of the spinning body frequencies — either the set $(\Upsilon_r, \Upsilon_\theta, \Upsilon_s)$ or $(\Omega_r, \Omega_\theta, \Omega_s)$, depending on which time parameterization is used.

In addition to solutions describing the coordinate-space motion of the smaller body, we need to describe how the orientation of the smaller body's spin evolves over its motion. We use the closed-form solution describing a parallel-transported vector presented in [144]. This solution uses a tetrad, originally developed in Refs. [165]–[167], with legs $\{e_{0\alpha}, e_{1\alpha}, e_{2\alpha}, e_{3\alpha}\}$; expressions for these can be found in Eqs. (48), (50) and (51) of Ref. [144]. The precession phase[6] $\psi_s(\lambda)$ is found by integrating up

$$\frac{d\psi_s}{d\lambda} = \sqrt{K}\left(\frac{(r^2+a^2)\hat{E} - a\hat{L}_z}{\hat{K} + r^2} + a\frac{\hat{L}_z - a(1-z^2)\hat{E}}{\hat{K} - a^2 z^2}\right) \,. \tag{5.22}$$

Although an analytic solution to (5.22) exists for geodesic orbits [144], we find it useful to explicitly integrate this equation numerically as we evolve through a sequence of orbits to make inspirals. In this vein, we comment that the terms on the right-hand side of (5.22) depend on the same orbital elements $\{p, e, x_I, q_r^S q_z^S, \phi_0, t_0\}$ that we use to characterize geodesics. We also note that although these functions are written most cleanly as functions of Mino-time λ, it is straightforward to convert to other time parameterizations.

5.3.3 Which orbits to use?

As discussed at length in the Introduction, our goal is to make a model of spinning body inspiral by supplementing a description of orbits which accurately describes motion on short

[6] Note that this phase was written ψ_p in Chapters 3 and 4, with the subscript p standing for "precession." We change notation here to avoid colliding with the use of subscript p to describe how certain forcing terms introduced later in the paper change an orbit's semi-latus rectum.

timescales with appropriately averaged radiative backreaction which describes how orbits evolve on long timescales. In essence, we want to treat inspiral as a sequence of orbits, with backreaction moving us from orbit to orbit in the sequence.

Which notion of orbits should we use? Since our goal is to make a model for an inspiraling spinning body, it is might seem clear that we should begin with orbits of spinning bodies — use the orbits discussed in Chapters 3 and 4, and evolve from orbit to orbit by computing orbit-averaged GW backreaction on those orbits. Unfortunately, implementing this scheme is not tenable in the short term. Studies of backreaction on generic spinning body orbits have only recently been undertaken [128], and data sets which cover enough parameter space to generate an astrophysically plausible generic inspiral do not yet exist. In addition, issues of principle remain which mean that, even if such data existed, we do not yet completely understand how to evolve from orbit to orbit using the orbit-averaged backreaction. In particular, we do not fully understand how to evolve a spinning body's Carter constant due to gravitational radiation reaction (see concluding discussion in Ref. [128]).

By contrast, computing backreaction on geodesic orbits is now rather straightforward. Large data sets exist describing backreaction for this case, and more data is being generated and made available in order to extend the "Fast EMRI Waveform" (FEW) models [98], [99], [189]. Furthermore, as we describe in more detail in the next section, it is possible to describe spinning body orbits as a sequence of geodesic orbits: we treat the worldline of a spinning body as a sequence of geodesics, with the sequence generated using the forcing terms (5.16)–(5.18).

Because our goal is to make a model describing spinning body inspiral using data and methods available now, the approach we take is to use geodesic orbits forced by a combination of the spin-curvature force and geodesic-averaged GW backreaction. After confirming that spinning body orbits constructed by forcing geodesics with the spin-curvature forcing terms agree with those constructed using the methods described in Chapters 3 and 4, we make spinning body inspirals by combining the spin-curvature force with orbit-averaged backreaction computed along geodesics.

As we discuss in more detail in our conclusions, it will be worthwhile to compare the results we find using this to results found by directly computing backreaction on spinning body orbits, once large data sets exist which make such calculations practical. To facilitate this eventual comparison, we release the *Mathematica* code and data which computes the expressions that we use to make the inspirals we develop here as supplementary material for this manuscript.

5.4 Forced geodesics

In this section, we construct spinning-body inspirals as a sequence of geodesic orbits, using an osculating geodesic (OG) framework to describe the inspiral worldline as a sequence of geodesic orbits. The OG technique generalizes the venerable method of osculating orbits [190]–[192] to relativity [178], [179], [193]. We follow very closely the framework laid out in Ref. [179], which we summarize in Appendix C.2. The key point necessary to understand this calculation is that, as described in Sec. 5.3, both geodesic orbits and the smaller body's

precession are entirely characterized by 7 parameters:

$$\mathcal{E}^A \doteq \{p, e, x_I, q_r^S, q_z^S, \phi_0, t_0\} \ . \tag{5.23}$$

As described at length in Sec. 5.3.1, the subset (p, e, x_I) are a geodesic's "principal orbital elements," and fully characterize the coordinate-space torus which a geodesic occupies. The remaining parameters $(q_r^S, q_z^S, \phi_0, t_0)$ are its "positional orbital elements," and can be regarded as setting the geodesic's initial coordinates on this torus.

The parameters (5.23) are all constants for geodesic motion. The OG framework promotes at least some of these parameters to dynamical variables under the influence of some non-geodesic acceleration a^μ. One can then regard the worldline as a "geodesic" whose parameters $\mathcal{E}^A$ evolve under the influence of this acceleration. See Appendix C.2 for a synopsis of how one develops these evolution equations, and Ref. [179] for a detailed derivation and discussion of the particular frameworks that we use.

We implement two OG schemes: The contravariant quasi-Keplerian formulation discussed in Appendix C.2.1, and the action-angle formulation discussed in Appendix C.2.2. Comparing the results of these two methods is useful for validating our computations. We also compare to the OG codes used in Refs. [101], [184] as an independent check of our implementation. Because of the relevance of the action-angle formulation for applying the near-identity transformation, we focus on this formulation for the remainder of this analysis.

5.4.1 Spinning body orbits as forced geodesics

We begin by demonstrating the equivalence between spinning-body orbits computed using the frequency-domain approach from Chapters 3 and 4 and the forced geodesic approach in this work; see also Appendix C.1 for discussion regarding different ways to parameterize spinning-body motion. First, we compute a spinning-body orbit using the method of Chapters 3 and 4. We select a (p, e, x_I) triplet that defines a geodesic with radial turning points $r_1 = p/(1-e)$ and $r_2 = p/(1+e)$ and polar turning point $z_1 = \sqrt{1-x_I^2}$. We then compute the spinning-body trajectory that has the same turning points (on average) as this geodesic [171], [172]. Note that the turning points of this spinning-body trajectory differ from the corresponding geodesic due to an $\mathcal{O}(S)$ correction, as discussed in Chapters 3 and 4.

Next we compute the same spinning-body trajectory with the OG approach used in this work. In order to do this, we find the triplet (p_{IC}, e_{IC}, x_{IC}) which defines a geodesic orbit with the same initial conditions (coordinate positions and four-velocities) as the spinning-body orbit we computed using the method in Chapters 3 and 4; details of the mapping between the two formulations are in Appendix C.1. We find that OG solutions match for many cycles the corresponding spinning-body orbit computed using the approach of Chapters 3 and 4. In Fig. 5.1, we show two example orbits to demonstrate this. In this figure, solid black curves show the radial motion for a spinning body computed using the OG method. The blue diamond markers show the same orbit computed using the frequency-domain method of Chapters 3 and 4. For reference, we show the orbit of a non-spinning body (red dotted curve) with matching parameters. Figure 5.1 shows that the three orbits agree in orbital phase at early times (left panels). At later times (right panels), the geodesic is completely dephased but the two spinning-body orbits remain matched.

Figure 5.1 also shows that, after many cycles, a slight difference develops between the solid black curves (spinning-body orbits generated via OG) and the blue diamonds (spinning-body orbits generated using the method of Chapters 3 and 4). The two methods are entirely equivalent up to first-order in secondary spin, but not at $O(S^2)$; the differences we see are quadratic in secondary spin (see Appendix C.1 for detailed discussion). In this vein, note that we used a rather non-extreme mass ratio $\varepsilon = 0.1$, far beyond the EMRI regime, in this figure. This "abuse" of the large-mass ratio limit was done in order to make the effects of spin-curvature coupling more apparent to the eye. At mass ratios appropriate for EMRI sources, bearing in mind that scaling as $O(S^2)$ means $O(\varepsilon^4)$, we expect differences to be far less apparent.

5.4.2 Backreaction and inspiral

The leading adiabatic backreaction requires only the orbit-averaged dissipative part of the first-order self force. Flux balance laws allow us to compute this using only knowledge of GW fluxes at the horizon and infinity. Such flux balance laws have the form

$$\left(\frac{d\mathcal{C}}{dt}\right)^{\text{orbit}} = -\left(\frac{d\mathcal{C}}{dt}\right)^{\infty} - \left(\frac{d\mathcal{C}}{dt}\right)^{H} . \tag{5.24}$$

where $\mathcal{C}$ corresponds to a conserved quantity along the geodesic such as E, L_z or Q. We can then calculate the transition of the worldline between each OG using rates of change dE/dt, dL_z/dt, dQ/dt to construct an inspiral.

Note that in this adiabatic construction we omit the conservative first-order self force as well as oscillatory pieces of the dissipative self force; both of these effects are included in Ref. [101]. In computing the GW fluxes, we only include the contribution of the "monopole" term of the secondary's stress-energy tensor, which arises from the smaller body's mass. We thus omit the impact of the "dipole" term to this stress-energy, which arises from the smaller body's spin, and is included in Refs. [124], [126]. Including effects which we neglect are natural points for further development and future work.

As described in Sec. 2.3.2, the rates of change of energy dE/dt at infinity and at the horizon are given by [175]

$$\left(\frac{dE}{dt}\right)^{\infty} = \sum_{lmkn} \frac{\left|Z^{\infty}_{lmkn}\right|^2}{4\pi\omega^2_{mkn}} , \tag{5.25}$$

$$\left(\frac{dE}{dt}\right)^{H} = \sum_{lmkn} \frac{\alpha_{lmkn}\left|Z^{H}_{lmkn}\right|^2}{4\pi\omega^2_{mkn}} ; \tag{5.26}$$

the corresponding rates of change of angular momentum dL_z/dt are [175]

$$\left(\frac{dL_z}{dt}\right)^{\infty} = \sum_{lmkn} \frac{m\left|Z^{\infty}_{lmkn}\right|^2}{4\pi\omega^3_{mkn}} , \tag{5.27}$$

$$\left(\frac{dL_z}{dt}\right)^{H} = \sum_{lmkn} \frac{\alpha_{lmkn} m\left|Z^{H}_{lmkn}\right|^2}{4\pi\omega^3_{mkn}} . \tag{5.28}$$

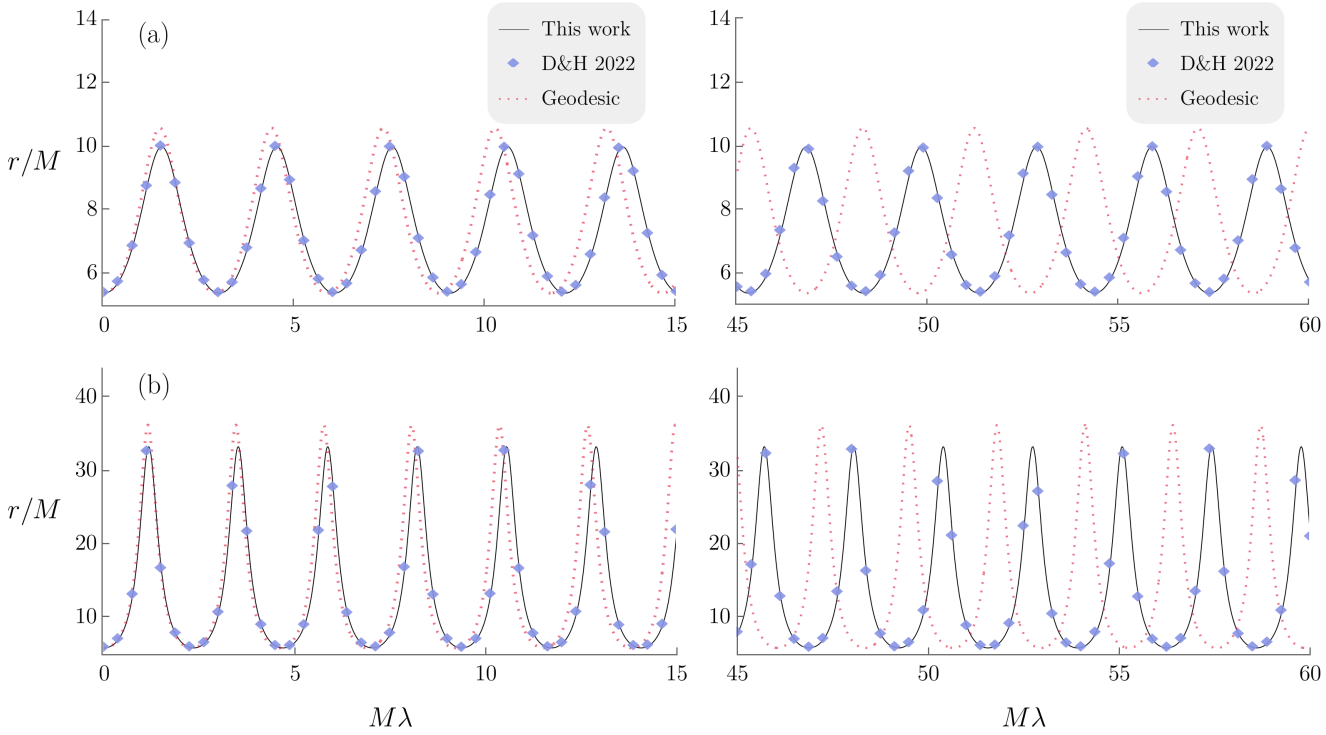

Figure 5.1: Comparison between spinning-body orbits computed using the OG approach in this work (solid black), spinning-body orbits computed using the frequency-domain approach in Chapters 3 and 4 (blue diamond markers), and a geodesic, non-spinning orbit with the same parameters (dotted red). The orbit shown in the top panels (a) has initial parameters given by $a = 0.7M$, $p_{IC} = 7.138$, $e_{IC} = 0.326$, and $x_{IC} = 0.966$ while the orbit shown in the bottom panels has initial parameters given by $a = 0.5M$, $p_{IC} = 10.122$, $e_{IC} = 0.721$, and $x_{IC} = 0.966$. The "IC" subscript indicates that these are "matched initial conditions" orbital parameters: the geodesic orbit defined by the triplet (p_{IC}, e_{IC}, x_{IC}) (plotted with the red dashed line) has the same initial conditions as the spinning-body orbit (plotted with the black solid line). There is also a "matched turning point" description of orbital parameters used in Chapters 3 and 4, where the geodesic defined by (p_{TP}, e_{TP}, x_{TP}) and the corresponding spinning-body orbit have matched turning points. For completeness, the "matched turning point" orbital elements for the two spinning-body orbits pictured here are: ($p_{TP} = 7$, $e_{TP} = 0.3$, $x_{TP} = 0.966$) for the top panels and ($p_{TP} = 10$, $e_{TP} = 0.7$, $x_{TP} = 0.966$) for the bottom panels. See Appendix C.1 for further details. The system has mass ratio $\varepsilon = 10^{-1}$; the small body's spin vector has $s = 1$ and $s_{\parallel} = s$. Note that this mass ratio is rather far from the EMRI limit; we use this value here to make the effects of spin-curvature coupling more apparent to the eye.

The coefficients $Z^{\infty,H}_{lmkn}$ are obtained by integrating homogeneous solutions of the separated radial Teukolsky equation against this equation's source term. See Sec. 2.3.1 of this thesis, as well as Sec. III of Ref. [26] for further details of this calculation. Eq. (6.1.2) gives the expression for α_{lmkn}. The mode frequency ω_{mkn} is related to the geodesic frequencies by

$$\omega_{mkn} = m\hat{\Omega}_\phi + k\hat{\Omega}_\theta + n\hat{\Omega}_r \ . \tag{5.29}$$

Contributions to the rate of change of the Carter constant Q similarly involve contributions from fields at infinity and fields on the horizon:

$$\left(\frac{dQ}{dt}\right)^\infty = \sum_{lmkn} |Z^\infty_{lmkn}|^2 \, \frac{\mathcal{L}_{mkn} + k\hat{\Upsilon}_\theta}{2\pi\omega^3_{mkn}} \ , \tag{5.30}$$

$$\left(\frac{dQ}{dt}\right)^H = \sum_{lmkn} \alpha_{lmkn} \left|Z^H_{lmkn}\right|^2 \, \frac{\mathcal{L}_{mkn} + k\hat{\Upsilon}_\theta}{2\pi\omega^3_{mkn}} \ . \tag{5.31}$$

where

$$\mathcal{L}_{mkn} = m\langle \cot^2\theta \rangle \hat{L}_z - a^2\omega_{mkn}\langle \cos^2\theta \rangle \hat{E} \ . \tag{5.32}$$

Here, $\langle f(\theta) \rangle$ denotes a particular averaging with respect to the orbital motion of functions of θ, defined in Eq. (2.82). It is straightforward to convert from rates of change of the constants of motion $(\hat{E}, \hat{L}_z, \hat{Q})$ to those of the orbital elements (p, e, x_I) which is the form we use in this article. See Appendix B of Ref. [26] for the explicit conversion between the two rates of change.

5.5 Near identity transformations

The OG framework described in the previous section is computationally expensive, requiring us to evaluate forcing terms multiple times per orbit cycle. The computational cost associated with this approach thus grows with the number of orbits, scaling inversely with the system's mass ratio. Near-identity transformations (NITs) have proven to be powerful tools for modeling EMRI systems [101], [104], [184], [185] by introducing an averaging that makes it possible to include inspiral physics without needing to track the system's cycle-by-cycle orbital-time dynamics, substantially reducing the model's computational cost. NITs are an established mathematical procedure [194], used in celestial mechanics and other domains, that averages a system's short timescale behaviour while preserving the secular evolution on longer timescales. In this section, we describe how to apply NITs to model the inspiral of spinning bodies, substantially reducing the computational cost of making such models. In our results (Secs. 5.6 and 5.7), we show that this reduction in computational cost does not involve a loss of modeling accuracy.

5.5.1 NIT background: Notation and generalities

We begin by introducing important notation and definitions which will be used throughout this section. Certain sets of related quantities will be organized into "vectors," denoted with an overarrow. For example, the set of principal orbital elements are organized into

a vector $\vec{P} = (p, e, x_I)$, the phases into $\vec{q} = (q_r, q_z)$, and extrinsic quantities $\vec{\mathcal{X}} = (t, \phi)$. As introduced in Sec. 5.3.2, we denote spin-precession phase by ψ_s. It is also useful to define a vector containing both orbital and spin phases: $\vec{Q} = (q_r, q_z, \psi_s)$. Finally, it will be useful later, particularly when we begin to construct waveforms, to refer to the complete set of phases including the azimuthal phase. We denote this set $\vec{\mathcal{Q}} = (q_r, q_z, \psi_s, \phi)$. (Notice that these "vectors" do not have a consistent number of components.) Figure 5.2 displays a schematic of the osculating orbit set-up we use in this analysis.

The NIT of a quantity A will be denoted by $\tilde{A}$ and defined by the form

$$\tilde{A} = A + \varepsilon \mathcal{A}^{(1)} + \varepsilon^2 \mathcal{A}^{(2)} + \mathcal{O}(\varepsilon^3) \,, \tag{5.33}$$

where the transformation functions $\mathcal{A}^{(n)}$ are required to be smooth, periodic functions of the orbital phases $\vec{q}$. The transformation functions introduced in this section are: $Y_j^{(n)}$, used to effect the NIT of the vector $\vec{P}$; $X_i^{(n)}$, used for the phase $\vec{q}$; $W_s^{(n)}$, used for the spin-precession phase ψ_s; and $Z_k^{(n)}$, used for the extrinsic quantities $\vec{\mathcal{X}}$. The superscript (n) indicates the term appears at n-th order in the expansion in mass ratio ε. After undergoing the NIT, these quantities are denoted with two accents, a tilde denoting the NIT, and the overarrow as our vector shorthand for these sets. For example, $\vec{\tilde{P}}$ denotes the set of transformed principal orbit elements $(\tilde{p}, \tilde{e}, \tilde{x}_I)$.

It will sometimes be useful to decompose functions into a Fourier series. We use the convention

$$A(\vec{P}, \vec{Q}) = \sum_{\vec{\kappa} \in \mathbb{Z}^{j_{\max}}} A_{\vec{\kappa}}(\vec{P}) e^{i\vec{\kappa}\cdot\vec{Q}} \,, \tag{5.34}$$

where $j_{\max}$ is the number of phases, and $\vec{\kappa}$ is a vector of integers with $j_{\max}$ components. Any component of $\vec{\kappa}$ which attaches to the spin phase runs over the set -1, 0, 1; the other components run formally from $-\infty$ to ∞. The dot product used in the exponent is the usual Euclidean, Cartesian one: $\vec{\kappa}\cdot\vec{Q} = \kappa_i Q_j \delta_{ij}$, where δ_{ij} is the identity. Using this Fourier series, we can split $A(\vec{P}, \vec{Q})$ into an averaged piece $\langle A \rangle (\vec{P})$ given by

$$\begin{aligned} \langle A \rangle (\vec{P}) &= A_{\vec{0}}(\vec{P}) \\ &= \frac{1}{(2\pi)^{j_{\max}}} \int \cdots \int_{\vec{Q}} A(\vec{P}, \vec{Q}) \, dq_1 \ldots dq_{j_{\max}} \,, \end{aligned} \tag{5.35}$$

and an oscillating piece given by

$$\breve{A}(\vec{P}, \vec{Q}) = A(\vec{P}, \vec{q}) - \langle A \rangle (\vec{P}) = \sum_{\vec{\kappa} \neq \vec{0}} A_{\vec{\kappa}}(\vec{P}) e^{i\vec{\kappa}\cdot\vec{Q}} \,. \tag{5.36}$$

Note that the Greek subscript with a vector accent (e.g., $A_{\vec{\kappa}}$) indicates a Fourier index, in contrast to a Latin subscript with no vector accent (e.g., A_j), which denotes a component of the vector.

5.5.2 Mino-time formulation

We begin by writing down the form of the equations that we want to average. First observe that the rate of change of the spin phase is given by (5.22). We define the right-hand side

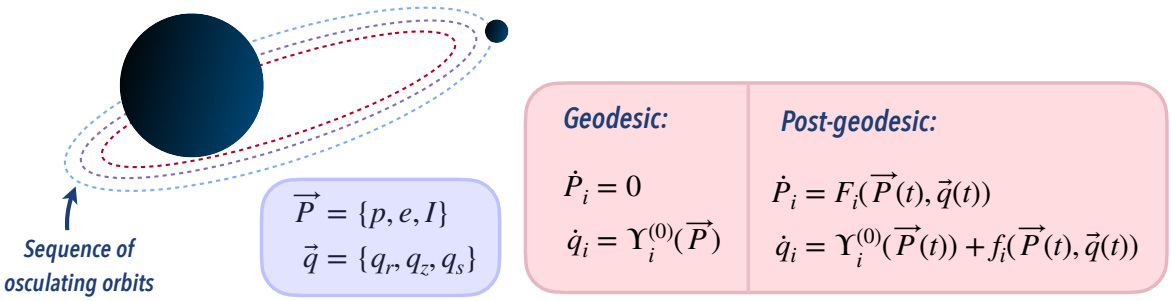

Figure 5.2: *Left.* Each osculating orbit is labeled by a set of constant parameters $\vec{P}$. A geodesic orbit has three associated phases denoted by the vector $\vec{q}$. *Right.* We use an action-angle formulation to describe the small body's orbital dynamics; in the geodesic limit, the time derivative of the angle variables $\dot{q}_i$ is equal to the frequencies Υ_i, while the parameters P_i are constant. When a post-geodesic effect is included, phase-dependent corrections F_i and f_i are added to the action-angle equations. This can be expressed as evolution through a sequence of osculating geodesic orbits $\{\vec{P}(t), \vec{q}(t)\}$.

of this equation as $f_s^{(0)}$:

$$\begin{aligned}\frac{d\psi_s}{d\lambda} &= \sqrt{\hat{K}}\left(\frac{(r^2+a^2)\hat{E} - a\hat{L}_z}{\hat{K}+r^2} + a\frac{\hat{L}_z - a(1-z^2)\hat{E}}{\hat{K}-a^2z^2}\right) \\ &\equiv f_s^{(0)} \ . \end{aligned} \tag{5.37}$$

The phase ψ_s has an analytic solution in the form

$$\psi_s = \Upsilon_s^{(0)}\lambda + \psi_{sr}(q_r) + \psi_{sz}(q_z) \ , \tag{5.38}$$

where $\Upsilon_s^{(0)}$ is the Mino-time spin frequency. (We add the superscript (0) to the various Mino-time geodesic frequencies when they are used in the NIT context, to emphasize that they do not include information about the secondary at $O(\varepsilon)$ or higher.) Expressions for $\psi_{sr}(q_r)$ and $\psi_{sz}(q_z)$ can be found in Eqs. (57) and (58) of Ref. [144] where they are denoted $\psi_r(q_r)$ and $\psi_z(q_z)$.

To post-adiabatic order, the equations of motion of the system can be written schematically as

$$\frac{dP_j}{d\lambda} = \varepsilon F_j^{(1)}(\vec{P}, \vec{q}, \psi_s) + \varepsilon^2 F_j^{(2)}(\vec{P}, \vec{q}, \psi_s) \ , \tag{5.39a}$$

$$\frac{dq_i}{d\lambda} = \Upsilon_i^{(0)}(\vec{P}) + \varepsilon f_i^{(1)}(\vec{P}, \vec{q}, \psi_s) \ , \tag{5.39b}$$

$$\frac{d\psi_s}{d\lambda} = f_s^{(0)}(\vec{P}, \vec{q}) \ , \tag{5.39c}$$

$$\frac{d\mathcal{X}_k}{d\lambda} = f_k^{(0)}(\vec{P}, \vec{q}) \ . \tag{5.39d}$$

Here, the forcing terms are given by

$$F_j^{(1)} = F_{j,\mathrm{GSF}}^{(1)}(\vec{P}, \vec{q}) + sF_{j,\mathrm{SCF}}^{(1)}(\vec{P}, \vec{q}, \psi_s) \ , \tag{5.40a}$$

$$f_i^{(1)} = f_{i,\mathrm{GSF}}^{(1)}(\vec{P},\vec{q}) + s f_{i,\mathrm{SCF}}^{(1)}(\vec{P},\vec{q},\psi_s)\ , \tag{5.40b}$$

$$F_j^{(2)} = F_{j,\mathrm{GSF}}^{(2)}(\vec{P},\vec{q})\ , \tag{5.40c}$$

where s is the spin of the secondary scaled such that $\|s\| \leq 1$ as discussed in Sec. 5.3.2. The terms $F_{i,\mathrm{GSF}}$ and $f_{i,\mathrm{GSF}}$ are due to the gravitational self-force, while $F_{i,\mathrm{SCF}}$ and $f_{i,\mathrm{SCF}}$ are due to the spin-curvature force. It is worth remarking that although these terms are derived from the gravitational self force and the spin-curvature force, they are not identical to these forces; they are essentially projections of certain components of these forces.

The averaged variables, $\tilde{P}_j$, $\tilde{q}_i$, $\tilde{\psi}_s$, and $\tilde{\mathcal{X}}_k$, are related to the OG variables P_j, q_i, ψ_s, and $\mathcal{X}_k$ via

$$\tilde{P}_j = P_j + \varepsilon Y_j^{(1)}(\vec{P},\vec{q},\tilde{\psi}_s) + \varepsilon^2 Y_j^{(2)}(\vec{P},\vec{q},\tilde{\psi}_s) + \mathcal{O}(\varepsilon^3)\ , \tag{5.41a}$$

$$\tilde{q}_i = q_i + \varepsilon X_i^{(1)}(\vec{P},\vec{q},\tilde{\psi}_s) + \varepsilon^2 X_i^{(2)}(\vec{P},\vec{q}\,,\tilde{\psi}_s) + \mathcal{O}(\varepsilon^3), \tag{5.41b}$$

$$\tilde{\psi}_s = \psi_s + W_s^{(0)}(\vec{P},\vec{q}) + \varepsilon W_s^{(1)}(\vec{P},\vec{q}\,,\tilde{\psi}_s) + \mathcal{O}(\varepsilon^2), \tag{5.41c}$$

$$\tilde{\mathcal{X}}_k = \mathcal{X}_k + Z_k^{(0)}(\vec{P},\vec{q}) + \varepsilon Z_k^{(1)}(\vec{P}\,,\vec{q}) + \mathcal{O}(\varepsilon^2). \tag{5.41d}$$

As noted previously, the transformation functions $Y_j^{(n)}$, $X_i^{(n)}$, $W_s^{(n)}$, and $Z_k^{(n)}$ are smooth, periodic functions of the orbital phases $\vec{Q}$. At leading order, Eqs. (5.41) are identity transformations for P_j and q_i, but not for $\mathcal{X}_k$ and ψ_s due to the presence of zeroth-order transformation terms $Z_k^{(0)}$ and $W_s^{(0)}$ respectively. Details about the derivation of Mino-time quantities are given in Appendix C.3.1 and a summary of relevant Mino-time definitions can be found in Appendix C.3.2.

In summary, the equations of motion for the averaged variables $\tilde{P}_j, \tilde{q}_i$, $\tilde{\psi}_s$, and $\tilde{\mathcal{X}}_k$ take the form

$$\frac{d\tilde{P}_j}{d\lambda} = \varepsilon \tilde{F}_j^{(1)}(\vec{\tilde{P}}) + \varepsilon^2 \tilde{F}_j^{(2)}(\vec{\tilde{P}}) + \mathcal{O}(\varepsilon^3)\ , \tag{5.42a}$$

$$\frac{d\tilde{q}_i}{d\lambda} = \Upsilon_i^{(0)}(\vec{\tilde{P}}) + \varepsilon \Upsilon_i^{(1)}(\vec{\tilde{P}}) + \mathcal{O}(\varepsilon^2)\ , \tag{5.42b}$$

$$\frac{d\tilde{\psi}_s}{d\lambda} = \Upsilon_s^{(0)}(\vec{\tilde{P}}) + \mathcal{O}(\varepsilon)\ , \tag{5.42c}$$

$$\frac{d\tilde{\mathcal{X}}_k}{d\lambda} = \Upsilon_k^{(0)}(\vec{\tilde{P}}) + \varepsilon \Upsilon_k^{(1)}(\vec{\tilde{P}}) + \mathcal{O}(\varepsilon^2)\ . \tag{5.42d}$$

The explicit forms for $\tilde{F}_j^{(1)}$, $\tilde{F}_j^{(2)}$, $\Upsilon_i^{(1)}$ and $\Upsilon_k^{(1)}$ can be found in Appendix C.3.2.

Crucially, the NIT equations of motion 5.42 are independent of the orbital phases $\vec{Q}$, meaning these differential equations are fast to evaluate. Another crucial point is that, in the extreme mass ratio limit $\varepsilon \to 0$, the solutions to the NIT equations 5.42 tend to the solutions for OG equations 5.39.

5.5.3 Boyer-Lindquist-time formulation

The above equations of motion 5.42 are parameterized in terms of Mino time λ. It is significantly more convenient for waveform generation purposes to have equations of motion

parameterized in terms of Boyer-Lindquist time. Thus, we perform a second averaging transformation as first outlined in Ref. [163] and implemented in Refs. [184], [185].

We relate the Mino-time averaged variables $\vec{\tilde{P}} = (\tilde{p}, \tilde{e}, \tilde{x}_I)$ and $\vec{\tilde{\mathcal{Q}}} = (\tilde{q}_r, \tilde{q}_z, \tilde{\psi}_s, \tilde{\phi})$ to the Boyer-Lindquist-time averaged variables $\vec{\mathcal{P}} = (p_\varphi, e_\varphi, x_\varphi)$ and $\vec{\varphi} = (\varphi_r, \varphi_z, \varphi_s, \varphi_\phi)$ via:

$$\mathcal{P}_j = \tilde{P}_j + \varepsilon \Pi_j^{(1)}(\vec{\tilde{P}}, \vec{\tilde{q}}) + \varepsilon^2 \Pi_j^{(2)}(\vec{\tilde{P}}, \vec{\tilde{q}}) + \mathcal{O}(\varepsilon^3) \,, \tag{5.43a}$$

$$\varphi_i = \tilde{\mathcal{Q}}_i + \Delta\varphi_i + \varepsilon \Psi_i^{(1)}(\vec{\tilde{P}}, \vec{\tilde{q}}) + \mathcal{O}(\varepsilon^2) \,, \tag{5.43b}$$

where the purely oscillatory term $\Delta\varphi_i = \Omega_i^{(0)}(\vec{\tilde{P}})\Delta t^{(0)}$ and $\Omega_i^{(0)}$ is the Boyer-Lindquist fundamental frequency of the tangent geodesic.

To obtain the equations of motion for $\vec{\mathcal{P}}$ and $\vec{\varphi}$, we take the time derivative of Eq. (5.43), substitute the expression for the NIT equations of motion, and then use the inverse transformation of Eq. (5.43) to ensure that all functions are expressed in terms of $\vec{\tilde{P}}$ and $\vec{\tilde{q}}$. We then expand order by order in ε. We chose the oscillatory functions Δt, $\Psi_i^{(1)}$, $\Pi_j^{(1)}$, and $\Pi_j^{(2)}$ in order to cancel out any oscillatory terms that appear at each order in ε. This results in averaged equations of motion that take the following form:

$$\frac{d\mathcal{P}_j}{dt} = \varepsilon \Gamma_j^{(1)}(\vec{\mathcal{P}}) + \varepsilon^2 \Gamma_j^{(2)}(\vec{\mathcal{P}}) + \mathcal{O}(\varepsilon^3) \,, \tag{5.44a}$$

$$\frac{d\varphi_\alpha}{dt} = \Omega_\alpha^{(0)}(\vec{\mathcal{P}}) + \varepsilon \Omega_\alpha^{(1)}(\vec{\mathcal{P}}) + \mathcal{O}(\varepsilon^2) \,. \tag{5.44b}$$

These equations of motion are related to the Mino time averaged equations of motion (5.42) with the adiabatic terms given by

$$\Gamma_j^{(1)} = \frac{\tilde{F}_j^{(0)}}{\Upsilon_t^{(0)}} \,, \quad \Omega_\alpha^{(0)} = \frac{\Upsilon_\alpha^{(0)}}{\Upsilon_t^{(0)}} \,, \tag{5.45a-b}$$

and the post-adiabatic terms given by

$$\Gamma_j^{(2)} = \frac{1}{\Upsilon_t^{(0)}} \left(\tilde{F}_j^{(2)} + \tilde{F}^{(1)} \frac{\partial}{\partial P_j} \left\langle \Pi_j^{(1)} \right\rangle - \left\langle f_t^{(0)} \Pi_k^{(1)} \right\rangle \frac{\partial \Gamma_j^{(1)}}{\partial P_k} - \Upsilon_t^{(1)} \Gamma_j^{(1)} \right) \,, \tag{5.46a}$$

$$\Omega_\alpha^{(1)} = \frac{1}{\Upsilon_t^{(0)}} \left(\Upsilon_\alpha^{(1)} - \left\langle f_t^{(0)} \Pi_k^{(1)} \right\rangle \frac{\partial \Omega_\alpha^{(0)}}{\partial P_k} - \Upsilon_t^{(1)} \Omega_\alpha^{(0)} \right) \,. \tag{5.46b}$$

This constrains the oscillating pieces of our transformation to be

$$\Delta t = \sum_{\kappa \neq 0} \frac{f_{t,\vec{\kappa}}^{(0)}}{-i\vec{\kappa} \cdot \vec{\Upsilon}^{(0)}} = -\breve{Z}_t^{(0)} \,, \breve{\Pi}_j^{(1)} = \sum_{\kappa \neq 0} \frac{f_{t,\vec{\kappa}}^{(0)}}{-i\vec{\kappa} \cdot \vec{\Upsilon}^{(0)}} \Gamma_j^{(1)} = -\breve{Z}_t^{(0)} \Gamma_j^{(1)} \,, \text{ and} \tag{5.47a}$$

$$\begin{aligned} \Psi_{\alpha,\vec{\kappa}}^{(1)} = & \frac{i}{\vec{\kappa} \cdot \vec{\Upsilon}^{(0)}} \left(\frac{\partial \Delta\varphi_{\alpha,\vec{\kappa}}}{\partial P_j} \tilde{F}_j^{(1)} - \frac{f_{t,\vec{\kappa}}^{(0)}}{\Upsilon_t^{(0)}} \Upsilon_t^{(1)} \Omega_t^{(0)} + \sum_{\vec{\kappa}' \neq \vec{0}} \left[\left(i\vec{\kappa}' \cdot \vec{X}_{\vec{\kappa}-\vec{\kappa}'}^{(1)} f_{t,\vec{\kappa}'}^{(0)} + Y_{j,\vec{\kappa}-\vec{\kappa}'}^{(1)} \frac{\partial f_{t,\vec{\kappa}'}^{(0)}}{\partial P_j} \right) \Omega_\alpha^{(0)} \right. \right. \\ & \left. \left. - \Pi_{j,\vec{\kappa}-\vec{\kappa}'}^{(1)} f_{t,\vec{\kappa}'}^{(0)} \frac{\partial \Omega_\alpha^{(0)}}{\partial P_j} \right] \right) \,. \end{aligned} \tag{5.47b}$$

We are free to chose the averaged pieces of $\Pi_j^{(1)}$, and we make the simplification that $\left\langle \Pi_j^{(1)} \right\rangle = 0$. With this and the identity $\left\langle f_t^{(0)} (\int f_t^{(0)} d\vec{q}) \right\rangle = 0$, we get the simplification $\left\langle f_t^{(0)} \Pi_j^{(1)} \right\rangle = 0$. The expressions for $\Gamma_j^{(2)}$ and $\Omega_\alpha^{(1)}$ then simplify to

$$\Gamma_j^{(2)} = \frac{1}{\Upsilon_t^{(0)}} \left(\tilde{F}_j^{(2)} - \Upsilon_t^{(1)} \Gamma_j^{(1)} \right) , \tag{5.48a}$$

$$\Omega_\alpha^{(1)} = \frac{1}{\Upsilon_t^{(0)}} \left(\Upsilon_\alpha^{(1)} - \Upsilon_t^{(1)} \Omega_\alpha^{(0)} \right) . \tag{5.48b}$$

A useful aspect of these equations of motion is that their solutions $\vec{\mathcal{P}}(t)$ and $\vec{\varphi}(t)$ are exactly what is required to feed into waveform generating schemes, as shown in Appendix B of [185]. Once these solutions are constructed, it is then straightforward to augment adiabatic waveform construction schemes [26], [98], [99] to include the post-adiabatic effects these solutions describe. It is also worth noting that the additional averaging associated with Boyer-Lindquist time could be circumvented by using closed-form expressions for the geodesic orbits in terms of action angles associated with Boyer-Lindquist frequencies, i.e., $\vec{\varphi}$. This has been achieved already for bound orbits in Schwarzschild spacetime via a small eccentricity expansion [195].

5.5.4 Averaged spinning-body equations of motion

In the previous sections, we derived equations of motion to post-adiabatic order by assuming that the gravitational self-force is known to $O(\varepsilon^2)$. As of now, it is only feasible to mass produce data describing the leading-order dissipative radiation reaction via flux balance laws (and this has only been done so far for a fairly limited range of parameters). Although tools exist to compute more of the first-order GSF [100], doing so is computationally expensive, and the second-order GSF for generic Kerr remains far off. This means that we set the second-order corrections to zero, $F_{j,\mathrm{GSF}}^{(2)} = 0$, and we have no conservative contributions from the self-force, $f_{i,\mathrm{GSF}}^{(1)} = 0$. The other force driving the evolution is the spin-curvature force which has no dissipative effects. As such, its orbit average is zero and so the terms which change the principal orbit elements, $F_{j,\mathrm{SCF}}^{(1)}$, vanish on average: $\left\langle F_{j,\mathrm{SCF}}^{(1)} \right\rangle = 0$. The resulting averaged equations of motion parameterized in Mino-time λ are given by:

$$\frac{d\tilde{p}}{d\lambda} = \varepsilon \tilde{F}_p^{(1)}(\tilde{p}, \tilde{e}, \tilde{x}_I) , \tag{5.49}$$

$$\frac{d\tilde{e}}{d\lambda} = \varepsilon \tilde{F}_e^{(1)}(\tilde{p}, \tilde{e}, \tilde{x}_I) , \tag{5.50}$$

$$\frac{d\tilde{x}_I}{d\lambda} = \varepsilon \tilde{F}_x^{(1)}(\tilde{p}, \tilde{e}, \tilde{x}_I) , \tag{5.51}$$

$$\frac{d\tilde{q}_r}{d\lambda} = \Upsilon_r^{(0)}(\tilde{p}, \tilde{e}, \tilde{x}_I) + \varepsilon s \Upsilon_r^{(1)}(\tilde{p}, \tilde{e}, \tilde{x}_I) , \tag{5.52}$$

$$\frac{d\tilde{q}_z}{d\lambda} = \Upsilon_z^{(0)}(\tilde{p}, \tilde{e}, \tilde{x}_I) + \varepsilon s \Upsilon_z^{(1)}(\tilde{p}, \tilde{e}, \tilde{x}_I) , \tag{5.53}$$

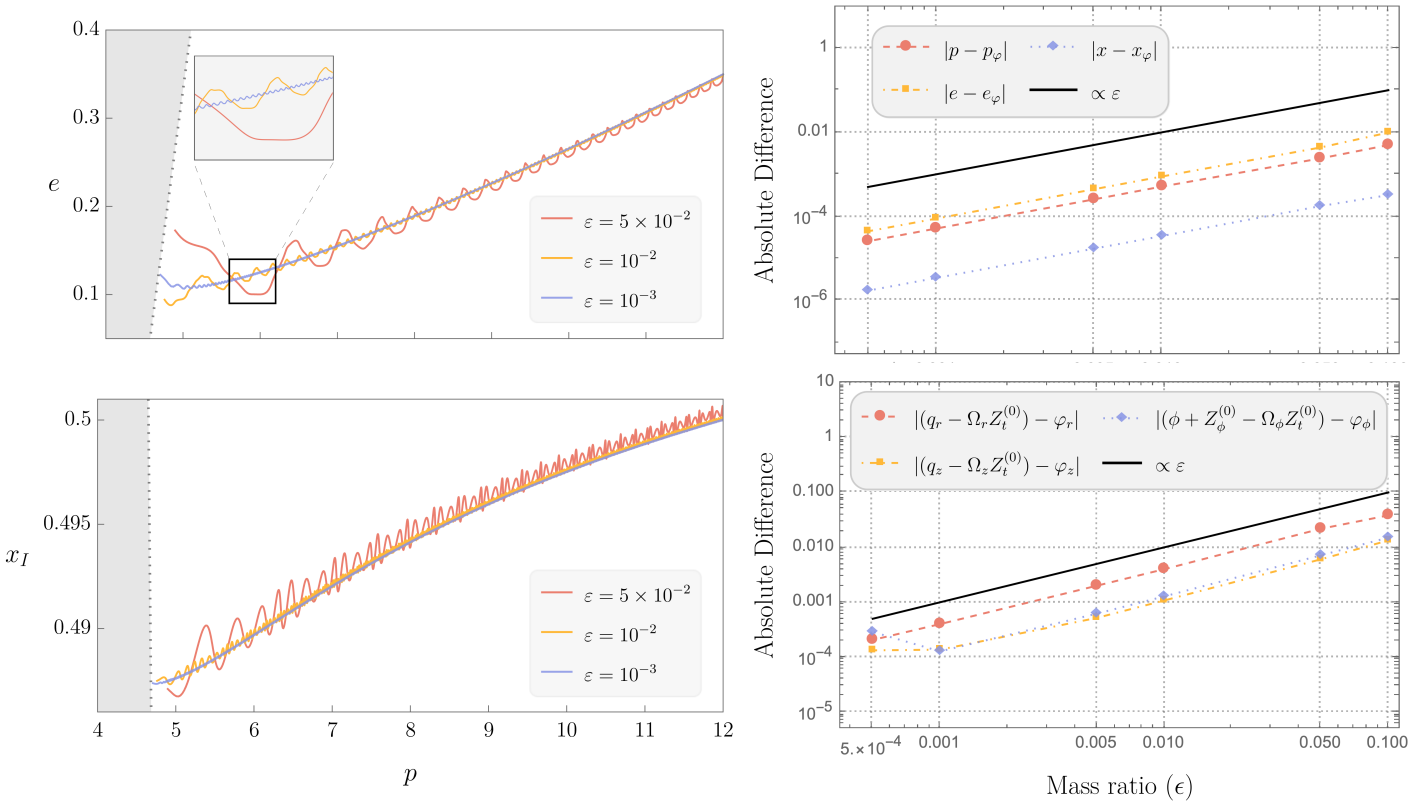

Figure 5.3: Spinning-body inspiral for different mass ratios. Left-hand panels show inspirals obtained using the OG equations of motion for mass ratios $\varepsilon = 5 \times 10^{-2}$ (red; large oscillations), $\varepsilon = 10^{-2}$ (yellow; medium oscillations) and $\varepsilon = 10^{-3}$ (blue, small oscillations). We again note that these mass ratios are larger than those expected for EMRI systems, and are used here in order to amplify the impact of spin-curvature coupling for visual purposes. The initial parameters used are $p = 12$, $e = 0.35$, $x_I = 0.5$, $q_r = 0$, and $q_z = 0$. Right-hand panels show the absolute difference in orbital elements of a spinning-body inspiral comparing the OG and NIT methods; NIT orbital elements are labeled with subscript φ. In these right-hand panels, we initially set $e = 0.22$, $x_I = 0.699$, $q_r = 0$, and $q_z = 0$. Data shown corresponds to the system evolving from $p = 9.45$ to $p = 9$. As expected, the absolute differences track with the ε curve (solid, black). For all data in this figure, the small body orbits a black hole with spin $a = 0.7M$ and the magnitude and orientation of the small body's spin is specified by $s = 1$, $s_\parallel = s$.

as well as

$$\frac{d\tilde{\psi}_s}{d\lambda} = \Upsilon_s^{(0)}(\tilde{p},\tilde{e},\tilde{x}_I)\ , \tag{5.54}$$

$$\frac{d\tilde{\phi}}{d\lambda} = \Upsilon_\phi^{(0)}(\tilde{p},\tilde{e},\tilde{x}_I) + \varepsilon s\Upsilon_\phi^{(1)}(\tilde{p},\tilde{e},\tilde{x}_I)\ , \tag{5.55}$$

$$\frac{d\tilde{t}}{d\lambda} = \Upsilon_t^{(0)}(\tilde{p},\tilde{e},\tilde{x}_I) + \varepsilon s\Upsilon_t^{(1)}(\tilde{p},\tilde{e},\tilde{x}_I)\ . \tag{5.56}$$

Many of these terms are simply related to the transformed force terms averaged over a single orbit, which are as follows:

$$\tilde{F}_p^{(1)} = \left\langle F_{p,\mathrm{GSF}}^{(1)} \right\rangle, \quad \tilde{F}_e^{(1)} = \left\langle F_{e,\mathrm{GSF}}^{(1)} \right\rangle \quad \tilde{F}_x^{(1)} = \left\langle F_{x,\mathrm{GSF}}^{(1)} \right\rangle, \tag{5.57a-c}$$

$$\Upsilon_r^{(1)} = \left\langle f_{r,\mathrm{SCF}}^{(1)} \right\rangle, \quad \Upsilon_z^{(1)} = \left\langle f_{z,\mathrm{SCF}}^{(1)} \right\rangle, \tag{5.57d-e}$$

$$\Upsilon_s^{(0)} = \left\langle f_s^{(0)} \right\rangle\ , \quad \Upsilon_\phi^{(0)} = \left\langle f_\phi^{(0)} \right\rangle\ , \quad \Upsilon_t^{(0)} = \left\langle f_t^{(0)} \right\rangle, \tag{5.57f-h}$$

where $\Upsilon_s^{(0)}$, $\Upsilon_\phi^{(0)}$, and $\Upsilon_t^{(0)}$ are the Mino-time precession, azimuthal, and time fundamental frequencies respectively which are known analytically [139], [144]. The remaining terms are more complicated and are given in terms of an operator $\mathcal{N}$ which we define in Appendix C.3.3. These remaining terms are given by:

$$\Upsilon_s^{(1)} = \mathcal{N}(f_s^{(0)})\ , \quad \Upsilon_\phi^{(1)} = \mathcal{N}(f_\phi^{(0)})\ , \quad \Upsilon_t^{(1)} = \mathcal{N}(f_t^{(0)})\ . \tag{5.57i-k}$$

The leading order near-identity transformation for the orbital elements needed for the initial conditions is given by:

$$\begin{aligned}\breve{Y}_j^{(1)} \equiv & \sum_{(\kappa_r,\kappa_z)\neq(0,0)} \frac{iF_{j,\mathrm{GSF},\kappa_r,\kappa_z}^{(1)}}{\kappa_r\Upsilon_r^{(0)} + \kappa_z\Upsilon_z^{(0)}} e^{i(\kappa_r q_r + \kappa_z q_z)} \\ & + \sum_{(\kappa_r,\kappa_z,\kappa_s)\neq(0,0,0)} \frac{isF_{j,\mathrm{SCF},\kappa_r,\kappa_z,\kappa_s}^{(1)}}{\kappa_r\Upsilon_r^{(0)} + \kappa_z\Upsilon_z^{(0)} + \kappa_s\Upsilon_s^{(0)}} \\ & \times e^{i(\kappa_r q_r + \kappa_z q_z + \kappa_s \psi_s)}\ .\end{aligned} \tag{5.58}$$

With this all in hand, we can now derive the averaged equations of motion parameterized by Boyer-Lindquist time t for the phases $\vec{\varphi} = \{\varphi_r, \varphi_z, \varphi_s, \varphi_\phi\}$ and orbital elements $\vec{\mathcal{P}} =$

$\{p_\varphi, e_\varphi, x_\varphi\}$ in form

$$\frac{dp_\varphi}{dt} = \varepsilon\Gamma_p^{(1)}(p_\varphi, e_\varphi, x_\varphi) + \varepsilon^2\Gamma_p^{(2)}(p_\varphi, e_\varphi, x_\varphi) \,, \tag{5.59a}$$

$$\frac{de_\varphi}{dt} = \varepsilon\Gamma_e^{(1)}(p_\varphi, e_\varphi, x_\varphi) + \varepsilon^2\Gamma_e^{(2)}(p_\varphi, e_\varphi, x_\varphi) \,, \tag{5.59b}$$

$$\frac{dx_\varphi}{dt} = \varepsilon\Gamma_x^{(1)}(p_\varphi, e_\varphi, x_{I,\varphi}) + \varepsilon^2\Gamma_x^{(2)}(p_\varphi, e_\varphi, x_\varphi) \,, \tag{5.59c}$$

$$\frac{d\varphi_r}{dt} = \Omega_r^{(0)}(p_\varphi, e_\varphi, x_\varphi) + \varepsilon s\Omega_r^{(1)}(p_\varphi, e_\varphi, x_\varphi) \,, \tag{5.59d}$$

$$\frac{d\varphi_z}{dt} = \Omega_z^{(0)}(p_\varphi, e_\varphi, x_\varphi) + \varepsilon s\Omega_z^{(1)}(p_\varphi, e_\varphi, x_\varphi) \,, \tag{5.59e}$$

$$\frac{d\varphi_s}{dt} = \Omega_s^{(0)}(p_\varphi, e_\varphi, x_\varphi) \,, \tag{5.59f}$$

$$\frac{d\varphi_\phi}{dt} = \Omega_\phi^{(0)}(p_\varphi, e_\varphi, x_\varphi) + \varepsilon s\Omega_\phi^{(1)}(p_\varphi, e_\varphi, x_\varphi) \,. \tag{5.59g}$$

The leading order terms in these equations are given by

$$\tilde{\Gamma}_p^{(1)} = \tilde{F}_p^{(1)}/\Upsilon_t^{(0)}, \quad \tilde{\Gamma}_e^{(1)} = \tilde{F}_e^{(1)}/\Upsilon_t^{(0)}, \quad \tilde{F}_x^{(1)} = \tilde{F}_x^{(1)}/\Upsilon_t^{(0)} \,, \tag{5.60a-c}$$

$$\tilde{\Omega}_r^{(0)} = \Upsilon_r^{(0)}/\Upsilon_t^{(0)}, \quad \tilde{\Omega}_z^{(0)} = \Upsilon_z^{(0)}/\Upsilon_t^{(0)}, \tag{5.60d-e}$$

$$\tilde{\Omega}_s^{(0)} = \Upsilon_s^{(0)}/\Upsilon_t^{(0)}, \quad \tilde{\Omega}_\phi^{(0)} = \Upsilon_\phi^{(0)}/\Upsilon_t^{(0)} \,. \tag{5.60f-g}$$

The sub-leading terms are given by

$$\Gamma_p^{(2)} = -\Upsilon_t^{(1)}\Gamma_p^{(1)}/\Upsilon_t^{(0)} \,, \tag{5.61a}$$

$$\Gamma_e^{(2)} = -\Upsilon_t^{(1)}\Gamma_e^{(1)}/\Upsilon_t^{(0)} \,, \tag{5.61b}$$

$$\Gamma_x^{(2)} = -\Upsilon_t^{(1)}\Gamma_x^{(1)}/\Upsilon_t^{(0)} \,, \tag{5.61c}$$

$$\Omega_r^{(1)} = \frac{1}{\Upsilon_t^{(0)}}\left(\Upsilon_r^{(1)} - \Upsilon_t^{(1)}\Omega_r^{(0)}\right) \,, \tag{5.61d}$$

$$\Omega_z^{(1)} = \frac{1}{\Upsilon_t^{(0)}}\left(\Upsilon_z^{(1)} - \Upsilon_t^{(1)}\Omega_z^{(0)}\right) \,, \tag{5.61e}$$

$$\Omega_\phi^{(1)} = \frac{1}{\Upsilon_t^{(0)}}\left(\Upsilon_\phi^{(1)} - \Upsilon_t^{(1)}\Omega_\phi^{(0)}\right) \,. \tag{5.61f}$$

The aligned spin case has equations in the same form as in the arbitrarily oriented case. The main difference is that we no longer have to evolve the precession phase ψ_s or φ_s. The other consequence is that the leading order NIT for the orbital elements reduces to

$$\breve{Y}_j^{(1)} \equiv \sum_{(\kappa_r,\kappa_z)\neq(0,0)} \frac{i\left(F^{(1)}_{j,\mathrm{GSF},\kappa_r,\kappa_z} + sF^{(1)}_{j,\mathrm{SCF},\kappa_r,\kappa_z}\right)}{\kappa_r\Upsilon_r^{(0)} + \kappa_z\Upsilon_z^{(0)}} \times e^{i(\kappa_r q_r + \kappa_z q_z)} \,. \tag{5.62}$$

The difference between the OG and averaged quantities scales linearly with the mass ratio as can be seen in Fig. 5.3. See Appendix C.4 for a discussion of the choice of initial conditions in the context of OG and NIT inspirals.

5.5.5 Implementation

To implement the NIT procedure in practice, we must perform a series of offline steps. We first generate a grid to cover a section of the 4-dimensional Kerr parameter space that we wish to examine. We fix $a/M = 0.7$, and choose our principal elements $P_j = (p, e, x_I)$ in the range from $P_{j,\min}$ to $P_{j,\max}$ in steps of $P_{j,\text{step}}$. For all the analyses we present in this paper, we use $e_{\min} = 0.05$, $e_{\max} = 0.22$, $e_{\text{step}} = 0.005$, and $x_{I,\min} = 0.69$, $x_{I,\max} = 0.701$, $x_{I,\text{step}} = 0.001$. The resolution we use in p varies depending on our goal. For the convergence study in Fig. 5.3, we use $p_{\min} = 9$, $p_{\max} = 9.5$, $p_{\text{step}} = 0.002$; for calculating the full trajectory, we use a coarser grid that covers a wider range of parameter space: $p_{\min} = 3.2$, $p_{\max} = 10$, $p_{\text{step}} = 0.02$. We select this region in order to avoid low order transient resonances[7] where our NIT procedure breaks down, though methods for dealing with resonances have been developed elsewhere [185].

At each point in this grid, we use a fast Fourier transform to numerically decompose the OG functions into Fourier modes, and then sum them together in accordance with Eqs. (5.57), (5.58), (5.60), and (5.60) to produce the averaged terms needed in our NIT equations of motion and the modes of the leading order transformation terms needed to set the initial conditions. These data are then interpolated using Hermite polynomials with *Mathematica*'s `Interpolate` function. Overall, these offline steps take about 3 hours running in parallel (10 cores) using 3-GHz-class Apple M1 processors.

By contrast, the online steps are computationally cheap. One loads the interpolants produced by the offline analysis, sets initial conditions using Eqs. (C.88), (C.89), and (C.90), and then numerically solves the equations using *Mathematica*'s `NDSolve`. The resulting equations of motion can then be solved in less than a second, regardless of mass ratio. This is compared with the minutes to multiple hours (depending on mass ratio) required by the OG method. In the supplementary material, we provide the interpolants, radiation-reaction data, and a *Mathematica* notebook to rapidly compute this trajectory.

5.6 Results I: Inspirals

We present our results in two parts: the inspirals we find combining spin-curvature coupling with radiation reaction (this section), and the waveforms produced by those inspirals (following section).

5.6.1 Aligned spin

We begin by examining a set of generic (inclined and eccentric) inspirals with aligned secondary spin and mass ratios $\varepsilon = 5 \times 10^{-2}$, 10^{-2}, and 10^{-3} (left panel of Fig. 5.3). As we have emphasized elsewhere, we expect astrophysical EMRI systems to have mass ratios of 10^{-4} or smaller; we use a larger mass ratio here to augment and clearly show spinning body effects. Each example we consider begins at $p = 12$, $e = 0.35$, $x_I = 0.5$. We look at inspiral

[7] Note that transient self-forced resonances are not a concern in this work because we do not include self-force terms that would produce them in this analysis. Such terms are likely to be incorporated in the future.

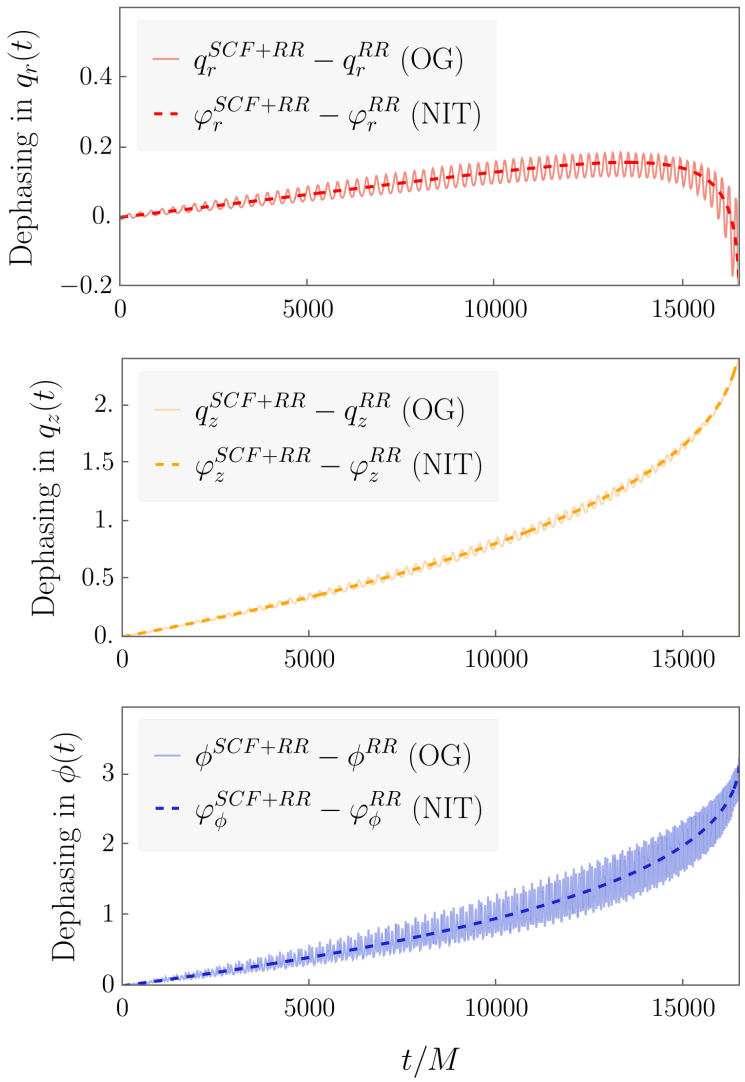

Figure 5.4: Dephasing in $q_r(t)$, $q_z(t)$, and $\phi(t)$ for a spinning body relative to a non-spinning body with mass ratio $\varepsilon = 10^{-2}$ orbiting a black hole with spin $a = 0.7M$. The magnitude and orientation of the small body's spin is specified by $s = 1$, $s_\parallel = s$. Dashed lines show the dephasing computed using the NIT; solid lines show the dephasing given by the OG equations. Top panel shows the radial dephasing $q_r^{SCF+RR} - q_r^{RR}$ (red), middle shows dephasing in the polar angle $q_z^{SCF+RR} - q_z^{RR}$ (yellow), and bottom shows dephasing in axial angle $\phi^{SCF+RR} - \phi^{RR}$ (blue). In all panels, solid lines show the OG computation, dashed shows the NIT results. The inspiral used for all panels has the initial conditions $p = 10$, $e = 0.2$, $x_I = 0.7$, $q_r = 0$, $q_z = 0$, and $\phi = 0$.

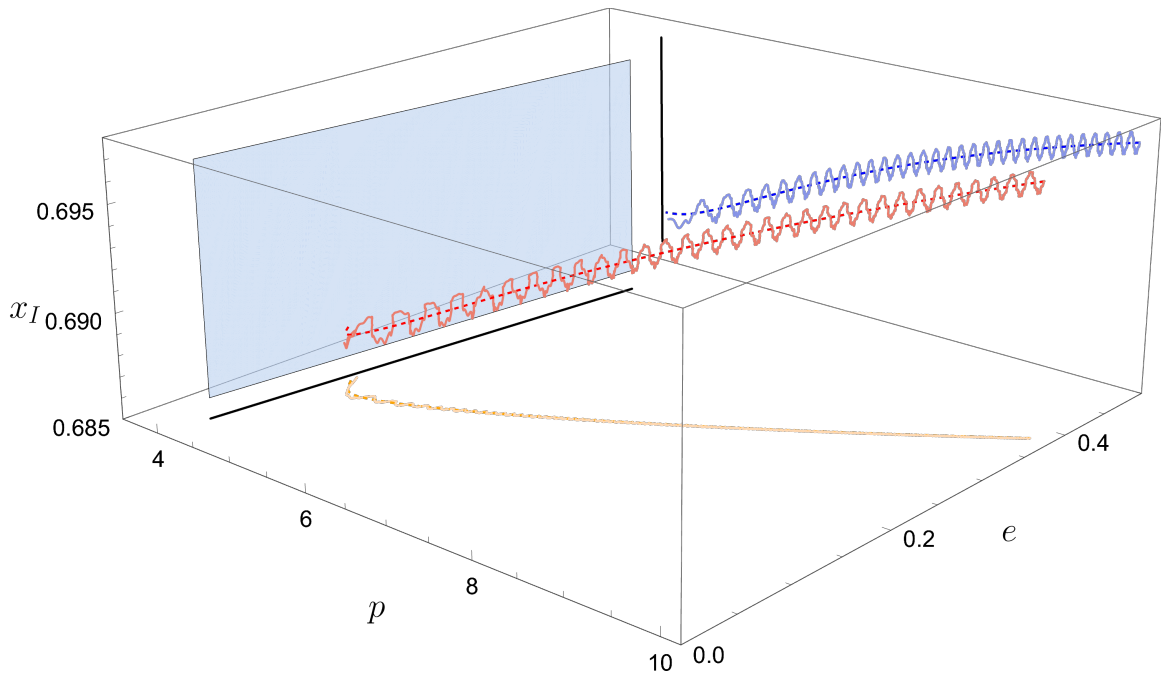

Figure 5.5: The trajectory in p-e-x_I space for an example generic inspiral. This inspiral (red curve) begins at $(p, e, x_I) = (10, 0.38, 0.6967)$ and ends at the LSO (the light blue plane). The dashed curves show a non-spinning body's inspiral; solid curves are for the inspiral of a spinning small body. The orange curves show the projection of the inspiral onto the p-e plane; the solid black line in this plane is the projection of the last stable orbit at the final value of x_I. (This projection is the same as the top panel of Fig. 5.6.) The blue curves show the projection of the inspiral onto the p-x_I plane; the solid black curve in this plane is the projection of the LSO at the final value of e. (This projection is the same as the bottom panel of Fig. 5.6.) We use mass-ratio $\varepsilon = 0.005$ and small-body spin $s = 1$, with $s_{\|} = 0.9$ and $\phi_s = \pi/2$. See Fig. 15 in Ref. [26] for comparison.

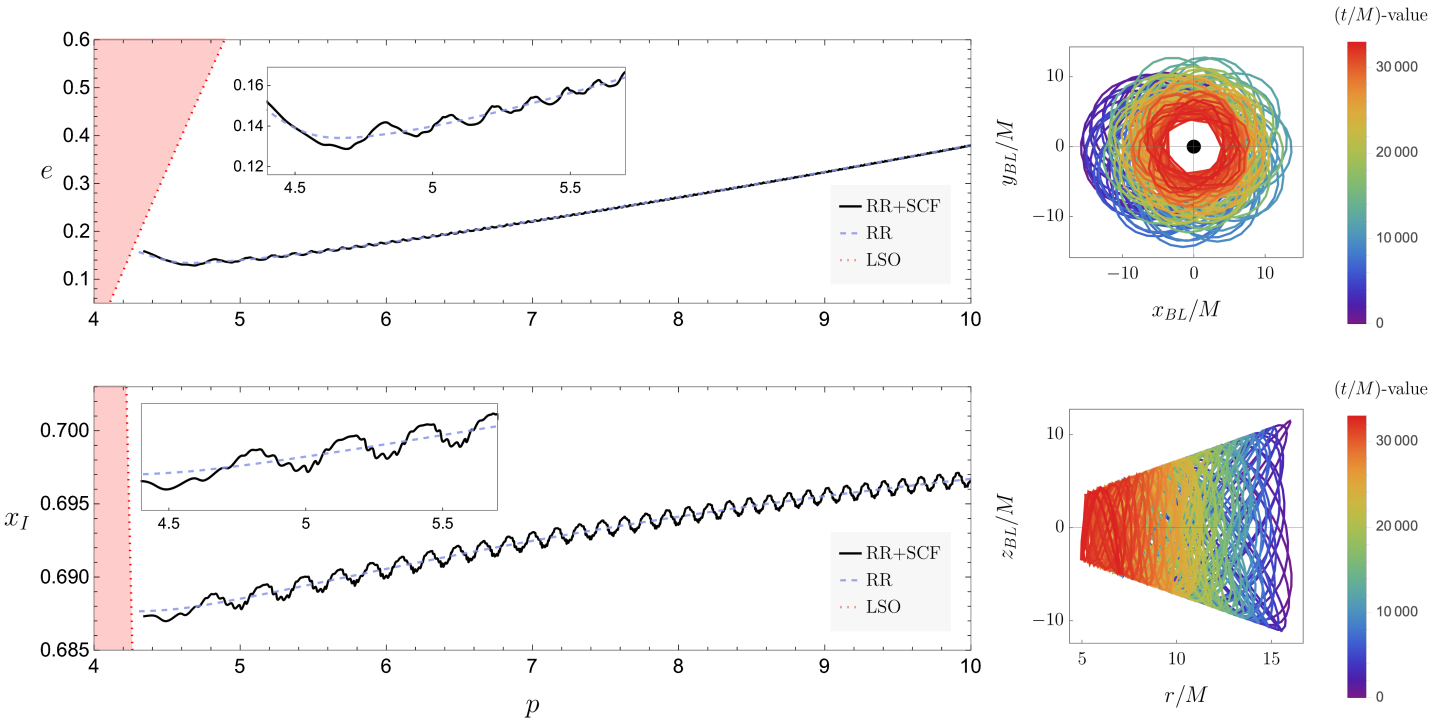

Figure 5.6: Evolution of p versus e (top left) and evolution of p versus x_I (bottom left) for the inspiral shown in Fig. 5.5. Solid black curves show spinning body inspiral; blue dashed curves show non-spinning body inspiral. In both plots, the last stable orbit (LSO) is shown by the red dotted curve. The insets show close-ups of inspiral near the LSO. Right-hand panels show projections of the worldline onto the x_{BL}-y_{BL} and r-z_{BL} planes (where x_{BL}, y_{BL}, z_{BL} are Cartesian-like representations of Boyer-Lindquist coordinates: $x_{BL} = r\sin\theta\cos\phi$, etc.), with color encoding the time evolution (early times in purple and late times in red). Parameters are identical to those used in Fig. 5.5.

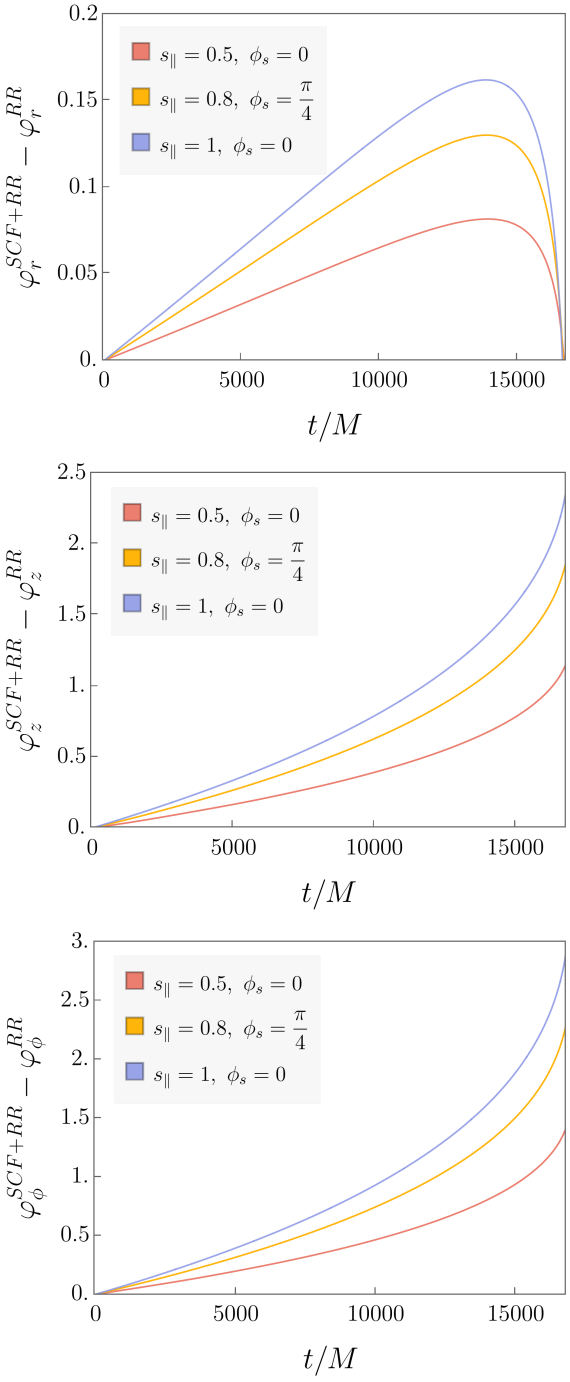

Figure 5.7: The averaged dephasing of $\varphi_r(t)$, $\varphi_z(t)$, and $\varphi_\phi(t)$ for a small body with a misaligned spin vector relative to a non-spinning body for three different values of spin alignment: $s_\parallel = 1$ (blue), $s_\parallel = 0.8$ (orange) and $s_\parallel = 0.5$ (red). The magnitude of the small body's spin is $s = 1$; ϕ_s is zero except for the orange curve which has $\phi_s = \pi/4$. The small body has mass ratio $\varepsilon = 10^{-2}$ and is orbiting a black hole with spin $a = 0.7M$. For all panels, $p = 10$, $e = 0.2$, $x_I = 0.7$, $q_r^S = 0$, $q_z^S = 0$, and $\phi = 0$ initially. In all three cases, the dephasing is simply proportional to $s_\parallel$: $s_\parallel = 1$ shows the largest effect; the curves with $s_\parallel = 0.8$ and $s_\parallel = 0.5$ track that curve, but with magnitudes smaller by factors of 0.8 and 0.5, respectively.

into black holes with $a/M = 0.7$. The left-hand panel of Fig. 5.3 shows these inspirals in the (p, e) plane (top) and the (p, x_I) plane (bottom). In all cases, p decreases due to radiation reaction until the system reaches the LSO (shown as a dotted line); e decreases for much of the inspiral, showing an uptick near the LSO (a well-known strong-field characteristic of GW driven inspiral [196]). The inspiral increases in inclination (corresponding to a decrease in x_I) all the way to the LSO, with no deep strong-field reversal of sign unlike the p-e trajectory.

In the left panel of Fig. 5.3, we see that the amplitude of the oscillations increases with increasing mass ratio ε, while the number of oscillations increases inversely with mass ratio. This is because the duration of inspiral scales inversely with ε, changing the number of orbital cycles the inspiral passes through before reaching the LSO. The difference between OG and averaged quantities also decreases with decreasing ε (right panel of Fig. 5.3); this is a useful validation of the NIT procedure. In the bottom right panel of Fig. 5.3), there is an uptick in the value of $|(\phi + Z_\phi^{(0)} - \Omega_\phi Z_t^{(0)}) - \varphi_\phi|$ for mass ratio $\varepsilon = 10^{-4}$; this is due to numerical error floor in the OG solver as well as interpolation error in the NIT solution. We expect this error could be reduced with a more computationally expensive online (higher precision numerical solver) or offline (higher precision interpolation) step.

The curves in Fig. 5.4 show the dephasing of a generic inspiral due to spin-curvature force. We show the difference between various phases computed using only adiabatic radiation reaction (denoted by "RR"), and radiation reaction plus the spin-curvature force (denote by "SCF + RR"). The dashed lines in all panels show the averaged (NIT) dephasing $\varphi_y^{SCF+RR} - \varphi_y^{RR}$; $y = r$ is shown in the top panel, $y = z$ in the middle, and $y = \phi$ in the bottom. (We remind the reader that φ_α represents the averaged phases parameterized in Boyer-Lindquist time.) The solid curves in the three panels show these dephasings computed using the OG equations.

The inclusion of the spin-curvature force, which is conservative [111], [188], will lead to secular changes to the evolution of the phases. In Fig. 5.4, we see secular corrections to the phases accumulate when post-adiabatic effects are included. The evolution of the radial dephasing $\varphi_r^{SCF+RR} - \varphi_r^{RR}$ is not monotonic, increasing to a maximum value and subsequently decreasing to less than zero. The secular dephasing of both $\varphi_z^{SCF+RR} - \varphi_z^{RR}$ and $\varphi_\phi^{SCF+RR} - \varphi_\phi^{RR}$ by contrast is monotonic.

As discussed in previous sections of this paper, short timescale oscillations in solutions to the OG equations of motion are removed by the NIT averaging procedure, isolating the longer timescale, secular evolution (compare the solid and dashed curves in Fig. 5.4). For more extreme mass ratios, the difference in time scales is significant, and it greatly reduces computational cost to compute on only the longer secular timescale. The oscillations in the solution to the OG equations contain harmonics of multiple frequencies; this complexity in harmonic structure is especially clear in the bottom panel of Fig. 5.4 which displays $\phi^{SCF+RR} - \phi^{RR}$. In this spin-aligned case, harmonics of Ω_r and Ω_z (or equivalently Ω_θ) contribute to the structure. In the spin-misaligned case we examine in the next section, harmonics of Ω_s are also present.

It is important to note that the total dephasing shown in Fig. 5.4 is independent of mass ratio; although we used $\varepsilon = 10^{-2}$ for this figure, we find exactly the same total dephasing with more extreme mass ratios. (Oscillations about the mean trend scale with mass ratio, so the oscillations at $\varepsilon = 10^{-5}$, for example, are a factor of 1000 smaller than those shown

in Fig. 5.4.) Because the spin-curvature force enters as a post-adiabatic effect, its integrated dephasing is independent of mass ratio (though scaling with the magnitude of $s_\parallel$). Going to a more extreme mass ratio significantly increases the total duration of inspiral and the number of cycles, making computation of the trajectory increasingly challenging when using the OG rather than the NIT.

5.6.2 Misaligned spin

We now look at an example of generic spinning body inspiral with misaligned small-body spin. The red curves in Fig. 5.5 show a generic inspiral, both with (solid line) and without (dashed line) the spin-curvature force. The orange curve shows the projection of the inspiral onto the p-e plane; the blue curve shows the projection onto the p-x_I plane. Just as in the aligned case, the projection onto the p-e plane shows a decrease in eccentricity throughout most of the inspiral, and then ticks up shortly before reaching the LSO (depicted by a black line). The inspiral increases in inclination (corresponding to a decrease in x_I) all the way to the LSO, with no deep strong-field reversal of sign unlike the p-e trajectory.

Figure 5.6 shows a more detailed depiction of the projections of the inspiral onto the p-e and p-x_I planes (leftmost panels of the first two rows). Each panel includes an inset which zooms in on the inspiral close to the LSO. The secular evolution of the principal orbital elements p, e, and x_I is unaffected by the presence of the spin-curvature force, but this force drives oscillations about the secular trajectory. Notice that the generic inspiral has harmonic structure at multiple timescales — the oscillations have a more complicated structure than we saw in the case of aligned inspirals. This more intricate harmonic structure is because there are terms in the equations of motion which are periodic with the four frequencies Ω_r, Ω_θ, Ω_ϕ, and Ω_s. Harmonics at frequency Ω_s are due to the precession of the small-body's spin vector. Oscillations in the x_I-p trajectory are particularly complex, involving beats between all four frequencies.

The right-hand panels of Fig. 5.6 show the inspiral trajectory in a Cartesian representation of the Boyer-Lindquist coordinates: we define $x_{BL} = r\sin\theta\cos\phi$, $y_{BL} = r\sin\theta\sin\phi$, $z_{BL} = r\cos\theta$, with r, θ, and ϕ the Boyer-Lindquist coordinates along the inspiral. In the r-z_{BL} inspiral projection, we see that the maximum $|z_{BL}|$ decreases as inspiral progresses. Although the inclination angle I increases during inspiral, the effect is quite small. The shrinking of r due to radiative backreaction is much more significant, so $|z_{BL}| = |r\cos\theta|$ decreases overall.

Figure 5.7 shows how the misalignment of the small-body spin modifies the inspiral. From top to bottom, the three panels show the dephasing of the spinning-body phases (φ_r^{SCF+RR}, φ_z^{SCF+RR}, and φ_ϕ^{SCF+RR}) relative to those of a non-spinning body (φ_r^{RR}, φ_z^{RR}, and φ_ϕ^{RR}). We see that the value of $\varphi_y^{SCF+RR} - \varphi_y^{RR}$, $y \in \{r, z, \phi\}$, is proportional to $s_\parallel$, as expected from previous analyses [84], [172]. In all three panels, the blue curve (corresponding to aligned spins, $s_\parallel = 1$), shows the largest dephasing. The maxima of the other two curves, $s_\parallel = 0.8$ (orange) and $s_\parallel = 0.5$ (red), are exactly 0.8 and 0.5 times the maximum of the $s_\parallel = 1$ curve, as expected. The component of the small body spin misaligned from the orbit does not play any role in this dephasing. See Appendix C.4.3 for a discussion about the selection of initial conditions in the case of inspirals with spin precession.

5.7 Results II: Waveforms

We wrap up our discussion of spinning-body inspirals by examining the waveforms these inspirals generate.

5.7.1 Waveform generation

We write the GW strain in the "multivoice" form [26]

$$\begin{aligned} h(t) &\equiv h_+(t) - ih_\times(t) \equiv \frac{1}{r}\sum_{lmkn} h_{lmkn}(t) \\ &= \frac{1}{r}\sum_{lmkn} H_{lmkn}(t) e^{i[m\varphi_{\rm S} - \Phi_{mkn}(t)]} \ . \end{aligned} \tag{5.63}$$

This form is found by promoting "snapshot" waveforms from a geodesic orbit into a sequence of snapshots in which the waveform's properties evolve as the inspiral proceeds. The amplitude of each waveform voice is given by

$$H_{lmkn}(t) = A_{lmkn}(t) S_{lm}\left[\vartheta_{\rm S}; a\omega_{mkn}(t)\right] \ , \tag{5.64}$$

where

$$A_{lmkn}(t) = -\frac{2Z^\infty_{lmkn}(t)}{\omega_{mkn}(t)^2} \ . \tag{5.65}$$

For adiabatic inspirals, the phase of each voice is

$$\begin{aligned} \Phi_{mkn}(t) &= \int_{t_0}^{t} \left[m\Omega_\phi(t') + k\Omega_\theta(t') + n\Omega_r(t')\right] dt' \\ &\equiv \int_{t_0}^{t} \omega_{mkn}(t') \ , dt' \ . \end{aligned} \tag{5.66}$$

The waveform h is measured at $(t,\, r,\, \vartheta_{\rm S},\, \varphi_{\rm S})$; the "S" on these angles denotes position on the sky, and distinguishes them from orbit coordinates (θ, ϕ), as well as from the Boyer-Lindquist NIT phases $\varphi_{r,z,\phi}$. The function $S_{lm}(\vartheta_{\rm S}; a\omega_{mkn})$ is a spheroidal harmonic of spin-weight -2. The strain h is decomposed onto a basis of spheroidal harmonics with indices lm, as well as into a discrete frequency spectrum labeled with indices mkn.

The dependence on time of the various quantities introduced in the waveform above are inherited from the dynamics of the binary's inspiral. For example, the complex amplitudes $Z^\infty_{lmkn}(\vec{P})$ are pre-evaluated by solving the radial Teukolsky equation on a grid of principal orbit elements, and are then interpolated to generate the waveform at arbitrary points within the grid domain. As the orbit underlying an EMRI evolves, the orbital elements $\vec{P}$ likewise evolve. We denote these evolving elements by $\vec{P}(t)$, where t parameterizes evolution along the inspiral as seen by a distant observer. The amplitude $Z^\infty_{lmkn}(t)$ is thus shorthand for $Z^\infty_{lmkn}[\vec{P}(t)]$, and likewise for other quantities which enter the waveform.

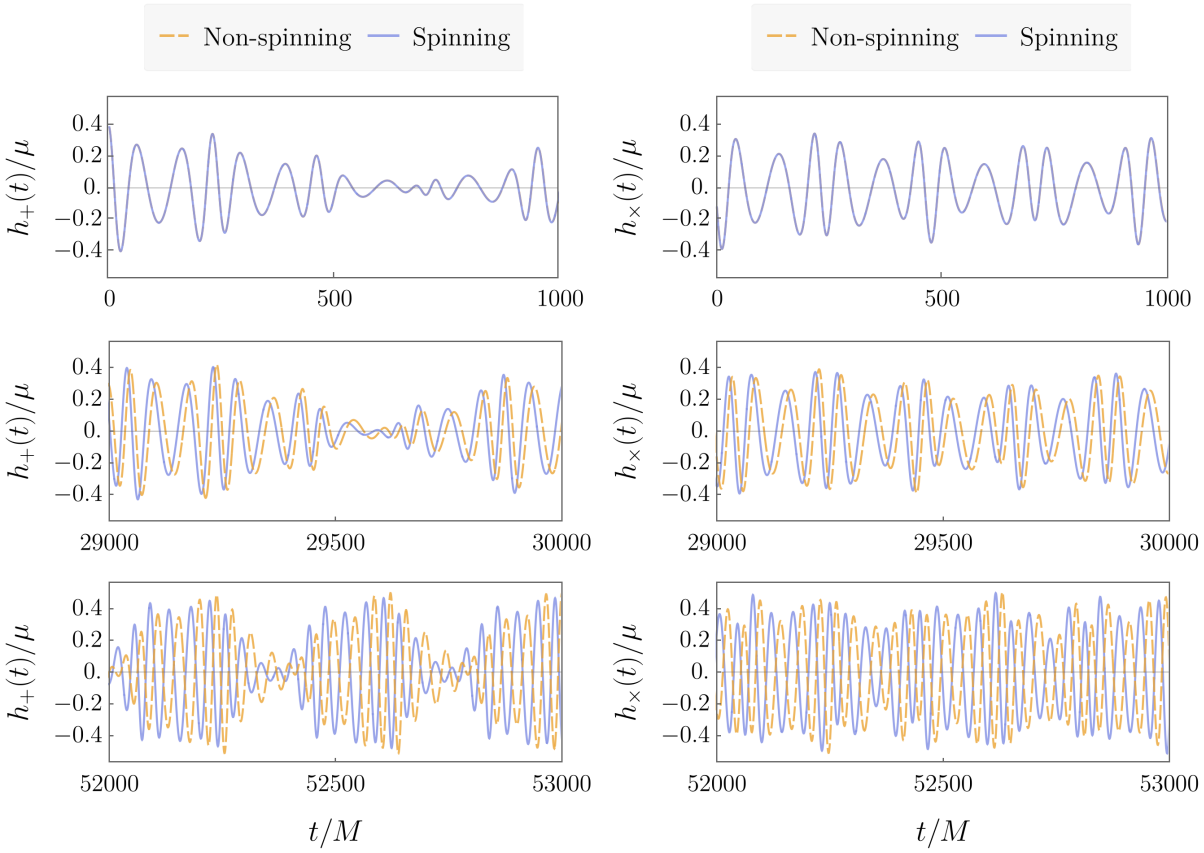

Figure 5.8: Evolution of h_+ and $h_\times$ for a generic inspiral with mass-ratio 10^{-3}. Top panel shows the part of the waveform corresponding to an early part of the inspiral, the middle panel shows an intermediate stage and the bottom panel shows the end of the inspiral. The blue (solid) and orange (dashed) curves correspond to spinning and non-spinning small bodies respectively. The mismatch between the two waveforms is 0.2067. Initial orbital parameters are: $p = 7.95$, $e = 0.22$, $x = 0.699$, $q_r = 0$, and $q_z = 0$. The small body orbits a black hole with spin $a = 0.7M$ and the magnitude and orientation of the small body's spin is specified by: $s = 1$ and $s_\parallel = s$. We use the code `GremlinInsp` to generate these waveforms using the NIT trajectory, with parameters $l_{max} = 2$, $k_{max} = 4$, and $n_{max} = 10$.

In Sec. 5.5.4, we wrote down expressions for the Boyer-Lindquist averaged equations of motion for the orbital phases (5.44b). In integral form, the expression for these phases is:

$$\begin{aligned}\varphi_\alpha(t) &= \int_{t_0}^{t} \left(\Omega_\alpha^{(0)}(t') + \varepsilon\Omega_\alpha^{(1)}(t') + \mathcal{O}(\varepsilon^2)\right) dt' \\ &= \int_{t_0}^{t} \left(\Omega_\alpha(t') + \mathcal{O}(\varepsilon^2)\right) dt' \ . \end{aligned} \tag{5.67}$$

These phases contribute to the waveform voices via

$$\Phi_{mkn}(t) = m\varphi_\phi(t) + k\varphi_\theta(t) + n\varphi_r(t) + \mathcal{O}(\varepsilon) \ . \tag{5.68}$$

The Boyer-Lindquist time averaged phases $\varphi_\alpha(t)$ are thus exactly equivalent to the input required for generating multi-voice Teukolsky waveforms [184]. Replacing the adiabatic phase (5.66) used in the waveform (5.63) with the phase (5.68) is thus a simple and computationally effective way to incorporate spin-curvature physics into inspiral waveforms. A generalization of this to include other post-geodesic forcing terms should likewise enable simple incorporation of other important post-adiabatic effects into EMRI waveforms.

We compute relativistic waveforms using `GremlinInsp`[8], which accepts as input a worldline (an HDF5 file with datasets $\{t,\ p(t),\ e(t),\ x_I(t),\ \Phi_r(t),\ \Phi_\theta(t),\ \Phi_\phi(t)\}$) and maximum values l_{max}, k_{max} and n_{max}. The waveform is assembled by performing the sum (5.63), where the amplitudes Z^{∞}_{lmkn} have been obtained by solving the Teukolsky equation with a point-particle source [26].

Note that the `FastEMRIWaveforms` waveform module takes the same inputs from the orbital dynamics [99]. As such, replacing the adiabatic equations of motion currently in place with the averaged equations of motion we have developed here, along with setting the initial conditions outlined in Appendix C.4, will provide a very convenient way to incorporate the conservative effects of an arbitrary secondary spin into EMRI waveforms efficient enough for LISA data analysis. At present, `FastEMRIWaveforms` can only produce fully relativistic waveforms for eccentric Schwarzschild inspirals. Work is in progress to extend this package to cover inspirals into Kerr black holes; once that it is done, it should not be difficult to adapt this package further to include the post-adiabatic effect of spin-curvature coupling.

In Figure 5.9, we compare waveforms generated using the OG trajectory instead of the NIT trajectory. When computing the waveform using the OG trajectory, we evaluate Φ_{mkn} using Eq. (5.68), replacing φ_ϕ with $\phi + Z^{(0)}_\phi - \Omega_\phi Z^{(0)}_t$, φ_z with $q_z - \Omega_z Z^{(0)}_t$ and φ_r with $q_r - \Omega_r Z^{(0)}_t$.

5.7.2 Waveform analysis

We conclude our analysis of waveforms by quantitatively comparing the different physical effects and modeling methods that we have used. To do this, we use a noise-weighted inner

[8] `GremlinInsp` is a subset of the `Gremlin` package, a C++ code developed by author Hughes to solve the frequency-domain Teukolsky equation for generic bound Kerr orbits. It is not yet in the public domain due to licensing issues, but an open-source version is under development. In the meantime, interested parties should contact Hughes regarding this code.

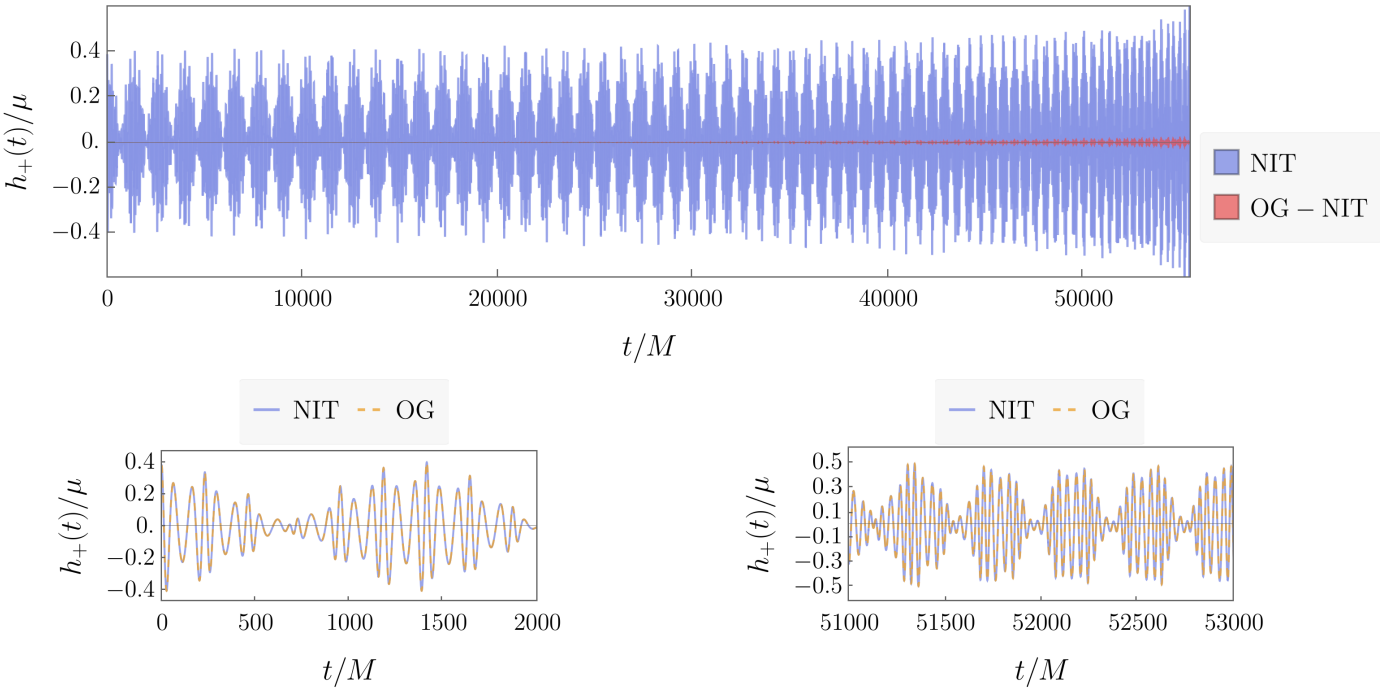

Figure 5.9: Comparison of waveforms computed from OG inspiral and NIT inspiral. Top panel shows h_+ for parameters identical to those used in Fig. 5.8. Blue curve shows waveform from a NIT inspiral for the entire domain we computed; red shows the difference between the OG and the NIT waveforms. Bottom left panel shows the early part of the inspiral; bottom right shows the end of inspiral. The blue solid and orange dashed curves corresponds to NIT and OG inspirals respectively. The mismatch between these two waveforms, computed using Eq. (5.71), is $\mathcal{M} = 3.462 \times 10^{-4}$.

product of two waveforms h_1 and h_2 given by [197]

$$\langle h_1|h_2\rangle = 2\int_0^\infty \frac{\tilde{h}_1^*(f)\tilde{h}_2(f)+\tilde{h}_1(f)\tilde{h}_2^*(f)}{S_n(f)}df \ , \tag{5.69}$$

where $\tilde{h}(f)$ is the Fourier transform of the time-domain waveform $h(t)$, $\tilde{h}^*(f)$ is the complex conjugate of $\tilde{h}(f)$, and $S_n(f)$ is the one-sided power spectral density (PSD) of detector noise. We use a white noise power spectrum here (i.e., noise independent of frequency); an analysis focusing on astrophysical waveform characteristics (as opposed to assessing more general aspects of waveform modeling) would use noise from a particular detector, such as that projected for the LISA mission [198]. The fractional waveform overlap $\mathcal{O}$ is defined by

$$\mathcal{O} = \frac{\langle h_1|h_2\rangle}{\sqrt{\langle h_1|h_1\rangle\langle h_2|h_2\rangle}} \ . \tag{5.70}$$

This measure equals equals 1 when $h_1 = h_2$; $\mathcal{O} = 0$ defines "orthogonal" waveforms. Note that, for white noise, $\mathcal{O}$ is independent of the noise amplitude; we thus set $S_n(f) = 1$ for these comparisons. A closely related notion is the fractional waveform mismatch, $\mathcal{M} = 1 - \mathcal{O}$. We use the `WaveformMatch` function from the SimulationTools package [199] to calculate waveform overlaps.

Using these tools to compare waveforms, we now consider how high the overlap should be for waveforms to be distinguishable in the context of LISA data science. Following the criteria defined in Ref. [200], two waveforms h_1 and h_2 are defined to be indistinguishable if they satisfy $\langle \delta h|\delta h\rangle < 1$, where $\delta h = h_1 - h_2$. The optimal signal-to-noise ratio (SNR) ρ is defined by $\rho^2 \equiv \langle h|h\rangle$. Combining these definitions and going to the limit $\rho_1 \simeq \rho_2 \equiv \rho$ yields the benchmark that two waveforms with mismatch $\mathcal{M}$ will be indistinguishable if their SNR satisfies

$$\rho \leq \frac{1}{\sqrt{2\mathcal{M}}} \ . \tag{5.71}$$

Two signals being distinguishable according to the criterion (5.71) is a necessary but not sufficient condition for detectability of a particular effect. A more concrete measure of whether an effect related to the source physics is detectable should be assessed using a Bayesian parameter estimation framework (i.e., inferring model parameters by combining prior knowledge with data using Bayes' theorem to form a posterior distribution).

Figures 5.8 and 5.9 display snapshots of gravitational waveforms. Figure 5.8 shows the plus and cross polarizations for a generic inspiral with mass-ratio 10^{-3}; the blue curve shows the waveform of a spinning body, while the orange curve shows the waveform of a non-spinning body. The top, middle and bottom panels display the early, intermediate and late stages of the inspiral. If the non-spinning and spinning-body inspirals are initially in phase at the beginning of the inspiral, the dephasing accumulates as the inspiral progresses. This dephasing accumulates a rather large mismatch of $\mathcal{M} = 0.2067$ between spinning and non-spinning waveforms. Using Eq. 5.71, these waveforms would be distinguishable for EMRI signals with SNR $\rho \gtrsim 1.5$. In other words, if these were real signals, they would be easily distinguishable.

Figure 5.9 compares OG and NIT models of h_+ for the spinning body generic inspiral shown in Fig. 5.8. The top panel shows the waveform of the entire inspiral, left bottom

shows early in the inspiral, and right bottom shows late times. The solid blue curve is the waveform computed using the NIT inspiral, while dashed orange corresponds to the waveform computed with the OG inspiral. In the bottom two panels of Fig. 5.8, we see that the NIT and OG curves lie almost exactly on top of each other, even late in the inspiral. The difference between the OG and NIT waveforms is shown by the red curve of the top panel of Fig. 5.9; a small mismatch, $\mathcal{M} \simeq 0.00035$, accumulates over the inspiral. According to the criterion (5.71), the OG and NIT waveforms would be distinguishable as EMRI signals with SNR greater than about 38. It's worth bearing in mind that this result is for mass ratio $\varepsilon = 10^{-3}$. The mismatch would be lower, and the SNR needed for signals to be distinguishable would be greater, for EMRI mass ratios $\varepsilon \lesssim 10^{-4}$. Waveforms computed using the OG and NIT techniques differ only slightly, despite their vastly different computational costs.

5.8 Conclusions

We have presented a framework to combine orbit-averaged point-particle GW backreaction with the orbital dynamics of spinning bodies to make inspiral worldlines and gravitational waveforms for spinning bodies bound to Kerr black holes in the extreme mass ratio limit. The inspirals and GWs produced by this framework are demonstrably incomplete (we discuss below aspects of this model which are ripe for improvement and additional work), but nonetheless make it possible to augment existing models of strong-field inspiral and waveform generation using data and methods available today. In this analysis, we computed trajectories and waveforms using both osculating geodesic (OG) and near-identity transformation (NIT) methods. In Sec. 5.7, we demonstrated that the NIT trajectory can be used to generate a waveform that includes spinning-secondary effects, with minimal mismatch relative to the OG waveform ($\mathcal{M} \approx 3.5 \times 10^{-4}$), and a speed up in computation of several orders of magnitude.

As tools for efficiently computing EMRI waveforms [98], [99] expand to cover more of the astrophysical parameter space, it should not be difficult using the methods and techniques we have presented to further augment these tools to include the influence of secondary spin. As show in Sec. 5.7, the leading impact on the waveforms' phase evolution can be found by "upgrading" the adiabatic inspiral phase, our Eq. (5.66), to a version that includes the post-adiabatic influence of secondary spin. This may be particularly useful in the short term for assessing the importance of spin effects for EMRI science. For example, previous work based on much simpler orbit geometries concluded that secondary spin is likely to have negligible impact on EMRI measurements [117], [118]; re-examining this question for generic orbits and spin orientations may change this conclusion. A further generalization of this problem may even be useful for examining the impact of secondary structure beyond spin (looking at, for example, the findings of Ref. [201] to a broader class of orbits). It should not be too challenging to generalize further to include the post-adiabatic influence of other important post-geodesic effects.

As discussed in Sec. 5.3, another way to approach this problem is to consider orbit-averaged backreaction directly applied to spinning body orbits, following the kind of calculations laid out in Ref. [128]. Indeed, given that spinning body orbits describe the behavior of these inspirals on timescales too short for radiation reaction to be apparent, one might

regard this as a more natural approach to this problem. Performing such a calculation will require large data sets describing backreaction onto spinning body orbits, as well as a better understanding of how to evolve the generalized Carter constant of a spinning body. In addition, the GWs produced by a spinning body are more complicated than those from a point body: an additional term, linear in the small body's spin tensor, enters the source term of the wave equation. This changes the instantaneous wave amplitude, and thus changes the rate at which GWs backreact on the system. The calculation we present here will be a useful tool for assessing the importance of different terms which enter the dynamics of backreaction for spinning-body orbits. By incorporating the linear-in-secondary-spin flux corrections to our calculation, it would be equivalent (to 1PA order) to using a spinning-body orbit formulation as the basis for the calculation from the outset. Comparing the two approaches would then be a useful validation for both formulations. We include *Mathematica* code and access to the data used to describe backreaction with this paper in order to facilitate making such comparisons.

An interesting direction to explore in future work is examining the difference between the waveforms generated in this analysis and those obtained via spinning-body orbits evolved with the first-order self-force from first principles, such as in Ref. [127]. Such a comparison should provide insight into whether the present computation on its own is sufficiently accurate to operate as an approximation in certain portions of the parameter space.

Secondary spin is one example of an important post-adiabatic effect. Other effects, especially those related to the gravitational self force [100], [202] are also critically important, and must also be included in order to develop accurate EMRI waveform models. As long as these terms can be considered independently, with each term contributing in a "modular" fashion, a framework based on osculating orbits may be particularly suitable to combining the impact of different post-adiabatic effects in a single unified model; by using osculating geodesics as the basis for the calculation, all the post-adiabatic effects will be parameterized in the same way and can be directly combined. The NIT technique is flexible and broadly applicable to many types of forcing terms [101]. We anticipate that the orders-of-magnitude NIT speed-up can be leveraged to produce comprehensive EMRI waveform models which include a variety of different effects. Such a model will be needed before too long in order to accurately assess the importance of various contributors to inspiral and EMRI waveforms.

Chapter 6

Asymptotic gravitational-wave fluxes from a spinning test body around a Kerr black hole

The first section of this chapter outlines how gravitational wave fluxes are computed for spinning body orbits along a generic trajectory, and is based on work previously published in Physical Review D (Viktor Skoupý, Georgios Lukes-Gerakopoulos, Lisa V. Drummond, and Scott A. Hughes, 2023) [128]. The second section presents ongoing work conducted in collaboration with Scott Hughes.

6.1 Computing spinning-body GW fluxes along a generic trajectory

In this section, we discuss how gravitational wave energy and angular momentum asymptotic fluxes from a spinning body are computed in the Newman-Penrose (NP) formalism up to a linear in secondary spin approximation. In particular, we describe how GW fluxes are computed for bodies moving on completely generic orbits in a Kerr spacetime.

6.1.1 Linearized trajectory in the frequency domain

The gravitational radiation fluxes are evaluated along a particular trajectory; we select this trajectory to be the linearized spinning-body orbit described in Chapters 3 and 4. In this parameterization, the orbits of a spinning particle are parameterized in Mino time as

$$u_t = -\hat{E} + u_t^S(\lambda) \,, \tag{6.1a}$$

$$u_\phi = \hat{L}_z + u_\phi^S(\lambda) \,, \tag{6.1b}$$

$$r = \frac{p}{1 + e\cos(\Upsilon_r \lambda + \delta\hat{\chi}_r(\lambda) + \delta\chi_r^S(\lambda))} + \delta\mathscr{r}^S(\lambda) \,, \tag{6.1c}$$

$$z = \sin I \cos\big(\Upsilon_z \lambda + \delta\hat{\chi}_z(\lambda) + \delta\chi_z^S(\lambda)\big) + \delta\mathscr{z}^S(\lambda) \tag{6.1d}$$

with

$$\Upsilon_r = \hat{\Upsilon}_r + \Upsilon_r^S \,, \qquad \Upsilon_z = \hat{\Upsilon}_z + \Upsilon_z^S \tag{6.1e}$$

where the hatted quantities denote geodesic quantities and quantities with index S are proportional to σ.[1] With these frequencies at hand, quantities in Eq. (6.1) parametrized with respect to λ can be expanded in the frequency domain as

$$f(\lambda) = \sum_{n,k,j} f_{nkj} e^{-in\Upsilon_r\lambda - ik\Upsilon_z\lambda - ij\Upsilon_s\lambda} \,. \tag{6.2}$$

The sums have different ranges and constraints depending on which function f we are expanding: $\delta\chi_r^S$ is summed only over positive and negative n; $\delta\chi_z^S$ is summed only over positive and negative k; k and j cannot be simultaneously zero for $\not{e}^S$ and n and j cannot be simultaneously zero for $\not{x}^S$. We truncate the n and k sums at $\pm n_{\rm max}$ and $\pm k_{\rm max}$. The index j is summed from -1 to 1. Equations (2.47)–(2.48) together with the normalization of the four-velocity $u^\mu u_\mu = -1$ are then used to find the quantities (6.1) in the frequency domain.

As in Sec. 4.3, we define the phases

$$w_r = \Upsilon_r\lambda \,, w_z = \Upsilon_z\lambda \,, w_s = \Upsilon_s\lambda \,. \tag{6.3a}$$

The coordinates can then be linearized with fixed phases as $r(w_r, w_z, w_s) = \hat{r}(w_r) + r^S(w_r, w_z, w_s)$, $z(w_r, w_z, w_s) = \hat{z}(w_z) + z^S(w_r, w_z, w_s)$, where the linear in spin parts can be expressed as

$$r^S = \frac{ep\delta\chi_r^S \sin(w_r + \delta\hat{\chi}_r)}{(1 + e\cos(w_r + \delta\hat{\chi}_r))^2} + \delta\not{e}^S \,. \tag{6.4}$$

$$z^S = -\sin I \delta\chi_z^S \sin(w_z + \delta\hat{\chi}_z) + \delta\not{x}^S \,. \tag{6.5}$$

For the calculation of gravitational-wave fluxes we need also the coordinate time and azimuthal coordinate. Both can be expressed as secularly growing part plus purely oscillating part, i.e.,

$$t = \Gamma\lambda + \Delta t(\Upsilon_r\lambda, \Upsilon_z\lambda, \Upsilon_s\lambda) \,, \tag{6.6}$$

$$\phi = \Upsilon_\phi\lambda + \Delta\phi(\Upsilon_r\lambda, \Upsilon_z\lambda, \Upsilon_s\lambda) \,, \tag{6.7}$$

where the oscillating parts Δt and $\Delta\phi$ cannot be separated, unlike in the geodesic case. These oscillating parts can be calculated from the four-velocity with respect to Carter-Mino time, $U^\mu \equiv \mathrm{d}x^\mu/\mathrm{d}\lambda = \Sigma u^\mu \equiv \Sigma \mathrm{d}x^\mu/\mathrm{d}\tau$. After integrating,

$$\frac{\mathrm{d}t}{\mathrm{d}\lambda} = U^t = \sum_{n,k,j} U^t_{nkj} e^{-in\Upsilon_r\lambda - ik\Upsilon_z\lambda - ij\Upsilon_s\lambda} \,, \tag{6.8}$$

the n,k,j-mode of $\Delta t(\lambda)$ in the frequency domain reads

$$\Delta t_{nkj} = \frac{U^t_{nkj}}{-in\Upsilon_r - ik\Upsilon_z - j\Upsilon_s} \,, \tag{6.9}$$

[1] Υ_s does not need to be expanded to first order in σ because it appears in terms proportional to σ.

where U^t_{nkj} is the harmonic mode of the four-velocity. By linearizing the above equation in spin, we obtain

$$\Delta t^S_{nkj} = \frac{iU^t_{S,nkj}}{n\hat{\Upsilon}_r + k\hat{\Upsilon}_z + j\Upsilon_s} - \frac{i\hat{U}^t_{nkj}(n\Upsilon^S_r + k\Upsilon^S_z)}{(n\hat{\Upsilon}_r + k\hat{\Upsilon}_z)^2} \,. \tag{6.10}$$

The second term is zero for $j = \pm 1$ and Υ^S_s is not needed, since the geodesic motion is independent of Υ_s. The linear in spin part of the t component of the four-velocity can be expressed as

$$U^t_S = \frac{\partial T}{\partial r} r^S + \frac{\partial T}{\partial z} z^S - \frac{\partial T}{\partial E} u^S_t + \frac{\partial T}{\partial L_z} u^S_\phi \tag{6.11}$$

where T is given by the right-hand side of Eq. (2.23). Similarly for $\Delta\phi^S$, we use U^ϕ to get $\Delta\phi_{nkj}$ and consequently $\Delta\phi^S_{nkj}$, in which U^ϕ_S is as Eq. (6.11), but instead of V^t we use V^ϕ.

The linear in spin parts of Γ and ϕ are respectively $U^t_{S,000}$ and $U^\phi_{S,000}$ [130]. The coordinate-time frequencies read

$$\Omega_r = \frac{\hat{\Upsilon}_r + \Upsilon^S_r}{\hat{\Gamma} + \Gamma^S} \,, \quad \Omega_z = \frac{\hat{\Upsilon}_z + \Upsilon^S_z}{\hat{\Gamma} + \Gamma^S} \,, \quad \Omega_\phi = \frac{\hat{\Upsilon}_\phi + \Upsilon^S_\phi}{\hat{\Gamma} + \Gamma^S} \,, \quad \Omega_s = \frac{\hat{\Upsilon}_s}{\hat{\Gamma} + \Gamma^S} \,. \tag{6.12a}$$

The approach to calculate the linear in spin parts of the trajectory is described in Chapters 3 and 4 as well as Refs. [129], [130]. Subsequent simplifications were made to the equations given in these chapters; details are given in Appendix D.1. Using these simplifications, $u^S_{t,nk}$ and $u^S_{\phi,nk}$ can be calculated as

$$u^S_{t,nk} = \frac{i\mathcal{R}_{t,nk}}{n\hat{\Upsilon}_r + k\hat{\Upsilon}_z} \,, \quad u^S_{\phi,nk} = \frac{i\mathcal{R}_{\phi,nk}}{n\hat{\Upsilon}_r + k\hat{\Upsilon}_z} \tag{6.13}$$

for $n \neq 0$ or $k \neq 0$, where $\mathcal{R}_{t,nk}$ and $\mathcal{R}_{\phi,nk}$ are Fourier coefficients of functions given in Eqs. (D.5). Then, the Fourier coefficients $u^S_{t,00}$, $u^S_{\phi,00}$, $\delta\chi^S_{r,n}$, $\delta\chi^S_{z,k}$, $\not{r}^S_{nk}$, $\not{z}^S_{nk}$ and the frequencies' components Υ^S_r and Υ^S_z were calculated as the least squares solution to the system of linear equations

$$\mathbf{M} \cdot \mathbf{v} + \mathbf{c} = 0 \,. \tag{6.14}$$

as shown in Appendix A.3.2. In the system of equations (6.14), the column vector $\mathbf{v}$ contains the unknown coefficients, the column vector $\mathbf{c}$ is given from Fourier expansion components of the functions $\mathcal{J}$, $\mathcal{V}$ and $\mathcal{P}$ in Eqs. (D.5) that are not coefficients of the unknown quantities, while the elements of the matrix $\mathbf{M}$ are calculated from the Fourier coefficients of functions $\mathcal{F}_{r,\not{r}}$, $\mathcal{G}_{r,\not{r},\theta,\not{z}}$, $\mathcal{H}_{r,\not{r},\theta,\not{z}}$, $\mathcal{I}_{1r,1\theta,2,3}$, $\mathcal{Q}_{\theta,\not{z}}$, $\mathcal{S}_{r,\not{r},\theta,\not{z}}$, $\mathcal{T}_{r,\not{r},\theta,\not{z}}$, $\mathcal{U}_{1r,1\theta,2,3}$, $\mathcal{K}_{r,\not{r},\theta,\not{z}}$, $\mathcal{M}_{r,\not{r},\theta,\not{z}}$, $\mathcal{N}_{1r,1\theta}$, which are functions of the geodesic quantities and they are given in the supplemental material of [130], i.e., the published version of Chapter 4.

6.1.2 Gravitational-wave fluxes from a spinning test body

As discussed in Section 2.3, perturbations of the Newman-Penrose curvature scalar,

$$\psi_4 = -C_{\alpha\beta\gamma\delta} n^\alpha \overline{m}^\beta n^\gamma \overline{m}^\delta \tag{6.15}$$

can be found by solving the the Teukolsky equation [203]

$$ {}_{-2}\mathcal{O}\,{}_{-2}\Psi(t,r,\theta,\phi) = 4\pi\Sigma T\,, \tag{6.16} $$

where ${}_{-2}\Psi = \zeta^4\psi_4$, ${}_{-2}\mathcal{O}$ is a second order differential operator, T is the source term defined from $T^{\mu\nu}$ and where $C_{\alpha\beta\gamma\delta}$ is the Weyl tensor. We solve the Eq. (6.16) in frequency domain, where it can be decomposed as Eq. (2.65) and separated into two ordinary differential equations, one for the radial part $R_{lm}(r,\omega)$ and one for the angular part S_{lm}, which is called the spin-weighted spheroidal harmonic.

The radial equation reads

$$ \mathcal{D}_{lm\omega}R_{lm}(r,\omega) = \mathcal{T}_{lm\omega}\,, \tag{6.17} $$

where $\mathcal{D}_{lm\omega}$ is a second order differential operator which depends on r, and $\mathcal{T}_{lm\omega}$ is the source term which we describe later. Because the source term is zero around the horizon and infinity, the function $R_{lm}(r,\omega)$ must satisfy boundary conditions at these points for the vacuum case [204]:

$$ R_{lm}(r,\omega) \approx Z^{\infty}_{lm\omega}r^3e^{i\omega r_*} \qquad r\to\infty\,, \tag{6.18a} $$

$$ R_{lm}(r,\omega) \approx Z^{H}_{lm\omega}\Delta e^{-i(\omega-m\Omega_H)r_*} \qquad r\to r_+\,, \tag{6.18b} $$

where $\Omega_H = a/(2Mr_+)$ is the rotation frequency at the horizon and r_* is the tortoise coordinate, as defined in Sec. 2.3.1. The amplitudes at infinity and at the horizon $Z^{\infty,H}_{lm\omega}$ can be determined using the Green function formalism as

$$ Z^{\infty,H}_{lm\omega} = \frac{1}{W}\int_{r_+}^{\infty}\frac{R^{H,\infty}_{lm}\mathcal{T}_{lm\omega}}{\Delta^2}\mathrm{d}r\,, \tag{6.19} $$

where $R^{H,\infty}_{lm}(r)$ are the solutions of the homogeneous radial Teukolsky equation satisfying boundary conditions at the horizon and at infinity, respectively, and

$$ W = \big((\partial_r R^{\infty}_{lm})R^{H}_{lm} - R^{\infty}_{lm}\partial_r R^{H}_{lm}\big)/\Delta \tag{6.20} $$

is the invariant Wronskian.

Following [205], the source term can be written

$$ \mathcal{T}_{lm\omega} = \int \mathrm{d}t\mathrm{d}\theta\mathrm{d}\phi\Delta^2\sum_{ab}\mathcal{T}_{ab}e^{i\omega t - im\phi} \tag{6.21} $$

where $ab = nn, n\bar{m}, \bar{m}\bar{m}$ and

$$ \mathcal{T}_{ab} = \sum_{i=0}^{I_{ab}}\frac{\partial^i}{\partial r^i}\Big(f^{(i)}_{ab}\sqrt{-g}T_{ab}\Big) \tag{6.22} $$

with $I_{nn} = 0$, $I_{n\bar{m}} = 1$, $I_{\bar{m}\bar{m}} = 2$. Note that the functions $f^{(i)}_{ab}$, which are defined in Appendix D.2, are slightly different than the definition in [205]. The projection of the stress-energy tensor into the tetrad can be written as [206]

$$ \sqrt{-g}T_{ab} = \int \mathrm{d}\tau\big((A^{\mathrm{m}}_{ab} + A^{\mathrm{d}}_{ab})\delta^4 - \partial_\rho\big(B^{\rho}_{ab}\delta^4\big)\big) \tag{6.23a} $$

where

$$A^{\rm m}_{ab} = P_{(a}v_{b)} \,, \tag{6.23b}$$
$$A^{\rm d}_{ab} = S^{cd}v_{(b}\gamma_{a)dc} + S^{c}{}_{(a}\gamma_{b)dc}v^{d} \,, \tag{6.23c}$$
$$B^{\rho}_{ab} = S^{\rho}{}_{(a}v_{b)} \tag{6.23d}$$

and the spin coefficients are defined as

$$\gamma_{adc} = \lambda_{a\mu;\rho}\lambda^{\mu}_{d}\lambda^{\rho}_{c} \,. \tag{6.24}$$

After substituting Eqs. (6.21), (6.22), (6.23a) into Eq. (6.19) and integrating over the delta functions, the amplitudes $Z^{\infty,H}_{lm\omega}$ can be computed as

$$Z^{\infty,H}_{lm\omega} = \int_{-\infty}^{\infty} \frac{{\rm d}\tau}{\Sigma} e^{i\omega t(\tau) - im\phi(\tau)} I^{\infty,H}_{lm\omega}(r(\tau), z(\tau), u_a(\tau), S_{ab}(\tau)) \,, \tag{6.25}$$

where $I^{\infty,H}_{lm\omega}$ is defined as

$$I^{\infty,H}_{lm\omega} = \frac{\Sigma}{W}\sum_{ab}\sum_{i=0}^{I_{ab}}(-1)^{i}\Bigg(\Bigg(\Big(A^{\rm m}_{ab} + A^{\rm d}_{ab} + i\Big(\omega B^{t}_{ab} - mB^{\phi}_{ab}\Big)\Big)f^{(i)}_{ab} + B^{r}_{ab}\frac{\partial f^{(i)}_{ab}}{\partial r} + B^{z}_{ab}\frac{\partial f^{(i)}_{ab}}{\partial z}\Bigg)\frac{{\rm d}^{i}R^{H,\infty}_{lm\omega}}{{\rm d}r^{i}} + B^{r}_{ab}f^{(i)}_{ab}\frac{{\rm d}^{i+1}R^{H,\infty}_{lm\omega}}{{\rm d}r^{i+1}}\Bigg) \,. \tag{6.26}$$

Explicit expressions for $A^{\rm m}_{ab}$, $A^{\rm d}_{ab}$ and B^{μ}_{ab} are given in Appendix D.2.

Following a similar procedure to [207], it can be proven that the amplitudes can be written as a sum over discrete frequencies

$$Z^{\infty,H}_{lm\omega} = \sum_{m,n,k,j} Z^{\infty,H}_{lmnkj}\delta(\omega - \omega_{mnkj}) \quad \text{with} \quad \omega_{mnkj} = m\Omega_{\phi} + n\Omega_{r} + k\Omega_{z} + j\Omega_{s} \,. \tag{6.27}$$

The partial amplitudes are given by

$$Z^{\infty,H}_{lmnkj} = \frac{1}{(2\pi)^{2}\Gamma}\int_{0}^{2\pi}{\rm d}w_{r}\int_{0}^{2\pi}{\rm d}w_{z}\int_{0}^{2\pi}{\rm d}w_{s}\; I^{\infty,H}_{lmnkj}(w_{r},w_{z},w_{s}) \times \exp(i\omega_{mnkj}\Delta t(w_{r},w_{z},w_{s}) - im\Delta\phi(w_{r},w_{z},w_{s}) + inw_{r} + ikw_{z} + ijw_{s}) \,, \tag{6.28}$$

where $I^{\pm}_{lmnkj}(w_r,w_z,w_s) = I^{\pm}_{lm\omega_{mnkj}}(r(w_r,w_z,w_s), z(w_r,w_z,w_s), u_a(w_r,w_z,w_s), S_{ab}(w_r,w_z,w_s))$. As in Sec. 2.3.2, the averaged energy and angular momentum fluxes can be derived as

$$\left\langle \mathcal{F}^{E} \right\rangle \equiv \left(\frac{dE}{dt}\right)^{\infty} + \left(\frac{dE}{dt}\right)^{H} = \sum_{l,m,n,k,j}\mathcal{F}^{E}_{lmnkj} \,, \tag{6.29a}$$

$$\left\langle \mathcal{F}^{J_z} \right\rangle \equiv \left(\frac{dJ_z}{dt}\right)^{\infty} + \left(\frac{dJ_z}{dt}\right)^{H} = \sum_{l,m,n,k,j}\mathcal{F}^{J_z}_{lmnkj} \,, \tag{6.29b}$$

with

$$\mathcal{F}^{E}_{lmnkj} = \frac{\left|Z^{\infty}_{lmnkj}\right|^2 + \alpha_{lmnkj}\left|Z^{H}_{lmnkj}\right|^2}{4\pi\omega^2_{mnkj}}\,, \tag{6.29c}$$

$$\mathcal{F}^{J_z}_{lmnkj} = \frac{m\left(\left|Z^{\infty}_{lmnkj}\right|^2 + \alpha_{lmnkj}\left|Z^{H}_{lmnkj}\right|^2\right)}{4\pi\omega^3_{mnkj}}\,, \tag{6.29d}$$

where α_{lmnkj} is given by Eq. .

Since all the terms proportional to the perpendicular component $\sigma_\perp$ are purely oscillating with frequency Ω_s, the only contribution to the fluxes from $\sigma_\perp$ comes from the modes with $j = \pm 1$. The amplitudes $Z^{\infty,H}_{lmnkj}$ for $j = \pm 1$ are proportional to $\sigma_\perp$ and, therefore, the fluxes for $j = \pm 1$ are quadratic in $\sigma_\perp$. We can neglect them in the linear order in σ and sum over l, m, n and k with $j = 0$.

The fluxes $\left\langle \mathcal{F}^{E} \right\rangle$ and $\left\langle \mathcal{F}^{J_z} \right\rangle$ defined above were computed for the first time in Ref. [128]. See Figures 8 and 9 as well as Table 2 in Appendix E of Ref. [128] for numerical values of the spinning-body fluxes. Note that since the trajectory is computed up to linear order in σ, the amplitudes and the fluxes are valid up to $\mathcal{O}(\sigma)$ as well. Because the Fourier series (6.2) of the linear in spin part of the trajectory is truncated at $\pm n_{\max}$ and $\pm k_{\max}$, only a finite number of n and k modes of the amplitudes $C^{\pm}_{lmnk}$ and of the fluxes can be calculated accurately.

In the absence of secondary spin, the leading-order adiabatic contribution to the GW phase can be determined by analyzing the GW fluxes at infinity and the horizon, which obey flux-balance laws governing the evolution of energy, angular momentum, and the Carter constant [208]. For spinning objects within the linear-in-secondary-spin approximation, flux-balance laws have only been rigorously proven for energy and angular momentum fluxes [209], [210]. If the evolution of the linear-in-spin Carter-constant analog derived by Rüdiger [211], [212] could be derived from asymptotic fluxes in a manner analogous to Eqs. (2.79) and (2.80), this would enable the computation of the secondary spin's entire impact on the waveform. This remains as the final piece which would enable the complete assessment of the secondary spin's influence on the GW phase in generic inspirals.

6.2 Computing spinning-body GW fluxes using shifted-geodesic approximation

This section outlines a preliminary analysis which builds on the framework laid out in the previous section. The speed of computation of the amplitudes and fluxes presented in Sec. 6.1.2 is limited by the time taken to calculate the spinning-body trajectory presented in Sec. 6.1.1. Here, we approximate the spinning-body trajectory as a geodesic with its associated frequencies shifted such that they correspond to the those of a spinning body. In this way, we can expedite our calculation by leveraging existing infrastructure for computing adiabatic gravitational-wave fluxes along geodesic orbits using the Teukolsky formalism, discussed in Sec. 5.7.1. In particular, we extend the framework of the `GREMLIN` package, which is a frequency-domain Teukolsky solver written in C++ and developed by Scott Hughes (see Refs. [186], [213] and [204]), with the Mano-Suzuki-Takasugi (MST) approach used for solving the homogeneous Teukolsky equation, as described in Refs. [214], [215].

As outlined in Sec. 6.1.1, the parameterization of the spinning-body orbit utilized to compute the fluxes in the previous section is:

$$r = \frac{pM}{1 + e\cos\left((\hat{\Upsilon}_r + \Upsilon_r^S)\lambda + \delta\hat{\chi}_r + \delta\chi_r^S\right)} + \delta\,\text{𝓇}_S \,, \tag{6.30}$$

$$\cos\theta = \sin I \cos\left((\hat{\Upsilon}_\theta + \Upsilon_\theta^S)\lambda + \delta\hat{\chi}_\theta + \delta\chi_\theta^S\right) + \delta\,\text{𝓏}_S \,, \tag{6.31}$$

where $\hat{\Upsilon}_r + \Upsilon_r^S$ and $\hat{\Upsilon}_\theta + \Upsilon_\theta^S$ are the radial and polar frequencies respectively; the true anomaly angles are given by

$$\delta\chi_r^S = \sum_{n=-\infty}^{\infty} \delta\chi_{r,n}^S e^{-inw_r} \,, \quad \text{and} \quad \delta\chi_\theta^S = \sum_{k=-\infty}^{\infty} \delta\chi_{\theta,k}^S e^{-ikw_\theta} \,; \tag{6.32}$$

the radial libration variation is

$$\delta\,\text{𝓇}_S = \sum_{j=-1}^{1}\sum_{n,k=-\infty}^{\infty} \delta\,\text{𝓇}_{S,jnk} e^{-i(nw_r + kw_\theta + jw_s)} \,, \tag{6.33}$$

where k and j cannot both be zero; and the polar libration variation is

$$\delta\,\text{𝓏}_S = \sum_{j=-1}^{1}\sum_{n,k=-\infty}^{\infty} \delta\,\text{𝓏}_{S,,jnk} e^{-i(nw_r + kw_\theta + jw_s)} \,, \tag{6.34}$$

where n and j cannot both be zero.

This framework assumes a reference geodesic is specified by the parameters p, e, I that were described in detail in Chapter 2. The trajectory of a spinning particle has the same turning points after averaging: the particle oscillates between its radial and polar turning points, but, unlike in the geodesic case, the radial turning points depend on z and the polar turning points depend on r. This dependence is encoded in the corrections 𝓇^S and 𝓏^S, respectively. We observe that $\delta\chi_r^S$ and $\delta\chi_\theta^S$ consist of purely radial and purely polar oscillations respectively, while motion that is not purely radial or purely polar is contained in the functions $\delta\,\text{𝓇}_S$ and $\delta\,\text{𝓏}_S$. Because of the corrections 𝓇^S and 𝓏^S, the radial and polar motion have contributions from a combination of all the frequencies $n\Upsilon_r + k\Upsilon_z + j\Upsilon_s$, where n, k, and j are integers.

The only $\mathcal{O}(\sigma)$-correction that grows secularly is due to the shift in frequencies Υ_r^S and Υ_θ^S. The $\mathcal{O}(\sigma)$-quantities $\delta\chi_r^S$, $\delta\chi_\theta^S$, $\delta\,\text{𝓇}_S$ and $\delta\,\text{𝓏}_S$ contain purely oscillatory contributions by definition. We therefore propose an approximation scheme that omits these purely oscillatary terms when we compute GW fluxes assiated with spinning-body trajectories. Our approximation scheme thus requires replacing Eqs. (6.30) and (6.31) with

$$r = \frac{pM}{1 + e\cos\left((\hat{\Upsilon}_r + \Upsilon_r^S)\lambda + \delta\hat{\chi}_r\right)} \,, \tag{6.35}$$

$$\cos\theta = \sin I \cos\left((\hat{\Upsilon}_\theta + \Upsilon_\theta^S)\lambda + \delta\hat{\chi}_\theta\right) \,, \tag{6.36}$$

when evaluating the amplitudes given by Eq. (6.28) and fluxes given by Eq. (6.29). We call this a "shifted geodesic" approximation, because Eqs. (6.35) and (6.36) have the same form as a geodesic orbit, except with shifted frequencies, $\hat{\Upsilon}_r + \Upsilon_r^S$ and $\hat{\Upsilon}_\theta + \Upsilon_\theta^S$. In the next section, we compute amplitudes and fluxes using this approximation for a simplified case (an equatorial orbit with a monopole source term).

6.2.1 Equatorial orbit and monopole source limit

As a first step, we consider equatorial, spin-aligned orbits; see Ref. [124] for a detailed analysis of GW fluxes from a spinning-body orbiting on an equatorial trajectory. Our analysis will initially include only the monopole term C^0_{ab} when computing GW fluxes using the shifted geodesic approximation; this represents a preliminary, proof-of-principle calculation, which we plan to extend to include the dipole contribution to the source, as well as more generic orbital and spin configurations.

The stress-energy tensor projected along the Newman-Penrose basis for a non-spinning particle is [135]:

$$T_{ab} = \frac{C_{ab}}{\sin\theta}\delta[r - r(t)]\delta[\theta - \theta(t)]\delta[\phi - \phi(t)] \,, \tag{6.37}$$

where, for example, C_{nn} is given by:

$$C_{nn} = \frac{d\lambda}{dt}\frac{\mu}{4\Sigma^2}\left[E(r^2+a^2) - aL_z + \frac{dr}{d\lambda}\right]^2 \,. \tag{6.38}$$

See Eqs. (3.29b) and (3.29c) of Ref. [135] for expressions $C_{\bar{m}\bar{m}}$ and $C_{n\bar{m}}$. For the stress-energy tensor associated with a spinning particle, we have additional spin-dependent contributions to the monopole term C^0_{ab}, as well as a dipole terms depending on the spin tensor [124], viz.,

$$T_{ab} = \frac{1}{\sqrt{-g}}\delta^3(C^0_{ab} - C^\sigma_{ab}) - \frac{1}{\sqrt{-g}}\partial_\rho\left((v^t)^{-1}S^{\rho(\mu}v^{\nu)}\delta^3\right)e^{(a)}_\mu e^{(b)}_\nu \,, \tag{6.39}$$

where

$$C^0_{ab} = (v^t)^{-1}P^{(\mu}v^{\nu)}e^{(a)}_\mu e^{(b)}_\nu \,, \tag{6.40}$$

and

$$C^\sigma_{ab} = (v^t)^{-1}S^{\rho(\mu}\Gamma^{\nu)}_{\rho\lambda}v^\lambda e^{(a)}_\mu e^{(b)}_\nu \,. \tag{6.41}$$

Explicit expressions for C^0_{nn}, $C^0_{n\bar{m}}$ $C^0_{\bar{m}\bar{m}}$ C^σ_{nn}, $C^\sigma_{n\bar{m}}$ and $C^\sigma_{n\bar{m}}$ can be found in Eqs. (B21)–(B26) of Ref. [124]. For example, after linearizing in spin, C^0_{nn} becomes:

$$C^0_{nn} = \frac{d\lambda}{dt}\left[\frac{\left(Er^2 - a(L_z - aE) + dr/d\lambda\right)^2}{4r^2} + \sigma\frac{(aE - L_z + aEr)(a^2E - aL_z + Er^2 + dr/d\lambda)}{2r^3}\right] \,, \tag{6.42}$$

We aim to implement and test the shifted geodesic scheme for general orbital configurations as future work. As a benchmark, we will compare our results with Refs. [205] and [216]. We discuss further future work in the next chapter.

Chapter 7

Conclusions

Gravitational waves are detected by correlating observed data with precomputed theoretical models, called waveform templates. For EMRI signals, even a model-induced error of a fraction of a cycle can degrade measurement of astrophysical parameters. To capitalize fully on the potential of EMRIs, extremely accurate waveforms which match the phase of observed GW data across hundreds of thousands of orbits are essential. Building such models is only possible using perturbation theory and requires the synthesis of many complex theoretical elements, including self-force (due to the secondary object's interaction with its own gravitational field) and spin-curvature force (due to coupling of the secondary object's spin with the background spacetime).

This thesis presents two approaches for describing the influence of the spin of a small-body on its own trajectory and the associated gravitational waveforms. These are: (1) a frequency-domain formulation of spinning-body motion discussed in Chapters 3 and 4, and (2) an osculating-orbit scheme presented in Chapter 5. We combined the osculating-orbit picture of spin-curvature force with the leading-order adiabatic backreaction due to gravitational radiation to obtain approximate inspirals and waveforms in Chapter 5. The frequency-domain description of Chapters 3 and 4 was used to compute gravitational wave fluxes of a spinning-secondary orbit along generic trajectories in Ref. [128]; I outline this calculation in Chapter 6.

7.1 Precisely computing bound orbits of spinning bodies

In this thesis, I presented a frequency-domain approach for the precise computation of spinning-body orbits around a rotating black hole. Chapter 3 discusses the methods involved in this framework as well as a detailed study of equatorial and nearly equatorial orbits, while Chapter 4 investigates completely generic (both inclined and eccentric) orbits with arbitrarily oriented spin. We characterize the behavior of these orbits and contrast them with geodesic (non-spinning) trajectories. I employed this framework to calculate corrections to the orbital frequencies Υ_r and Υ_θ due to the secondary black hole's spin. This analysis enables the influence of secondary spin on observable gravitational wave phases to be quantified, which is essential for improving the accuracy of EMRI models for LISA.

Employing this framework, we calculated GW fluxes for completely general EMRI orbits

with a spinning secondary black hole for the first time in Ref. [128]; this analysis is discussed in Chapter 6. When computing gravitational radiation produced by a spinning body, one must include both the monopole source term associated with a point body, as well as an additional dipole term, which is linear in the small body's spin tensor. In Chapter 6, I described how gravitational wave fluxes along generic trajectories are computed with both of these source terms in the wave equation. I also outlined a "shifted geodesic" approximation scheme which aims to increase the efficiency of the spinning-body GW flux calculation.

One future objective is a systematic investigation of the behaviour of the spin-induced frequency corrections across the astrophysical parameter space. A catalog detailing these frequencies and their dependence on orbital and spin parameters will be valuable for the development of EMRI waveform models. Once such a catalog is established, the "shifted geodesic" approximation scheme which was discussed in Chapter 6, in combination with existing architecture for computing gravitational-wave fluxes for non-spinning particles [204], [213], could be used to develop efficient spinning-body waveform models. Another interesting direction for future work is to investigate the role of quadratic-order spin terms and the spin-induced quadrupole in the solutions of the Mathisson–Papapetrou equations and confirm numerically the existence of a Carter-constant analog at quadrupole-order [93]. Beyond the inspiral, the influence of the spin of the secondary on the transition from inspiral to a plunge into the larger black hole remains an open question to explore. This transition phase constitutes a significant part of the observed signal for intermediate mass-ratio inspirals.

7.2 Rapidly computing inspirals of spinning bodies

In Chapter 5, I introduced a osculating-orbit-based framework which combines orbit-averaged point-particle gravitational-wave backreaction with the orbital dynamics of spinning bodies. This framework rapidly generates inspiral worldlines for spinning bodies orbiting Kerr black holes in the extreme mass-ratio regime. The speed-up in trajectory computation by several orders of magnitude is achieved through a mathematical technique called a near-identity transformation (NIT), which is well-suited to the adiabatic evolution of an EMRI system. I demonstrated that the NIT trajectory can be used to generate a waveform that includes spinning-secondary effects, with minimal mismatch relative to the waveform computed using the trajectory generated with osculating geodesic methods.

The gravitational waveforms generated using this framework in Chapter 5 are incomplete, but provide a basis to enhance existing models of strong-field waveform generation using currently-available data. The framework's modular design allows for straightforward future inclusion of other important effects due to the astrophysical environment or the coupling of the small black hole to its own gravitational field. Due to the modularity of these terms, a flexible framework using osculating orbits and near-identity transformations may be particularly appropriate for combining the impact of many different post-adiabatic effects. Leveraging the orders-of-magnitude NIT speed-up, we aim to produce comprehensive EMRI waveforms which encompass all effects necessary for production-quality LISA signal models.

Previous studies have suggested that secondary spin may be challenging to measure in EMRI waveforms. However, these analyses were based on simpler (circular, equatorial and spin-aligned) orbital geometries. An interesting future direction would therefore be to assess

the detectability of secondary spin for generic orbits and spin orientations. Therefore, a detailed analysis of the measurability of secondary spin effects using the generic waveforms of Chapter 5 could provide interesting insight into this question. Finally, the astrophysical environment can leave a detectable imprint on the EMRI waveform: characterizing the transition where relativistic two-body effects (such as spin-curvature force) dominate over environmental effects (within a modular, NIT-based framework such as that presented in Chapter 5) could allow for the development of efficient waveform construction methods.

Appendix A

Chapter 3 Appendices

A.1 Explicit expression for the radial shift of a spinning body's orbit

In this paper, we seek periodic solutions to the linear-in-spin Mathisson-Pappaptrou equations. As outlined in Sec. 3.5, we characterize the radial coordinate of spinning-body orbits using the parameterization

$$r(\lambda) = \frac{pM}{1 + e\cos(w_r + \delta\hat{\chi}_r(w_r) + \delta\chi_r^S)} \,, \tag{A.1}$$

where

$$\delta\hat{\chi}_r(w_r) = \sum_{n=-\infty}^{\infty} \delta\hat{\chi}_{r,n} e^{-inw_r} \,, \tag{A.2}$$

$$\delta\chi_r^S = \sum_{n=-\infty}^{\infty} \delta\chi_{r,n}^S e^{-inw_r} \,, \tag{A.3}$$

and where

$$w_r = (\hat{\Upsilon}_r + \Upsilon_r^S)\lambda \,. \tag{A.4}$$

The quantities written with hat accents, $\hat{\Upsilon}_r$ and $\delta\hat{\chi}_r$, are computed using geodesic quantities — $\hat{\Upsilon}_r$ is the Mino-time radial frequency for the geodesic with semi-latus rectum p and eccentricity e, and $\delta\hat{\chi}_r$ describes the oscillating contribution to the true anomaly for that geodesic. The quantities $\delta\chi_r^S$ and Υ_r^S are both $\mathcal{O}(S)$.

Although $\delta\hat{\chi}_r$ is computed using geodesic quantities, notice that as implemented in this formula we include $\mathcal{O}(S)$ terms in it via the mean anomaly angle w_r. The Fourier coefficients $\delta\hat{\chi}_{r,n}$ are identical to those for a geodesic orbit, but the angle w_r in the exponent of Eq. (A.2) includes an $\mathcal{O}(S)$-term associated with the impact of the small body's spin on the orbit, Υ_r^S. This takes into account the fact that the spinning-body orbit's frequencies are shifted by Υ_r^S from those of the geodesic which shares its radial turning points.

Our goal in this Appendix is examine how the spinning body's orbit is shifted from the trajectory of the geodesic which shares the same turning points. To expedite this comparison,

in this Appendix we write the function $\delta\hat{\chi}_r$ with an argument of either w_r or $\hat{w}_r$, where $\hat{w}_r = \hat{\Upsilon}_r\lambda$. When we use $\delta\hat{\chi}_r(w_r)$, this is the function which parameterizes in part the true anomaly of a spinning body's orbit. This function's form is given explicitly by Eq. (A.2); it oscillates in phase with the radial motion $r(\lambda)$ of the spinning body. On the other hand, $\delta\hat{\chi}_r(\hat{w}_r)$ is the function that appears in the parameterization (A.6) of the geodesic orbit. It is identical to the form in Eq. (A.2) except with $w_r \to \hat{w}_r$. It oscillates in phase with the radial motion $\hat{r}(\lambda)$ of the geodesic orbit.

As discussed in Sec. 3.2.2, we can define the difference between the spinning body's orbit and that of the geodesic which shares its turning points as follows:

$$\delta r_S(\lambda) \equiv r(\lambda) - \hat{r}(\lambda) \,, \tag{A.5}$$

where $r(\lambda)$ describes the radial motion of a spinning body's orbit, and $\hat{r}(\lambda)$ describes the radial motion of the geodesic which shares its radial turning points. Note that $\delta r_S(\lambda) = \mathcal{O}(S)$.

We expect $\delta r_S(\lambda)$ to contain secularly growing terms due to the difference in frequencies between the geodesic and the spinning body's motion. For the parameterization defined in Eq. (A.1), the explicit expressions for $\hat{r}(\lambda)$ and $\delta r_S(\lambda)$ are:

$$\hat{r}(\lambda) = \frac{pM}{1 + e\cos\left(\hat{w}_r + \delta\hat{\chi}_r(\hat{w}_r)\right)} \tag{A.6}$$

and

$$\delta r_S(\lambda) = pMe\frac{\Upsilon^S_r\lambda\left(1 - i\sum_n n\delta\hat{\chi}_{r,n}e^{-in\hat{w}_r}\right) + \delta\chi^S_r}{\left(1 + e\cos\left(\hat{w}_r + \delta\hat{\chi}_r(\hat{w}_r)\right)\right)^2}\sin\left(\hat{w}_r + \delta\hat{\chi}_r(\hat{w}_r)\right) \,, \tag{A.7}$$

where we have used the fact that $\Upsilon^S_r = \mathcal{O}(S)$. The secular growth of δr_S apparent in Eq. (A.7) is a somewhat troublesome mathematical artefact of the fact that we are comparing two integrable systems that have slightly different frequencies. This is troublesome because we would like to think of the spinning body's orbit as "close to" the geodesic which shares its turning points. Though this describes the behavior of δr_S for small λ, this quantity evolves such that it eventually cannot be regarded as a perturbation.

To address this, we compare the two solutions in such a way that we avoid secularly growing terms, following a Poincare-Lindstedt-type approach [182]. We begin by shifting the frequency of the geodesic solution so that it matches the frequency of the spinning-body orbit. Let us define

$$\hat{r}_{\rm shift}(\lambda) = \frac{pM}{1 + e\cos\left(w_r + \delta\hat{\chi}_r(w_r)\right)} \,. \tag{A.8}$$

This is just Eq. (A.6), but with the geodesic mean anomaly $\hat{w}_r = \hat{\Upsilon}_r\lambda$ replaced by the mean anomaly $w_r = (\hat{\Upsilon}_r + \Upsilon^S_r)\lambda$. We then define

$$\delta r^{\rm shift}_S(\lambda) = r(\lambda) - \hat{r}_{\rm shift}(\lambda) \,, \tag{A.9}$$

where again $r(\lambda)$ describes the radial motion of a spinning body's orbit. We introduce the superscript label "shift" to distinguish this quantity from that introduced in Eq. (A.5), noting

that its frequency is shifted from the geodesic frequency. Using Eqs. (A.1) and (A.8), we find

$$\delta r_S^{\rm shift}(\lambda) = pMe\frac{\delta\chi_r^S(w_r)\sin\left[w_r+\delta\hat{\chi}_r(w_r)\right]}{\left(1+e\cos\left[w_r+\delta\hat{\chi}_r(w_r)\right]\right)^2}\,. \tag{A.10}$$

The quantity $\delta r_S^{\rm shift}(\lambda)$ does not grow secularly, but is instead periodic at the radial period $\Lambda_r = 2\pi/\left(\hat{\Upsilon}_r + \Upsilon_r^S\right)$. We can use Fourier expansions quite naturally to describe $\delta r_S^{\rm shift}(\lambda)$ which is advantageous for the frequency-domain approach we use in this paper.

A.2 Comparison with Saijo et al., 1998: Aligned spin, equatorial orbits

Considerable work has been done previously on equatorial orbits with aligned spin. Almost all such work uses the equations of motion describing a spinning body confined to the equatorial plane that were derived by Saijo et al. [67]. Saijo et al. use the conserved quantities E^S, L^S, $S^2 = S^\alpha S_\alpha$ and $-\mu^2 = p^\alpha p_\alpha$ in order to derive these equations; their full derivation is in Ref. [67] (see also Refs. [68] and [66] for similar related discussion). We present the equations for Kerr spacetime below in Eqs. (A.11) – (A.15).

The radial component of Eq. (2.47), taking the limit of a body confined to an equatorial orbit with aligned spin, can be written

$$\Sigma_s\Lambda_s\frac{dr}{d\tau} = \pm\sqrt{R_s}\,, \tag{A.11}$$

where

$$R_s = P_s^2 - \Delta\left(\frac{\Sigma_s^2}{r^2} + \left[L_z^S - (a+s_\parallel\mu)E^S\right]^2\right)\,, \tag{A.12}$$

$$P_s = \left[(r^2+a^2) + as_\parallel\mu\left(1+\frac{M}{r}\right)\right]E^S - \left(a+\frac{s_\parallel\mu M}{r}\right)L_z^S\,, \tag{A.13}$$

$$\Sigma_s = r^2\left(1-\frac{s_\parallel^2\mu^2 M}{r^3}\right)\,, \tag{A.14}$$

$$\Lambda_s = 1 - \frac{3s_\parallel^2\mu^2 Mr\left[L_z^S-(a+s_\parallel\mu)E^S\right]^2}{\Sigma_s^3}\,. \tag{A.15}$$

We begin our discussion with the Schwarzschild limit, for which we find particularly compact and convenient expressions.

A.2.1 Schwarzschild spacetime

Linearizing in the small body's spin, Eq. (A.11) reduces to a simple form, as presented in Appendix B.3 of Ref. [73]. We reproduce the result here in our notation, noting that our

parameter $s_\parallel$ is dimensionless, and so differs from the correspond spin parameter used in Ref. [73] by a factor of μ:

$$\left(\frac{dr}{d\tau}\right)^2 = (E^S)^2 - \left(V_{\rm eff}^{\rm Schw}\right)^2 + 2s_\parallel \mu \frac{\hat{E}\hat{L}_z}{r^2}\left(1 - \frac{3M}{r}\right) + \mathcal{O}(S^2) \,, \tag{A.16}$$

where $V_{\rm eff}^{\rm Schw}$ is the usual effective potential for the Schwarzschild metric, but using the angular momentum for a spinning-body orbit:

$$\left(V_{\rm eff}^{\rm Schw}\right)^2 = \left(1 - \frac{2M}{r}\right)\left(1 + \frac{(L_z^S)^2}{r^2}\right) \,. \tag{A.17}$$

Equation (A.16) is Eq. (B14) of Ref. [73], adapted to our notation and linearizing in spin.

Circular equatorial orbits

To find the energy and angular momentum corresponding for a body in circular orbit with its spin aligned with the orbit, begin by requiring $dr/d\tau = 0$. This yields a quadratic equation for E^S whose solution to linear order in s is

$$\begin{aligned}(E^S)^2 &= (V_{\rm eff}^{\rm Schw}) - s_\parallel \mu \frac{\hat{L}_z}{r^2}\left(1 - \frac{3M}{r}\right) \\ &\equiv V_{\rm eff}^{\rm Schw,spin} \,.\end{aligned} \tag{A.18}$$

Further requiring $\partial V_{\rm eff}^{\rm Schw,spin}/\partial r = 0$ yields the solutions

$$E^S = \frac{r - 2M}{\sqrt{r(r-3M)}} - \frac{s_\parallel \mu}{2r}\left(\frac{M}{r-3M}\right)^{3/2} \,, \tag{A.19}$$

$$L_z^S = \frac{r\sqrt{M}}{\sqrt{r-3M}} + \frac{s_\parallel \mu}{2}\frac{(r-2M)(2r-9M)}{\sqrt{r}(r-3M)^{3/2}} \,. \tag{A.20}$$

These expressions match exactly with Eq. (3.37) and (3.38) in the limit $a = 0$; these expressions can also be found[1] in Eq. (B17) and (B18) of Ref. [73]. Similarly, the expressions in Eqs. (54) and (55) of Ref. [68] reduce to (A.19) in the first order in spin limit.

Eccentric equatorial orbits

Next we consider eccentric equatorial orbits. We begin again with Eq. (A.16), but now multiply by $\Sigma^2 = r^4$, using $d/d\lambda = \Sigma\, d/d\tau$ to change into an expression for $(dr/d\lambda)^2$:

$$\begin{aligned}\left(\frac{dr}{d\lambda}\right)^2 &= r^4(E^S)^2 - r\,(r-2M)\left(r^2 + (L_z^S)^2\right) + 2s_\parallel \mu r \hat{E}\hat{L}_z\,(r-3M) + \mathcal{O}(S^2) \\ &\equiv R_s^{\rm Schw}(r) \,.\end{aligned} \tag{A.21}$$

[1] Note that Eq. (B18) in Ref. [73] contains a typographical error in the denominator; the $r - 2m_2$ should be $r - 3m_2$.

With this formulation of Eq. (A.16), we can straightforwardly compute Υ_r^S, δE^S and δL^S and compare with results we obtain elsewhere in this work.

We begin by substituting $E^S = \hat{E} + \delta E^S$, $L_z^S = \hat{L}_z + \delta L_z^S$, with δE^S and δL_z^S both $\mathcal{O}(S)$, into Eq. (A.21) and expand to first order in spin, yielding

$$R_s^{\rm Schw}(r) = R^{\rm Schw}(r) + \delta R_s^{\rm Schw}(r) + \mathcal{O}(S^2) \,, \tag{A.22}$$

where

$$R^{\rm Schw}(r) = r^4\hat{E} - r(r-2M)(r^2+\hat{L}_z) \,, \tag{A.23}$$

$$\delta R_s^{\rm Schw}(r) = 2r\left[s_\parallel \mu (r-3M)\hat{E}\hat{L}_z + r^3\hat{E}\delta E^S - (r-2M)\hat{L}_z\delta L_z^S\right] \,. \tag{A.24}$$

Using $dr/d\lambda = 0$ at the turning points $r = pM/(1\pm e)$ yields the well-known results

$$\hat{E} = \sqrt{\frac{(p-2)^2-4e^2}{p(p-3-e^2)}} \,, \quad \hat{L}_z = \frac{pM}{\sqrt{p-3-e^2}} \tag{A.25}$$

describing these orbit integrals for Schwarzschild geodesics. Requiring that $r = pM/(1\pm e)$ remaining turning points for the spinning bodies orbit, we require $\delta R_s^{\rm Schw} = 0$ at these points as well. This yields

$$\delta E^S = -\frac{s_\parallel \mu}{M}\frac{(1-e^2)^2}{2p(p-3-e^2)^{3/2}} \,, \tag{A.26}$$

$$\delta L_z^S = s_\parallel \mu \frac{(2p-9-3e^2)\sqrt{(p-2)^2-4e^2}}{2p^{1/2}(p-3-e^2)^{3/2}} \,. \tag{A.27}$$

These expressions are identical to those in Eqs. (46) of Ref. [71] with $r_a = pM/(1-e)$ and $r_p = pM/(1+e)$.

Next, we use Eq. (3) in Ref. [139] to calculate Λ_r, but using $R_s^{\rm Schw}(r)$ as defined in Eq. (A.21):

$$\Lambda_r = 2\int_{r_{min}}^{r_{max}} \frac{dr}{\sqrt{R_s^{\rm Schw}(r)}} \,, \tag{A.28}$$

with

$$r_{min} = \frac{pM}{1+e} \,, \quad r_{max} = \frac{pM}{1-e} \,. \tag{A.29}$$

Using the parameterization of radial motion defined by Eq. (3.72), we turn equation (A.28) into an integral over χ_r:

$$\Lambda_r = 2\int_0^\pi \frac{1}{\sqrt{R_s^{\rm Schw}(\chi_r)}}\frac{dr}{d\chi_r}d\chi_r \,, \tag{A.30}$$

where

$$r = \frac{pM}{1+e\cos\chi_r} \,, \quad \frac{dr}{d\chi_r} = \frac{peM\sin\chi_r}{1+e\cos\chi_r} \,. \tag{A.31}$$

Noting that $\Lambda_r = \hat{\Lambda}_r + \Lambda_r^S$, we break this integral into geodesic and $\mathcal{O}(S)$ pieces:

$$\hat{\Lambda}_r = 2\int_0^\pi \frac{1}{\sqrt{R^{\rm Schw}(\chi_r)}}\frac{dr}{d\chi_r}d\chi_r \ , \tag{A.32}$$

$$\Lambda_r^S = -\int_0^\pi \frac{\delta R_s^{\rm Schw}(\chi_r)}{R^{\rm Schw}(\chi_r)^{3/2}}\frac{dr}{d\chi_r}d\chi_r \ . \tag{A.33}$$

The definitions $\Upsilon_r = 2\pi/\Lambda_r$ and $\Upsilon_r = \hat{\Upsilon}_r + \Upsilon_r^S$ yielding

$$\hat{\Upsilon}_r = \frac{2\pi}{\hat{\Lambda}_r} \ , \quad \Upsilon_r^S = -\frac{2\pi\Lambda_r^S}{\hat{\Lambda}_r^2} \ . \tag{A.34}$$

This allows us to at last evaluate Υ_r^S as a simple quadrature:

$$\Upsilon_r^S = \frac{2\pi}{\hat{\Lambda}_r^2}\int_0^\pi \frac{\delta R_s^{\rm Schw}(r)}{R^{\rm Schw}(r)^{3/2}}\frac{dr}{d\chi_r}d\chi_r \ , \tag{A.35}$$

which we write explicitly as

$$\Upsilon_r^S = -\frac{2\pi s_\parallel \mu}{\hat{\Lambda}_r^2 M^2}\int_0^\pi \frac{(e^2-3-2e\cos\chi_r)\sqrt{(p-2)^2-4e^2}}{p\sqrt{p-3-e^2}(p-6-2e\cos\chi_r)^{3/2}}d\chi_r \ . \tag{A.36}$$

Equations (A.26), (A.27) and (A.36) expanded to second-order in eccentricity, yield expressions that match Eqs. (3.132), (3.133) and (3.128).

A.2.2 Kerr spacetime

We now consider Eq. (A.11) to leading order in spin, but for general Kerr parameter a:

$$\begin{aligned}\left(\frac{dr}{d\lambda}\right)^2 &= [E^S(r^2+a^2) - aL_z^S]^2 - \Delta[r^2 + (L_z^S - aE^S)^2] \\ &\quad + 2as_\parallel\mu M\frac{\left[\hat{L}_z^2 - 2a\hat{E}\hat{L}_z + a^2\hat{E}^2\right]}{r} \\ &\quad + 2s_\parallel\mu r\hat{E}\left[\hat{L}_z(r-3M) + 3Ma\hat{E}\right] + \mathcal{O}(S^2) \\ &\quad \equiv R_s^{\rm Kerr}(r) \ .\end{aligned} \tag{A.37}$$

Circular equatorial orbits

To compute the energy and axial angular momentum of a spinning body in an aligned circular Kerr orbit, we need to find E^S and L_z^S such that $R_s^{\rm Kerr}(r) = 0$ and $\partial R_s^{\rm Kerr}(r)/\partial r = 0$. This gives expressions that match Eqs. (3.37) and (3.38). Hackmann et al. also have expressions for E^S and L_z^S that are exact in spin for general a; compare Eqs. (48) and (49) of Ref. [68]. Piovano et al. likewise provide E^S and L_z^S in slightly different notation; compare Eqs. (59) and (60) of Ref. [217].

Eccentric equatorial orbits

As in our Schwarzschild analysis, we insert $E^S = \hat{E} + \delta E^S$, $L_z^S = \hat{L}_z + \delta L_z^S$ into Eq. (A.37) and expand to first order in spin, yielding

$$R_s^{\rm Kerr}(r) = R^{\rm Kerr}(r) + \delta R_s^{\rm Kerr}(r) + \mathcal{O}(S^2) \,, \tag{A.38}$$

where

$$R^{\rm Kerr}(r) = [\hat{E}(r^2+a^2) - a\hat{L}_z]^2 - \Delta[r^2 + (\hat{L}_z - a\hat{E})^2] \,, \tag{A.39}$$

and where

$$\begin{aligned}\delta R_s^{\rm Kerr} = 2\Bigg\{ & a s_\parallel \mu M \frac{\left[\hat{L}_z^2 - 2a\hat{E}\hat{L}_z + a^2\hat{E}^2\right]}{r} + s_\parallel \mu r \hat{E}\left[\hat{L}_z(r-3M) + 3aM\hat{E}\right] \\ & + ar\left[2M\left(\hat{E}\delta L^S + \hat{L}_z \delta E^S\right) - a\hat{E}\delta E^S(r+2M)\right] \\ & + r\left[\hat{L}_z \delta L^S (r-2M) - \hat{E}\delta E^S r^3\right]\Bigg\} \,. \end{aligned} \tag{A.40}$$

Note that $R^{\rm Kerr}(r)$ is given by Eq. (2.20) with $\hat{Q} \to 0$. Expressions for $\hat{E}$ and $\hat{L}_z$ which are exact in eccentricity are given in Eqs. (A.1) and (A.2) of Ref. [144].

As in the Schwarzschild analysis, we solve for δE^S and δL_z^S by requiring $\delta R_s^{\rm Kerr} = 0$ at $r = pM/(1 \pm e)$. This yields closed-form expressions for $\delta E^S(p,e)$ and $\delta L_z^S(p,e)$ analogous to Eqs. (A.26) and (A.27) which apply for general a, but are quite lengthy and cumbersome. We refer the reader to Eqs. (81) and (83) of Ref. [71] for expressions for E^S and L_z^S to first order in small body spin derived by Mukherjee et al., as well as to Eqs. (38) and (39) of Ref. [124] for exact-in-S expressions for E^S and L_z^S derived by Skoupý et al. Both Skoupý et al. and Mukherjee et al. write their expressions in terms of $r_a = pM/(1-e)$ and $r_p = pM/(1+e)$. To first order in e, the results for δE^S and δL_z^S reduce to Eqs. (3.37) – (3.38), but with $v = \sqrt{1/p}$.

We evaluate Υ_r^S using a formulation analogous to what was done in Sec. A.2.1, replacing the Schwarzschild function $R_s^{\rm Schw}(r)$ with $R_s^{\rm Kerr}(r)$:

$$\Upsilon_r^S = \frac{2\pi}{\hat{\Lambda}_r^2} \int_0^\pi \frac{\delta R_s^{\rm Kerr}(r)}{R^{\rm Kerr}(r)^{3/2}} \frac{dr}{d\chi_r} d\chi_r \,. \tag{A.41}$$

Expanded to first order in eccentricity, this reproduces Eq. (3.91).

A.3 Explicit frequency-domain expressions

A.3.1 Coefficient functions

In Sec. 3.5.1, we examine spinning-body motion in the equatorial plane using a frequency-domain expansion. We linearize the radial component of the first Matthisson-Papapetrou equation (2.47) in small-body spin and re-express it in terms of quantities which are unknown

(i.e., $\delta\chi_r^S$, Υ_r^S, $u_{t,0}^S$ and $u_{\phi,0}^S$) and Fourier coefficients of functions along geodesics (i.e., $\mathcal{F}_r$, $\mathcal{G}_r$, $\mathcal{H}_r$, $\mathcal{I}_{1r}$, $\mathcal{I}_2$, $\mathcal{I}_3$ and $\mathcal{J}$). This yields Eq. (3.148).

We also linearize the constraint $u^\alpha u_\alpha = -1$ in small-body spin, writing down the corresponding equation (3.149) in terms of the same set of unknowns as well as coefficients $\mathcal{K}_r$, $\mathcal{M}_r$, $\mathcal{N}_{1r}$, $\mathcal{N}_2$, $\mathcal{N}_3$ and $\mathcal{P}$ that likewise arise from known geodesics. We follow a similar procedure in Sec. 3.5.2 to compute the nearly equatorial motion of a precessing spinning body. In this case, we also linearize the θ-component of Eq. (2.47) in small-body spin, obtaining Eq. (3.157). In the nearly equatorial limit, the only non-zero coefficients in this equation are $\mathcal{Q}_\vartheta$, T_ϑ and $\mathcal{V}$.

In this Appendix, we provide explicit expressions for the Schwarzschild case of the various functions which we then expand in the Fourier domain. These expressions for the functions appearing in Eq. (3.148) are given by:

$$\mathcal{F}_r(\lambda) = \frac{ep\sin\hat{\chi}_r}{(1+e\cos\hat{\chi}_r)^2}\,, \quad \mathcal{G}_r(\lambda) = \frac{ep\left(\delta\hat{\chi}_r'(\lambda)+\hat{\Upsilon}_r\right)\left(e(\cos(2\hat{\chi}_r)+3)-2(p-2)\cos\hat{\chi}_r\right)}{(1+e\cos\hat{\chi}_r)^2(2e\cos\hat{\chi}_r-p+2)}\,, \tag{A.42}$$

$$\begin{aligned}
\mathcal{H}_r(\lambda) = -\frac{ep}{4(e\cos\hat{\chi}_r+1)^3(p-2-2e\cos\hat{\chi}_r)^2}\Bigg\{&-2\sin\hat{\chi}_r\Big[2\hat{L}_z^2\left(e^2(p-3)-(p-2)^2\right)\\
&+\hat{\Upsilon}_r^2\left(e^2(15-6p)-2(p-2)^2\right)+4\hat{E}^2(p-3)p^2\Big]\\
&+e\Big[2\sin(2\hat{\chi}_r)\Big(\hat{L}_z^2\left(2e^2+p^2-8p+12\right)-\hat{\Upsilon}_r^2\left(7e^2+(p-2)p\right)+6\hat{E}^2p^2\Big)\\
&+e\Big(e\left(2\hat{L}_z^2-\hat{\Upsilon}_r^2\right)\sin(4\hat{\chi}_r)+\sin(3\hat{\chi}_r)\left(2(2p-3)\hat{\Upsilon}_r^2-4\hat{L}_z^2(p-3)\right)\Big)\Big]\\
&-2\delta\hat{\chi}_r'(\lambda)\sin\hat{\chi}_r\left(\delta\hat{\chi}_r'(\lambda)+2\hat{\Upsilon}_r\right)\Big[e^2(e\cos(3\hat{\chi}_r)+(6-4p)\cos(2\hat{\chi}_r))\\
&+e\left(15e^2+2(p-2)p\right)\cos\hat{\chi}_r-2\left(e^2(4p-9)+(p-2)^2\right)\Big]\\
&+2\delta\hat{\chi}_r''(\lambda)(e(\cos(2\hat{\chi}_r)-3)-2\cos\hat{\chi}_r)(p-2-2e\cos\hat{\chi}_r)^2\Bigg\}\,,
\end{aligned} \tag{A.43}$$

$$\mathcal{I}_{1r}(\lambda) = \frac{ep\left(\Xi_2(\lambda)\sin\hat{\chi}_r\right)}{(e\cos\hat{\chi}_r+1)^2} + \frac{ep\left(\Xi_1(\lambda)+1\right)\left(\delta\hat{\chi}_r'(\lambda)+\hat{\Upsilon}_r\right)\left(e(\cos(2\hat{\chi}_r)+3)-2(p-2)\cos\hat{\chi}_r\right)}{(e\cos\hat{\chi}_r+1)^2(2e\cos\hat{\chi}_r-p+2)}\,, \tag{A.44}$$

$$\mathcal{I}_2(\lambda) = -\frac{2\hat{E}p^3}{(e\cos\hat{\chi}_r+1)^2(p-2-2e\cos\hat{\chi}_r)}\,, \quad \mathcal{I}_3(\lambda) = \hat{L}_z\left(4-\frac{2p}{e\cos\hat{\chi}_r+1}\right)\,, \tag{A.45}$$

$$\mathcal{J}(\lambda) = \frac{3\hat{E}\hat{L}_z S_\theta(1+e\cos\hat{\chi}_r)}{p} - \frac{2\hat{E}p^3\delta u_t^S(\lambda)}{(1+e\cos\hat{\chi}_r)^2(p-2-2e\cos\hat{\chi}_r)} - \frac{2\hat{L}_z\delta u_\phi^S(\lambda)(p-2-2e\cos\hat{\chi}_r)}{(1+e\cos\hat{\chi}_r)} , \tag{A.46}$$

where we have defined

$$\Xi_1(\lambda) = -i\sum_{n=-n_{\rm max}}^{n_{\rm max}} n\delta\hat{\chi}_{r,n}e^{-in\hat{\Upsilon}_r\lambda} , \quad \text{and} \quad \Xi_2(\lambda) = -2\hat{\Upsilon}_r\sum_{n=-n_{\rm max}}^{n_{\rm max}} n^2\delta\hat{\chi}_{r,n}e^{-in\hat{\Upsilon}_r\lambda} . \tag{A.47}$$

Here $\Xi_1(\lambda)$ and $\Xi_2(\lambda)$ are functions that depend on the Fourier coefficients of geodesic radial true anomaly $\delta\hat{\chi}_r$. We also write down the expressions for the functions which appear in Eq. (3.149) explicitly, again limiting ourselves here to the Schwarzschild limit:

$$\mathcal{K}_r(\lambda) = \frac{2e^2\sin^2\hat{\chi}_r\left(\delta\hat{\chi}_r'(\lambda)+\hat{\Upsilon}_r\right)}{p(p-2-2e\cos\hat{\chi}_r)} , \tag{A.48}$$

$$\begin{aligned}\mathcal{M}_r(\lambda) = \frac{e}{2p^2(p-2-2e\cos\hat{\chi}_r)^2}\Bigg\{&\sin\hat{\chi}_r\left(4\hat{L}_z^2\left(e^2(p-3)-(p-2)^2\right)-5e^2p\hat{\Upsilon}_r^2+4\hat{E}^2p^3\right)\\ &+e\Bigg[e\left(\sin(3\hat{\chi}_r)\left(4\hat{L}_z^2(p-3)-p\hat{\Upsilon}_r^2\right)-2e\hat{L}_z^2\sin(4\hat{\chi}_r)\right)\\ &-2\sin(2\hat{\chi}_r)\left(\hat{L}_z^2\left(2e^2+p^2-8p+12\right)-(p-2)p\hat{\Upsilon}_r^2\right)\Bigg]\\ &-2ep\delta\hat{\chi}_r'(\lambda)\sin\hat{\chi}_r\left(\delta\hat{\chi}_r'(\lambda)+2\hat{\Upsilon}_r\right)\left(e(\cos(2\hat{\chi}_r)+3)-2(p-2)\cos\hat{\chi}_r\right)\Bigg\} ,\end{aligned} \tag{A.49}$$

$$\mathcal{N}_{1r}(\lambda) = \frac{2e^2(\Xi_1(\lambda)+1)\left(\delta\hat{\chi}_r'(\lambda)+\hat{\Upsilon}_r\right)\sin^2\hat{\chi}_r}{p(p-2-2e\cos\hat{\chi}_r)} , \quad \mathcal{N}_2(\lambda) = \frac{2p\hat{E}}{p-2-2e\cos\hat{\chi}_r} , \tag{A.50}$$

$$\mathcal{N}_3(\lambda) = \frac{2\hat{L}_z(1+e\cos\hat{\chi}_r)^2}{p^2} , \quad \text{and} \quad \mathcal{P}(\lambda) = \frac{2p\hat{E}\delta u_t^S(\lambda)}{p-2-2e\cos\hat{\chi}_r} + \frac{2\hat{L}_z\delta u_\phi^S(\lambda)\left(1+e\cos\hat{\chi}_r\right)^2}{p^2} . \tag{A.51}$$

In the nearly equatorial limit, the only non-zero functions which appear in Eq. (3.157) are

$$\mathcal{Q}_\vartheta(\lambda) = 1 , \quad T_\vartheta(\lambda) = \hat{L}_z^2 , \tag{A.52}$$

$$\mathcal{V}(\lambda) = \frac{3\hat{L}_z(1+e\cos\hat{\chi}_r)\left(S_r\hat{E}(p-2-2e\cos\hat{\chi}_r)+eS_t(\hat{\Upsilon}_r+\delta\hat{\chi}_r'(\lambda))\sin\hat{\chi}_r\right)}{p(p-2-2e\cos\hat{\chi}_r)} . \tag{A.53}$$

In the Supplemental Material accompanying this paper, we include a *Mathematica* notebook which computes these expressions for general Kerr (i.e., for $a \neq 0$) [181].

A.3.2 Matrix System

As discussed in Sec. 3.5.1, our procedure to solve for the spinning body's orbit in the frequency domain involves writing the functions $\mathcal{F}_r$, $\mathcal{G}_r$, $\mathcal{H}_r$, $\mathcal{I}_{1r}$, $\mathcal{I}_2$, $\mathcal{I}_3$ $\mathcal{J}$, $\mathcal{K}_r$, $\mathcal{M}_r$, $\mathcal{N}_{1r}$, $\mathcal{N}_2$,

$\mathcal{N}_3$ and $\mathcal{P}$ as Fourier expansions of the form

$$f(\lambda) = \sum_{n=-n_{\rm max}}^{n_{\rm max}} f_n e^{-in\hat{\Upsilon}_r\lambda} \,. \tag{A.54}$$

We similarly express the unknown function $\delta\chi_r^S(\lambda)$ as a Fourier expansion,

$$\delta\chi_r^S(\lambda) = \sum_{n=-n_{\rm max}}^{n_{\rm max}} \delta\chi_{r,n}^S e^{-in\hat{\Upsilon}_r\lambda} \,, \tag{A.55}$$

aiming to solve for its Fourier coefficients $\delta\chi_{r,n}^S$.

To do so, we insert expansions (A.54) and (A.55) into Eqs. (3.148) and (3.149). This yields a system of linear equations in the frequency-domain which allows us to solve for the unknown variables $\delta\chi_r^S$, Υ_r^S, $u_{\phi,0}^S$ and $u_{t,0}^S$. This system of equations can be written

$$\mathbf{M}\cdot\mathbf{v} + \mathbf{c} = 0 \,. \tag{A.56}$$

To get a sense of the character of this system of equations, for the choice $n_{\rm max} = 1$, the matrix $\mathbf{M}$ and vectors $\mathbf{v}$ and $\mathbf{c}$ are given explicitly by

$$\mathbf{M} = \begin{pmatrix} -\mathcal{F}_{r,0}\hat{\Upsilon}_r^2 - i\mathcal{G}_{r,0}\hat{\Upsilon}_r - \mathcal{H}_{r,0} & 0 & \mathcal{I}_{1r,1} & \mathcal{I}_{2,1} & \mathcal{I}_{3,1} \\ -\mathcal{F}_{r,-1}\hat{\Upsilon}_r^2 - i\mathcal{G}_{r,-1}\hat{\Upsilon}_r - \mathcal{H}_{r,-1} & -\mathcal{F}_{r,1}\hat{\Upsilon}_r^2 + i\mathcal{G}_{r,1}\hat{\Upsilon}_r + \mathcal{H}_{r,1} & \mathcal{I}_{1r,0} & \mathcal{I}_{2,0} & \mathcal{I}_{3,0} \\ 0 & -\mathcal{F}_{r,0}\hat{\Upsilon}_r^2 + i\mathcal{G}_{r,0}\hat{\Upsilon}_r + \mathcal{H}_{r,0} & \mathcal{I}_{1r,-1} & \mathcal{I}_{2,-1} & \mathcal{I}_{3,-1} \\ \mathcal{M}_{r,0} - i\mathcal{K}_{r,0}\hat{\Upsilon}_r & 0 & \mathcal{N}_{1r,1} & \mathcal{N}_{2,1} & \mathcal{N}_{3,1} \\ \mathcal{M}_{r,-1} - i\mathcal{K}_{r,-1}\hat{\Upsilon}_r & \mathcal{M}_{r,1} + i\mathcal{K}_{r,1}\hat{\Upsilon}_r & \mathcal{N}_{1r,0} & \mathcal{N}_{2,0} & \mathcal{N}_{3,0} \\ 0 & \mathcal{M}_{r,0} + i\mathcal{K}_{r,0}\hat{\Upsilon}_r & \mathcal{N}_{1r,-1} & \mathcal{N}_{2,-1} & \mathcal{N}_{3,-1} \end{pmatrix} , \tag{A.57}$$

$$\mathbf{v} = \begin{pmatrix} \delta\chi_{r,1}^S \\ \delta\chi_{r,-1}^S \\ \Upsilon_r^S \\ u_{t,0}^S \\ u_{\phi,0}^S \end{pmatrix} \,, \quad \text{and} \quad \mathbf{c} = \begin{pmatrix} \mathcal{J}_1 \\ \mathcal{J}_0 \\ \mathcal{J}_{-1} \\ \mathcal{P}_1 \\ \mathcal{P}_0 \\ \mathcal{P}_{-1} \end{pmatrix} \,. \tag{A.58}$$

Note that $\mathbf{M}$ is not a square matrix; the system is slightly overconstrained. We use the `PseudoInverse` *Mathematica* function to find the values of $\delta\chi_{r,1}^S$, $\delta\chi_{r,-1}^S$, Υ_r^S, $u_{t,0}^S$, $u_{\phi,0}^S$ that satisfy the system of the equations to within a certain tolerance. (We strongly emphasize that $n_{\rm max} = 1$ is too small to accurate describe spinning-body orbits in almost all cases; this is merely used to illustrate the character of this system of linear equations.)

In the case of a nearly equatorial orbit, the polar and radial equations decouple such that we can solve Eq. (A.56) above independently of the equation for the θ-motion. The θ-equation (3.157) has only three non-zero coefficients in the nearly equatorial limit, Eqs. (A.52) – (A.53). We insert the values for $\mathcal{Q}_\vartheta$ and T_ϑ and write $\mathcal{V}$ as a Fourier expansion of the form

$$f(\lambda) = \sum_{j=-1}^{1} \sum_{n=-n_{\rm max}}^{n_{\rm max}} f_{jn} e^{-ij\Upsilon_s\lambda} e^{-in\hat{\Upsilon}_r\lambda} \,. \tag{A.59}$$

We also write $\delta\vartheta_S$ as a Fourier expansion,

$$\delta\vartheta_S(\lambda) = \sum_{j=-1}^{1} \sum_{n=-n_{\max}}^{n_{\max}} \delta\vartheta_{S,jn} e^{-ij\Upsilon_s\lambda} e^{-in\hat{\Upsilon}_r\lambda} \,. \tag{A.60}$$

We take $n_{\max} = 1$ again, obtaining the following solution for Fourier coefficients of $\delta\vartheta_S$:

$$\begin{pmatrix} \delta\vartheta_{S,-1,-1} \\ \delta\vartheta_{S,0,-1} \\ \delta\vartheta_{S,1,-1} \\ \delta\vartheta_{S,-1,0} \\ \delta\vartheta_{S,0,0} \\ \delta\vartheta_{S,1,0} \\ \delta\vartheta_{S,-1,1} \\ \delta\vartheta_{S,0,1} \\ \delta\vartheta_{S,1,1} \end{pmatrix} = - \begin{pmatrix} \frac{\mathcal{V}_{-1,-1}}{\hat{L}_z^2 - (\hat{\Upsilon}_r + \Upsilon_s)^2} \\ \frac{\mathcal{V}_{0,-1}}{\hat{L}_z^2 - \hat{\Upsilon}_r^2} \\ \frac{\mathcal{V}_{1,-1}}{\hat{L}_z^2 - (\hat{\Upsilon}_r - \Upsilon_s)^2} \\ \frac{\mathcal{V}_{-1,0}}{\hat{L}_z^2 - \Upsilon_s^2} \\ 0 \\ \frac{\mathcal{V}_{1,0}}{\hat{L}_z^2 - \Upsilon_s^2} \\ \frac{\mathcal{V}_{-1,1}}{\hat{L}_z^2 - (\hat{\Upsilon}_r - \Upsilon_s)^2} \\ \frac{\mathcal{V}_{0,1}}{\hat{L}_z^2 - \hat{\Upsilon}_r^2} \\ \frac{\mathcal{V}_{1,1}}{\hat{L}_z^2 - (\hat{\Upsilon}_r + \Upsilon_s)^2} \end{pmatrix} . \tag{A.61}$$

Appendix B

Chapter 4 Appendices

B.1 Reference geodesics

There are different mappings that can be constructed from the triplet of constants (p, e, I) defining a geodesic (i.e., the "reference" geodesic) to a particular spinning-body orbit. The choice of reference geodesic we use in this article is discussed in Sec. 4.3.1. In brief, we find spinning-body orbits for which the "purely radial" and "purely polar" components of the motion have the same turning points as the reference geodesic; see Sec. 4.3.1 for mathematical details. However, there are other physically equivalent mappings which can be used instead and may be particularly useful in certain circumstances. We outline three approaches that have appeared in the literature below.

B.1.1 Reference geodesic has the same turning points as the spinning-body orbit

The definition of reference geodesic we use in this work is most similar to that used by Mukherjee et al. in Ref. [71] and Skoupý et al. in Ref. [124]. In Refs. [71] and [124], they study eccentric equatorial orbits where the spin is aligned, and in this case the reference geodesic has the same radial *turning points* as the spinning-body orbit under consideration. In our approach, we generalize this for generic orbital configurations and misaligned small-body spin: The purely radial and purely polar parts of the spinning-body motion are constrained to have the same libration range as the corresponding reference geodesic. Complementary to this, there are additional corrections to the libration range due to motion that is not purely radial, or purely polar (see Sec. 4.3.1). For example, if the reference geodesic is equatorial, the corresponding spinning-body orbit is not equatorial except in the aligned spin case. Instead, it lies $\mathcal{O}(S)$ out of the equatorial plane. An example of a reference geodesic with the same radial turning points as the corresponding spinning-body orbit is shown in Fig. B.1(a).

B.1.2 Reference geodesic has the same initial conditions as the spinning-body orbit

In the analyses by Bini et al., the reference geodesic is defined as the geodesic that has the same *initial conditions* as the corresponding spinning-body orbit [64], [65]. Work by Mashhoon et al. takes a similar approach [63]. For example, in Ref. [64], analytic expressions for a spinning-body orbit with the same initial position and 4-velocity as a circular equatorial reference geodesic is obtained; this calculation can represent a scenario where spin-curvature force is "turned on" at a certain point along a geodesic orbit and subsequent spinning-body motion is computed. An example of a reference geodesic with the same initial conditions as the corresponding spinning-body orbit is presented in Fig. B.1(b).

B.1.3 Reference geodesic has the same constants of motion as the spinning-body orbit

In the analysis by Witzany in Ref. [84], the "fiducial" geodesic is taken to be the geodesic with the same *constants of motion* as the spinning-body orbit, modulo a $-2as_{\parallel}\mathrm{sgn}(L_z - aE)$ correction to the definition of the Carter constant K. The inclusion of the $-2as_{\parallel}\mathrm{sgn}(L_z - aE)$ term in the choice of fiducial mapping ensures that the formulae for the turning point corrections presented in Eq. (48) of Ref. [84] are finite for motion in the equatorial plane. The turning point spin-corrections corresponding to those constants of motion are then computed and used to parameterize the orbital motion. An example of a reference geodesic with the same constants of motion as the corresponding spinning-body orbit is presented in Fig. B.1(c). See App. B.2 for a detailed discussion of the approach in Ref. [84] and an explicit comparison with our formulation for the case of equatorial, aligned-spin orbits in a Schwarzschild background.

B.2 Comparison with Witzany, 2019

In Ref. [84], Witzany outlines an approach for obtaining the equations of motion for spinning bodies to first-order in spin using the Hamilton-Jacobi equation. This approach yields the equations of motion Eqs. 46(a) – (c) in Ref. [84] which we reproduce here:

$$\frac{dr}{d\lambda} = \pm\Delta\sqrt{w_r'^2 - e_{0r}e^{\kappa}_{C;r}e_{\kappa B}\tilde{s}^{CD}}, \tag{B.1}$$

$$\frac{d\theta}{d\lambda} = \pm\sqrt{w_\theta'^2 - e_{0\theta}e^{\kappa}_{C;\theta}e_{\kappa B}\tilde{s}^{CD}}, \tag{B.2}$$

$$\frac{d\psi_p}{d\lambda} = \sqrt{\hat{K}}\left(\frac{(r^2+a^2)\hat{E} - a\hat{L}_z}{\hat{K}+r^2} + a\frac{\hat{L}_z - a(1-z^2)\hat{E}}{\hat{K}-a^2z^2}\right), \tag{B.3}$$

where the tetrad e^{κ}_{C} is the parallel transported tetrad given by Eqs. (2.55) – (2.56) in Sec. 2.2.4. Here B, C and D are labels for the tetrad legs. Note that ψ_p in Eq. (B.3) is denoted ϕ in Ref. [84]; Eq. (B.3) is identical to Eq. (2.57). The expressions for $\tilde{s}_{CD}$ are underneath Eq.

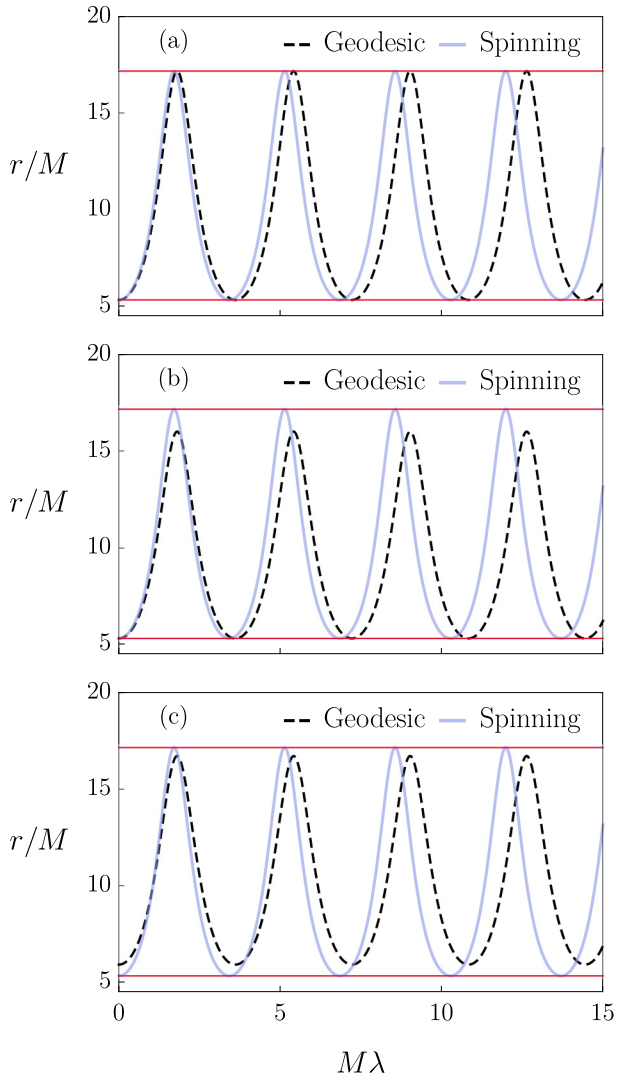

Figure B.1: Example of radial motion for an aligned, spinning body in an equatorial orbit around a non-rotating black hole ($a = 0$). All panels show r versus λ for a spinning body (blue) and corresponding reference geodesic (black, dashed) orbit. Radial turning points, corresponding to $p = 8.13721$, $e = 0.525726$, of the spinning body's orbit are shown by the solid red lines. Different choices of reference geodesic for the same spinning-body orbit are shown in (a), (b) and (c). *Top.* (a) The spinning-body orbit and reference geodesic have the same turning points. *Middle.* (b) The spinning-body orbit and reference geodesic have the same initial conditions. *Bottom.* (c) The spinning-body orbit and reference geodesic have the same constants of motion. In making these plots, we have used $s_{\|} = s$ and $\mu s/M = 0.05$.

(33) in Ref. [84]. From Eqs. (B.1) – (B.3), we can find the turning points of the equations of motion using the condition that the 4-velocities vanish:

$$(w_y')^2 - e_{0y} e^{\kappa}_{C;y} e_{D\kappa} s^{CD} = 0, \tag{B.4}$$

where $y = r,\ \theta$. Using condition (B.4), Witzany derives analytical expressions for the corrections to the turning points due to the small body's spin. These expressions can be found in Eqs. 48(a) – (f) of Ref. [84] and apply for fully generic orbits in the first order in S limit.

B.2.1 Description of the two approaches

The framework used in Ref. [84] is an alternative method for calculating spinning-body orbital frequencies Υ_r and Υ_θ. In an approach analogous to that used by Carter in Ref. [145], Witzany uses the Hamilton-Jacobi equation to obtain expressions for $dr/d\lambda$ and $d\theta/d\lambda$, yielding Eqs. (B.1) – (B.3). The Mino-time frequencies Υ_r and Υ_θ are then calculated by integrating these velocities with respect to angle-type coordinates; this procedure is in turn analogous to that used in Refs. [135], [139] to compute geodesic Mino-time frequencies. The approach we use in this article is to solve the Mathisson-Papapetrou equations (2.47) – (2.48) directly in the frequency-domain. We introduce a frequency correction explicitly into our parameterization and solve for it as one of the unknowns in a linear-algebraic system.

The orbital motion of the spinning body is parameterized differently in the two descriptions. In Ref. [84], analytic expressions for the corrections to the turning points are obtained using the aforementioned Eqs. (B.1) – (B.2). The spinning body's motion is then parameterized in terms of these analytic expressions for the turning points. In our analysis, we do not have explicit expressions for turning point corrections built into our parameterization. Instead, we divide the corrections to the motion of the spinning body into two categories: We include corrections which do not alter the libration range relative to the reference geodesic ($\delta\chi_r^S,\ \delta\chi_\theta^S$), as well as corrections which do modify the libration range ($\delta\,\text{ɤ}_S,\ \delta\,\text{ƙ}_S$).

In summary, in Ref. [84], the constants of motion (E, L_z, K) associated with a certain geodesic (called the "fiducial geodesic", as discussed in App. B.1.3) are selected, and the turning point corrections for the corresponding spinning-body orbit with the same constants of motion are computed (modulo a $-2as_\parallel \mathrm{sgn}(L_z - aE)$ adjustment to K), whereupon the frequency corrections can be obtained. Contrastingly, in our framework, we begin by choosing the turning points (p, e, I) for a particular reference geodesic. We then compute the spinning-body orbit which has purely radial and purely polar motion constrained to match the turning points of the reference geodesic. The concomitant frequency corrections and constants of motion for that orbit can then be computed. We show below that our method is consistent with Ref. [84] for orbits in the equatorial plane with aligned small body spin[1]; we leave a detailed comparison of the frequency corrections for fully generic orbits for future work.

[1] As mentioned in Ref. [84], Witzany conducted a similar consistency check using the effective potential given by Tod et al. [66] and Hackmann et al. [68].

B.2.2 Numerical comparison of the two approaches

We compare between the method described in this paper and that presented in Ref. [84] by evaluating the expressions for the radial turning point corrections. For equatorial orbits of a small body with aligned spin and $a = 0$, Eqs. 48(a) – (f) in Ref. [84] become:

$$\mathcal{G} = L_z^S E^S r^2 \,, \quad \mathcal{I} = \frac{d}{dr}\left(\frac{(E^S r^2)^2}{\Delta} - r^2\right) \,, \tag{B.5}$$

$$e_{0y} e_{C\kappa;y} e_D^\kappa = 2\frac{E^S L_z^S \left[r(L_z^S)^2 - Mr^2 - 3M(L_z^S)^2\right]}{r\left[(L_z^S)^2 + r^2\right](r-2M)^2} \,, \tag{B.6}$$

$$\delta r = -s\mu \frac{2\mathcal{G} + \Delta\left[(L_z^S)^2 + r^2\right] e_{0y} e_{C\kappa;y} e_D^\kappa}{\mathcal{I}\left[(L_z^S)^2 + r^2\right]}\bigg|_{r_{gt}} \,, \tag{B.7}$$

where δr is the radial turning point correction evaluated at the fiducial geodesic turning points, which are denoted r_{gt}. This reduces to a simple expression for δr:

$$\delta r = s\mu \frac{E^S L_z^S (r-2M)(r-3M)}{r\left[(r-2M)^2 - r(E^S)^2(r-3M)\right]}\bigg|_{r=r_{gt}} \,. \tag{B.8}$$

Note that E^S and L_z^S here are the energy and angular momentum of the spinning-body orbit. As discussed in App. B.1.3, the fiducial geodesic is the geodesic orbit that has the same energy and angular momentum as the spinning-body orbit we are considering, i.e., $\hat{E}_{\rm fid} = E^S$ and $\hat{L}_{\rm z,fid} = L_z^S$. Eq. (B.8) is evaluated at the turning points of the fiducial geodesic, r_{gt1} and r_{gt2}, and gives the correction to these turning points $\delta r(r_{gt1})$ and $\delta r(r_{gt2})$ due to the spin of the small body.

Procedure for computing turning points

As discussed in Appendix B.1, the approach in Ref. [84] is to consider a fiducial geodesic which has the same constants of motion as the spinning-body orbit; this fiducial geodesic has turning points given by r_{gt1} and r_{gt2}. The turning point corrections are then computed using Eqs. 48(a) – (f) in Ref. [84].

1. We begin with the constants of motion for a spinning-body orbit with semi-latus rectum p and eccentricity e. The energy E^S and angular momentum L_z^S corresponding to this choice of p and e are given by

$$E^S = \hat{E} + \delta E^S \,, \quad L_z^S = \hat{L}_z + \delta L_z^S \,, \tag{B.9}$$

where expressions for $\hat{E}$, $\hat{L}_z$, δE^S and δL_z^S are given by Eqs. (B15), (B16) and (B17) of Ref. [218]. We reproduce these equations below:

$$\hat{E} = \sqrt{\frac{(p-2)^2 - 4e^2}{p(p-3-e^2)}} \,, \quad \hat{L}_z = \frac{pM}{\sqrt{p-3-e^2}}, \tag{B.10}$$

$$\delta E^S = -\frac{s\mu}{M}\frac{(1-e^2)^2}{2p(p-3-e^2)^{3/2}} \,, \tag{B.11}$$

$$\delta L_z^S = s\mu \frac{(2p-9-3e^2)\sqrt{(p-2)^2 - 4e^2}}{2p^{1/2}(p-3-e^2)^{3/2}} \,. \tag{B.12}$$

2. By using $\hat{E}_{\rm fid} = E^S$ and $\hat{L}_{\rm z,fid} = L_z^S$ and inverting equations (B.10), we can find expressions for the semi-latus rectum $p_{\rm fid}$ and eccentricity $e_{\rm fid}$ of a geodesic orbit, given E^S and L_z^S. Notice that these are *not* that same as semi-latus rectum and eccentricity of the spinning-body orbit — they are the semi-latus rectum and eccentricity corresponding to a geodesic orbit that has the same energy E^S and angular momentum L_z^S as the spinning-body orbit we are considering.

3. Then, the fiducial turning points can be found, using:

$$r_{gt1} = \frac{p_{\rm fid} M}{1 - e_{\rm fid}} , \quad r_{gt2} = \frac{p_{\rm fid} M}{1 + e_{\rm fid}} . \tag{B.13}$$

4. Next, we evaluate Eq. (B.8) to find δr at each of these fiducial turning points: $\delta r(r_{gt1})$ is the correction to the fiducial apastron and $\delta r(r_{gt2})$ is the correction to the fiducial periastron. We add these corrections to find the spin-correction turning points:

$$r_{st1} = r_{gt1} + \delta r(r_{gt1}) , \quad r_{st2} = r_{gt2} + \delta r(r_{gt2}) . \tag{B.14}$$

5. We can convert these turning points r_{st1} and r_{st1} into semi-latus rectum p and eccentricty e of the spinning-body orbit using:

$$pM = \frac{2 r_{st1} r_{st2}}{r_{st1} + r_{st2}} , \quad e = \frac{r_{st1} - r_{st2}}{r_{st1} + r_{st2}} . \tag{B.15}$$

Numerical example

We follow the procedure outlined in Sec. B.2.2 with a specific numerical example. For this example case, we already know the turning points of the radial motion and we verify that the turning points computed using Eq. (B.8) are consistent. Consider a spinning-body orbit with small-body spin $\mu s = 0.001M$, semi-latus rectum $pM = 7M$ and eccentricity $e = 0.4$.

1. From Eq. (B.9), this orbit has $E^S = 0.951965$ and $L_z^S = 3.57273M$.

2. Using $\hat{E}_{\rm fid} = E^S$ and $\hat{L}_{\rm z,fid} = L_z^S$ and inverting equations (B.10), we find that $p_{\rm fid} = 7.05356$ and $e_{\rm fid} = 0.394709$.

3. Next, we find the fiducial turning points r_{gt1} and r_{gt2} using Eqs. (B.13); they are $r_{gt1} = 11.6532M$ and $r_{gt1} = 5.05737M$.

4. Then, we find that $\delta r(r_{gt1}) = 0.0135323M$ and $\delta r(r_{gt2}) = -0.0517264M$. The spinning-body turning points are $r_{st1} = 11.6667M$ and $r_{st2} = 5.00564M$.

5. The spinning-body p and e are found using Eq. (B.15): $p = 7.00553$ and $e = 0.399527$. We have recovered the expected p and e for this orbit.

Appendix C

Chapter 5 Appendices

C.1 Spinning-body parameterizations

We have freedom in how we parameterize the motion of a spinning body, in the sense that we can construct various mappings between the triplet of constants (p, e, x_I) which defines a "reference" geodesic, to a specific spinning-body orbit. In Appendix A of [172], three such mappings are discussed: (1) the turning points of the reference geodesic match those of the spinning-body orbit; (2) the initial conditions of the reference geodesic match those of the spinning-body orbit; and (3) the constants of motion $(\hat{E}, \hat{L}_z, \hat{K})$ of the reference geodesic match the constants of the spinning-body orbit. In this section, we will primarily discuss the parameterizations (1) and (2) and how to map between them.

References [171], [172] use parameterization (1): the turning points of the spinning-body orbit match those of a chosen reference geodesic defined by (p, e, x_I). Those references show how to compute the frequency corrections $\Upsilon^S_r(p, e, x_I)$, $\Upsilon^S_\theta(p, e, x_I)$, and $\Upsilon^S_\phi(p, e, x_I)$ due to the small body's spin, relative to the frequencies of a reference geodesic with the same turning points. Because of the additional harmonic complexity of spinning-body orbits relative to geodesics, the turning points of the non-spinning and spinning body orbits are matched in an orbit-averaged sense: the radial turning points of the "purely radial" piece of the spinning-body orbit are matched with the radial turning points of the geodesic, and likewise for the "purely polar" motion. "Purely radial" means the contributions to the orbital motion that contains only harmonics of Υ_r or $\hat{\Upsilon}_r$; "purely polar" means contributions that contain only harmonics of Υ_θ or $\hat{\Upsilon}_\theta$. The equatorial spinning-body inspirals computed in [126] also use this parameterization.

By construction, the perturbed motion found by solving the OG equations uses parameterization (2): the initial orbit coordinates and initial components of the four-velocity are the same for the spinning and non-spinning orbits. We use this parameterization in this work, which was also used in [101]. Parameterization (3), choosing the constants of motion (E, L_z, K) of a spinning-body orbit to match those of a reference geodesic, is used in [84], [219].

Because different parameterizations are used by different analyses, it is important to consider the mapping between the different choices, and to show that they describe the same orbits. We begin by choosing a triplet (p_{TP}, e_{TP}, x_{TP}) that defines a geodesic with radial

turning points $r_1 = p_{TP}/(1-e_{TP})$ and $r_2 = p_{TP}/(1+e_{TP})$, and with polar turning point $z_1 = \sqrt{1-x_{TP}^2}$. Using the approach of [171], [172], we first compute the spinning-body trajectory that has the same turning points (on average) as this geodesic. We next want to find the *same* spinning-body orbit via the "matched initial conditions" parameterization, using the OG method presented in this paper.

To do this, we select initial values of (r, z) by choosing one of the radial and polar turning points of the spinning-body orbit we evaluated in the matched turning point parameterization. We label these choices r_{TP} and z_{TP}. We use the subscript "IC" to denote the triplet (p_{IC}, e_{IC}, x_{IC}) associated with a geodesic which has the same *initial conditions* as the spinning-body orbit under consideration. The geodesic orbit defined by r_G and z_G needs to initially have the same values of r and z, so we equate $r_G(p_{IC}, e_{IC}, x_{IC}, q_{r0})$ and $z_G(p_{IC}, e_{IC}, x_{IC}, q_{z0})$ as given in Eqs. (16)–(17) of Ref. [144]. For convenience, we choose the spinning-body orbit to be at a turning point initially. The initial geodesic velocities must match, so we solve $R[r(p_{IC}, e_{IC}, x_{IC}, q_{r0})] = 0$ and $\Theta[z(p_{IC}, e_{IC}, x_{IC}, q_{z0}) = 0$ where the functions $R(r)$ and $\Theta(\theta)$ are given by equations (2.20) and (2.21).

We now have four equations and five unknowns, $(p_{IC}, e_{IC}, x_{IC}, q_{r0}, q_{z0})$. To close this system, we find the initial value of $(d\phi/d\lambda)_{TP}$ of a spinning-body in the fixed turning point parameterization and equate it to $d\phi/d\lambda$ for a geodesic using $\Phi[r(p_{IC}, e_{IC}, x_{IC}, q_{r0}, q_{z0})]$, given in Eq. (2.22). The final set of equations we solve is

$$r_G(p_{IC}, e_{IC}, x_{IC}, q_{r0}) = r_{TP} \,, \tag{C.1}$$

$$z_G(p_{IC}, e_{IC}, x_{IC}, q_{z0}) = z_{TP} \,, \tag{C.2}$$

$$R[r(p_{IC}, e_{IC}, x_{IC}, q_{r0})] = 0 \,, \tag{C.3}$$

$$\Theta[r(p_{IC}, e_{IC}, x_{IC}, q_{z0})] = 0 \,, \tag{C.4}$$

$$\Phi[r(p_{IC}, e_{IC}, x_{IC}, q_{r0}, q_{z0})] = \left(\frac{d\phi}{d\lambda}\right)_{TP} \,. \tag{C.5}$$

We solve the above equations to find the triplet (p_{IC}, e_{IC}, x_{IC}). We can then compute the spinning-body orbit corresponding to this choice of initial geodesic (p_{IC}, e_{IC}, x_{IC}). We now have a mapping between (p_{TP}, e_{TP}, x_{TP}) and (p_{IC}, e_{IC}, x_{IC}); this is how we compute the orbits in 5.4.1.

Note that the two parameterizations are not linearized in secondary spin in exactly the same way. Feeding into the OG equations is the forcing term from the linearized MPD equations, Eq. (5.16). Beyond this point, the OG formulation does not assume the forcing term to be small and does not further linearize in spin. However, in the "turning point matched" prescription of Refs. [171], [172], the expressions for the radial and polar trajectories, our Eqs. (5.19) and (5.20), which have been explicitly divided into geodesic and secondary-spin pieces, are substituted into the MPD equations. After this substitution, we then linearize the MPD equations. This leads to a slight difference in the equations of motion between the two prescriptions at the $\mathcal{O}(S^2)$ level. These two prescriptions are equivalent up to linear-order in secondary spin, but are not identical at $\mathcal{O}(S^2)$. This is responsible for the slight drift seen after long integration times when comparing our methods for computing spinning-body orbits, discussed at the end of Sec. 5.4.1.

Note that we use the fact that we can evaluate the frequencies $(\Omega_r, \Omega_z, \Omega_\phi)$ associated with a spinning-body orbit in both parameterizations in order to relate the reference geodesic

triplets (p_{TP}, e_{TP}, x_{TP}) and (p_{IC}, e_{IC}, x_{IC}) in the two parameterizations. Explicitly, we find the mapping $(p_{TP}, e_{TP}, x_{TP}) \to (p_{IC}, e_{IC}, x_{IC})$ by solving the equations:

$$\Omega_r(p_{IC}, e_{IC}, x_{IC}) = \Omega_r(p_{TP}, e_{TP}, x_{TP}) \,, \tag{C.6}$$
$$\Omega_z(p_{IC}, e_{IC}, x_{IC}) = \Omega_z(p_{TP}, e_{TP}, x_{TP}) \,, \tag{C.7}$$
$$\Omega_\phi(p_{IC}, e_{IC}, x_{IC}) = \Omega_\phi(p_{TP}, e_{TP}, x_{TP}) \,. \tag{C.8}$$

C.2 Forced motion via osculating geodesic orbital elements

In this appendix, we briefly discuss how to compute forced motion of a body in spacetime through a sequence of geodesic orbits, showing how the forcing terms lead to evolution of the orbital elements which characterize geodesics. This synopsis is based on the discussion presented in Ref. [179].

Begin by writing the geodesic equation

$$\frac{d^2x^\alpha}{d\tau^2} = -\Gamma^\alpha{}_{\beta\gamma}\frac{dx^\beta}{d\tau}\frac{dx^\gamma}{d\tau} \tag{C.9}$$

in the form

$$\ddot{x}^\alpha = a^\alpha_{\rm geo} \,, \tag{C.10}$$

where overdot denotes $d/d\tau$. As observed in Sec. 5.3.1, bound Kerr geodesics can be described by seven parameters:

$$\mathcal{E}^A \doteq \{p, e, x_I, \chi_r^S, \chi_\theta^S, \phi_0, t_0\} \,. \tag{C.11}$$

The capital Latin index introduced here ranges from 1 to 7; the symbol $\doteq$ means "the components on the left-hand side are given by the elements of the set on the right-hand side." In this set, p, e, and x_I are the principal orbital elements describing the geometry of the orbit and χ_r^S, χ_θ^S, ϕ_0, and t_0 are the positional orbital elements that specify initial conditions.

The parameters $\mathcal{E}^A$ are strictly constant on a geodesic, and can be expressed as functions of spatial position and spatial velocity in an orbit. In other words, we can write

$$\mathcal{E}^A = \mathcal{E}^A(x^\alpha, \dot{x}^\alpha) \,. \tag{C.12}$$

Using the chain rule, we write the rate of change of $\mathcal{E}^A$

$$\dot{\mathcal{E}}^A = \frac{\partial \mathcal{E}^A}{\partial x^\alpha}\dot{x}^\alpha + \frac{\partial \mathcal{E}^A}{\partial \dot{x}^\alpha}\ddot{x}^\alpha \,. \tag{C.13}$$

Using Eq. (C.10) and requiring $\mathcal{E}^A$ to be constant on a geodesic, we obtain

$$\dot{\mathcal{E}}^A = \frac{\partial \mathcal{E}^A}{\partial x^\alpha}\dot{x}^\alpha + \frac{\partial \mathcal{E}^A}{\partial \dot{x}^\alpha}a^\alpha_{\rm geo} = 0 \,. \tag{C.14}$$

Consider now forced motion. In the presence of a perturbing force, the geodesic equation generalizes to

$$\frac{d^2x^\alpha}{d\tau^2} + \Gamma^\alpha{}_{\beta\gamma}\frac{dx^\beta}{d\tau}\frac{dx^\gamma}{d\tau} = a^\alpha \ . \tag{C.15}$$

The non-geodesic acceleration a^α is subject to the constraint

$$a^\alpha u_\alpha = 0 \ . \tag{C.16}$$

Equation (C.15) can be written

$$\ddot{x}^\alpha = a^\alpha_{\rm geo} + a^\alpha \ . \tag{C.17}$$

Our aim is to convert Eq. (C.17) into a set of equations for the evolution of orbital elements $\mathcal{E}^A$. This requires a mapping $\{x^\alpha, \dot{x}^\alpha\} \to \mathcal{E}^A$. We assert that, at each moment along the worldline, a geodesic can be found with the same $(x^\alpha, \dot{x}^\alpha)$ as the accelerated body. This assertion is known as the *osculation condition*. Stated plainly, we assert that [178]

$$x^\alpha(\tau) = x^\alpha_{\rm geo}(\mathcal{E}^A, \tau) \ , \tag{C.18}$$

$$\dot{x}^\alpha(\tau) = \dot{x}^\alpha_{\rm geo}(\mathcal{E}^A, \tau) \ , \tag{C.19}$$

where $x^\alpha(\tau)$ represents the coordinates of the true worldline, and $x^\alpha_{\rm geo}(\mathcal{E}^A, \tau)$ represents the coordinates of a geodesic worldline with orbital elements $\mathcal{E}^A$. Note that the time derivative in Eq. (C.19) holds $\mathcal{E}^A$ fixed. Note also that the osculation condition involves 4 components of x^α and 4 components of $\dot{x}^\alpha$, one of which is constrained either by the condition $a^\alpha u_\alpha = 0$ or $u^\alpha u_\alpha = -1$. The 8 components plus 1 constraint thus map to the 7 parameters $\mathcal{E}^A$, so the number of orbital elements matches the number of degrees of freedom [178].

Under the influence of a perturbing force which accelerates the worldline by a^α relative to a geodesic, the parameters $\mathcal{E}^A$ do not remain constant. We promote them to dynamical variables called *osculating orbital elements*. The accelerated trajectory x^α is then described by a sequence of geodesics with parameters

$$\mathcal{E}^A(t) \doteq \{p(t), e(t), x_I(t), \chi^S_r(t), \chi^S_\theta(t), \phi_0(t), t_0(t)\} \ . \tag{C.20}$$

Here t is simply Boyer-Lindquist coordinate time along the inspiral, which we use as our parameter along the inspiral worldline. Other parameter choices could be used (e.g., proper time τ along the inspiral, or Mino time λ). Boyer-Lindquist time is particularly convenient, as it is the time measured by distant observers. Note that we have written both ϕ_0 and t_0 as though they are promoted to dynamical quantities; we will soon show that the equations governing them do not need to be evolved, and they can be left as constants.

What remains is to prescribe how to dynamically evolve these elements. We again use the chain rule and Eq. (C.17) to evaluate $\dot{\mathcal{E}}^A(\tau)$, yielding

$$\dot{\mathcal{E}}^A = \frac{\partial \mathcal{E}^A}{\partial x^\alpha}\dot{x}^\alpha + \frac{\partial \mathcal{E}^A}{\partial \dot{x}^\alpha}a^\alpha_{\rm geo} + \frac{\partial \mathcal{E}^A}{\partial \dot{x}^\alpha}a^\alpha \ . \tag{C.21}$$

Taking advantage of Eq. (C.14), we obtain

$$\dot{\mathcal{E}}^A = \frac{\partial \mathcal{E}^A}{\partial \dot{x}^\alpha}a^\alpha \ . \tag{C.22}$$

Multiplying both sides of Eq. (C.14) by $\partial x^\beta_{\rm geo}/\partial \mathcal{E}^A$ and both sides of Eq. (C.22) by $\partial \dot{x}^\beta_{\rm geo}/\partial \mathcal{E}^A$ yields a particularly useful form of these equations:

$$\frac{\partial x^\beta_{\rm geo}}{\partial \mathcal{E}^A}\dot{\mathcal{E}}^A = 0 \,, \tag{C.23}$$

$$\frac{\partial \dot{x}^\beta_{\rm geo}}{\partial \mathcal{E}^A}\dot{\mathcal{E}}^A = a^\beta \,. \tag{C.24}$$

To derive Eq. (C.24), note that Eq. (C.19) implies

$$\frac{\partial \dot{x}^\beta_{\rm geo}}{\partial \mathcal{E}^A}\frac{\partial \mathcal{E}^A}{\partial \dot{x}^\alpha} = \delta^\beta{}_\alpha \,. \tag{C.25}$$

These expressions can be used to derive explicit equations for osculating orbital element evolution, and can be written in either contravariant or covariant form (see Secs. III D 1 and 2 of Ref. [179]).

C.2.1 Quasi-Keplerian evolution equations

Following the approach used in Ref. [178], we use the contravariant formulation (see Sec. III D 2 of [179]). Expanding Eq. (C.23) yields

$$\frac{\partial r}{\partial p}p' + \frac{\partial r}{\partial e}e' + \frac{\partial r}{\partial x_I}x_I{}' + \frac{\partial r}{\partial \chi^S_r}\chi^{S\prime}_r + \frac{\partial r}{\partial \chi^S_\theta}\chi^{S\prime}_\theta = 0 \,, \tag{C.26}$$

$$\frac{\partial \theta}{\partial p}p' + \frac{\partial \theta}{\partial e}e' + \frac{\partial \theta}{\partial x_I}x_I{}' + \frac{\partial \theta}{\partial \chi^S_r}\chi^{S\prime}_r + \frac{\partial \theta}{\partial \chi^S_\theta}\chi^{S\prime}_\theta = 0 \,, \tag{C.27}$$

$$\frac{\partial \phi}{\partial p}p' + \frac{\partial \phi}{\partial e}e' + \frac{\partial \phi}{\partial x_I}x'_I + \frac{\partial \phi}{\partial \chi^S_r}\chi^{S\prime}_r + \frac{\partial \phi}{\partial \chi^S_\theta}\chi^{S\prime}_\theta + \phi'_0 = 0 \,, \tag{C.28}$$

$$\frac{\partial t}{\partial p}p' + \frac{\partial t}{\partial e}e' + \frac{\partial t}{\partial x_I}x'_I + \frac{\partial t}{\partial \chi^S_r}\chi^{S\prime}_r + \frac{\partial t}{\partial \chi^S_\theta}\chi^{S\prime}_\theta + t'_0 = 0 \,. \tag{C.29}$$

Prime represents differentiation with respect to the variable that parameterizes the trajectory, $t^{\rm i}$.

Equations (C.28) and (C.29), which govern the evolution of the axial offset ϕ_0 and time offset t_0, contain elliptic integrals which are introduced due to terms like $\partial t/\partial p$. Computing such integrals at each time step introduces additional computational expense. Instead of evolving Eqs. (C.28) and (C.29), we find ϕ and t along the worldline by using the geodesic expressions computed along the instantaneous orbit, as was done in Refs. [179] and [178]. Rewriting Eqs. (2.22) and (2.23)), these equations are

$$\begin{aligned}\frac{d\phi}{d\lambda} &= \Phi_r(r, E, L_z, Q) + \Phi_\theta(\theta, E, L_z, Q) \\ &= \Phi_r[p(\lambda), e(\lambda), x_I(\lambda), \chi^S_r(\lambda)] \\ &\quad + \Phi_\theta[p(\lambda), e(\lambda), x_I(\lambda), \chi^S_\theta(\lambda)] \,,\end{aligned} \tag{C.30}$$

$$\begin{aligned}\frac{dt}{d\lambda} &= T_r(r, E, L_z, Q) + T_\theta(\theta, E, L_z, Q) \\ &= T_r[p(\lambda), e(\lambda), x_I(\lambda), \chi^S_r(\lambda)] \\ &\quad + T_\theta[p(\lambda), e(\lambda), x_I(\lambda), \chi^S_\theta(\lambda)] \,.\end{aligned} \tag{C.31}$$

Integrating up Eqs. (C.30) and (C.31) for ϕ and t along the inspiral is equivalent to solving (C.28) and (C.29). Observe that Eqs. (C.26) – (C.29) arise from Eq. (C.23), which in turn arises from (C.14). Equation (C.14) simply states that the geodesic equation $\ddot{x}^\alpha = a^\alpha_{\rm geo}$ holds when the osculating elements $\mathcal{E}^A$ are constant. When $\{p, e, x_I, \chi_r^S, \chi_\theta^S\}$ are all constant, Eqs. (C.30) and (C.31) yield geodesic solutions; when $\{p, e, x_I, \chi_r^S, \chi_\theta^S\}$ are evolving, we obtain the solution for forced motion.

We therefore need only consider Eqs. (C.26) and (C.27). We rearrange these equations to obtain

$$\chi_r^{S\prime} = \frac{1}{\partial r/\partial \chi_r^S}\left(\frac{\partial r}{\partial p}p' + \frac{\partial r}{\partial e}e' + \frac{\partial r}{\partial x_I}x_I'\right) \equiv X_r^S(\mathcal{E}^A)\ , \tag{C.32}$$

$$\chi_\theta^{S\prime} = \frac{1}{\partial \theta/\partial \chi_\theta^S}\left(\frac{\partial \theta}{\partial p}p' + \frac{\partial \theta}{\partial e}e' + \frac{\partial \theta}{\partial x_I}x_I'\right) \equiv X_\theta^S(\mathcal{E}^A)\ . \tag{C.33}$$

We next expand Eq. (C.24) just as we expanded (C.23):

$$\frac{\partial \dot{r}}{\partial p}p' + \frac{\partial \dot{r}}{\partial e}e' + \frac{\partial \dot{r}}{\partial x_I}x_I' + \frac{\partial \dot{r}}{\partial \chi_r^S}\chi_r^{S\prime} + \frac{\partial \dot{r}}{\partial \chi_\theta^S}\chi_\theta^{S\prime} = a^r\tau'\ , \tag{C.34}$$

$$\frac{\partial \dot{\theta}}{\partial p}p' + \frac{\partial \dot{\theta}}{\partial e}e' + \frac{\partial \dot{\theta}}{\partial x_I}x_I' + \frac{\partial \dot{\theta}}{\partial \chi_r^S}\chi_r^{S\prime} + \frac{\partial \dot{\theta}}{\partial \chi_\theta^S}\chi_\theta^{S\prime} = a^\theta\tau'\ , \tag{C.35}$$

$$\frac{\partial \dot{\phi}}{\partial p}p' + \frac{\partial \dot{\phi}}{\partial e}e' + \frac{\partial \dot{\phi}}{\partial x_I}x_I' + \frac{\partial \dot{\phi}}{\partial \chi_r^S}\chi_r^{S\prime} + \frac{\partial \dot{\phi}}{\partial \chi_\theta^S}\chi_\theta^{S\prime} = a^\phi\tau'\ , \tag{C.36}$$

$$\frac{\partial \dot{t}}{\partial p}p' + \frac{\partial \dot{t}}{\partial e}e' + \frac{\partial \dot{t}}{\partial x_I}x_I' + \frac{\partial \dot{t}}{\partial \chi_r^S}\chi_r^{S\prime} + \frac{\partial \dot{t}}{\partial \chi_\theta^S}\chi_\theta^{S\prime} = a^t\tau'\ , \tag{C.37}$$

Following Refs. [178], [179], we use the condition $a^\alpha u_\alpha = 0$ to eliminate Eq. (C.37). Following [179], we define the useful expression

$$\mathcal{L}_b(c) \equiv \frac{\partial \dot{c}}{\partial b} - \frac{\partial r/\partial b}{\partial r/\partial \chi_r^S}\frac{\partial \dot{c}}{\partial \chi_r^S} - \frac{\partial \theta/\partial b}{\partial \theta/\partial \chi_\theta^S}\frac{\partial \dot{c}}{\partial \chi_\theta^S}\ , \tag{C.38}$$

where b denotes p, e or x_I, and where c denotes r, θ or ϕ. This definition allows us to write Eqs. (C.34) – (C.36) in the convenient form

$$p' = \frac{\tau'}{D}\Big((\mathcal{L}_e(\theta)\mathcal{L}_{x_I}(\phi) - \mathcal{L}_e(\phi)\mathcal{L}_{x_I}(\theta))a^r + (\mathcal{L}_{x_I}(r)\mathcal{L}_e(r) - \mathcal{L}_{x_I}(\phi)\mathcal{L}_e(r))a^\theta + (\mathcal{L}_e(r)\mathcal{L}_{x_I}(\theta) - \mathcal{L}_e(\theta)\mathcal{L}_{x_I}(r))a^\phi \Big) , \tag{C.39}$$

$$e' = \frac{\tau'}{D}\Big((\mathcal{L}_{x_I}(\theta)\mathcal{L}_p(\phi) - \mathcal{L}_{x_I}(\phi)\mathcal{L}_p(\theta))a^r + (\mathcal{L}_p(r)\mathcal{L}_{x_I}(r) - \mathcal{L}_p(\phi)\mathcal{L}_{x_I}(r))a^\theta + (\mathcal{L}_{x_I}(r)\mathcal{L}_p(\theta) - \mathcal{L}_{x_I}(\theta)\mathcal{L}_p(r))a^\phi \Big) , \tag{C.40}$$

$$x_I' = \frac{\tau'}{D}\Big((\mathcal{L}_p(\theta)\mathcal{L}_e(\phi) - \mathcal{L}_p(\phi)\mathcal{L}_e(\theta))a^r + (\mathcal{L}_e(r)\mathcal{L}_p(r) - \mathcal{L}_e(\phi)\mathcal{L}_p(r))a^\theta + (\mathcal{L}_p(r)\mathcal{L}_e(\theta) - \mathcal{L}_p(\theta)\mathcal{L}_e(r))a^\phi \Big) , \tag{C.41}$$

$$D = \mathcal{L}_p(r)\left(\mathcal{L}_e(\theta)\mathcal{L}_{x_I}(\phi) - \mathcal{L}_{x_I}(\theta)\mathcal{L}_e(\phi)\right) - \mathcal{L}_e(r)\left(\mathcal{L}_p(\theta)\mathcal{L}_{x_I}(\phi) - \mathcal{L}_{x_I}(\theta)\mathcal{L}_p(\phi)\right) + \mathcal{L}_{x_I}(r)\left(\mathcal{L}_p(\theta)\mathcal{L}_e(\phi) - \mathcal{L}_p(\phi)\mathcal{L}_e(\theta)\right) . \tag{C.42}$$

Equations (C.39)–(C.41) tell us how to evolve the principal orbital elements, given non-geodesic accelerations $a^{r,\theta,\phi}$.

We further substitute these equations into Eqs. (C.32)–(C.33) in order to obtain the evolution of the phase constants χ_r^S and χ_θ^S. This gives us a closed system of ordinary differential equations which allow us to evolve p, e, x_I, χ_r^S, and χ_θ^S given the non-geodesic accelerations $a^{r,\theta,\phi}$. Augmenting with two auxiliary equations for t and ϕ, Eqs. (C.30) and (C.31), yields a complete scheme for evolving the elements of our phase space, $\{p, e, x_I, \chi_r^S, \chi_\theta^S, \phi, t\}$.

C.2.2 Action-angle evolution equations

Action-angle coordinates are very useful for formulating near-identity transformations. In the action-angle picture, the OG equations of motion are given by [101]

$$\frac{dP_j}{d\lambda} = F_j(\vec{P}, \vec{q}) , \tag{C.43}$$

$$\frac{dq_i}{d\lambda} = \hat{\Upsilon}_i(\vec{P}) + f_i^{(1)}(\vec{P}, \vec{q}) . \tag{C.44}$$

Here, $\vec{P} = \{p, e, x_I\}$ and $\vec{q} = \{q_r, q_z\}$. We write the explicit forms for these equations below. The $F_j(\vec{P}, \vec{q})$ terms are given by

$$\frac{dp}{d\lambda} = \frac{2}{(r_1 + r_2)^2}\left[r_2^2\frac{dr_1}{d\lambda} + r_1^2\frac{dr_2}{d\lambda}\right]^{-1} \equiv F_p , \tag{C.45}$$

$$\frac{de}{d\lambda} = \frac{2}{(r_1 + r_2)^2}\left[r_2\frac{dr_1}{d\lambda} + r_1\frac{dr_2}{d\lambda}\right]^{-1} \equiv F_e , \tag{C.46}$$

$$\frac{dx_I}{d\lambda} = -\frac{z_-}{x_I}\frac{dz_-}{d\lambda} \equiv F_{x_I} . \tag{C.47}$$

The $f_i^{(1)}$ terms are given by

$$\frac{dq_{i,0}}{d\lambda} = -\frac{1}{\partial x_G^i/\partial q_i}\left(\frac{\partial x_G^i}{\partial P_j}\frac{dP_j}{d\lambda}\right) \equiv f_i^{(1)}. \tag{C.48}$$

For detail about the derivation of these expressions, refer to Appendix C of Ref. [101].

C.3 Near-identity transformation details

In this appendix, we describe in some detail the equations underlying the NIT. Further details can be found in Refs. [101], [104], [184], [185].

C.3.1 Mino-time NIT derivation

Inverse NIT

Recall that the expressions for the transformed variables in terms of our original variables, i.e., $\tilde{P}_j(\vec{P},\vec{q})$, $\tilde{q}_i(\vec{P},\vec{q})$, and $\tilde{\psi}_s(\vec{P},\vec{q},\psi_s)$, are defined by Eqs. (5.41). We observe that the inverse relationships can be found by requiring that their composition with the transformations in Eqs. (5.41) must give the identity transformation and expanding order by order in ε. This results in:

$$P_j = \tilde{P}_j - \varepsilon Y_j^{(1)}(\vec{\tilde{P}},\vec{\tilde{q}},\tilde{\psi}_s) + \mathcal{O}(\varepsilon^2)\,, \tag{C.49a}$$

$$q_i = \tilde{q}_i - \varepsilon X_i^{(1)}(\vec{\tilde{P}},\vec{\tilde{q}},\tilde{\psi}_s) + \mathcal{O}(\varepsilon^2)\,, \tag{C.49b}$$

$$\begin{aligned}\psi_s = \tilde{\psi}_s &- W_s^{(0)}(\vec{\tilde{P}},\vec{\tilde{q}}) \\ &- \varepsilon\left(W_s^{(1)}(\vec{\tilde{P}},\vec{\tilde{q}},\tilde{\psi}_s) - \frac{\partial W_s^{(0)}(\vec{\tilde{P}},\vec{\tilde{q}})}{\partial \tilde{P}_j} Y_j^{(1)}(\vec{\tilde{P}},\vec{\tilde{q}})\right. \\ &\left. - \frac{\partial W_s^{(0)}(\vec{\tilde{P}},\vec{\tilde{q}})}{\partial \tilde{q}_i} X_i^{(1)}(\vec{\tilde{P}},\vec{\tilde{q}})\right) + \mathcal{O}(\varepsilon^2)\,.\end{aligned} \tag{C.49c}$$

Note that we do not invert to the same order in ε as the original transformation as the next order terms are not required to 1PA order.

Transformed equations of motion

To demonstrate how one obtains equations of motion for the transformed variables we will first look at the equations of motion for the orbital elements $\tilde{P}_j$. One takes the Mino time derivative of $\tilde{P}_j(\vec{P},\vec{q})$ as stated in Eqs. (5.41), substitutes the original equations of motion for the original variables from Eqs. (5.39) and then uses the inverse transformation Eqs. (C.49) to ensure that all the terms on the right hand side are in terms of the transformed variables.

One then expands in powers of ε and truncates at the desired order, i.e.,

$$\begin{aligned}\dot{\tilde{P}}_j =&\dot{P}_j + \varepsilon \dot{Y}_j^{(1)}(\vec{P},\vec{q},\psi_s) + \mathcal{O}(\varepsilon^2)\\ =&\varepsilon\Bigg(F_j^{(1)}(\vec{P},\vec{q},\psi_s) + \frac{\partial Y_j^{(1)}}{\partial q_i}(\vec{P},\vec{q},\psi_s)\Upsilon_i^{(0)}(\vec{P})\\ &+ \frac{\partial Y_j^{(1)}}{\partial \psi_s}(\vec{P},\vec{q},\psi_s)\Upsilon_s^{(0)}(\vec{P})\Bigg) + \mathcal{O}(\varepsilon^2)\\ =&\varepsilon\Bigg(F_j^{(1)}(\vec{\tilde{P}},\vec{\tilde{q}},\tilde{\psi}_s) + \frac{\partial Y_j^{(1)}}{\partial \tilde{q}_i}(\vec{\tilde{P}},\vec{\tilde{q}},\tilde{\psi}_s)\Upsilon_i^{(0)}(\vec{\tilde{P}})\\ &+ \frac{\partial Y_j^{(1)}}{\partial \tilde{\psi}_s}(\vec{\tilde{P}},\vec{\tilde{q}},\tilde{\psi}_s)\Upsilon_s^{(0)}(\vec{\tilde{P}})\Bigg) + \mathcal{O}(\varepsilon^2)\end{aligned} \tag{C.50}$$

Note that since the transformation to the NIT variables is near-identity, one does not see any corrections at the current order in the expansion, but these terms manifest at higher orders. Repeating these steps for the orbital elements through to $\mathcal{O}(\varepsilon^2)$ and the orbital and spin precession phases to $\mathcal{O}(\varepsilon)$, we obtain the following results:

$$\frac{d\tilde{P}_j}{d\lambda} = \varepsilon \tilde{F}_j^{(1)}(\vec{\tilde{P}},\vec{\tilde{q}},\tilde{\psi}_s) + \varepsilon^2 \tilde{F}_j^{(2)}(\vec{\tilde{P}},\vec{\tilde{q}},\tilde{\psi}_s) + \mathcal{O}(\varepsilon^3)\ , \tag{C.51a}$$

$$\frac{d\tilde{q}_i}{d\lambda} = \Upsilon_i^{(0)}(\vec{\tilde{P}}) + \varepsilon \Upsilon_i^{(1)}(\vec{\tilde{P}},\vec{\tilde{q}},\tilde{\psi}_s) + \mathcal{O}(\varepsilon^2)\ , \tag{C.51b}$$

$$\frac{d\tilde{\psi}_s}{d\lambda} = \Upsilon_s^{(0)}(\vec{\tilde{P}},\vec{\tilde{q}},\tilde{\psi}_s) + \varepsilon \Upsilon_s^{(1)}(\vec{\tilde{P}},\vec{\tilde{q}},\tilde{\psi}_s) + \mathcal{O}(\varepsilon^2)\ , \tag{C.51c}$$

where

$$\Upsilon_s^{(0)} = f_s^{(0)} + \frac{\partial W_j^{(1)}}{\partial \tilde{q}_i}\Upsilon_i^{(0)}\ , \tag{C.52a}$$

$$\tilde{F}_j^{(1)} = F_j^{(1)} + \frac{\partial Y_j^{(1)}}{\partial \tilde{q}_i}\Upsilon_i^{(0)} + \frac{\partial Y_j^{(1)}}{\partial \tilde{\psi}_s}\Upsilon_s^{(0)}\ , \tag{C.52b}$$

$$\begin{aligned}\Upsilon_s^{(1)} =& \frac{\partial W_s^{(1)}}{\partial \tilde{q}_i}\Upsilon_i^{(0)} + \frac{\partial W_s^{(1)}}{\partial \tilde{\psi}_s}\Upsilon_s^{(0)}\\ &- \frac{\partial f_s^{(0)}}{\partial \tilde{P}_j}Y_j^{(1)} - \frac{\partial f_s^{(0)}}{\partial \tilde{q}_i}X_i^{(1)}\ ,\end{aligned} \tag{C.52c}$$

$$\Upsilon_i^{(1)} = f_i^{(1)} + \frac{\partial X_i^{(1)}}{\partial \tilde{q}_k}\Upsilon_k^{(0)} + \frac{\partial X_i^{(1)}}{\partial \tilde{\psi}_s}\Upsilon_s^{(0)} - \frac{\partial \Upsilon_i^{(0)}}{\partial \tilde{P}_j}Y_j^{(1)}\ , \tag{C.52d}$$

$$\begin{aligned}\tilde{F}_j^{(2)} =& F_j^{(2)} + \frac{\partial Y_j^{(2)}}{\partial \tilde{q}_i}\Upsilon_i^{(0)} + \frac{\partial Y_j^{(1)}}{\partial \tilde{q}_i}f_i^{(1)} + \frac{\partial Y_j^{(1)}}{\partial \tilde{P}_k}F_k^{(1)}\\ &- \frac{\partial \tilde{F}_j^{(1)}}{\partial \tilde{P}_k}Y_k^{(1)} - \frac{\partial \tilde{F}_j^{(1)}}{\partial \tilde{q}_i}X_i^{(1)} - \frac{\partial \tilde{F}_j^{(1)}}{\partial \tilde{\psi}_s}W_s^{(1)}\ .\end{aligned} \tag{C.52e}$$

Note that all functions on the right hand side are evaluated at $\vec{\tilde{P}}$, $\vec{\tilde{q}}$, and $\tilde{\psi}_s$ and that we have adopted the convention that all repeated roman indices are summed over. Notice also that $\Upsilon_s^{(1)}$ will be suppressed by a factor of the mass-ratio: every term it appears in is proportional to secondary spin, and therefore will not contribute at 1PA order. We include these terms here for completeness, but only the 1PA contributions appear in Sec. 5.5.4.

Cancellation of oscillating terms at adiabatic order

We can recast the expression for $\Upsilon_s^{(0)}$ as

$$\begin{aligned}\Upsilon_s^{(0)} &= f_s^{(0)} + \frac{\partial W_s^{(1)}}{\partial \tilde{q}_i}\Upsilon_i^{(0)} \\ &= \left\langle f_s^{(0)} \right\rangle + \sum_{\vec{\kappa}\neq\vec{0}} \left(f_{s,\vec{\kappa}}^{(0)} + i(\vec{\kappa}\cdot\vec{\Upsilon}^{(0)})\breve{W}_{s,\vec{\kappa}}^{(0)} \right) e^{i\vec{\kappa}\cdot\vec{q}} \, .\end{aligned} \tag{C.53}$$

As such, we can cancel the oscillatory pieces of $\Upsilon_s^{(0)}$ by choosing the oscillatory part of $W_s^{(0)}$ to be

$$\breve{W}_{j,\vec{\kappa}}^{(0)} \equiv \frac{i}{\vec{\kappa}\cdot\vec{\Upsilon}^{(0)}} f_{s,\vec{\kappa}}^{(0)}(\vec{P}) = -(\psi_{sr}(q_r) + \psi_{sz}(q_z)) \, . \tag{C.54}$$

Conveniently, this is related to the oscillating pieces of the geodesic solution for the spin phase which is known analytically. Due to the separability of this solution, this transformation is always well defined, even in the presence of orbital resonances where $\vec{\kappa}_{\rm res} = \{k_r, k_z\}$ where $k_r, k_z \in \mathbb{Z}$, such that $\vec{\kappa}_{\rm res}\cdot\vec{\Upsilon}^{(0)} = k_r\Upsilon_r^{(0)} + k_z\Upsilon_z^{(0)} = 0$.

We can continue with this analysis and recast the expression for $\tilde{F}_j^{(1)}$ as

$$\begin{aligned}\tilde{F}_j^{(1)} &= F_j^{(1)} + \frac{\partial Y_j^{(1)}}{\partial \tilde{q}_i}\Upsilon_i^{(0)} + \frac{\partial Y_j^{(1)}}{\partial \tilde{\psi}_s}\Upsilon_s^{(0)} = F_j^{(1)} + \frac{\partial Y_j^{(1)}}{\partial \tilde{Q}_k}\Upsilon_k^{(0)} \\ &= \left\langle F_j^{(1)} \right\rangle + \sum_{\vec{\kappa}\neq\vec{0}} \left(F_{j,\vec{\kappa}}^{(1)} + i(\vec{\kappa}\cdot\vec{\Upsilon}^{(0)})\breve{Y}_{j,\vec{\kappa}}^{(1)} \right) e^{i\vec{\kappa}\cdot\vec{Q}} \, .\end{aligned} \tag{C.55}$$

As such, we can cancel the oscillatory pieces of $\tilde{F}_j^{(1)}$ by choosing the oscillatory part of $Y_j^{(1)}$ to be

$$\breve{Y}_{j,\vec{\kappa}}^{(1)} \equiv \frac{i}{\vec{\kappa}\cdot\vec{\Upsilon}^{(0)}} F_{j,\vec{\kappa}}^{(1)}(\vec{P}) \, . \tag{C.56}$$

Clearly, one can only make this choice so long as there is no $\vec{\kappa}_{\rm res} = \{\kappa_r, \kappa_z, \kappa_s\}$ where $\kappa_r, \kappa_z, \kappa_s \in \mathbb{Z}$, such that $\vec{\kappa}_{\rm res}\cdot\vec{\Upsilon}^{(0)} = \kappa_r\Upsilon_r^{(0)} + \kappa_z\Upsilon_z^{(0)} + \kappa_s\Upsilon_s^{(0)} = 0$. This is occasionally the case in the presence of resonances, where the spin, radial, or polar frequencies become commensurate. We have carefully chosen our data grids so that we do not encounter such orbits in our study.

Cancellation of oscillating terms at post-adiabatic order

Using the above choice for $\breve{Y}_j^{(1)}$, the equation for $\Upsilon_i^{(1)}$ becomes

$$\begin{aligned}\Upsilon_i^{(1)} &= f_i^{(1)} - \frac{\partial \Upsilon_i^{(0)}}{\partial \tilde{P}_j} Y_j^{(1)} + \frac{\partial X_i^{(1)}}{\partial \tilde{q}_k} \Upsilon_k^{(0)} + \frac{\partial X_i^{(1)}}{\partial \tilde{\psi}_s} \Upsilon_s^{(0)} \\ &= f_i^{(1)} - \frac{\partial \Upsilon_i^{(0)}}{\partial \tilde{P}_j} Y_j^{(1)} + \frac{\partial X_i^{(1)}}{\partial \tilde{Q}_k} \Upsilon_k^{(0)} \\ &= \left\langle f_i^{(1)} \right\rangle - \frac{\partial \Upsilon_i^{(0)}}{\partial \tilde{P}_j} \left\langle Y_j^{(1)} \right\rangle \\ &+ \sum_{\vec{\kappa} \neq \vec{0}} \left(f_{i,\vec{\kappa}}^{(1)} + i(\vec{\kappa} \cdot \vec{\Upsilon}^{(0)}) \breve{X}_{i,\vec{\kappa}}^{(1)} - \frac{i}{\vec{\kappa} \cdot \vec{\Upsilon}^{(0)}} \frac{\partial \Upsilon_i^{(0)}}{\partial \tilde{P}_j} F_{j,\vec{\kappa}}^{(1)} \right) e^{i\vec{\kappa} \cdot \vec{Q}} \, .\end{aligned} \tag{C.57}$$

As a result, we can remove the oscillating pieces of $\Upsilon_i^{(1)}$ by choosing

$$\breve{X}_{i,\vec{\kappa}}^{(1)} \equiv \frac{i}{\vec{\kappa} \cdot \vec{\Upsilon}^{(0)}} f_{i,\vec{\kappa}}^{(1)} + \frac{1}{(\vec{\kappa} \cdot \vec{\Upsilon}^{(0)})^2} \frac{\partial \Upsilon_i^{(0)}}{\partial P_j} F_{j,\vec{\kappa}}^{(1)} \, . \tag{C.58}$$

Similarly, looking at the equation for $\Upsilon_s^{(1)}$, we see that:

$$\begin{aligned}\Upsilon_s^{(1)} =& \frac{\partial W_s^{(1)}}{\partial \tilde{q}_i} \Upsilon_i^{(0)} + \frac{\partial W_s^{(1)}}{\partial \tilde{\psi}_s} \Upsilon_s^{(0)} - \frac{\partial f_s^{(0)}}{\partial \tilde{P}_j} Y_j^{(1)} - \frac{\partial f_s^{(0)}}{\partial \tilde{q}_i} X_i^{(1)} \\ =& \frac{\partial W_s^{(1)}}{\partial \tilde{q}_k} \Upsilon_k^{(0)} - \frac{\partial f_s^{(0)}}{\partial \tilde{P}_j} Y_j^{(1)} - \frac{\partial f_s^{(0)}}{\partial \tilde{q}_i} X_i^{(1)} \\ =& \frac{\partial W_s^{(1)}}{\partial \tilde{q}_k} \Upsilon_s^{(0)} - \left\langle \frac{\partial f_s^{(0)}}{\partial \tilde{P}_j} Y_j^{(1)} \right\rangle - \left\langle \frac{\partial f_s^{(0)}}{\partial \tilde{q}_i} X_i^{(1)} \right\rangle \\ &- \left\{ \frac{\partial f_s^{(0)}}{\partial \tilde{P}_j} Y_j^{(1)} \right\} - \left\{ \frac{\partial f_s^{(0)}}{\partial \tilde{q}_i} X_i^{(1)} \right\} \\ =& - \left\langle \frac{\partial f_s^{(0)}}{\partial \tilde{P}_j} Y_j^{(1)} \right\rangle - \left\langle \frac{\partial f_s^{(0)}}{\partial \tilde{q}_i} X_i^{(1)} \right\rangle \\ &+ \sum_{\vec{\kappa} \neq \vec{0}} \left(i(\vec{\kappa} \cdot \vec{\Upsilon}^{(0)}) \breve{W}_{s,\vec{\kappa}}^{(1)} - \sum_{\vec{\kappa}' \neq \vec{0}} \left[\frac{\partial f_{s,\kappa'}^{(0)}}{\partial \tilde{P}_j} Y_{j,\vec{\kappa}-\vec{\kappa}'}^{(1)} + \frac{\partial f_{s,\vec{\kappa}'}^{(0)}}{\partial \tilde{q}_i} X_{i\vec{\kappa}-\vec{\kappa}'}^{(1)} \right] \right) e^{i\vec{\kappa} \cdot \vec{Q}} \, ,\end{aligned} \tag{C.59}$$

where we introduced the additional notation $\{\cdot\}$ to denote the oscillatory part of a product of two purely oscillatory functions $\breve{A}$ and $\breve{B}$, which can be expressed in terms of their Fourier modes by

$$\left\{ \breve{A} \breve{B} \right\} = \sum_{\vec{\kappa} \neq \vec{0}} \sum_{\vec{\kappa}' \neq \vec{0}} A_{\vec{\kappa}'} B_{\vec{\kappa}-\vec{\kappa}'} \, . \tag{C.60}$$

From this we obtain

$$\breve{W}^{(1)}_{s,\vec{\kappa}} = \frac{i}{\vec{\kappa}\cdot\vec{\Upsilon}^{(0)}}\left(\sum_{\vec{\kappa}'\neq\vec{0}}\left[\frac{\partial f^{(0)}_{s,\kappa'}}{\partial\tilde{P}_j}Y^{(1)}_{j,\vec{\kappa}-\vec{\kappa}'} + \frac{\partial f^{(0)}_{s,\vec{\kappa}'}}{\partial\tilde{q}_i}X^{(1)}_{i\vec{\kappa}-\vec{\kappa}'}\right]\right) . \tag{C.61}$$

Using the above choice for $\breve{Y}^{(1)}_j$, we can express the oscillatory part of the expression for $\tilde{F}^{(2)}_j$ as

$$\begin{aligned}
\breve{\tilde{F}}^{(2)}_j =& \breve{F}^{(2)}_j + \frac{\partial\breve{Y}^{(2)}_j}{\partial\tilde{\mathcal{Q}}_k}\Upsilon^{(0)}_k + \left\{\frac{\partial Y^{(1)}_j}{\partial\tilde{q}_i}f^{(1)}_i\right\} \\
&+ \left\{\frac{\partial Y^{(1)}_j}{\partial\tilde{P}_k}F^{(1)}_k\right\} - \frac{\partial\left\langle F^{(1)}_j\right\rangle}{\partial\tilde{P}_k}\breve{Y}^{(1)}_k \\
=&\sum_{\vec{\kappa}\neq\vec{0}}\Bigg(F^{(2)}_{j,\vec{\kappa}} + i(\vec{\kappa}\cdot\vec{\Upsilon}^{(0)})\breve{Y}^{(2)}_{j,\vec{\kappa}} + \frac{\partial\left\langle Y^{(1)}_j\right\rangle}{\partial\tilde{P}_k}F^{(1)}_{k,\vec{\kappa}} \\
&- i\frac{\partial\left\langle F^{(1)}_j\right\rangle}{\partial\tilde{P}_k}\frac{F_{k,\vec{\kappa}}}{\vec{\kappa}\cdot\vec{\Upsilon}^{(0)}} + \sum_{\vec{\kappa}'\neq\vec{0}}\Bigg(i\frac{F^{(1)}_{k,\vec{\kappa}-\vec{\kappa}'}}{\vec{\kappa}'\cdot\vec{\Upsilon}^{(0)}}\Bigg(\frac{\partial F^{(1)}_{j,\vec{\kappa}'}}{\partial\tilde{P}_k} \\
&- \frac{F^{(1)}_{j,\vec{\kappa}'}}{\vec{\kappa}'\cdot\vec{\Upsilon}^{(0)}}\frac{\partial(\vec{\kappa}'\cdot\vec{\Upsilon}^{(0)})}{\partial\tilde{P}_k}\Bigg) - \frac{\vec{\kappa}'\cdot\vec{f}^{(1)}_{\vec{\kappa}-\vec{\kappa}'}}{\vec{\kappa}'\cdot\vec{\Upsilon}^{(0)}}F^{(1)}_{j,\vec{\kappa}'}\Bigg)\Bigg)e^{i\vec{\kappa}\cdot\vec{Q}} ,
\end{aligned} \tag{C.62}$$

Thus we can remove the oscillatory part of $\tilde{F}^{(2)}_j$ by choosing

$$\begin{aligned}
\breve{Y}^{(2)}_{j,\vec{\kappa}} =& \frac{i}{\vec{\kappa}\cdot\vec{\Upsilon}^{(0)}}\Bigg(F^{(2)}_{j,\vec{\kappa}} + \frac{\partial\left\langle Y^{(1)}_j\right\rangle}{\partial\tilde{P}_k}F^{(1)}_{k,\vec{\kappa}} \\
&- i\frac{\partial\left\langle F^{(1)}_j\right\rangle}{\partial\tilde{P}_k}\frac{F^{(1)}_{k,\vec{\kappa}}}{\vec{\kappa}\cdot\vec{\Upsilon}^{(0)}} + \sum_{\vec{\kappa}'\neq\vec{0}}\Bigg(i\frac{F^{(1)}_{k,\vec{\kappa}-\vec{\kappa}'}}{\vec{\kappa}'\cdot\vec{\Upsilon}^{(0)}}\Bigg(\frac{\partial F^{(1)}_{j,\vec{\kappa}'}}{\partial\tilde{P}_k} \\
&- \frac{F^{(1)}_{j,\vec{\kappa}'}}{\vec{\kappa}'\cdot\vec{\Upsilon}^{(0)}}\frac{\partial(\vec{\kappa}'\cdot\vec{\Upsilon}^{(0)})}{\partial\tilde{P}_k}\Bigg) - \frac{\vec{\kappa}'\cdot\vec{f}^{(1)}_{\vec{\kappa}-\vec{\kappa}'}}{\vec{\kappa}'\cdot\vec{\Upsilon}^{(0)}}F^{(1)}_{j,\vec{\kappa}'}\Bigg)\Bigg) .
\end{aligned} \tag{C.63}$$

Freedom in the averaged pieces

With the oscillatory pieces of the NIT equations of motion removed, terms in the equations of motion become

$$\tilde{F}^{(1)}_j = \left\langle F^{(1)}_j\right\rangle , \quad \Upsilon^{(0)}_s = \left\langle f^{(0)}_s\right\rangle , \tag{C.64a-b}$$

$$\Upsilon^{(1)}_i = \left\langle f^{(1)}_i\right\rangle - \frac{\partial\Upsilon^{(0)}_i}{\partial\tilde{P}_j}\left\langle Y^{(1)}_j\right\rangle , \tag{C.64a}$$

and

$$\begin{aligned}\Upsilon_s^{(1)} =& -\left\langle \frac{\partial \breve{f}_s^{(0)}}{\partial \tilde{P}_j} \breve{Y}_j^{(1)} \right\rangle - \left\langle \frac{\partial \breve{f}_s^{(0)}}{\partial \tilde{q}_i} \breve{X}_i^{(1)} \right\rangle \\ & - \frac{\partial \left\langle f_s^{(0)} \right\rangle}{\partial \tilde{P}_j} \left\langle Y_j^{(1)} \right\rangle \ ,\end{aligned} \tag{C.65}$$

$$\begin{aligned}\tilde{F}_j^{(2)} =& \left\langle F_j^{(2)} \right\rangle + \left\langle \frac{\partial \breve{Y}_j^{(1)}}{\partial \tilde{q}_i} \breve{f}_i^{(1)} \right\rangle + \left\langle \frac{\partial \breve{Y}_j^{(1)}}{\partial \tilde{P}_k} F_k^{(1)} \right\rangle \\ & + \frac{\partial \left\langle Y_j^{(1)} \right\rangle}{\partial \tilde{P}_k} \left\langle F_k^{(1)} \right\rangle - \frac{\partial \left\langle F_j^{(1)} \right\rangle}{\partial \tilde{P}_k} \left\langle Y_k^{(1)} \right\rangle \ .\end{aligned} \tag{C.66}$$

Note that we still have freedom to set the averaged pieces of the transformation functions from Eqs. (5.41), i.e., $\left\langle Y_j^{(1)} \right\rangle$, $\left\langle Y_j^{(2)} \right\rangle$, $\left\langle W_s^{(0)} \right\rangle$, $\left\langle W_s^{(1)} \right\rangle$, and $\left\langle X_i^{(1)} \right\rangle$, to be anything we choose. There are many valid and interesting choices that one could make that are explored in Refs. [101], [104], [185]. For this work, we make use of the simplest choice: $\left\langle Y_j^{(1)} \right\rangle = \left\langle Y_j^{(2)} \right\rangle = \left\langle W_s^{(0)} \right\rangle = \left\langle W_s^{(1)} \right\rangle = \left\langle X_i^{(1)} \right\rangle = 0$, as this makes it easy to compare between OG and NIT inspirals. It also has the benefit of drastically simplifying equations of motion to

$$\tilde{F}_j^{(1)} = \left\langle F_j^{(1)} \right\rangle \ , \Upsilon_s^{(0)} = \left\langle f_s^{(0)} \right\rangle \ , \Upsilon_i^{(1)} = \left\langle f_i^{(1)} \right\rangle \ , \tag{C.67a-c}$$

and

$$\Upsilon_s^{(1)} = -\left\langle \frac{\partial \breve{f}_s^{(0)}}{\partial \tilde{P}_j} \breve{Y}_j^{(1)} \right\rangle - \left\langle \frac{\partial \breve{f}_s^{(0)}}{\partial \tilde{q}_i} \breve{X}_i^{(1)} \right\rangle \ , \tag{C.68}$$

$$\tilde{F}_j^{(2)} = \left\langle F_j^{(2)} \right\rangle + \left\langle \frac{\partial \breve{Y}_j^{(1)}}{\partial \tilde{q}_i} \breve{f}_i^{(1)} \right\rangle + \left\langle \frac{\partial \breve{Y}_j^{(1)}}{\partial \tilde{P}_k} F_k^{(1)} \right\rangle \ . \tag{C.69}$$

Evolution of extrinsic quantities

Now we look to remove the oscillatory pieces of the evolution equations for the extrinsic quantities $\vec{\mathcal{X}}$:

$$\frac{d\mathcal{X}}{d\lambda} = f_k^{(0)}(\vec{P}, \vec{q}) \ . \tag{C.70}$$

Since these terms do not depend directly on the spin phase ψ, this calculation goes through the same as in the non-spinning case. Substituting the inverse transformation (C.49) and re-expanding in ε we can write this as an equation involving only the NIT variables $\vec{\tilde{P}}$ and $\vec{\tilde{q}}$,

$$\frac{d\mathcal{X}}{d\lambda} = f_k^{(0)} - \varepsilon \left(\frac{\partial f_k^{(0)}}{\partial \tilde{P}_j} Y_j^{(1)} + \frac{\partial f_k^{(0)}}{\partial \tilde{q}_i} X_i^{(1)} \right) + \mathcal{O}(\varepsilon^2) \ , \tag{C.71}$$

where all of the functions on the right hand side are now functions of $\vec{\tilde{P}}$ and $\vec{\tilde{q}}$. In order to remove the oscillatory pieces of the equations, we make use of a new set of extrinsic quantities $\vec{\tilde{\mathcal{X}}}$ that are related to the original quantities by the following transformation:

$$\tilde{\mathcal{X}}_k = \mathcal{X}_k + Z_k^{(0)}(\vec{\tilde{P}}, \vec{\tilde{q}}) + \varepsilon Z_k^{(1)}(\vec{\tilde{P}}, \vec{\tilde{q}}) \ . \tag{C.72}$$

We note that since this transformation has a zeroth order in mass ratio term $Z_k^{(0)}$, it is not an near-identity transformation. Thus when we produce waveforms it will be necessary to be able to calculate $Z_k^{(0)}$ explicitly.

We then take the time derivative of (C.72), substitute the equations of motion for $\vec{\mathcal{X}}$ and expand order by order to obtain equations of motion for $\vec{\tilde{\mathcal{X}}}$:

$$\frac{d\tilde{\mathcal{X}}_k}{d\lambda} = \Upsilon_k^{(0)} + \varepsilon \Upsilon_k^{(1)} + \mathcal{O}(\varepsilon^2) \ , \tag{C.73}$$

where

$$\Upsilon_k^{(0)} = f_k^{(0)} + \frac{\partial Z_k^{(0)}}{\partial \tilde{q}_i} \Upsilon_i^{(0)} \ , \tag{C.74a}$$

$$\begin{aligned} \Upsilon_k^{(1)} =& \frac{\partial Z_k^{(0)}}{\partial \tilde{q}_i} \Upsilon_i^{(1)} + \frac{\partial Z_k^{(0)}}{\partial \tilde{P}_j} \tilde{F}_j^{(1)} + \frac{\partial Z_k^{(1)}}{\partial \tilde{q}_i} \Upsilon_i^{(0)} \\ & - \frac{\partial f_k^{(0)}}{\partial \tilde{P}_j} Y_j^{(1)} - \frac{\partial f_k^{(0)}}{\partial \tilde{q}_i} X_i^{(1)} \ . \end{aligned} \tag{C.74b}$$

We can now remove the oscillating pieces of the functions $\Upsilon_k^{(0)}$ by solving the equations

$$0 = \breve{f}_k^{(0)} + \frac{\partial \breve{Z}_k^{(0)}}{\partial \tilde{q}_i} \Upsilon_i^{(0)} \ , \tag{C.75a}$$

$$\begin{aligned} 0 =& \frac{\partial \breve{Z}_k^{(0)}}{\partial \tilde{q}_i} \Upsilon_i^{(1)} + \frac{\partial \breve{Z}_k^{(0)}}{\partial \tilde{P}_j} \tilde{F}_j^{(1)} + \frac{\partial \breve{Z}_k^{(1)}}{\partial \tilde{q}_i} \Upsilon_i^{(0)} \\ & - \left\{ \frac{\partial f_k^{(0)}}{\partial \tilde{P}_j} Y_j^{(1)} \right\} - \left\{ \frac{\partial f_k^{(0)}}{\partial \tilde{q}_i} X_i^{(1)} \right\} \ , \end{aligned} \tag{C.75b}$$

for the oscillatory parts of the transformation $\breve{Z}_k^{(0)}$ and $\breve{Z}_k^{(1)}$. The first of these is satisfied by using the oscillating pieces for the analytic solutions for the geodesic motion of t and ϕ,

$$\breve{Z}_k^{(0)} = -\breve{\mathcal{X}}_{k,r}(q_r) - \breve{\mathcal{X}}_{k,z}(q_z) \ . \tag{C.76}$$

It is unclear whether the equation for $Z_k^{(1)}$ would yield analytic solutions, but it can be solved numerically. Since we only need to know the extrinsic quantities to $\mathcal{O}(\varepsilon)$ to generate waveforms, we do not need to be able to calculate this explicitly and it is sufficient to know that a solution exists.

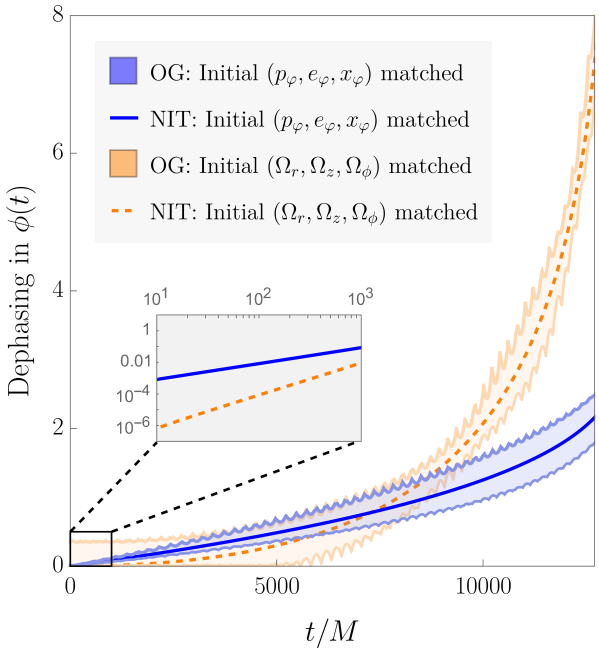

Figure C.1: Dephasing in $\phi(t)$ of a spinning-body orbit relative to a non-spinning body orbit for two different choices of initial conditions. The system has mass ratio $\varepsilon = 10^{-2}$ and the small body orbits a black hole with spin $a = 0.7M$. The magnitude and orientation of the small body's spin is specified by $s = 1$, $s_\parallel = s$. The blue curves correspond to matching initial orbital elements $(p_\varphi, e_\varphi, x_\varphi)$ while the orange curves denotes matching the initial Boyer-Lindquist frequencies $(\Omega_r, \Omega_z, \Omega_\phi)$. The solid curves show the averaged dephasing of $\phi(t)$, i.e., $\varphi_\phi^{RR+SCF} - \varphi_\phi^{RR}$ while the shading shows the dephasing of $\phi(t)$ given directly by the OG equations, i.e., $\phi^{RR+SCF} - \phi^{RR}$. Initially, $p = 9.5$, $e = 0.19$, and $x_I = 0.699$.

Now the forcing functions only depend only on $\vec{\tilde{P}}$ and are given by

$$\Upsilon_k^{(0)} = \left\langle f_k^{(0)} \right\rangle , \tag{C.77a}$$

$$\begin{aligned} \Upsilon_k^{(1)} =& \frac{\partial \left\langle Z_k^{(0)} \right\rangle}{\partial \tilde{P}_j} \tilde{F}_j^{(1)} - \frac{\partial \left\langle f_k^{(0)} \right\rangle}{\partial \tilde{P}_j} \left\langle Y_j^{(1)} \right\rangle \\ & - \left\langle \frac{\partial \breve{f}_k^{(0)}}{\partial \tilde{P}_j} \breve{Y}_j^{(1)} \right\rangle - \left\langle \frac{\partial \breve{f}_k^{(0)}}{\partial \tilde{q}_i} \breve{X}_i^{(1)} \right\rangle . \end{aligned} \tag{C.77b}$$

Again, we have freedom in the average pieces of the transformation functions which we use to simplify this problem further. As before, we chose the simplest option and set $\left\langle Z_k^{(0)} \right\rangle = \left\langle Z_k^{(1)} \right\rangle = 0$ which along with our previous choices simplifies the expression for $\Upsilon_k^{(1)}$ to be

$$\Upsilon_k^{(1)} = - \left\langle \frac{\partial \breve{f}_k^{(0)}}{\partial \tilde{P}_j} \breve{Y}_j^{(1)} \right\rangle - \left\langle \frac{\partial \breve{f}_k^{(0)}}{\partial \tilde{q}_i} \breve{X}_i^{(1)} \right\rangle . \tag{C.78}$$

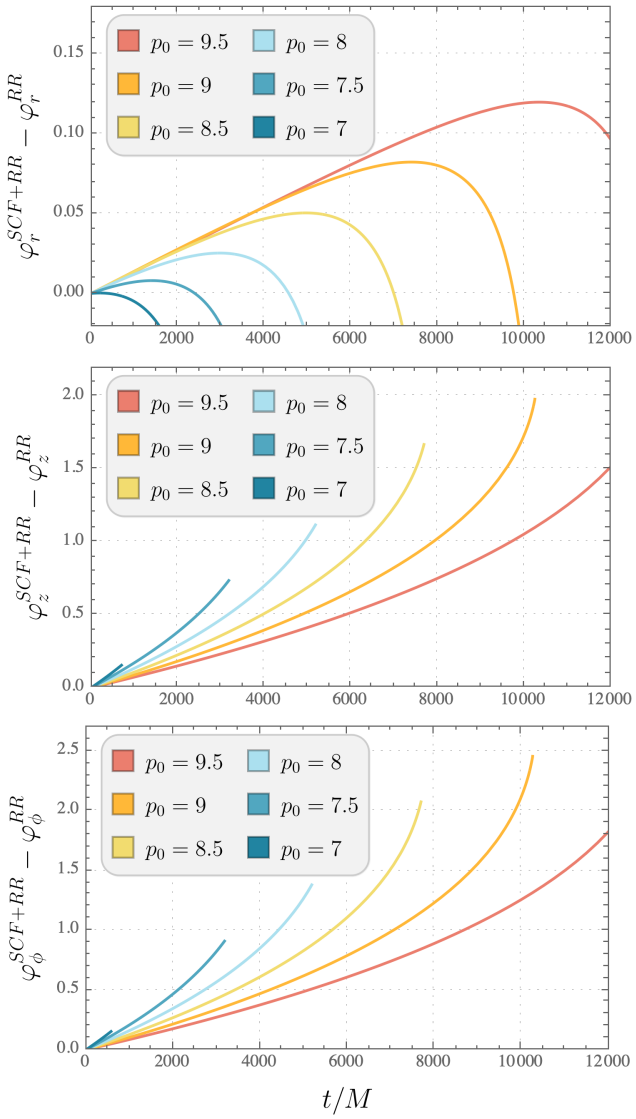

Figure C.2: Averaged dephasing in $q_r(t)$, $q_z(t)$, and $\phi(t)$ for a spinning body relative to a non-spinning body with mass ratio $\varepsilon = 10^{-2}$ orbiting a black hole with spin $a = 0.7M$; the small body's spin is given $s = 1$, $s_\parallel = s$. The top panel shows $\varphi_r^{SCF+RR} - \varphi_r^{RR}$, the middle panel shows $\varphi_z^{SCF+RR} - \varphi_z^{RR}$ and the bottom panel shows $\varphi_\phi^{SCF+RR} - \varphi_\phi^{RR}$. Different colors correspond to different initial p values for the inspiral; duration of inspiral also correlates with initial p (inspiral with $p_0 = 9.5$ is longest, that with $p_0 = 7$ is shortest, etc.). For all panels, $e = 0.2$, $x_I = 0.7$, $q_r = 0$, $q_z = 0$, and $\phi = 0$ initially.

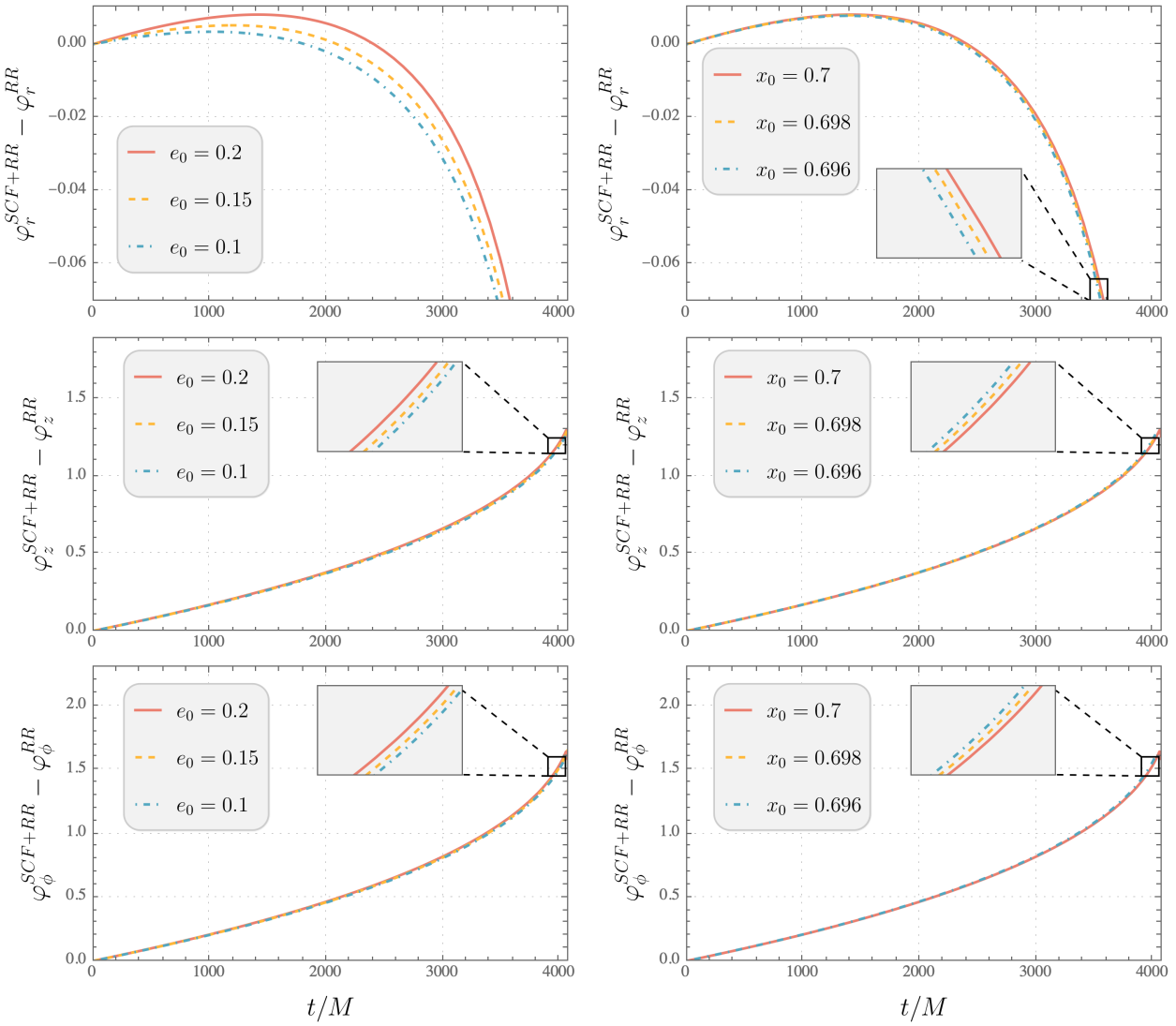

Figure C.3: Averaged dephasing in $q_r(t)$, $q_z(t)$, and $\phi(t)$ for a spinning body relative to a non-spinning body with mass ratio $\varepsilon = 10^{-2}$ orbiting a black hole with spin $a = 0.7M$; the small body's spin has $s = 1$, $s_\parallel = s$. The top row shows $\varphi_r^{SCF+RR} - \varphi_r^{RR}$, the middle row shows $\varphi_z^{SCF+RR} - \varphi_z^{RR}$ and the bottom row shows $\varphi_\phi^{SCF+RR} - \varphi_\phi^{RR}$. In the left column, the different colors correspond to different initial e values for the inspiral; in the right column, the different colors correspond to different initial values of x_I. For all panels, $p = 7.5$ and $x_I = 0.7$ initially. For the left column, the initial value of x_I is 0.7 and for the right column the initial value of e is 0.2.

C.3.2 Summary of Mino-time quantities

We chose the average pieces of the transformation terms to be $\left\langle Y_j^{(1)} \right\rangle = \left\langle Y_j^{(2)} \right\rangle = \left\langle X_i^{(1)} \right\rangle = \left\langle W_s^{(0)} \right\rangle = \left\langle W_s^{(1)} \right\rangle = \left\langle Z_k^{(0)} \right\rangle = \left\langle Z_k^{(1)} \right\rangle = 0$ and so the transformed forcing functions are related to the original functions by

$$\tilde{F}_j^{(1)} = \left\langle F_j^{(1)} \right\rangle \ , \quad \Upsilon_s^{(0)} = \left\langle f_s^{(0)} \right\rangle \ , \tag{C.79a-b}$$

$$\Upsilon_i^{(1)} = \left\langle f_i^{(1)} \right\rangle \ , \quad \Upsilon_k^{(0)} = \left\langle f_k^{(0)} \right\rangle \ , \tag{C.79c-d}$$

$$\Upsilon_s^{(1)} = -\left\langle \frac{\partial \breve{f}_s^{(0)}}{\partial \tilde{P}_j} \breve{Y}_j^{(1)} \right\rangle - \left\langle \frac{\partial \breve{f}_s^{(0)}}{\partial \tilde{q}_i} \breve{X}_i^{(1)} \right\rangle \ , \tag{C.79e}$$

$$\tilde{F}_j^{(2)} = \left\langle F_j^{(2)} \right\rangle + \left\langle \frac{\partial \breve{Y}_j^{(1)}}{\partial \tilde{q}_i} \breve{f}_i^{(1)} \right\rangle + \left\langle \frac{\partial \breve{Y}_j^{(1)}}{\partial \tilde{P}_k} \breve{F}_k^{(1)} \right\rangle \ , \tag{C.79f}$$

$$\Upsilon_k^{(1)} = -\left\langle \frac{\partial \breve{f}_k^{(0)}}{\partial \tilde{P}_j} \breve{Y}_j^{(1)} \right\rangle - \left\langle \frac{\partial \breve{f}_k^{(0)}}{\partial \tilde{q}_i} \breve{X}_i^{(1)} \right\rangle \ . \tag{C.79g}$$

In deriving these equations of motion, we have constrained the oscillating pieces of the transformation functions to be

$$\breve{Y}_j^{(1)} \equiv \sum_{\vec{\kappa} \neq \vec{0}} \frac{i}{\vec{\kappa} \cdot \vec{\Upsilon}} F_{j,\vec{\kappa}}^{(1)} e^{i\vec{\kappa}\cdot\vec{Q}}, \tag{C.80}$$

$$\breve{X}_i^{(1)} \equiv \sum_{\vec{\kappa} \neq \vec{0}} \left(\frac{i}{\vec{\kappa} \cdot \vec{\Upsilon}} f_{i,\vec{\kappa}}^{(1)} + \frac{1}{(\vec{\kappa} \cdot \vec{\Upsilon})^2} \frac{\partial \Upsilon_i}{\partial P_j} F_{j,\vec{\kappa}}^{(1)} \right) e^{i\vec{\kappa}\cdot\vec{Q}} \ , \tag{C.81}$$

$$\breve{W}_{s,\vec{\kappa}}^{(1)} \equiv \sum_{\vec{\kappa} \neq \vec{0}} \frac{i}{\vec{\kappa} \cdot \vec{\Upsilon}^{(0)}} \left(\sum_{\vec{\kappa}' \neq \vec{0}} \left[\frac{\partial f_{s,\kappa'}^{(0)}}{\partial \tilde{P}_j} Y_{j,\vec{\kappa}-\vec{\kappa}'}^{(1)} + \frac{\partial f_{s,\vec{\kappa}'}^{(0)}}{\partial \tilde{q}_i} X_{i\vec{\kappa}-\vec{\kappa}'}^{(1)} \right] \right) e^{i\vec{\kappa}\cdot\vec{Q}} \ . \tag{C.82}$$

In order to generate waveforms, one only needs to know the transformations in Eq. (5.41) to zeroth order in the mass ratio so that the error is $\mathcal{O}(\varepsilon)$ i.e.,

$$P_j = \tilde{P}_j + \mathcal{O}(\varepsilon) \ , \tag{C.83a}$$

$$q_i = \tilde{q}_i + \mathcal{O}(\varepsilon) \ , \tag{C.83b}$$

$$\psi_s = \tilde{\psi}_s - W_s^{(0)}(\vec{\tilde{P}}, \vec{\tilde{q}}) + \mathcal{O}(\varepsilon) \ , \tag{C.83c}$$

$$\mathcal{X}_k = \tilde{\mathcal{X}}_k - Z_k^{(0)}(\vec{\tilde{P}}, \vec{\tilde{q}}) + \mathcal{O}(\varepsilon) \ . \tag{C.83d}$$

where the zeroth order transformation term for the spin precession phase $\breve{W}_k^{(0)}$ is known analytically from Eq. (5.38)

$$\breve{W}_{j,\vec{\kappa}}^{(0)} = -\psi_{sr}(q_r) - \psi_{sz}(q_z) \ . \tag{C.84}$$

Moreover, the zeroth order transformation term for the extrinsic quantities $\breve{Z}_k^{(0)}$ are also known analytically as they are related to the oscillatory parts of the analytic solutions for the geodesic equations for t and ϕ by

$$\breve{Z}_k^{(0)} = -\breve{\mathcal{X}}_{k,r}(q_r) - \breve{\mathcal{X}}_{k,z}(q_z) \,. \tag{C.85}$$

C.3.3 NIT Operator

By substituting the explicit forms of the transformation functions $Y_j^{(1)}$ and $X_i^{(1)}$ into the expressions for $\tilde{F}_j^{(2)}$ and $\tilde{\mathcal{X}}_k^{(1)}$, we identify a common functional form $\mathcal{N}(A)$ which allows us to compactly write $\tilde{F}_j^{(2)} = \left\langle F_j^{(2)} \right\rangle + \mathcal{N}(F_j^{(1)})$ and $\tilde{\mathcal{X}}_k^{(1)} = \mathcal{N}(\mathcal{X}_k^{(0)})$. The expression for $\mathcal{N}(A)$ is given by:

$$\begin{aligned}\mathcal{N}(A) = \sum_{(n,k,j)\neq(0,0,0)} \frac{i}{\Upsilon^{(0)}_{nkj}} \Bigg[& iA_{knj}\left(n f^{(1)}_{r,-n-k-j} + k f^{(1)}_{z,-n-k-j}\right) + \\ & \frac{\partial A_{nkj}}{\partial \tilde{p}} F^{(1)}_{p,-n-k-j} + \frac{\partial A_{nkj}}{\partial \tilde{e}} F^{(1)}_{e,-n-k-j} + \frac{\partial A_{nkj}}{\partial \tilde{x}} F^{(1)}_{x,-n-k-j} \\ & - \frac{A_{nkj}}{\Upsilon^{(0)}_{knj}}\left(\frac{\partial \Upsilon^{(0)}_{nkj}}{\partial \tilde{p}} F^{(1)}_{p,-n-k-j} + \frac{\partial \Upsilon^{(0)}_{nkj}}{\partial \tilde{e}} F^{(1)}_{e,-n-k-j} + \frac{\partial \Upsilon^{(0)}_{nkj}}{\partial \tilde{x}} F^{(1)}_{x,-n-k-j}\right)\Bigg] \,,\end{aligned} \tag{C.86}$$

where $\Upsilon^{(0)}_{nkj} = n\Upsilon^{(0)}_r + k\Upsilon^{(0)}_z + j\Upsilon^{(0)}_s$. Note that we make use of the result that the averaged part of the product of two oscillatory functions can be expressed in terms of its Fourier modes by:

$$\left\langle \breve{A}\breve{B} \right\rangle = \sum_{\vec{\kappa}\neq\vec{0}} A_{\vec{\kappa}} B_{-\vec{\kappa}} \,. \tag{C.87}$$

Also note that for the problem that we are solving in this work with the radiation reaction driven only by the GW fluxes and the conservative effects coming only from the spin-curvature force, we find that $\mathcal{N}(F_p^{(1)})$, $\mathcal{N}(F_e^{(1)})$, and $\mathcal{N}(F_{x_I}^{(1)})$ are numerically consistent with zero. This is to be expected as there is no interplay between the modes of the dissipative and conservative forces [101]. We would not expect this to hold if one were to include the first order conservative GSF needed for 1PA inspiral calculations.

C.4 Initial conditions

C.4.1 OG and NIT

To be able to directly compare between OG and NIT inspirals in Mino-time, we will need to match their initial conditions to sufficient accuracy. To maintain an overall phase difference of $\mathcal{O}(\varepsilon)$ in the course of an inspiral, the initial values of the phases and extrinsic quantities

need only be known to zeroth order in ε. However, we need to know the initial values of the orbital elements $\vec{P}$ to linear order in ε and so we use

$$\tilde{P}_j(0) \simeq P_j(0) + \varepsilon Y_j^{(1)}\big(\vec{P}(0), \vec{q}(0), \psi_s(0) - \breve{W}^{(0)}(\vec{P}(0), \vec{q}(0))\big) \ . \tag{C.88}$$

When comparing between OG inspirals and NIT inspirals that are parameterized by Boyer-Lindquist time t, we set the initial conditions for the phases of the OG inspiral and match the initial conditions for the $\vec{\varphi}$ phases via:

$$\varphi_\alpha(0) = \tilde{\mathcal{Q}}_\alpha(0) + \Delta\varphi_\alpha(\vec{\tilde{P}}(0), \vec{\tilde{q}}(0)) + \mathcal{O}(\varepsilon) \ , \tag{C.89}$$

where $\tilde{\mathcal{Q}}_\alpha(0)$ are given by Eqs. (C.83) and $\tilde{P}_j(0)$ is given by Eq. (C.88). However, we to maintain subradian accuracy in the phases, we need to know the initial conditions for the orbital elements to sub-leading order via:

$$\mathcal{P}_j(0) = \tilde{P}_j(0) + \varepsilon \Pi_j^{(1)}\big(\vec{P}(0), \vec{q}(0)\big) + \mathcal{O}(\varepsilon^2) \ . \tag{C.90}$$

C.4.2 Adiabatic and post-adiabatic

There are different approaches to matching initial conditions when comparing adiabatic and post-adiabatic inspirals. As discussed in Refs. [101]–[103], matching the initial values of orbital parameters $(p_\varphi, e_\varphi, x_\varphi)$ between adiabatic and post-adiabatic inspirals leads to a linearly growing error in the orbital phases. By instead matching the initial Boyer-Lindquist frequencies Ω_r, Ω_ϕ, and Ω_z, we will instead have quadratic growth in t. Explicitly, we can choose initial conditions $(p_\varphi^{RR+SCF}, e_\varphi^{RR+SCF}, x_\varphi^{RR+SCF})$ for the inspiral that includes spin-curvature force and then find the initial conditions for the radiation-reaction-only inspiral $(p_\varphi^{RR}, e_\varphi^{RR}, x_\varphi^{RR})$ by solving the simultaneous equations:

$$\begin{aligned}
&\Omega_r^{RR+SCF}(p_\varphi^{RR+SCF}, e_\varphi^{RR+SCF}, x_\varphi^{RR+SCF}) \\
&= \Omega_r^{RR}(p_\varphi^{RR}, e_\varphi^{RR}, x_\varphi^{RR}) \ , &\text{(C.91)}\\
&\Omega_z^{RR+SCF}(p_\varphi^{RR+SCF}, e_\varphi^{RR+SCF}, x_\varphi^{RR+SCF}) \\
&= \Omega_z^{RR}(p_\varphi^{RR}, e_\varphi^{RR}, x_\varphi^{RR}) \ , &\text{(C.92)}\\
&\Omega_\phi^{RR+SCF}(p_\varphi^{RR+SCF}, e_\varphi^{RR+SCF}, x_\varphi^{RR+SCF}) \\
&= \Omega_\phi^{RR}(p_\varphi^{RR}, e_\varphi^{RR}, x_\varphi^{RR}) \ . &\text{(C.93)}
\end{aligned}$$

We explicitly demonstrate the difference in the choice of initial conditions for the post-adiabatic terms considered in this work in Fig. C.1. In Fig. C.1, the solid curves show the averaged dephasing of $\phi(t)$, i.e., $\varphi_\phi^{RR+SCF} - \varphi_\phi^{RR}$. The blue curve corresponds to the initial $(p_\varphi, e_\varphi, x_\varphi)$ values matching between the radiation-reaction only and the radiation-reaction plus spin-curvature inspirals. The orange curve corresponds to the initial $(\Omega_r, \Omega_z, \Omega_\phi)$ values matching between the radiation-reaction only and the radiation-reaction plus spin-curvature inspirals. The blue curve grows linearly with t while the orange one grows quadratically with t. This can be seen clearly in the inset of Fig. C.1; on a log-log scale, the slopes of the orange line is twice that of the blue line. Note that, in the results presented in this article, we match initial orbital parameters $(p_\varphi, e_\varphi, x_\varphi)$ between adiabatic and post-adiabatic inspirals.

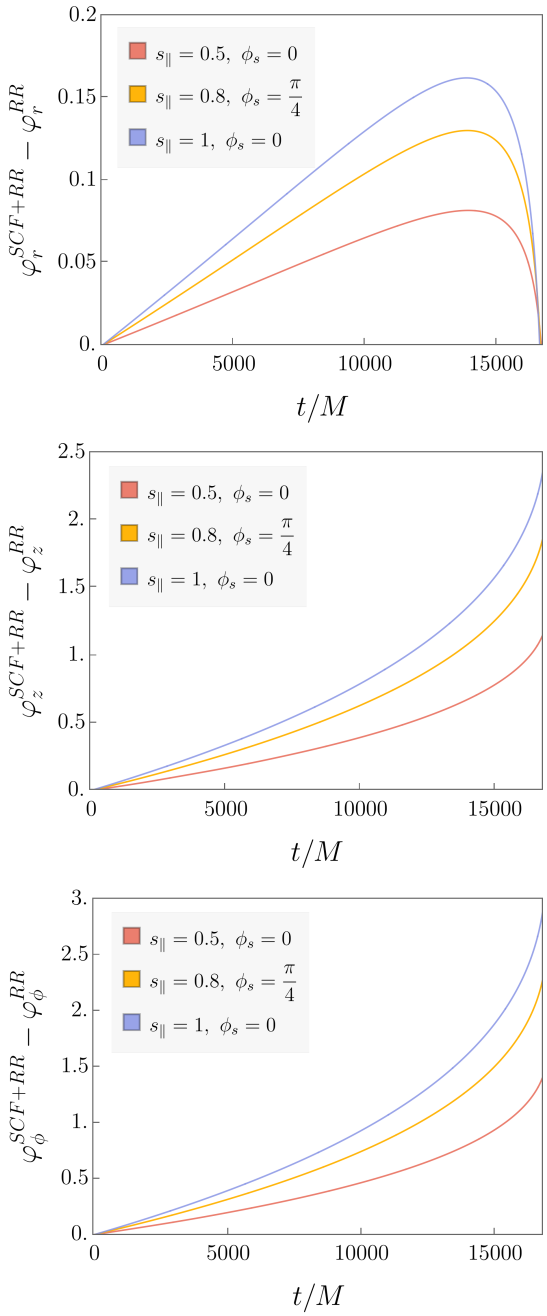

Figure C.4: Orbital evolution of a small body with a misaligned spin vector. The top panel shows $p(t)$ (solid) and $p_\varphi(t)$ (dashed); middle shows $e(t)$ and $e_\varphi(t)$; and the bottom panel shows $x_I(t)$ and $x_\varphi(t)$. In all the panels, we plot orbital element evolution for three values of spin alignment $s_\parallel = 1$ (blue), $s_\parallel = 0.8$ (orange) and $s_\parallel = 0.5$ (red) using the NIT equations of motion (dashed) and the OG equations of motion (solid). Especially in the middle and bottom panels, the different OG tracks can also be distinguished by the magnitude of the oscillations, which scale with $s_\perp$ and are thus smallest for $s_\parallel = 1$ and largest for $s_\parallel = 0.5$. (The NIT tracks pass roughly the centers of the OG oscillations.) The magnitude of the small body's spin is $s = 1$; ϕ_s is zero except for the orange curve which has $\phi_s = \pi/4$. The small body has mass ratio $\varepsilon = 10^{-2}$ and is orbiting a black hole with spin $a = 0.7M$. For all panels, $p = 10$, $e = 0.2$, $x_I = 0.7$, $q_r = 0$, $q_z = 0$, and $\phi = 0$ initially.

C.4.3 Varying initial conditions

Figure C.2 depicts the dephasing of the radial, polar and axial phases due to spin-curvature force during an inspiral. As in Fig. 5.4, the top, middle and bottom panels display $\varphi_\alpha^{SCF+RR} - \varphi_\alpha^{RR}$ with $\alpha \in \{r, z, \phi\}$ respectively. Different-colored curves correspond to different initial p values: Red corresponds to a larger initial p value while blue corresponds to a smaller initial p value that is closer to the LSO. Because the monotonic evolution of the dephasing of the polar and axial phases (middle and bottom panels), the curves that begin closer to the LSO do not accumulate as much dephasing before the plunge. However, for the case of the radial phase the initial value of p will affect where the maximum of the dephasing will occur, because the evolution is not monotonic.

Figure C.3 depicts the dephasing of the radial, polar and axial phases due to spin-curvature force with different curves on the same plot corresponding to different initial e (left column) and x_I (right column) values. The red curves correspond to a larger initial e or x_I value, yellow is an intermediate value and blue is the smallest value. As in Fig. C.2, the top, middle and bottom panels display $\varphi_\alpha^{SCF+RR} - \varphi_\alpha^{RR}$ with $\alpha \in \{r, z, \phi\}$ respectively. The initial e_0 values we plot are evenly spaced by $\Delta e = 0.05$ and initial x_I values are evenly spaced by $\Delta x = 0.002$. Consider the insets of the two plots in the middle row; these curves show the evolution of $\varphi_\alpha^{SCF+RR} - \varphi_\alpha^{RR}$. Observe that even separation in e does not correspond to even separation in $\varphi_\alpha^{SCF+RR} - \varphi_\alpha^{RR}$-space (middle left) while even separation in x_I does correspond to roughly even separation in $\varphi_\alpha^{SCF+RR} - \varphi_\alpha^{RR}$-space (middle right).

In Fig. C.4, the solid lines show the the evolution of the orbital elements (p, e, x_I) under the OG equations of motion, while the dashed lines show the averaged evolution of the orbital elements $(p_\varphi, e_\varphi, x_\varphi)$ under the NIT equations of motion. The oscillations depicted by the solid curves exhibit harmonics of several frequencies: The spin-aligned case ($s_\parallel = 1$, blue curve) contains harmonic of Ω_r and Ω_z while the spin-misaligned cases ($s_\parallel \neq 1$, orange and red curves) contain harmonics of three frequencies Ω_r, Ω_z and Ω_s. The additional harmonic structure introduced by spin-precession is most evident in the evolution of e shown in middle right panel.

The effect of the perpendicular spin component $s_\perp$ is most evident in the evolution of x_I in the bottom right panel. We can clearly see that the amplitude of the oscillations in x_I increase with increasing $s_\perp$, i.e., decreasing $s_\parallel$. In addition, when there is a non-zero initial spin-precession phase ($\phi_s \neq 0$, orange curve), we can see that the oscillations in x_I are out-of-phase with the $\phi_s \neq 0$ (red) curve. Because the initial conditions we use for the NIT equations of motion are determined by the oscillations present in the OG equations (as described in Appendix C.4), the NIT (dotted) curve for the misaligned spin cases (red and orange curves) have slightly different initial conditions and evolution compared to the aligned spin curve (blue).

Appendix D

Chapter 6 Appendices

These Appendices are based on the Appendix of [128]; we include them here for completeness.

D.1 Trajectory formulae

In this Appendix we present formulae derived to calculate the linear in spin contribution to the trajectory. We use the tetrad from Eqs. (47)–(51) in [220] where $\tilde{e}_2^\mu$ and e_3^μ have opposite sign to align e_3^μ with total angular momentum and to have right-handed system. Then the right hand side of MPD equations can be written as

$$f^\mu_{\rm MPD} = -\frac{1}{2} e^\mu_A \eta^{AB} R_{B0CD} S^{CD} \,, \tag{D.1}$$

where R_{B0CD} are components of the Riemann tensor in the Marck tetrad. Because of the way this tetrad is constructed [221] and the fact that the Riemann tensor has a simple form in the Kinnersley tetrad, the components can be simplified to

$$R_{1012} = \frac{3\sqrt{(\hat{K}+r^2)(\hat{K}-a^2z^2)}\Big(\Big(a^2z^2(\hat{K}+r^2) - r^2(\hat{K}-a^2z^2)\Big)I_1 + arz(2\hat{K}+r^2-a^2z^2)I_2\Big)}{\hat{K}\Sigma^2} \,, \tag{D.2a}$$

$$R_{3012} = \frac{6arz(\hat{K}+r^2)(\hat{K}-a^2z^2)I_1}{\hat{K}\Sigma^2} + \left(1 + 3\frac{-a^2z^2(\hat{K}+r^2)^2 + r^2(\hat{K}-a^2z^2)^2}{\hat{K}\Sigma^2}\right) I_2 \,, \tag{D.2b}$$

$$R_{2013} = -I_2 \,, \tag{D.2c}$$

$$R_{1023} = -R_{3012} + R_{2013} \,, \tag{D.2d}$$

$$R_{3023} = R_{1012} \,, \tag{D.2e}$$

and $R_{2012} = R_{1013} = R_{3013} = R_{2023} = 0$, where

$$I_1 = \frac{Mr(r^2 - 3a^2z^2)}{\Sigma^3} \,, \tag{D.3}$$

$$I_2 = \frac{Maz(3r^2 - a^2z^2)}{\Sigma^3} \,. \tag{D.4}$$

The functions $\mathcal{R}_{t,\phi}$, $\mathcal{J}$, $\mathcal{V}$, and $\mathcal{P}$ from Eqs. (3.24), (4.62), and (4.63) in [130] can be simplified to

$$\mathcal{R}_t = \Sigma f_t^{\rm MPD} \,, \tag{D.5a}$$
$$\mathcal{R}_\phi = \Sigma f_\phi^{\rm MPD} \,, \tag{D.5b}$$
$$\mathcal{J} = -\Sigma^2 f_{\rm MPD}^r + \mathcal{I}_2 \delta u_t^S + \mathcal{I}_3 \delta u_\phi^S \,, \tag{D.5c}$$
$$\mathcal{V} = -\Sigma^2 f_{\rm MPD}^\theta + \mathcal{U}_2 \delta u_t^S + \mathcal{U}_3 \delta u_\phi^S \,, \tag{D.5d}$$
$$\mathcal{P} = \mathcal{N}_2 \delta u_t^S + \mathcal{N}_3 \delta u_\phi^S \,, \tag{D.5e}$$

where $\mathcal{I}_{2,3}$, $\mathcal{U}_{2,3}$ and $\mathcal{N}_{2,3}$ can be found in the supplemental material of [129]. These simplifications make the calculation of the trajectory significantly faster.

D.2 Source term

In this Appendix we present explicit expressions for the functions appearing in the source term for the calculation of the partial amplitudes in Eq. (6.26).

Whereas $A^{\rm m}_{ab}$ is entirely given by Eq. (6.23b) with $P_a = \mu u_a$ and $v_a = u_a$ in the linear order, the terms in $A^{\rm d}_{ab}$ can be expressed with NP spin coefficients as

$$S^{cd}\gamma_{ndc} = S_{ln}(\gamma+\bar\gamma) + S_{n\bar m}(-\bar\pi+\bar\alpha+\beta) + S_{nm}(-\pi+\alpha+\bar\beta) + S_{m\bar m}(-\mu+\bar\mu) \,, \tag{D.6a}$$
$$S^{cd}\gamma_{\bar m dc} = S_{ln}(\pi+\bar\tau) + S_{n\bar m}\bar\rho + S_{nm}(\alpha+\bar\beta) + S_{l\bar m}(-\bar\gamma+\gamma) + S_{m\bar m}(-\alpha+\bar\beta) \,, \tag{D.6b}$$
$$S^{c}{}_{n}\gamma_{ndc}u^d = S_{ln}(\gamma+\bar\gamma)u_n + S_{n\bar m}((\bar\alpha+\beta)u_n - \mu u_m) + S_{nm}((\alpha+\bar\beta)u_n + \bar\mu u_{\bar m}) \,, \tag{D.6c}$$
$$S^{c}{}_{\bar m}\gamma_{\bar m dc}u^d = S_{n\bar m}(-\pi u_l) + S_{l\bar m}(\bar\tau u_n - (\bar\gamma-\gamma)u_{\bar m}) - S_{m\bar m}(-(-\alpha+\bar\beta)u_{\bar m}) \,, \tag{D.6d}$$
$$\begin{aligned} S^{c}{}_{(n}\gamma_{\bar m)dc}u^d = {} & (S_{ln}(\bar\tau u_n - (\bar\gamma-\gamma)u_{\bar m}) + S_{n\bar m}(\bar\rho u_n - \mu u_l - (\bar\alpha-\beta+\bar\pi)u_{\bar m} - \pi u_m) \\ & S_{nm}(-(-\alpha+\bar\beta)u_{\bar m}) + S_{l\bar m}(\gamma+\bar\gamma)u_n - S_{m\bar m}((\alpha+\bar\beta)u_n - \bar\mu u_{\bar m}))/2 \end{aligned} \tag{D.6e}$$

The tetrad components of the spin tensor for $\sigma_\perp = 0$ can be expressed as

$$S_{ln} = -\sigma_\parallel \frac{r(\hat K - a^2 z^2)}{\sqrt{\hat K}\Sigma} \,, \qquad S_{nm} = \sigma_\parallel \frac{\zeta}{\sqrt{\hat K}} u_m u_n \,, \tag{D.7a}$$
$$S_{l\bar m} = -\sigma_\parallel \frac{\zeta}{\sqrt{\hat K}} u_l u_{\bar m} \,, \qquad S_{m\bar m} = \sigma_\parallel \frac{iaz(\hat K + r^2)}{\sqrt{\hat K}\Sigma} \,, \tag{D.7b}$$

while the terms from the partial derivative for the dipole term have the form

$$i(\omega S^t{}_n - mS^\phi{}_n) = \frac{a\omega(1-z^2)-m}{\sqrt{2(1-z^2)}\Sigma}(\zeta S_{n\bar{m}} - \bar{\zeta}S_{nm}) - \frac{iK}{2\Sigma}S_{ln}\,, \tag{D.8a}$$

$$i(\omega S^t{}_{\bar{m}} - mS^\phi{}_{\bar{m}}) = -iK\left(\frac{S_{n\bar{m}}}{\Delta} + \frac{S_{l\bar{m}}}{2\Sigma}\right) + \frac{a\omega(1-z^2)-m}{\sqrt{2(1-z^2)}\zeta}S_{m\bar{m}}\,, \tag{D.8b}$$

$$S^r{}_n = \frac{\Delta}{2\Sigma}S_{ln}\,, \tag{D.8c}$$

$$S^r{}_{\bar{m}} = -S_{n\bar{m}} + \frac{\Delta}{2\Sigma}S_{l\bar{m}}\,, \tag{D.8d}$$

$$S^z{}_n = \frac{\sqrt{1-z^2}(S_{n\bar{m}}\zeta + S_{nm}\bar{\zeta})}{\sqrt{2}\Sigma}\,, \tag{D.8e}$$

$$S^z{}_{\bar{m}} = -\frac{\sqrt{1-z^2}S_{m\bar{m}}}{\sqrt{2}\zeta}\,, \tag{D.8f}$$

where $K = (r^2+a^2)\omega - am$. The functions $f^{(i)}_{ab}$ are given by

$$f^{(0)}_{nn} = -\frac{2\zeta^2}{\Delta^2}\left(\mathcal{L}^\dagger_1\mathcal{L}^\dagger_2 - 2ia\zeta^{-1}\sqrt{1-z^2}\mathcal{L}^\dagger_2\right)S\,, \tag{D.9a}$$

$$f^{(0)}_{n\bar{m}} = \frac{2\sqrt{2}\zeta^2}{\bar{\zeta}\Delta}\left(\left(\frac{iK}{\Delta} + \zeta^{-1} + \bar{\zeta}^{-1}\right)\mathcal{L}^\dagger_2 - a\sqrt{1-z^2}\frac{K}{\Delta}\left(\bar{\zeta}^{-1} - \zeta^{-1}\right)\right)S\,, \tag{D.9b}$$

$$f^{(1)}_{n\bar{m}} = \frac{2\sqrt{2}\zeta^2}{\bar{\zeta}\Delta}\left(\mathcal{L}^\dagger_2 + ia\sqrt{1-z^2}\left(\bar{\zeta}^{-1} - \zeta^{-1}\right)\right)S\,, \tag{D.9c}$$

$$f^{(0)}_{\bar{m}\bar{n}} = \frac{\zeta^2}{\bar{\zeta}^2}\left(i\partial_r\left(\frac{K}{\Delta}\right) - 2i\zeta^{-1}\frac{K}{\Delta} + \left(\frac{K}{\Delta}\right)^2\right)S\,, \tag{D.9d}$$

$$f^{(1)}_{\bar{m}\bar{n}} = -\frac{2\zeta^2}{\bar{\zeta}^2}\left(\zeta^{-1} + i\frac{K}{\Delta}\right)S\,, \tag{D.9e}$$

$$f^{(2)}_{\bar{m}\bar{n}} = -\frac{\zeta^2}{\bar{\zeta}^2}S\,, \tag{D.9f}$$

where

$$\mathcal{L}^\dagger_n = -\sqrt{1-z^2}\left(\partial_z - \frac{m-nz}{1-z^2} + a\omega\right)\,. \tag{D.10}$$

References

[1] LIGO Scientific Collaboration and Virgo Collaboration, "Observation of gravitational waves from a binary black hole merger," *PRL*, vol. 116, p. 061 102, 6 Feb. 2016. DOI: 10.1103/PhysRevLett.116.061102. [Online]. Available: https://link.aps.org/doi/10.1103/PhysRevLett.116.061102.

[2] B. L. Webster and P. Murdin, "Cygnus X-1-a Spectroscopic Binary with a Heavy Companion ?" *Nature*, vol. 235, no. 5332, pp. 37–38, Jan. 1972. DOI: 10.1038/235037a0.

[3] C. T. Bolton, "Identification of Cygnus X-1 with HDE 226868," *Nature*, vol. 235, no. 5336, pp. 271–273, Feb. 1972. DOI: 10.1038/235271b0.

[4] F. Özel, D. Psaltis, R. Narayan, and J. E. McClintock, "The Black Hole Mass Distribution in the Galaxy," *The Astrophysical Journal*, vol. 725, no. 2, pp. 1918–1927, Dec. 2010. DOI: 10.1088/0004-637X/725/2/1918. arXiv: 1006.2834 [astro-ph.GA].

[5] LIGO Scientific Collaboration and Virgo Collaboration, "GW190814: Gravitational Waves from the Coalescence of a 23 Solar Mass Black Hole with a 2.6 Solar Mass Compact Object," *The Astrophysical Journal Letters*, vol. 896, no. 2, L44, p. L44, Jun. 2020. DOI: 10.3847/2041-8213/ab960f. arXiv: 2006.12611 [astro-ph.HE].

[6] The LIGO Scientific Collaboration, the Virgo Collaboration, and the KAGRA Collaboration, "Observation of Gravitational Waves from the Coalescence of a $2.5 - 4.5\ M_\odot$ Compact Object and a Neutron Star," *arXiv e-prints*, arXiv:2404.04248, arXiv:2404.04248, Apr. 2024. DOI: 10.48550/arXiv.2404.04248. arXiv: 2404.04248 [astro-ph.HE].

[7] T. Jayasinghe, K. Z. Stanek, T. A. Thompson, *et al.*, "A unicorn in monoceros: the 3 $M_\odot$ dark companion to the bright, nearby red giant V723 Mon is a non-interacting, mass-gap black hole candidate," *MNRAS*, vol. 504, no. 2, pp. 2577–2602, Jun. 2021. DOI: 10.1093/mnras/stab907. arXiv: 2101.02212 [astro-ph.SR].

[8] T. A. Thompson, C. S. Kochanek, K. Z. Stanek, *et al.*, "A noninteracting low-mass black hole-giant star binary system," *Science*, vol. 366, no. 6465, pp. 637–640, Nov. 2019. DOI: 10.1126/science.aau4005. arXiv: 1806.02751 [astro-ph.HE].

[9] A. M. Ghez, S. Salim, N. N. Weinberg, *et al.*, "Measuring Distance and Properties of the Milky Way's Central Supermassive Black Hole with Stellar Orbits," *The Astrophysical Journal*, vol. 689, no. 2, pp. 1044–1062, Dec. 2008. DOI: 10.1086/592738. arXiv: 0808.2870 [astro-ph].

[10] Event Horizon Telescope Collaboration, "First M87 Event Horizon Telescope Results. I. The Shadow of the Supermassive Black Hole," *The Astrophysical Journal Letters*, vol. 875, no. 1, L1, p. L1, Apr. 2019. DOI: 10.3847/2041-8213/ab0ec7. arXiv: 1906.11238 [astro-ph.GA].

[11] Event Horizon Telescope Collaboration, "First Sagittarius A* Event Horizon Telescope Results. I. The Shadow of the Supermassive Black Hole in the Center of the Milky Way," *The Astrophysical Journal Letters*, vol. 930, no. 2, L12, p. L12, May 2022. DOI: 10.3847/2041-8213/ac6674.

[12] Á. Bogdán, A. D. Goulding, P. Natarajan, *et al.*, "Evidence for heavy-seed origin of early supermassive black holes from a z $\approx$ 10 X-ray quasar," *Nature Astronomy*, vol. 8, pp. 126–133, Jan. 2024. DOI: 10.1038/s41550-023-02111-9. arXiv: 2305.15458 [astro-ph.GA].

[13] LIGO Scientific Collaboration and Virgo Collaboration, "GW190521: A Binary Black Hole Merger with a Total Mass of 150 $M_\odot$," *Physical Review Letters*, vol. 125, no. 10, 101102, p. 101 102, Sep. 2020. DOI: 10.1103/PhysRevLett.125.101102. arXiv: 2009.01075 [gr-qc].

[14] J. Paynter, R. Webster, and E. Thrane, "Evidence for an intermediate-mass black hole from a gravitationally lensed gamma-ray burst," *Nature Astronomy*, vol. 5, pp. 560–568, Jun. 2021. DOI: 10.1038/s41550-021-01307-1. arXiv: 2103.15414 [astro-ph.HE].

[15] The LIGO Scientific Collaboration, the Virgo Collaboration, and the KAGRA Collaboration, "Tests of General Relativity with GWTC-3," *arXiv e-prints*, arXiv:2112.06861, arXiv:2112.06861, Dec. 2021. DOI: 10.48550/arXiv.2112.06861. arXiv: 2112.06861 [gr-qc].

[16] LIGO Scientific Collaboration and Virgo Collaboration, "Tests of general relativity with binary black holes from the second LIGO-Virgo gravitational-wave transient catalog," *Physical Review D*, vol. 103, no. 12, 122002, p. 122 002, Jun. 2021. DOI: 10.1103/PhysRevD.103.122002. arXiv: 2010.14529 [gr-qc].

[17] C. W. F. Everitt, D. B. DeBra, B. W. Parkinson, *et al.*, "Gravity probe b: Final results of a space experiment to test general relativity," *Phys. Rev. Lett.*, vol. 106, p. 221 101, 22 May 2011. DOI: 10.1103/PhysRevLett.106.221101. [Online]. Available: https://link.aps.org/doi/10.1103/PhysRevLett.106.221101.

[18] C. L. Rodriguez, M. Zevin, C. Pankow, V. Kalogera, and F. A. Rasio, "Illuminating Black Hole Binary Formation Channels with Spins in Advanced LIGO," *The Astrophysical Journal Letters*, vol. 832, no. 1, L2, p. L2, Nov. 2016. DOI: 10.3847/2041-8205/832/1/L2. arXiv: 1609.05916 [astro-ph.HE].

[19] R. P. Kerr, "Gravitational Field of a Spinning Mass as an Example of Algebraically Special Metrics," *Physical Review Letters*, vol. 11, no. 5, pp. 237–238, Sep. 1963. DOI: 10.1103/PhysRevLett.11.237.

[20] M. Bailes, B. K. Berger, P. R. Brady, *et al.*, "Gravitational-wave physics and astronomy in the 2020s and 2030s," *Nature Reviews Physics*, vol. 3, no. 5, pp. 344–366, Jan. 2021. DOI: 10.1038/s42254-021-00303-8.

[21] Nanograv Collaboration, "The NANOGrav 15 yr Data Set: Evidence for a Gravitational-wave Background," *The Astrophysical Journal Letters*, vol. 951, no. 1, L8, p. L8, Jul. 2023. DOI: 10.3847/2041-8213/acdac6. arXiv: 2306.16213 [astro-ph.HE].

[22] C. Berry, S. Hughes, C. Sopuerta, A. Chua, A. Heffernan, K. Holley-Bockelmann, D. Mihaylov, C. Miller, and A. Sesana, "The unique potential of extreme mass-ratio inspirals for gravitational-wave astronomy," *Bulletin of the American Astronomical Society*, vol. 51, no. 3, 42, p. 42, May 2019. DOI: 10.48550/arXiv.1903.03686. arXiv: 1903.03686 [astro-ph.HE].

[23] J. R. Gair, C. Tang, and M. Volonteri, "LISA extreme-mass-ratio inspiral events as probes of the black hole mass function," *Physical Review D*, vol. 81, no. 10, 104014, p. 104 014, May 2010. DOI: 10.1103/PhysRevD.81.104014. arXiv: 1004.1921 [astro-ph.GA].

[24] P. Amaro-Seoane, J. R. Gair, M. Freitag, M. C. Miller, I. Mandel, C. J. Cutler, and S. Babak, "TOPICAL REVIEW: Intermediate and extreme mass-ratio inspirals—astrophysics, science applications and detection using LISA," *Classical and Quantum Gravity*, vol. 24, no. 17, R113–R169, Sep. 2007. DOI: 10.1088/0264-9381/24/17/R01. arXiv: astro-ph/0703495 [astro-ph].

[25] L. Barack and C. Cutler, "LISA capture sources: Approximate waveforms, signal-to-noise ratios, and parameter estimation accuracy," *Physical Review D*, vol. 69, no. 8, 082005, p. 082 005, Apr. 2004. DOI: 10.1103/PhysRevD.69.082005. arXiv: gr-qc/0310125 [gr-qc].

[26] S. A. Hughes, N. Warburton, G. Khanna, A. J. K. Chua, and M. L. Katz, "Adiabatic waveforms for extreme mass-ratio inspirals via multivoice decomposition in time and frequency," *Phys. Rev. D*, vol. 103, p. 104 014, 10 May 2021. DOI: 10.1103/PhysRevD.103.104014. [Online]. Available: https://link.aps.org/doi/10.1103/PhysRevD.103.104014.

[27] T. Hinderer and É. É. Flanagan, "Two-timescale analysis of extreme mass ratio inspirals in Kerr spacetime: Orbital motion," *Physical Review D*, vol. 78, no. 6, 064028, p. 064 028, Sep. 2008. DOI: 10.1103/PhysRevD.78.064028. arXiv: 0805.3337 [gr-qc].

[28] É. E. Flanagan, S. A. Hughes, and U. Ruangsri, "Resonantly enhanced and diminished strong-field gravitational-wave fluxes," *Physical Review D*, vol. 89, no. 8, 084028, p. 084 028, Apr. 2014. DOI: 10.1103/PhysRevD.89.084028. arXiv: 1208.3906 [gr-qc].

[29] U. Ruangsri and S. A. Hughes, "Census of transient orbital resonances encountered during binary inspiral," *Physical Review D*, vol. 89, no. 8, 084036, p. 084 036, Apr. 2014. DOI: 10.1103/PhysRevD.89.084036. arXiv: 1307.6483 [gr-qc].

[30] C. P. L. Berry, R. H. Cole, P. Cañizares, and J. R. Gair, "Importance of transient resonances in extreme-mass-ratio inspirals," *Physical Review D*, vol. 94, no. 12, 124042, p. 124 042, Dec. 2016. DOI: 10.1103/PhysRevD.94.124042. arXiv: 1608.08951 [gr-qc].

[31] M. Mathisson, "Republication of: The mechanics of matter particles in general relativity," *General Relativity and Gravitation*, vol. 42, no. 4, pp. 989–1010, Apr. 2010. DOI: 10.1007/s10714-010-0938-z.

[32] A. Papapetrou, "Spinning Test-Particles in General Relativity. I," *Proceedings of the Royal Society of London Series A*, vol. 209, no. 1097, pp. 248–258, Oct. 1951. DOI: 10.1098/rspa.1951.0200.

[33] W. G. Dixon, "Dynamics of Extended Bodies in General Relativity. II. Moments of the Charge-Current Vector," *Proceedings of the Royal Society of London Series A*, vol. 319, no. 1539, pp. 509–547, Nov. 1970. DOI: 10.1098/rspa.1970.0191.

[34] M. Kesden, D. Gerosa, R. O'Shaughnessy, E. Berti, and U. Sperhake, "Effective Potentials and Morphological Transitions for Binary Black Hole Spin Precession," *Physical Review Letters*, vol. 114, no. 8, 081103, p. 081 103, Feb. 2015. DOI: 10.1103/PhysRevLett.114.081103. arXiv: 1411.0674 [gr-qc].

[35] D. Gerosa, M. Kesden, U. Sperhake, E. Berti, and R. O'Shaughnessy, "Multi-timescale analysis of phase transitions in precessing black-hole binaries," *Physical Review D*, vol. 92, no. 6, 064016, p. 064 016, Sep. 2015. DOI: 10.1103/PhysRevD.92.064016. arXiv: 1506.03492 [gr-qc].

[36] D. Gerosa, M. Kesden, R. O'Shaughnessy, A. Klein, E. Berti, U. Sperhake, and D. Trifirò, "Precessional Instability in Binary Black Holes with Aligned Spins," *Physical Review Letters*, vol. 115, no. 14, 141102, p. 141 102, Oct. 2015. DOI: 10.1103/PhysRevLett.115.141102. arXiv: 1506.09116 [gr-qc].

[37] G. Cho and H. M. Lee, "Analytic Keplerian-type parametrization for general spinning compact binaries with leading order spin-orbit interactions," *Physical Review D*, vol. 100, no. 4, 044046, p. 044 046, Aug. 2019. DOI: 10.1103/PhysRevD.100.044046. arXiv: 1908.02927 [gr-qc].

[38] M. Mould and D. Gerosa, "Endpoint of the up-down instability in precessing binary black holes," *Physical Review D*, vol. 101, no. 12, 124037, p. 124 037, Jun. 2020. DOI: 10.1103/PhysRevD.101.124037. arXiv: 2003.02281 [gr-qc].

[39] S. Tanay, L. C. Stein, and J. T. Gálvez Ghersi, "Integrability of eccentric, spinning black hole binaries up to second post-Newtonian order," *Physical Review D*, vol. 103, no. 6, 064066, p. 064 066, Mar. 2021. DOI: 10.1103/PhysRevD.103.064066. arXiv: 2012.06586 [gr-qc].

[40] S. Tanay, G. Cho, and L. C. Stein, "Action-angle variables of a binary black-hole with arbitrary eccentricity, spins, and masses at 1.5 post-Newtonian order," *arXiv e-prints*, arXiv:2110.15351, arXiv:2110.15351, Oct. 2021. arXiv: 2110.15351 [gr-qc].

[41] C. O. Lousto, H. Nakano, Y. Zlochower, and M. Campanelli, "Statistical studies of spinning black-hole binaries," *Phys. Rev. D*, vol. 81, p. 084 023, 8 Apr. 2010. DOI: 10.1103/PhysRevD.81.084023. [Online]. Available: https://link.aps.org/doi/10.1103/PhysRevD.81.084023.

[42] D. A. Hemberger, G. Lovelace, T. J. Loredo, L. E. Kidder, M. A. Scheel, B. Szilágyi, N. W. Taylor, and S. A. Teukolsky, "Final spin and radiated energy in numerical simulations of binary black holes with equal masses and equal, aligned or antialigned spins," *Phys. Rev. D*, vol. 88, p. 064 014, 6 Sep. 2013. DOI: 10.1103/PhysRevD.88.064014. [Online]. Available: https://link.aps.org/doi/10.1103/PhysRevD.88.064014.

[43] M. Boyle, L. E. Kidder, S. Ossokine, and H. P. Pfeiffer, "Gravitational-wave modes from precessing black-hole binaries," *arXiv e-prints*, arXiv:1409.4431, arXiv:1409.4431, Sep. 2014. arXiv: 1409.4431 [gr-qc].

[44] S. Ossokine, M. Boyle, L. E. Kidder, H. P. Pfeiffer, M. A. Scheel, and B. Szilágyi, "Comparing post-Newtonian and numerical relativity precession dynamics," *Physical Review D*, vol. 92, no. 10, 104028, p. 104 028, Nov. 2015. DOI: 10.1103/PhysRevD.92.104028. arXiv: 1502.01747 [gr-qc].

[45] C. O. Lousto and J. Healy, "Flip-flopping binary black holes," *Phys. Rev. Lett.*, vol. 114, p. 141 101, 14 Apr. 2015. DOI: 10.1103/PhysRevLett.114.141101. [Online]. Available: https://link.aps.org/doi/10.1103/PhysRevLett.114.141101.

[46] C. O. Lousto, J. Healy, and H. Nakano, "Spin flips in generic black hole binaries," *Physical Review D*, vol. 93, no. 4, 044031, p. 044 031, Feb. 2016. DOI: 10.1103/PhysRevD.93.044031. arXiv: 1506.04768 [gr-qc].

[47] T. Damour, "Coalescence of two spinning black holes: An effective one-body approach," *Phys. Rev. D*, vol. 64, p. 124 013, 12 Nov. 2001. DOI: 10.1103/PhysRevD.64.124013. [Online]. Available: https://link.aps.org/doi/10.1103/PhysRevD.64.124013.

[48] T. Damour, P. Jaranowski, and G. Schäfer, "Hamiltonian of two spinning compact bodies with next-to-leading order gravitational spin-orbit coupling," *Physical Review D*, vol. 77, no. 6, 064032, p. 064 032, Mar. 2008. DOI: 10.1103/PhysRevD.77.064032. arXiv: 0711.1048 [gr-qc].

[49] A. Nagar, "Effective one-body Hamiltonian of two spinning black holes with next-to-next-to-leading order spin-orbit coupling," *Physical Review D*, vol. 84, no. 8, 084028, p. 084 028, Oct. 2011. DOI: 10.1103/PhysRevD.84.084028. arXiv: 1106.4349 [gr-qc].

[50] S. Balmelli and P. Jetzer, "Effective-one-body Hamiltonian with next-to-leading order spin-spin coupling for two nonprecessing black holes with aligned spins," *Physical Review D*, vol. 87, no. 12, 124036, p. 124 036, Jun. 2013. DOI: 10.1103/PhysRevD.87.124036. arXiv: 1305.5674 [gr-qc].

[51] S. Balmelli and P. Jetzer, "Effective-one-body Hamiltonian with next-to-leading order spin-spin coupling," *Physical Review D*, vol. 91, no. 6, 064011, p. 064 011, Mar. 2015. DOI: 10.1103/PhysRevD.91.064011. arXiv: 1502.01343 [gr-qc].

[52] S. Balmelli and T. Damour, "New effective-one-body hamiltonian with next-to-leading order spin-spin coupling," *Phys. Rev. D*, vol. 92, p. 124 022, 12 Dec. 2015. DOI: 10.1103/PhysRevD.92.124022. [Online]. Available: https://link.aps.org/doi/10.1103/PhysRevD.92.124022.

[53] M. Khalil, J. Steinhoff, J. Vines, and A. Buonanno, "Fourth post-Newtonian effective-one-body Hamiltonians with generic spins," *Physical Review D*, vol. 101, no. 10, 104034, p. 104 034, May 2020. DOI: 10.1103/PhysRevD.101.104034. arXiv: 2003.04469 [gr-qc].

[54] P. Rettegno, F. Martinetti, A. Nagar, D. Bini, G. Riemenschneider, and T. Damour, "Comparing effective-one-body Hamiltonians for spin-aligned coalescing binaries," *Physical Review D*, vol. 101, no. 10, 104027, p. 104 027, May 2020. DOI: 10.1103/PhysRevD.101.104027. arXiv: 1911.10818 [gr-qc].

[55] H. Lim and C. L. Rodriguez, "Relativistic three-body effects in hierarchical triples," *Physical Review D*, vol. 102, no. 6, 064033, p. 064 033, Sep. 2020. DOI: 10.1103/PhysRevD.102.064033. arXiv: 2001.03654 [astro-ph.HE].

[56] O. Semerák, "Spinning test particles in a Kerr field - I," *Monthly Notices of the Royal Astronomical Society*, vol. 308, no. 3, pp. 863–875, Sep. 1999. DOI: 10.1046/j.1365-8711.1999.02754.x.

[57] R. M. Plyatsko, O. B. Stefanyshyn, and M. T. Fenyk, "Mathisson-Papapetrou-Dixon equations in the Schwarzschild and Kerr backgrounds," *Classical and Quantum Gravity*, vol. 28, no. 19, 195025, p. 195 025, Oct. 2011. DOI: 10.1088/0264-9381/28/19/195025. arXiv: 1110.1967 [gr-qc].

[58] K. J. Li, K. Wu, and D. Singh, "Spin dynamics of a millisecond pulsar orbiting closely around a massive black hole," *Monthly Notices of the Royal Astronomical Society*, vol. 485, no. 1, pp. 1053–1066, May 2019. DOI: 10.1093/mnras/stz389. arXiv: 1902.03146 [astro-ph.HE].

[59] T. Hinderer, A. Buonanno, A. H. Mroué, *et al.*, "Periastron advance in spinning black hole binaries: comparing effective-one-body and numerical relativity," *Physical Review D*, vol. 88, no. 8, 084005, p. 084 005, Oct. 2013. DOI: 10.1103/PhysRevD.88.084005. arXiv: 1309.0544 [gr-qc].

[60] C. Chicone, B. Mashhoon, and B. Punsly, "Relativistic motion of spinning particles in a gravitational field," *Physics Letters A*, vol. 343, no. 1-3, pp. 1–7, Aug. 2005. DOI: 10.1016/j.physleta.2005.05.072. arXiv: gr-qc/0504146 [gr-qc].

[61] D. Singh, "Perturbation method for classical spinning particle motion. i. kerr space-time," *Phys. Rev. D*, vol. 78, p. 104 028, 10 Nov. 2008. DOI: 10.1103/PhysRevD.78.104028. [Online]. Available: https://link.aps.org/doi/10.1103/PhysRevD.78.104028.

[62] D. Singh, "An analytic perturbation approach for classical spinning particle dynamics," *General Relativity and Gravitation*, vol. 40, no. 6, pp. 1179–1192, Jun. 2008. DOI: 10.1007/s10714-007-0597-x. arXiv: 0706.0928 [gr-qc].

[63] B. Mashhoon and D. Singh, "Dynamics of extended spinning masses in a gravitational field," *Phys. Rev. D*, vol. 74, p. 124 006, 12 Dec. 2006. DOI: 10.1103/PhysRevD.74.124006. [Online]. Available: https://link.aps.org/doi/10.1103/PhysRevD.74.124006.

[64] D. Bini, A. Geralico, and R. T. Jantzen, "Spin-geodesic deviations in the Schwarzschild spacetime," *General Relativity and Gravitation*, vol. 43, no. 4, pp. 959–975, Apr. 2011. DOI: 10.1007/s10714-010-1111-4. arXiv: 1408.4946 [gr-qc].

[65] D. Bini and A. Geralico, "Spin-geodesic deviations in the kerr spacetime," *Phys. Rev. D*, vol. 84, p. 104 012, 10 Nov. 2011. DOI: 10.1103/PhysRevD.84.104012. [Online]. Available: https://link.aps.org/doi/10.1103/PhysRevD.84.104012.

[66] K. P. Tod, F. de Felice, and M. Calvani, "Spinning test particles in the field of a black hole.," *Nuovo Cimento B Serie*, vol. 34, pp. 365–379, Aug. 1976. DOI: 10.1007/BF02728614.

[67] M. Saijo, K.-i. Maeda, M. Shibata, and Y. Mino, "Gravitational waves from a spinning particle plunging into a kerr black hole," *Phys. Rev. D*, vol. 58, p. 064 005, 6 Aug. 1998. DOI: 10.1103/PhysRevD.58.064005. [Online]. Available: https://link.aps.org/doi/10.1103/PhysRevD.58.064005.

[68] E. Hackmann, C. Lämmerzahl, Y. N. Obukhov, D. Puetzfeld, and I. Schaffer, "Motion of spinning test bodies in Kerr spacetime," *Physical Review D*, vol. 90, no. 6, 064035, p. 064 035, Sep. 2014. DOI: 10.1103/PhysRevD.90.064035. arXiv: 1408.1773 [gr-qc].

[69] M. A. Abramowicz and M. Calvani, "Spinning particles orbiting the Kerr black hole," *Monthly Notices of the Royal Astronomical Society*, vol. 189, no. 3, pp. 621–626, Dec. 1979, ISSN: 0035-8711. DOI: 10.1093/mnras/189.3.621. eprint: https://academic.oup.com/mnras/article-pdf/189/3/621/3216577/mnras189-0621.pdf. [Online]. Available: https://doi.org/10.1093/mnras/189.3.621.

[70] M. Calvani, "Spinning particles orbiting the Kerr black hole: cosmic censorship at work," *Il Nuovo Cimento A*, vol. 58, pp. 364–370, 1980. DOI: https://doi.org/10.1007/BF02730262.

[71] S. Mukherjee and S. Tripathy, "Resonant orbits for a spinning particle in Kerr spacetime," *arXiv e-prints*, arXiv:1905.04061, arXiv:1905.04061, May 2019. arXiv: 1905.04061 [gr-qc].

[72] S. Suzuki and K.-I. Maeda, "Innermost stable circular orbit of a spinning particle in Kerr spacetime," *Physical Review D*, vol. 58, no. 2, 023005, p. 023 005, Jul. 1998. DOI: 10.1103/PhysRevD.58.023005. arXiv: gr-qc/9712095 [gr-qc].

[73] M. Favata, "Conservative corrections to the innermost stable circular orbit (ISCO) of a Kerr black hole: A new gauge-invariant post-Newtonian ISCO condition, and the ISCO shift due to test-particle spin and the gravitational self-force," *Physical Review D*, vol. 83, no. 2, 024028, p. 024 028, Jan. 2011. DOI: 10.1103/PhysRevD.83.024028. arXiv: 1010.2553 [gr-qc].

[74] P. I. Jefremov, O. Y. Tsupko, and G. S. Bisnovatyi-Kogan, "Innermost stable circular orbits of spinning test particles in Schwarzschild and Kerr space-times," *Physical Review D*, vol. 91, no. 12, 124030, p. 124 030, Jun. 2015. DOI: 10.1103/PhysRevD.91.124030. arXiv: 1503.07060 [gr-qc].

[75] O. Y. Tsupko, G. S. Bisnovatyi-Kogan, and P. I. Jefremov, "Parameters of innermost stable circular orbits of spinning test particles: Numerical and analytical calculations," *Gravitation and Cosmology*, vol. 22, no. 2, pp. 138–147, Apr. 2016. DOI: 10.1134/S0202289316020158. arXiv: 1605.04189 [gr-qc].

[76] M. Zhang and W.-B. Liu, "Innermost stable circular orbits of charged spinning test particles," *Physics Letters B*, vol. 789, pp. 393–398, 2019, ISSN: 0370-2693. DOI: https://doi.org/10.1016/j.physletb.2018.12.051. [Online]. Available: http://www.sciencedirect.com/science/article/pii/S0370269318309869.

[77] Y.-P. Zhang, S.-W. Wei, P. Amaro-Seoane, J. Yang, and Y.-X. Liu, "Motion deviation of test body induced by spin and cosmological constant in extreme mass ratio inspiral binary system," *European Physical Journal C*, vol. 79, no. 10, 856, p. 856, Oct. 2019. DOI: 10.1140/epjc/s10052-019-7334-y. arXiv: 1812.06345 [gr-qc].

[78] G. E. Tauber, "Canonical Formalism and Equations of Motion for a Spinning Particle in General Relativity," *International Journal of Theoretical Physics*, vol. 27, no. 3, pp. 335–344, Mar. 1988. DOI: 10.1007/BF00668898.

[79] E. Barausse, E. Racine, and A. Buonanno, "Hamiltonian of a spinning test particle in curved spacetime," *Physical Review D*, vol. 80, no. 10, 104025, p. 104 025, Nov. 2009. DOI: 10.1103/PhysRevD.80.104025. arXiv: 0907.4745 [gr-qc].

[80] J. Vines, D. Kunst, J. Steinhoff, and T. Hinderer, "Canonical Hamiltonian for an extended test body in curved spacetime: To quadratic order in spin," *Physical Review D*, vol. 93, no. 10, 103008, p. 103 008, May 2016. DOI: 10.1103/PhysRevD.93.103008. arXiv: 1601.07529 [gr-qc].

[81] E. Barausse and A. Buonanno, "Improved effective-one-body Hamiltonian for spinning black-hole binaries," *Physical Review D*, vol. 81, no. 8, 084024, p. 084 024, Apr. 2010. DOI: 10.1103/PhysRevD.81.084024. arXiv: 0912.3517 [gr-qc].

[82] E. Barausse and A. Buonanno, "Extending the effective-one-body Hamiltonian of black-hole binaries to include next-to-next-to-leading spin-orbit couplings," *Physical Review D*, vol. 84, no. 10, 104027, p. 104 027, Nov. 2011. DOI: 10.1103/PhysRevD.84.104027. arXiv: 1107.2904 [gr-qc].

[83] V. Witzany, J. Steinhoff, and G. Lukes-Gerakopoulos, "Hamiltonians and canonical coordinates for spinning particles in curved space-time," *Classical and Quantum Gravity*, vol. 36, no. 7, 075003, p. 075 003, Apr. 2019. DOI: 10.1088/1361-6382/ab002f. arXiv: 1808.06582 [gr-qc].

[84] V. Witzany, "Hamilton-Jacobi equation for spinning particles near black holes," *Physical Review D*, vol. 100, no. 10, 104030, p. 104 030, Nov. 2019. DOI: 10.1103/PhysRevD.100.104030. arXiv: 1903.03651 [gr-qc].

[85] J. Levin, "Gravity Waves, Chaos, and Spinning Compact Binaries," *Physical Review Letters*, vol. 84, no. 16, pp. 3515–3518, Apr. 2000. DOI: 10.1103/PhysRevLett.84.3515. arXiv: gr-qc/9910040 [gr-qc].

[86] N. J. Cornish and J. Levin, "Gravitational Waves from Spinning Compact Binaries," *arXiv e-prints*, gr-qc/0207016, gr–qc/0207016, Jul. 2002. arXiv: gr-qc/0207016 [astro-ph].

[87] J. Levin, "Chaos and order in models of black hole pairs," *Phys. Rev. D*, vol. 74, p. 124 027, 12 Dec. 2006. DOI: 10.1103/PhysRevD.74.124027. [Online]. Available: https://link.aps.org/doi/10.1103/PhysRevD.74.124027.

[88] S. Suzuki and K.-I. Maeda, "Chaos in Schwarzschild spacetime: The motion of a spinning particle," *Physical Review D*, vol. 55, no. 8, pp. 4848–4859, Apr. 1997. DOI: 10.1103/PhysRevD.55.4848. arXiv: gr-qc/9604020 [gr-qc].

[89] M. D. Hartl, "Dynamics of spinning test particles in kerr spacetime," *Physical Review D*, vol. 67, p. 024 005, 2 Jan. 2003. DOI: 10.1103/PhysRevD.67.024005. [Online]. Available: https://link.aps.org/doi/10.1103/PhysRevD.67.024005.

[90] M. D. Hartl, "Survey of spinning test particle orbits in Kerr spacetime," *Physical Review D*, vol. 67, no. 10, 104023, p. 104 023, May 2003. DOI: 10.1103/PhysRevD.67.104023. arXiv: gr-qc/0302103 [gr-qc].

[91] O. Zelenka, G. Lukes-Gerakopoulos, V. Witzany, and O. Kopáček, "Growth of resonances and chaos for a spinning test particle in the Schwarzschild background," *Physical Review D*, vol. 101, no. 2, 024037, p. 024 037, Jan. 2020. DOI: 10.1103/PhysRevD.101.024037. arXiv: 1911.00414 [gr-qc].

[92] G. Compère and A. Druart, "Complete set of quasi-conserved quantities for spinning particles around Kerr," *SciPost Physics*, vol. 12, no. 1, 012, p. 012, Jan. 2022. DOI: 10.21468/SciPostPhys.12.1.012. arXiv: 2105.12454 [gr-qc].

[93] G. Compère, A. Druart, and J. Vines, "Generalized Carter constant for quadrupolar test bodies in Kerr spacetime," *arXiv e-prints*, arXiv:2302.14549, arXiv:2302.14549, Feb. 2023. DOI: 10.48550/arXiv.2302.14549. arXiv: 2302.14549 [gr-qc].

[94] Y. Mino, "Perturbative approach to an orbital evolution around a supermassive black hole," *Phys. Rev. D*, vol. 67, p. 084 027, 8 Apr. 2003. DOI: 10.1103/PhysRevD.67.084027. [Online]. Available: https://link.aps.org/doi/10.1103/PhysRevD.67.084027.

[95] S. Isoyama, R. Fujita, H. Nakano, N. Sago, and T. Tanaka, "Flux-balance formulae for extreme mass-ratio inspirals," *Progress of Theoretical and Experimental Physics*, vol. 2019, no. 1, Jan. 2019, 013E01, ISSN: 2050-3911. DOI: 10.1093/ptep/pty136. eprint: https://academic.oup.com/ptep/article-pdf/2019/1/013E01/27512784/pty136.pdf. [Online]. Available: https://doi.org/10.1093/ptep/pty136.

[96] S. Drasco and S. A. Hughes, "Gravitational wave snapshots of generic extreme mass ratio inspirals," *Phys. Rev. D*, vol. 73, p. 024 027, 2 Jan. 2006. DOI: 10.1103/PhysRevD.73.024027. [Online]. Available: https://link.aps.org/doi/10.1103/PhysRevD.73.024027.

[97] R. Fujita and M. Shibata, "Extreme mass ratio inspirals on the equatorial plane in the adiabatic order," *Phys. Rev. D*, vol. 102, p. 064 005, 6 Sep. 2020. DOI: 10.1103/PhysRevD.102.064005. [Online]. Available: https://link.aps.org/doi/10.1103/PhysRevD.102.064005.

[98] A. J. K. Chua, M. L. Katz, N. Warburton, and S. A. Hughes, "Rapid generation of fully relativistic extreme-mass-ratio-inspiral waveform templates for lisa data analysis," *Phys. Rev. Lett.*, vol. 126, p. 051 102, 5 Feb. 2021. DOI: 10.1103/PhysRevLett.126.051102. [Online]. Available: https://link.aps.org/doi/10.1103/PhysRevLett.126.051102.

[99] M. L. Katz, A. J. K. Chua, L. Speri, N. Warburton, and S. A. Hughes, "Fast extreme-mass-ratio-inspiral waveforms: New tools for millihertz gravitational-wave data analysis," *Phys. Rev. D*, vol. 104, p. 064 047, 6 Sep. 2021. DOI: 10.1103/PhysRevD.104.064047. [Online]. Available: https://link.aps.org/doi/10.1103/PhysRevD.104.064047.

[100] M. van de Meent, "Gravitational self-force on generic bound geodesics in kerr spacetime," *Phys. Rev. D*, vol. 97, p. 104 033, 10 May 2018. DOI: 10.1103/PhysRevD.97.104033. [Online]. Available: https://link.aps.org/doi/10.1103/PhysRevD.97.104033.

[101] P. Lynch, M. van de Meent, and N. Warburton, "Eccentric self-forced inspirals into a rotating black hole," *Class. Quant. Grav.*, vol. 39, no. 14, p. 145 004, 2022. DOI: 10.1088/1361-6382/ac7507. arXiv: 2112.05651 [gr-qc].

[102] N. Warburton, S. Akcay, L. Barack, J. R. Gair, and N. Sago, "Evolution of inspiral orbits around a schwarzschild black hole," *Phys. Rev. D*, vol. 85, p. 061 501, 6 Mar. 2012. DOI: 10.1103/PhysRevD.85.061501. [Online]. Available: https://link.aps.org/doi/10.1103/PhysRevD.85.061501.

[103] T. Osburn, N. Warburton, and C. R. Evans, "Highly eccentric inspirals into a black hole," *Phys. Rev. D*, vol. 93, p. 064 024, 6 Mar. 2016. DOI: 10.1103/PhysRevD.93.064024. [Online]. Available: https://link.aps.org/doi/10.1103/PhysRevD.93.064024.

[104] M. van de Meent and N. Warburton, "Fast self-forced inspirals," *Classical and Quantum Gravity*, vol. 35, no. 14, p. 144 003, Jun. 2018. DOI: 10.1088/1361-6382/aac8ce. [Online]. Available: https://doi.org/10.1088/1361-6382/aac8ce.

[105] A. Pound, B. Wardell, N. Warburton, and J. Miller, "Second-Order Self-Force Calculation of Gravitational Binding Energy in Compact Binaries," *Physical Review Letters*, vol. 124, no. 2, 021101, p. 021 101, Jan. 2020. DOI: 10.1103/PhysRevLett.124.021101. arXiv: 1908.07419 [gr-qc].

[106] N. Warburton, A. Pound, B. Wardell, J. Miller, and L. Durkan, "Gravitational-Wave Energy Flux for Compact Binaries through Second Order in the Mass Ratio," *Physical Review Letters*, vol. 127, no. 15, 151102, p. 151 102, Oct. 2021. DOI: 10.1103/PhysRevLett.127.151102. arXiv: 2107.01298 [gr-qc].

[107] B. Wardell, A. Pound, N. Warburton, J. Miller, L. Durkan, and A. Le Tiec, "Gravitational waveforms for compact binaries from second-order self-force theory," *arXiv e-prints*, arXiv:2112.12265, arXiv:2112.12265, Dec. 2021. DOI: 10.48550/arXiv.2112.12265. arXiv: 2112.12265 [gr-qc].

[108] A. Albertini, A. Nagar, A. Pound, N. Warburton, B. Wardell, L. Durkan, and J. Miller, "Comparing second-order gravitational self-force, numerical relativity, and effective one body waveforms from inspiralling, quasicircular, and nonspinning black hole binaries," *Physical Review D*, vol. 106, no. 8, 084061, p. 084 061, Oct. 2022. DOI: 10.1103/PhysRevD.106.084061. arXiv: 2208.01049 [gr-qc].

[109] A. Albertini, A. Nagar, A. Pound, N. Warburton, B. Wardell, L. Durkan, and J. Miller, "Comparing second-order gravitational self-force and effective one body waveforms from inspiralling, quasicircular and nonspinning black hole binaries. II. The large-mass-ratio case," *Physical Review D*, vol. 106, no. 8, 084062, p. 084 062, Oct. 2022. DOI: 10.1103/PhysRevD.106.084062. arXiv: 2208.02055 [gr-qc].

[110] M. van de Meent, A. Buonanno, D. P. Mihaylov, S. Ossokine, L. Pompili, N. Warburton, A. Pound, B. Wardell, L. Durkan, and J. Miller, "Enhancing the seobnrv5 effective-one-body waveform model with second-order gravitational self-force fluxes," 2023. arXiv: 2303.18026 [gr-qc].

[111] F. M. Blanco and É. É. Flanagan, "Motion of a spinning particle under the conservative piece of the self-force is Hamiltonian to first order in mass and spin," *arXiv e-prints*, arXiv:2302.10233, arXiv:2302.10233, Feb. 2023. DOI: 10.48550/arXiv.2302.10233. arXiv: 2302.10233 [gr-qc].

[112] N. Warburton, T. Osburn, and C. R. Evans, "Evolution of small-mass-ratio binaries with a spinning secondary," *Physical Review D*, vol. 96, no. 8, 084057, p. 084 057, Oct. 2017. DOI: 10.1103/PhysRevD.96.084057. arXiv: 1708.03720 [gr-qc].

[113] E. Harms, G. Lukes-Gerakopoulos, S. Bernuzzi, and A. Nagar, "Spinning test body orbiting around a Schwarzschild black hole: Circular dynamics and gravitational-wave fluxes," *Physical Review D*, vol. 94, no. 10, 104010, p. 104 010, Nov. 2016. DOI: 10.1103/PhysRevD.94.104010. arXiv: 1609.00356 [gr-qc].

[114] G. Lukes-Gerakopoulos, E. Harms, S. Bernuzzi, and A. Nagar, "Spinning test body orbiting around a Kerr black hole: Circular dynamics and gravitational-wave fluxes," *Physical Review D*, vol. 96, no. 6, 064051, p. 064 051, Sep. 2017. DOI: 10.1103/PhysRevD.96.064051. arXiv: 1707.07537 [gr-qc].

[115] L. M. Burko and G. Khanna, "Self-force gravitational waveforms for extreme and intermediate mass ratio inspirals. III. Spin-orbit coupling revisited," *Physical Review D*, vol. 91, no. 10, 104017, p. 104 017, May 2015. DOI: 10.1103/PhysRevD.91.104017. arXiv: 1503.05097 [gr-qc].

[116] E. A. Huerta, J. R. Gair, and D. A. Brown, "Importance of including small body spin effects in the modelling of intermediate mass-ratio inspirals. II. Accurate parameter extraction of strong sources using higher-order spin effects," *Physical Review D*, vol. 85, no. 6, 064023, p. 064 023, Mar. 2012. DOI: 10.1103/PhysRevD.85.064023. arXiv: 1111.3243 [gr-qc].

[117] G. A. Piovano, A. Maselli, and P. Pani, "Extreme mass ratio inspirals with spinning secondary: A detailed study of equatorial circular motion," *Physical Review D*, vol. 102, no. 2, 024041, p. 024 041, Jul. 2020. DOI: 10.1103/PhysRevD.102.024041. arXiv: 2004.02654 [gr-qc].

[118] G. A. Piovano, R. Brito, A. Maselli, and P. Pani, "Assessing the detectability of the secondary spin in extreme mass-ratio inspirals with fully relativistic numerical waveforms," *Physical Review D*, vol. 104, no. 12, 124019, p. 124 019, Dec. 2021. DOI: 10.1103/PhysRevD.104.124019. arXiv: 2105.07083 [gr-qc].

[119] S. Akcay, S. R. Dolan, C. Kavanagh, J. Moxon, N. Warburton, and B. Wardell, "Dissipation in extreme mass-ratio binaries with a spinning secondary," *Physical Review D*, vol. 102, no. 6, 064013, p. 064 013, Sep. 2020. DOI: 10.1103/PhysRevD.102.064013. arXiv: 1912.09461 [gr-qc].

[120] A. Nagar, F. Messina, C. Kavanagh, G. Lukes-Gerakopoulos, N. Warburton, S. Bernuzzi, and E. Harms, "Factorization and resummation: A new paradigm to improve gravitational wave amplitudes. iii. the spinning test-body terms," *Phys. Rev. D*, vol. 100, p. 104 056, 10 Nov. 2019. DOI: 10.1103/PhysRevD.100.104056. [Online]. Available: https://link.aps.org/doi/10.1103/PhysRevD.100.104056.

[121] W.-B. Han, "Gravitational radiation from a spinning compact object around a supermassive Kerr black hole in circular orbit," *Physical Review D*, vol. 82, no. 8, 084013, p. 084 013, Oct. 2010. DOI: 10.1103/PhysRevD.82.084013. arXiv: 1008.3324 [gr-qc].

[122] E. Harms, G. Lukes-Gerakopoulos, S. Bernuzzi, and A. Nagar, "Asymptotic gravitational wave fluxes from a spinning particle in circular equatorial orbits around a rotating black hole," *Phys. Rev. D*, vol. 93, p. 044 015, 4 Feb. 2016. DOI: 10.1103/PhysRevD.93.044015. [Online]. Available: https://link.aps.org/doi/10.1103/PhysRevD.93.044015.

[123] G. Lukes-Gerakopoulos, E. Harms, S. Bernuzzi, and A. Nagar, "Spinning test body orbiting around a kerr black hole: Circular dynamics and gravitational-wave fluxes," *Phys. Rev. D*, vol. 96, p. 064 051, 6 Sep. 2017. DOI: 10.1103/PhysRevD.96.064051. [Online]. Available: https://link.aps.org/doi/10.1103/PhysRevD.96.064051.

[124] V. Skoupý and G. Lukes-Gerakopoulos, "Spinning test body orbiting around a kerr black hole: Eccentric equatorial orbits and their asymptotic gravitational-wave fluxes," *Phys. Rev. D*, vol. 103, p. 104 045, 10 May 2021. DOI: 10.1103/PhysRevD.103.104045. [Online]. Available: https://link.aps.org/doi/10.1103/PhysRevD.103.104045.

[125] T. Tanaka, Y. Mino, M. Sasaki, and M. Shibata, "Gravitational waves from a spinning particle in circular orbits around a rotating black hole," *Phys. Rev. D*, vol. 54, pp. 3762–3777, 6 Sep. 1996. DOI: 10.1103/PhysRevD.54.3762. [Online]. Available: https://link.aps.org/doi/10.1103/PhysRevD.54.3762.

[126] V. Skoupý and G. Lukes-Gerakopoulos, "Adiabatic equatorial inspirals of a spinning body into a Kerr black hole," *arXiv e-prints*, arXiv:2201.07044, arXiv:2201.07044, Jan. 2022. arXiv: 2201.07044 [gr-qc].

[127] J. Mathews, A. Pound, and B. Wardell, "Self-force calculations with a spinning secondary," *Physical Review D*, vol. 105, no. 8, 084031, p. 084 031, Apr. 2022. DOI: 10.1103/PhysRevD.105.084031. arXiv: 2112.13069 [gr-qc].

[128] V. Skoupý, G. Lukes-Gerakopoulos, L. V. Drummond, and S. A. Hughes, "Asymptotic gravitational-wave fluxes from a spinning test body on generic orbits around a kerr black hole," *Phys. Rev. D*, vol. 108, p. 044 041, 4 Aug. 2023. DOI: 10.1103/PhysRevD.108.044041. [Online]. Available: https://link.aps.org/doi/10.1103/PhysRevD.108.044041.

[129] L. V. Drummond and S. A. Hughes, "Precisely computing bound orbits of spinning bodies around black holes. I. General framework and results for nearly equatorial orbits," *Physical Review D*, vol. 105, no. 12, 124040, p. 124 040, Jun. 2022. DOI: 10.1103/PhysRevD.105.12404010.48550/arXiv.2201.13334. arXiv: 2201.13334 [gr-qc].

[130] L. V. Drummond and S. A. Hughes, "Precisely computing bound orbits of spinning bodies around black holes. II. Generic orbits," *Physical Review D*, vol. 105, no. 12, 124041, p. 124 041, Jun. 2022. DOI: 10.1103/PhysRevD.105.12404110.48550/arXiv.2201.13335. arXiv: 2201.13335 [gr-qc].

[131] L. V. Drummond, P. Lynch, A. G. Hanselman, D. R. Becker, and S. A. Hughes, "Extreme mass-ratio inspiral and waveforms for a spinning body into a kerr black hole via osculating geodesics and near-identity transformations," *Phys. Rev. D*, vol. 109, p. 064 030, 6 Mar. 2024. DOI: 10.1103/PhysRevD.109.064030. [Online]. Available: https://link.aps.org/doi/10.1103/PhysRevD.109.064030.

[132] W. Schmidt, "Celestial mechanics in Kerr spacetime," *Classical and Quantum Gravity*, vol. 19, no. 10, pp. 2743–2764, May 2002. DOI: 10.1088/0264-9381/19/10/314. arXiv: gr-qc/0202090 [gr-qc].

[133] P. Rana and A. Mangalam, "Astrophysically relevant bound trajectories around a Kerr black hole," *Classical and Quantum Gravity*, vol. 36, no. 4, 045009, p. 045 009, Feb. 2019. DOI: 10.1088/1361-6382/ab004c. arXiv: 1901.02730 [gr-qc].

[134] G. V. Kraniotis, "Precise relativistic orbits in Kerr and Kerr (anti) de Sitter spacetimes," *Classical and Quantum Gravity*, vol. 21, no. 19, pp. 4743–4769, Oct. 2004. DOI: 10.1088/0264-9381/21/19/016. arXiv: gr-qc/0405095 [gr-qc].

[135] S. Drasco and S. A. Hughes, "Rotating black hole orbit functionals in the frequency domain," *Physical Review D*, vol. 69, no. 4, 044015, p. 044 015, Feb. 2004. DOI: 10.1103/PhysRevD.69.044015. arXiv: astro-ph/0308479 [astro-ph].

[136] E. Hackmann and C. Lämmerzahl, "Geodesic equation in schwarzschild-(anti-)de sitter space-times: Analytical solutions and applications," *Phys. Rev. D*, vol. 78, p. 024 035, 2 Jul. 2008. DOI: 10.1103/PhysRevD.78.024035. [Online]. Available: https://link.aps.org/doi/10.1103/PhysRevD.78.024035.

[137] J. Levin and G. Perez-Giz, "A periodic table for black hole orbits," *Physical Review D*, vol. 77, no. 10, 103005, p. 103 005, May 2008. DOI: 10.1103/PhysRevD.77.103005. arXiv: 0802.0459 [gr-qc].

[138] J. Levin and G. Perez-Giz, "Homoclinic orbits around spinning black holes. I. Exact solution for the Kerr separatrix," *Physical Review D*, vol. 79, no. 12, 124013, p. 124 013, Jun. 2009. DOI: 10.1103/PhysRevD.79.124013. arXiv: 0811.3814 [gr-qc].

[139] R. Fujita and W. Hikida, "Analytical solutions of bound timelike geodesic orbits in Kerr spacetime," *Classical and Quantum Gravity*, vol. 26, no. 13, 135002, p. 135 002, Jul. 2009. DOI: 10.1088/0264-9381/26/13/135002. arXiv: 0906.1420 [gr-qc].

[140] E. Hackmann, C. Lämmerzahl, V. Kagramanova, and J. Kunz, "Analytical solution of the geodesic equation in kerr-(anti-) de sitter space-times," *Phys. Rev. D*, vol. 81, p. 044 020, 4 Feb. 2010. DOI: 10.1103/PhysRevD.81.044020. [Online]. Available: https://link.aps.org/doi/10.1103/PhysRevD.81.044020.

[141] N. Warburton, L. Barack, and N. Sago, "Isofrequency pairing of geodesic orbits in kerr geometry," *Phys. Rev. D*, vol. 87, p. 084 012, 8 Apr. 2013. DOI: 10.1103/PhysRevD.87.084012. [Online]. Available: https://link.aps.org/doi/10.1103/PhysRevD.87.084012.

[142] R. H. Boyer and R. W. Lindquist, "Maximal Analytic Extension of the Kerr Metric," *Journal of Mathematical Physics*, vol. 8, no. 2, pp. 265–281, Feb. 1967. DOI: 10.1063/1.1705193.

[143] R. Penrose, "Naked Singularities," in *Sixth Texas Symposium on Relativistic Astrophysics*, D. J. Hegyi, Ed., vol. 224, Jan. 1973, p. 125. DOI: 10.1111/j.1749-6632.1973.tb41447.x.

[144] M. van de Meent, "Analytic solutions for parallel transport along generic bound geodesics in Kerr spacetime," *arXiv e-prints*, arXiv:1906.05090, arXiv:1906.05090, Jun. 2019. arXiv: 1906.05090 [gr-qc].

[145] B. Carter, "Global Structure of the Kerr Family of Gravitational Fields," *Phys. Rev.*, vol. 174, pp. 1559–1571, 5 Oct. 1968. DOI: 10.1103/PhysRev.174.1559. [Online]. Available: https://link.aps.org/doi/10.1103/PhysRev.174.1559.

[146] L. C. Stein and N. Warburton, "Location of the last stable orbit in Kerr spacetime," *Physical Review D*, vol. 101, no. 6, 064007, p. 064 007, Mar. 2020. DOI: 10.1103/PhysRevD.101.064007. arXiv: 1912.07609 [gr-qc].

[147] S. A. Hughes, N. Warburton, G. Khanna, A. J. K. Chua, and M. L. Katz, "Adiabatic waveforms for extreme mass-ratio inspirals via multivoice decomposition in time and frequency," *Physical Review D*, vol. 103, no. 10, 104014, p. 104 014, May 2021. DOI: 10.1103/PhysRevD.103.104014. arXiv: 2102.02713 [gr-qc].

[148] *Kerrgeodesics mathematica package*, bhptoolkit.org/KerrGeodesics.

[149] M. Mathisson, "Republication of: New mechanics of material systems," *General Relativity and Gravitation*, vol. 42, no. 4, pp. 1011–1048, Apr. 2010. DOI: 10.1007/s10714-010-0939-y.

[150] D. Bini, P. Fortini, A. Geralico, and A. Ortolan, "Quadrupole effects on the motion of extended bodies in Kerr spacetime," *Classical and Quantum Gravity*, vol. 25, no. 12, 125007, p. 125 007, Jun. 2008. DOI: 10.1088/0264-9381/25/12/125007. arXiv: 0910.2842 [gr-qc].

[151] D. Bini and A. Geralico, "Deviation of quadrupolar bodies from geodesic motion in a kerr spacetime," *Phys. Rev. D*, vol. 89, p. 044 013, 4 Feb. 2014. DOI: 10.1103/PhysRevD.89.044013. [Online]. Available: https://link.aps.org/doi/10.1103/PhysRevD.89.044013.

[152] J. Steinhoff and D. Puetzfeld, "Multipolar equations of motion for extended test bodies in general relativity," *Phys. Rev. D*, vol. 81, p. 044 019, 4 Feb. 2010. DOI: 10.1103/PhysRevD.81.044019. [Online]. Available: https://link.aps.org/doi/10.1103/PhysRevD.81.044019.

[153] R. Rudiger, "Conserved Quantities of Spinning Test Particles in General Relativity. I," *Proceedings of the Royal Society of London Series A*, vol. 375, no. 1761, pp. 185–193, Mar. 1981. DOI: 10.1098/rspa.1981.0046.

[154] L. Filipe Costa and J. Natário, "Center of mass, spin supplementary conditions, and the momentum of spinning particles," *arXiv e-prints*, arXiv:1410.6443, arXiv:1410.6443, Oct. 2014. arXiv: 1410.6443 [gr-qc].

[155] G. Lukes-Gerakopoulos, J. Seyrich, and D. Kunst, "Investigating spinning test particles: Spin supplementary conditions and the hamiltonian formalism," *Phys. Rev. D*, vol. 90, p. 104 019, 10 Nov. 2014. DOI: 10.1103/PhysRevD.90.104019. [Online]. Available: https://link.aps.org/doi/10.1103/PhysRevD.90.104019.

[156] K. Kyrian and O. Semerák, "Spinning test particles in a Kerr field - II," *Monthly Notices of the Royal Astronomical Society*, vol. 382, no. 4, pp. 1922–1932, Dec. 2007. DOI: 10.1111/j.1365-2966.2007.12502.x.

[157] B. Mikóczi, "Spin supplementary conditions for spinning compact binaries," *Phys. Rev. D*, vol. 95, p. 064 023, 6 Mar. 2017. DOI: 10.1103/PhysRevD.95.064023. [Online]. Available: https://link.aps.org/doi/10.1103/PhysRevD.95.064023.

[158] G. Lukes-Gerakopoulos, "Time parameterizations and spin supplementary conditions of the Mathisson-Papapetrou-Dixon equations," *Physical Review D*, vol. 96, no. 10, 104023, p. 104 023, Nov. 2017. DOI: 10.1103/PhysRevD.96.104023. arXiv: 1709.08942 [gr-qc].

[159] I. Timogiannis, G. Lukes-Gerakopoulos, and T. A. Apostolatos, "Spinning test body orbiting around a Schwarzschild black hole: Comparing Spin Supplementary Conditions for Circular Equatorial Orbits," *arXiv e-prints*, arXiv:2104.11183, arXiv:2104.11183, Apr. 2021. arXiv: 2104.11183 [gr-qc].

[160] W. Tulczyjew, "Motion of multipole particles in general relativity theory binaries," *Acta Phys. Polon. B*, vol. 18, pp. 393–409, 1959.

[161] A. Pound, "Motion of small objects in curved spacetimes: An introduction to gravitational self-force," *arXiv e-prints*, arXiv:1506.06245, arXiv:1506.06245, Jun. 2015. arXiv: 1506.06245 [gr-qc].

[162] L. Barack and A. Pound, "Self-force and radiation reaction in general relativity," *Reports on Progress in Physics*, vol. 82, no. 1, 016904, p. 016 904, Jan. 2019. DOI: 10.1088/1361-6633/aae552. arXiv: 1805.10385 [gr-qc].

[163] A. Pound and B. Wardell, "Black hole perturbation theory and gravitational self-force," *arXiv e-prints*, arXiv:2101.04592, arXiv:2101.04592, Jan. 2021. arXiv: 2101.04592 [gr-qc].

[164] U. Ruangsri, S. J. Vigeland, and S. A. Hughes, "Gyroscopes orbiting black holes: A frequency-domain approach to precession and spin-curvature coupling for spinning bodies on generic Kerr orbits," *Physical Review D*, vol. 94, no. 4, 044008, p. 044 008, Aug. 2016. DOI: 10.1103/PhysRevD.94.044008. arXiv: 1512.00376 [gr-qc].

[165] J. .-. Marck, "Solution to the Equations of Parallel Transport in Kerr Geometry; Tidal Tensor," *Proceedings of the Royal Society of London Series A*, vol. 385, no. 1789, pp. 431–438, Feb. 1983. DOI: 10.1098/rspa.1983.0021.

[166] J.-A. Marck, "Parallel-tetrad on null geodesics in Kerr-Newman space-time," *Physics Letters A*, vol. 97, no. 4, pp. 140–142, 1983, ISSN: 0375-9601. DOI: https://doi.org/10.1016/0375-9601(83)90197-4. [Online]. Available: https://www.sciencedirect.com/science/article/pii/0375960183901974.

[167] N. Kamran and J.-A. Marck, "Parallel-propagated frame along the geodesics of the metrics admitting a Killing-Yano tensor," *Journal of Mathematical Physics*, vol. 27, no. 6, pp. 1589–1591, Jun. 1986. DOI: 10.1063/1.527072.

[168] D. Bini, A. Geralico, and R. T. Jantzen, "Black hole geodesic parallel transport and the marck reduction procedure," *Phys. Rev. D*, vol. 99, p. 064 041, 6 Mar. 2019. DOI: 10.1103/PhysRevD.99.064041. [Online]. Available: https://link.aps.org/doi/10.1103/PhysRevD.99.064041.

[169] D. Bini, A. Geralico, and R. T. Jantzen, "Gyroscope precession along general timelike geodesics in a Kerr black hole spacetime," *Physical Review D*, vol. 95, no. 12, 124022, p. 124 022, Jun. 2017. DOI: 10.1103/PhysRevD.95.124022. arXiv: 1703.09525 [gr-qc].

[170] C. Chicone and B. Mashhoon, "Tidal dynamics in kerr spacetime," *Classical and Quantum Gravity*, vol. 23, no. 12, pp. 4021–4033, May 2006. DOI: 10.1088/0264-9381/23/12/002. [Online]. Available: https://doi.org/10.1088/0264-9381/23/12/002.

[171] L. V. Drummond and S. A. Hughes, "Precisely computing bound orbits of spinning bodies around black holes. I. General framework and results for nearly equatorial orbits," *Physical Review D*, vol. 105, no. 12, 124040, p. 124 040, Jun. 2022. DOI: 10.1103/PhysRevD.105.124040. arXiv: 2201.13334 [gr-qc].

[172] L. V. Drummond and S. A. Hughes, "Precisely computing bound orbits of spinning bodies around black holes. II. Generic orbits," *Physical Review D*, vol. 105, no. 12, 124041, p. 124 041, Jun. 2022. DOI: 10.1103/PhysRevD.105.124041. arXiv: 2201.13335 [gr-qc].

[173] S. A. Teukolsky, "Perturbations of a Rotating Black Hole. I. Fundamental Equations for Gravitational, Electromagnetic, and Neutrino-Field Perturbations," *The Astrophysical Journal*, vol. 185, pp. 635–648, Oct. 1973. DOI: 10.1086/152444.

[174] E. Newman and R. Penrose, "An Approach to Gravitational Radiation by a Method of Spin Coefficients," *Journal of Mathematical Physics*, vol. 3, no. 3, pp. 566–578, May 1962. DOI: 10.1063/1.1724257.

[175] S. A. Teukolsky and W. H. Press, "Perturbations of a rotating black hole. III. Interaction of the hole with gravitational and electromagnetic radiation.," *The Astrophysical Journal*, vol. 193, pp. 443–461, Oct. 1974. DOI: 10.1086/153180.

[176] N. Sago, T. Tanaka, W. Hikida, K. Ganz, and H. Nakano, "Adiabatic Evolution of Orbital Parameters in Kerr Spacetime," *Progress of Theoretical Physics*, vol. 115, no. 5, pp. 873–907, May 2006. DOI: 10.1143/PTP.115.873. arXiv: gr-qc/0511151 [gr-qc].

[177] M. van de Meent and H. P. Pfeiffer, "Intermediate mass-ratio black hole binaries: Applicability of small mass-ratio perturbation theory," *arXiv e-prints*, arXiv:2006.12036, arXiv:2006.12036, Jun. 2020. arXiv: 2006.12036 [gr-qc].

[178] A. Pound and E. Poisson, "Osculating orbits in Schwarzschild spacetime, with an application to extreme mass-ratio inspirals," *Physical Review D*, vol. 77, no. 4, 044013, p. 044 013, Feb. 2008. DOI: 10.1103/PhysRevD.77.044013. arXiv: 0708.3033 [gr-qc].

[179] J. R. Gair, É. É. Flanagan, S. Drasco, T. Hinderer, and S. Babak, "Forced motion near black holes," *Physical Review D*, vol. 83, no. 4, 044037, p. 044 037, Feb. 2011. DOI: 10.1103/PhysRevD.83.044037. arXiv: 1012.5111 [gr-qc].

[180] J. Mathews, A. Pound, and B. Wardell, "Self-Force Calculations with a Spinning Secondary," *arXiv e-prints*, arXiv:2112.13069, arXiv:2112.13069, Dec. 2021. arXiv: 2112.13069 [gr-qc].

[181] See Supplemental Material at [URL will be inserted by publisher] for a *Mathematica* notebook which presents expressions for the functions in Equations (3.24), (4.43) – (4.45), (4.52) – (4.54), and (4.62) – (4.64).

[182] J. Kevorkian and J. D. Cole, *Multiple scale and singular perturbation methods* (Applied mathematical sciences; vol. 114), eng. New York: Springer, 1996, ISBN: 0387942025.

[183] J. McCart, T. Osburn, and J. Y. J. Burton, "Highly eccentric extreme-mass-ratio-inspiral waveforms via fast self-forced inspirals," *Phys. Rev. D*, vol. 104, no. 8, p. 084 050, 2021. DOI: 10.1103/PhysRevD.104.084050. arXiv: 2109.00056 [gr-qc].

[184] P. Lynch, M. van de Meent, and N. Warburton, "Self-forced inspirals with spin-orbit precession," *arXiv e-prints*, arXiv:2305.10533, arXiv:2305.10533, May 2023. DOI: 10.48550/arXiv.2305.10533. arXiv: 2305.10533 [gr-qc].

[185] P. Lynch, "Efficient trajectory calculations for extreme mass-ratio inspirals using near-identity (averaging) transformations," Available electronically at http://hdl.handle.net/10197/13347, Ph.D. dissertation, University College Dublin, 2022.

[186] S. A. Hughes, "Evolution of circular, nonequatorial orbits of kerr black holes due to gravitational-wave emission," *Phys. Rev. D*, vol. 61, p. 084 004, 8 Mar. 2000. DOI: 10.1103/PhysRevD.61.084004. [Online]. Available: https://link.aps.org/doi/10.1103/PhysRevD.61.084004.

[187] S. Drasco and S. A. Hughes, "Rotating black hole orbit functionals in the frequency domain," *Physical Review D*, vol. 69, no. 4, 044015, p. 044 015, Feb. 2004. DOI: 10.1103/PhysRevD.69.044015. arXiv: astro-ph/0308479 [astro-ph].

[188] V. Witzany, J. Steinhoff, and G. Lukes-Gerakopoulos, "Hamiltonians and canonical coordinates for spinning particles in curved space-time," *Classical and Quantum Gravity*, vol. 36, no. 7, 075003, p. 075 003, Apr. 2019. DOI: 10.1088/1361-6382/ab002f. arXiv: 1808.06582 [gr-qc].

[189] *FastEMRIWaveforms package*, bhptoolkit.org/FastEMRIWaveforms_main.html.

[190] F. Moulton, *An Introduction to Celestial Mechanics* (Dover books in astronomy). Dover Publications, 1970, ISBN: 9780486646879. [Online]. Available: https://books.google.com/books?id=URPSrBntwdAC.

[191] L. G. Taff, *Celestial mechanics : a computational guide for the practitioner*. 1985.

[192] G. Beutler, *Methods of celestial mechanics. Vol. I: Physical, mathematical, and numerical principles*. 2005.

[193] C. W. Lincoln and C. M. Will, "Coalescing binary systems of compact objects to (post)$^{5/2}$-Newtonian order: Late-time evolution and gravitational-radiation emission," *Physical Review D*, vol. 42, no. 4, pp. 1123–1143, Aug. 1990. DOI: 10.1103/PhysRevD.42.1123.

[194] J. Kevorkian, "Perturbation techniques for oscillatory systems with slowly varying coefficients," *SIAM Review*, vol. 29, no. 3, pp. 391–461, 1987, ISSN: 00361445. [Online]. Available: http://www.jstor.org/stable/2031238 (visited on 09/13/2023).

[195] V. Witzany, "Action-angle coordinates for black-hole geodesics I: Spherically symmetric and Schwarzschild," *arXiv e-prints*, arXiv:2203.11952, arXiv:2203.11952, Mar. 2022. DOI: 10.48550/arXiv.2203.11952. arXiv: 2203.11952 [gr-qc].

[196] N. Loutrel, S. Liebersbach, N. Yunes, and N. Cornish, "Nature abhors a circle," *Classical and Quantum Gravity*, vol. 36, no. 1, 01LT01, 01LT01, Jan. 2019. DOI: 10.1088/1361-6382/aaf1ec. arXiv: 1801.09009 [gr-qc].

[197] D. G. Keppel, "Signatures and Dynamics of Compact Binary Coalescences and a Search in LIGO's S5 Data," Available electronically at https://thesis.library.caltech.edu/1901/, Ph.D. dissertation, California Institute of Technology, 2009.

[198] T. Robson, N. J. Cornish, and C. Liu, "The construction and use of LISA sensitivity curves," *Classical and Quantum Gravity*, vol. 36, no. 10, 105011, p. 105 011, May 2019. DOI: 10.1088/1361-6382/ab1101. arXiv: 1803.01944 [astro-ph.HE].

[199] *SimulationTools*, (simulationtools.org).

[200] L. Lindblom, B. J. Owen, and D. A. Brown, "Model Waveform Accuracy Standards for Gravitational Wave Data Analysis," *Phys. Rev. D*, vol. 78, p. 124 020, 2008. DOI: 10.1103/PhysRevD.78.124020. arXiv: 0809.3844 [gr-qc].

[201] M. Rahman and A. Bhattacharyya, "Prospects for determining the nature of the secondaries of extreme mass-ratio inspirals using the spin-induced quadrupole deformation," *Physical Review D*, vol. 107, no. 2, 024006, p. 024 006, Jan. 2023. DOI: 10.1103/PhysRevD.107.024006. arXiv: 2112.13869 [gr-qc].

[202] B. Wardell, A. Pound, N. Warburton, J. Miller, L. Durkan, and A. Le Tiec, "Gravitational Waveforms for Compact Binaries from Second-Order Self-Force Theory," *Physical Review Letters*, vol. 130, no. 24, 241402, p. 241 402, Jun. 2023. DOI: 10.1103/PhysRevLett.130.241402. arXiv: 2112.12265 [gr-qc].

[203] S. A. Teukolsky, "Perturbations of a rotating black hole. 1. Fundamental equations for gravitational electromagnetic and neutrino field perturbations," *Astrophys. J.*, vol. 185, pp. 635–647, 1973. DOI: 10.1086/152444.

[204] S. A. Hughes, N. Warburton, G. Khanna, A. J. K. Chua, and M. L. Katz, "Adiabatic waveforms for extreme mass-ratio inspirals via multivoice decomposition in time and frequency," *Physical Review D*, vol. 103, no. 10, 104014, p. 104 014, May 2021. DOI: 10.1103/PhysRevD.103.104014. arXiv: 2102.02713 [gr-qc].

[205] G. A. Piovano, A. Maselli, and P. Pani, "Extreme mass ratio inspirals with spinning secondary: A detailed study of equatorial circular motion," *Physical Review D*, vol. 102, no. 2, 024041, p. 024 041, Jul. 2020. DOI: 10.1103/PhysRevD.102.024041. arXiv: 2004.02654 [gr-qc].

[206] T. Tanaka, Y. Mino, M. Sasaki, and M. Shibata, "Gravitational waves from a spinning particle in circular orbits around a rotating black hole," *Physical Review D*, vol. 54, pp. 3762–3777, 1996. DOI: 10.1103/PhysRevD.54.3762. arXiv: gr-qc/9602038 [gr-qc].

[207] S. Drasco and S. A. Hughes, "Gravitational wave snapshots of generic extreme mass ratio inspirals," *Phys.Rev.*, vol. D73, p. 024 027, 2006. DOI: 10.1103/PhysRevD.73.024027. arXiv: gr-qc/0509101 [gr-qc].

[208] N. Sago, T. Tanaka, W. Hikida, K. Ganz, and H. Nakano, "Adiabatic Evolution of Orbital Parameters in Kerr Spacetime," *Progress of Theoretical Physics*, vol. 115, no. 5, pp. 873–907, May 2006. DOI: 10.1143/PTP.115.873. arXiv: gr-qc/0511151 [gr-qc].

[209] S. Akcay, S. R. Dolan, C. Kavanagh, J. Moxon, N. Warburton, and B. Wardell, "Dissipation in extreme mass-ratio binaries with a spinning secondary," *Phys. Rev. D*, vol. 102, no. 6, 064013, p. 064 013, 2020. DOI: 10.1103/PhysRevD.102.064013. arXiv: 1912.09461 [gr-qc].

[210] J. Mathews, A. Pound, and B. Wardell, "Self-force calculations with a spinning secondary," *Physical Review D*, vol. 105, no. 8, 084031, p. 084 031, Apr. 2022. DOI: 10.1103/PhysRevD.105.084031. arXiv: 2112.13069 [gr-qc].

[211] R. Rüdiger, "Conserved quantities of spinning test particles in general relativity. I," *Proc. R. Soc. Lond. A*, vol. 375, pp. 185–193, 1981. DOI: 10.1098/rspa.1981.0046.

[212] R. Rüdiger, "Conserved quantities of spinning test particles in general relativity. II," *Proc. R. Soc. Lond. A*, vol. 385, pp. 229–239, 1981. DOI: 10.1098/rspa.1981.0046.

[213] S. Drasco and S. A. Hughes, "Gravitational wave snapshots of generic extreme mass ratio inspirals," *Phys. Rev. D*, vol. 73, p. 024 027, 2 Jan. 2006. DOI: 10.1103/PhysRevD.73.024027. [Online]. Available: https://link.aps.org/doi/10.1103/PhysRevD.73.024027.

[214] R. Fujita and H. Tagoshi, "New Numerical Methods to Evaluate Homogeneous Solutions of the Teukolsky Equation," *Progress of Theoretical Physics*, vol. 112, no. 3, pp. 415–450, Sep. 2004, ISSN: 0033-068X. DOI: 10.1143/PTP.112.415. eprint: https://academic.oup.com/ptp/article-pdf/112/3/415/5382220/112-3-415.pdf. [Online]. Available: https://doi.org/10.1143/PTP.112.415.

[215] R. Fujita and H. Tagoshi, "New Numerical Methods to Evaluate Homogeneous Solutions of the Teukolsky Equation. II: — Solutions of the Continued Fraction Equation —," *Progress of Theoretical Physics*, vol. 113, no. 6, pp. 1165–1182, Jun. 2005, ISSN: 0033-068X. DOI: 10.1143/PTP.113.1165. eprint: https://academic.oup.com/ptp/article-pdf/113/6/1165/5285582/113-6-1165.pdf. [Online]. Available: https://doi.org/10.1143/PTP.113.1165.

[216] V. Skoupý and G. Lukes-Gerakopoulos, "Spinning test body orbiting around a Kerr black hole: Eccentric equatorial orbits and their asymptotic gravitational-wave fluxes," *Physical Review D*, vol. 103, no. 10, 104045, p. 104 045, May 2021. DOI: 10.1103/PhysRevD.103.104045. arXiv: 2102.04819 [gr-qc].

[217] G. A. Piovano, A. Maselli, and P. Pani, "Extreme mass ratio inspirals with spinning secondary: a detailed study of equatorial circular motion," *arXiv e-prints*, arXiv:2004.02654, arXiv:2004.02654, Apr. 2020. arXiv: 2004.02654 [gr-qc].

[218] L. V. Drummond and S. A. Hughes, "Precisely computing bound orbits of spinning bodies around black holes I: Nearly equatorial orbits," In prep.

[219] V. Witzany and G. A. Piovano, "Analytic solutions for the motion of spinning particles near spherically symmetric black holes and exotic compact objects," *arXiv e-prints*, arXiv:2308.00021, arXiv:2308.00021, Jul. 2023. DOI: 10.48550/arXiv.2308.00021. arXiv: 2308.00021 [gr-qc].

[220] M. van de Meent, "Analytic solutions for parallel transport along generic bound geodesics in Kerr spacetime," *Classical and Quantum Gravity*, vol. 37, no. 14, 145007, p. 145 007, Jul. 2020. DOI: 10.1088/1361-6382/ab79d5. arXiv: 1906.05090 [gr-qc].

[221] V. Witzany, "Hamilton-Jacobi equation for spinning particles near black holes," *Physical Review D*, vol. 100, no. 10, 104030, p. 104 030, Nov. 2019. DOI: 10.1103/PhysRevD.100.104030. arXiv: 1903.03651 [gr-qc].